Measurement of the CsI calorimeter performance and K_L momentum spectrum for the J-PARC KOTO experiment

Osaka University
Kazufumi Sato

January, 2015

Abstract

The J-PARC KOTO experiment studies the $K_L \to \pi^0\nu\bar{\nu}$ decay by observing two photons from the π^0 using a CsI electromagnetic calorimeter. The calorimeter measures the energy and position of the two photons, and the shapes of electromagnetic showers made by the photons. These are important information to distinguish the signal events from the background events. The energy and position resolutions of the CsI calorimeter, however, had not been fully measured yet in the KOTO experimental condition. The shower shapes had been studied based on a Monte Carlo simulation, but the consistency between real data and the simulation had not been checked yet.

I measured these resolutions and shower shapes in the engineering runs conducted in 2012, by using a spectrometer to track charged particles from K_L decays. The momentum-analyzed electrons from the $K_L \to \pi e\nu$ decays were used as references for the measurement. This was the first test of the calorimeter performance with the actual calorimeter, and also with almost the same condition for the calorimeter operation with the KOTO physics run.

The energy and position resolutions of the CsI calorimeter with the total energy E were measured to be $\sigma_E/E = 0.66\% \oplus 1.81\%/\sqrt{E[GeV]}$ and $\sigma_X = 1.99 \oplus 3.95/\sqrt{E[GeV]}$ mm for 2.5 cm $\times$ 2.5 cm crystals, and $\sigma_E/E = 1.71\% \oplus 1.31\%/\sqrt{E[GeV]}$ and $\sigma_X = 6.17 \oplus 4.01/\sqrt{E[GeV]}$ mm for 5 cm $\times$ 5 cm crystals.

Data – Monte Carlo inconsistencies were found in variables related to the shower shapes. I tested several Monte Carlo conditions, and found that the consistency was improved by modifying the bremsstrahlung model used in the Geant4 simulation.

The engineering runs were also the unique opportunity to measure both charged particles and photons. Taking this opportunity, the momentum spectrum of the K_L beam was measured with the $K_L \to \pi^+\pi^-$ and $K_L \to \pi^+\pi^-\pi^0$ decays, by using the spectrometer and the calorimeter cooperatively. The spectrum shape in > 4 GeV/c region was determined for the first time in KOTO.

Acknowledgment

This thesis could not be achieved without enormous support from many people. First of all, I would like to express my deepest appreciation to my supervisor, Prof. Taku Yamanaka. He gave me a wonderful opportunity for the research in high energy physics. He always warmly supported everything for my study. Through discussions with him, I learned the method of physical thinking.

I would like to thank all the collaborators of the KOTO experiment for their grateful contributions to the engineering runs. I am thankful to Y. Tajima for helping to prepare drift chambers and teaching me the know-how of their operation. I present my appreciation to KEK members, T. Komatsubara, G. Y. Lim, T. Nomura, and H. Watanabe for arrangements of the experimental preparation. Thanks to their support, purchasing and transportation of tools, installing the detectors in the experimental area, and any other experimental setups were prepared smoothly. I would like to appreciate K. Shiomi for the overall management of the runs. I wish to express my appreciation to T. Inagaki, N. Sasao, J. Comfort, S. Suzuki, Y. W. Wah, and M. Campbell for giving me invaluable support and advice on my analysis. I am also grateful to H. Nanjo who is dominantly maintaining the KOTO Monte Carlo system. The operation of the CsI calorimeter in the runs was achieved by enormous efforts of many members. M. Togawa and R. Yongdok directed stacking the crystals. T. Masuda prepared the HV control system for each PMT. The DAQ system was developed by M. Campbell, M. Tecchio, J. Xu and other members of Michigan University. Y. Sugiyama maintained the calorimeter operation through the runs. Y. Yanagida and Y. Nakaya largely contributed for the preparation of the other equipments such as the light guides and insulation sheets. I sincerely thank them for their great efforts.
The installation and cabling for the spectrometer were helped by many staff and students. I would like to acknowledge Y. Maeda, D. Naito, M. Sasaki, N. Kawasaki, H. Yokota, S. Bannno, and T. Shimogawa for giving me a support. In particular, T. Shimogawa gave help not only for the experiment, but also for the daily life during my stay in KEK.
I wish to express my appreciation to the members of Osaka KOTO group, M. Togawa, R. Murayama, Y. Sugiyama, M. Isoe, and K. Miyazaki. They gave me many thoughtful ideas for my analysis through weekly meetings. My special thanks go to E. Iwai

and J. W. Lee who worked on their own thesis around the time of my work. I really enjoyed discussions with them on physics and analysis.

I also appreciate all members of Yamanaka group at Osaka University. I would like to thank K. Hanagaki for his invaluable advice on physics. My special thank goes to Y. Yamauchi, M. Endo, Y. Arai and R. tsuji. I was always relaxed and cheered up by chatting with them. I am also deeply thankful to a secretary of the group, K. Kawahara, for her grateful support.

Finally, I would like to thank my mother Hiroko Sato. She always supports what I want to do. I am sorry for my late father Hideki Sato that I could not complete my work while he was alive. I give sincere thanks to him.

Kazufumi Sato
Osaka, Japan.
February 2015

Contents

List of Figures

List of Tables

Chapter 1

Introduction

Particles and antiparticles were considered to be described with the same Lagrangian. Although quantum numbers between them are opposite each other, it seems that they have no difference in the reaction. This symmetry is called "CP invariance" because particles and antiparticles are related each other through CP conversion. But this symmetry must be violated in order for our universe to exist, because our universe is made of not antiparticles but dominantly particles. A CP violating phenomenon was first observed in a K-meson system by Cronin and Fitch *et al.* in 1964 [6]. The observed phenomenon was explained by the mixing of two CP states in the K-meson system, and called "indirect CP violation". The existence of another type of CP violation which arising from decay amplitudes, called "direct CP violation", was confirmed by FNAL KTeV experiment and CERN NA48 experiment by using K-meson in 1999 [7,8]. In the 2000s, Belle experiment and Babar experiment made a precise measurement of parameters of CP violation with B-meson [9,10], and their result can be fully explained with the theory by Kobayashi and Maskawa [11]. This theory is now considered as one of the center part of the Standard Model of particle physics. This theory is, however, not sufficient to explain the CP asymmetry of the universe. There must be another source of CP violation beyond the Standard Model that we do not know yet.

The rare decays of K and B mesons will play an important role to search for such origin of CP violation beyond the Standard Model. In particular, $K_L \to \pi^0\nu\bar{\nu}$ decay is one of the most sensitive probe. The branching ratio of $K_L \to \pi^0\nu\bar{\nu}$ is predicted with a high degree of precision in the Standard Model. If a new physics exists, the branching ratio could be different from this prediction.

Although several experiments have searched for $K_L \to \pi^0\nu\bar{\nu}$ decay, this decay has not been observed yet. J-PARC KOTO experiment is trying to make the first observation of this rare decay. This thesis describes several studies that we have conducted in the engineering runs in the first half of 2012, to lead the KOTO experiment to a success.

This chapter reveals the purpose and outline of this thesis. I will start from introducing the theory of CP violation followed by that of $K_L \to \pi^0\nu\bar{\nu}$ decay. I will then explain the KOTO experiment. Finally I will describe the theme of this thesis.

1.1 CP Violation in Standard Model

1.1.1 CP Violation

"CP" represents the multiplication of operations of Charge conjugation (C) and Parity inversion (P). CP can be interpreted as an operation to exchange particles and antiparticles. If a Lagrangian is not invariant under this operation, it is said that "CP is violated".

In the standard model, the charged current of weak interaction, or the interaction involving a W boson, can violate CP. The Lagrangian for the charged current is described as

$$\mathcal{L} = -\frac{g_w}{2\sqrt{2}} \left(\bar{u}_i \gamma^\mu (1-\gamma^5) V_{ij} d_j W_\mu^+ + \bar{d}_j \gamma^\mu (1-\gamma^5) V_{ij}^* u_j W_\mu^- \right), \tag{1.1}$$

where u_i (d_i) represents up(down)-type quark and subscripts i and j denote the generation of quarks. The V_{ij} is a complex constant representing the strength of coupling constant between u_i and d_j. Because there are three generations, V is interpreted as a 3×3 matrix, which is called Cabibbo-Kobayashi-Maskawa matrix (CKM matrix). Under a CP conversion, the Lagrangian changes as:

$$\mathcal{L}_{CP} \equiv (CP)\mathcal{L}(CP)^{-1} = -\frac{g_w}{2\sqrt{2}} \left(\bar{u}_i \gamma^\mu (1-\gamma^5) V_{ij}^* d_j W_\mu^+ + \bar{d}_j \gamma^\mu (1-\gamma^5) V_{ij} u_j W_\mu^- \right). \tag{1.2}$$

If a CP violation exists, these two Lagrangian should not be equal. Comparing Eq. (1.1) and Eq. (1.2), that condition is satisfied if V includes complex elements, *ie*:

$$\mathcal{L} \neq \mathcal{L}_{CP} \Rightarrow V_{ij} \neq V_{ij}^*. \tag{1.3}$$

Hense, the study of CP violation in the standard model is the study of the magnitude of an imaginary component in the CKM matrix.

1.1.2 Unitarity Triangle

CKM matrix can be parameterized by three mixing angles, θ_{12}, θ_{23}, and θ_{13}, and a CP-violating phase δ as

$$\begin{aligned} V &\equiv \begin{pmatrix} V_{ud} & V_{us} & V_{ub} \\ V_{cd} & V_{cs} & V_{cb} \\ V_{td} & V_{ts} & V_{tb} \end{pmatrix} \\ &= \begin{pmatrix} c_{12}c_{13} & s_{12}c_{13} & s_{13}e^{-i\delta} \\ -s_{12}c_{23} - c_{12}s_{23}s_{13}e^{-i\delta} & c_{12}c_{23} - s_{12}s_{23}s_{13}e^{-i\delta} & s_{12}c_{13} \\ s_{12}s_{23} - c_{12}c_{23}s_{13}e^{-i\delta} & -c_{12}s_{23} - s_{12}c_{23}s_{13}e^{-i\delta} & c_{23}c_{13} \end{pmatrix} \end{aligned} \tag{1.4}$$

where $s_{ij} = \sin\theta_{ij}$ and $c_{ij} = \cos\theta_{ij}$.

Because the CKM matrix is unitary, it satisfies a unitarity condition,

$$V_{ud}V_{ub}^* + V_{cd}V_{cb}^* + V_{td}V_{tb}^* = 0. \tag{1.5}$$

This condition is represented as a triangle in the complex plane, as shown in Fig. 1.1.

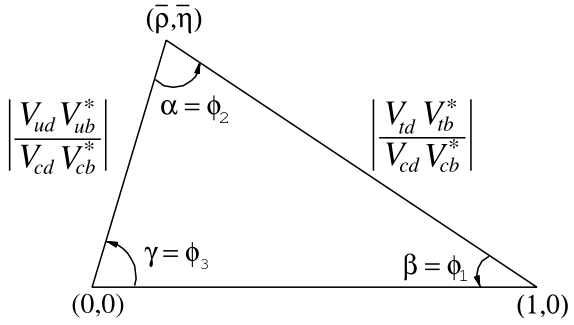

Figure 1.1: The unitarity triangle

Each side of the triangle is divided by $V_{cd}V_{cb}^*$, so two vertices of the base are exactly (0,0) and (1,0). The top vertex is $(\bar{\rho}, \bar{\eta})$, where $\bar{\rho}$ and $\bar{\eta}$ are defined as [12]:

$$\bar{\rho} = \rho\left(1 - \frac{\lambda^2}{2}\right) \text{ and } \bar{\eta} = \eta\left(1 - \frac{\lambda^2}{2}\right), \tag{1.6}$$

where Wolfenstein parameters, ρ, η, and λ, are used for convenience [13]. The ρ, η, and λ are related to the CKM matrix elements as

$$\lambda = s_{12}, \quad A\lambda^2 = s_{23}, \quad A\lambda^3(\rho + i\eta) = s_{13}e^{i\delta}. \tag{1.7}$$

From Eq. (1.6) and Eq. (1.7),

$$\bar{\eta} \propto \mathrm{Im}(e^{i\delta}). \tag{1.8}$$

Thus, the magnitude of the imaginary part in the CKM matrix is visualized as the height of the unitarity triangle, $\bar{\eta}$.

1.2 $K_L \to \pi^0\nu\bar{\nu}$ Decay

The $K_L \to \pi^0\nu\bar{\nu}$ decay is one of the most sensitive probe to study the origin of CP violation. In the standard model, we can derive the height of the unitarity triangle $\bar{\eta}$ directly from the branching ratio of this decay with a small theoretical uncertainty. Also, the branching ratio has a possibility to be different from the expectation of the standard model if a new physics beyond the standard model exists.

1.2.1 $K_L \to \pi^0\nu\bar{\nu}$ Decay in the Standard Model

The leading diagrams of the decay from a K^0 to a $\pi^0\nu\bar{\nu}$ state are shown in Fig. 1.2. Each of three diagrams has an electoroweak loop with a virtual top quark. Conse-

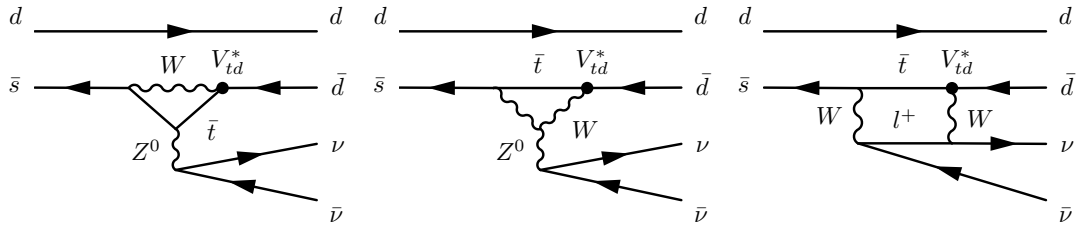

Figure 1.2: Leading diagrams of $K^0 \to \pi^0\nu\bar{\nu}$

quently the amplitude of K^0 includes a CKM matrix element $V_{ts}V_{td}^*$. In contrast, the amplitude of $\bar{K}^0$ includes $V_{ts}^*V_{td}$ because the flowing direction of quarks are opposite.

Because the particle K_L is the mixture of K^0 and $\bar{K}^0$ states:

$$|K_L > \ \sim \ \frac{1}{\sqrt{2}}\left(|K^0 > -|\bar{K}^0 >\right), \tag{1.9}$$

K_L decay amplitude, $A(K_L \to \pi^0\nu\bar{\nu})$, is also a mixture of the amplitudes of K^0 and $\bar{K}^0$. Due to the minus sign of Eq. (1.9), the real part of K^0 and $\bar{K}^0$ cancel out each other. As a result, only the imaginary part of $V_{ts}^*V_{td}$ remains, as:

$$\begin{aligned} A(K_L \to \pi^0\nu\bar{\nu}) &\propto A(K^0 \to \pi^0\nu\bar{\nu}) - A(\bar{K}^0 \to \pi^0\nu\bar{\nu}) \\ &\propto Im\,(V_{ts}^*V_{td}) \\ &\propto \bar{\eta}, \end{aligned} \tag{1.10}$$

where Eq. (1.4), Eq. (1.6), and Eq. (1.7) were used. Thus, the branching ratio of $K_L \to \pi^0\nu\bar{\nu}$ decay is directly related to the height of the unitarity triangle $\bar{\eta}$.

In a quantitative form, the branching ratio can be represented as [14]

$$Br(K_L \to \pi^0\nu\bar{\nu}) = \kappa \left(\frac{Im\,(V_{ts}^* V_{td})}{\lambda^5} X(x_t) \right)^2, \tag{1.11}$$

where $X(x_t)$ is relevant to the top quark in the loop, and κ summarizes all other contributions. The $X(x_t)$ is well studied and precisely calculated including QCD corrections [15,16]. The κ is difficult to calculate because it includes a hadronic matrix element, but it can be extracted from the branching ratio of $K_L \to \pi e\nu$ which is a well-known leading decay channel of K_L [17,18]. The branching ratio in the Standard Model is then estimated [19] as

$$Br(K_L \to \pi^0\nu\bar{\nu}) = 2.43 \pm 0.39, \tag{1.12}$$

with a small theoretical uncertainties of only 2%.

1.2.2 $K_L \to \pi^0\nu\bar{\nu}$ Decay beyond the Standard Model

The $K_L \to \pi^0\nu\bar{\nu}$ decay occurs via loop diagrams. If a new particle which is predicted in some new physics models beyond the standard model propagates in the loop, the branching of the $K_L \to \pi^0\nu\bar{\nu}$ decay will be different from the standard model prediction. One of such new physics models is the Minimal Supersymmetric Standard Model (MSSM) which is the minimal extension to the standard model including features of supersymmetry theory. In the MSSM, the $K_L \to \pi^0\nu\bar{\nu}$ decay is possible to have a new CP-violating phase. As a result, the branching ratio is possible to be a few times 10^{-10}, that is, 10 times larger than the standard model prediction [20].

Some new physics models predict that the deviation of the branching ratio of the $K_L \to \pi^0\nu\bar{\nu}$ decay from the standard model prediction will correlate with that of the $K^+ \to \pi^+\nu\bar{\nu}$ decay. The predicted correlation in Minimal Flavor Violation model and other three new physics models [1] are shown in Fig. 1.3. The branching ratio of $K^+ \to \pi^+\nu\bar{\nu}$ decay was measured by BNL E949 group as $Br(K^+ \to \pi^+\nu\bar{\nu}) = 1.73^{+1.15}_{-1.05} \times 10^{-10}$ [21], and a further precise measurement by CERN NA62 group is in preparation. Combining their results, the measurement of the branching ratio of $K_L \to \pi^0\nu\bar{\nu}$ decay can put a strong restriction on some physics models.

1.2.3 History of $K_L \to \pi^0\nu\bar{\nu}$ Search

Several experiments to search for the $K_L \to \pi^0\nu\bar{\nu}$ decay were conducted as shown in Fig. 1.4. The upper limit of the branching ratio is given by KEK E391a group [22], as

$$Br(K_L \to \pi^0\nu\bar{\nu}) = 2.6 \times 10^{-8} (90\% C.L.). \tag{1.13}$$

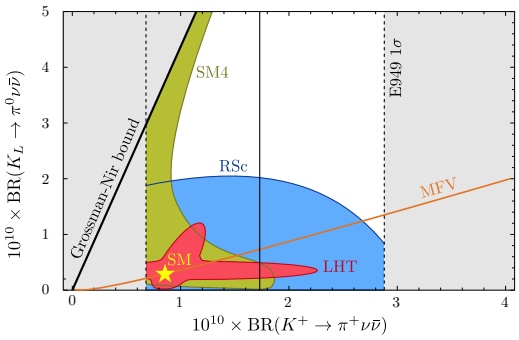

Figure 1.3: Predicted correlation between the branching ratio of $K_L \to \pi^0\nu\bar{\nu}$ decay and $K_+ \to \pi^+\nu\bar{\nu}$ decay in various new physics models. The grey area was ruled out experimentally. The SM prediction point is marked by a star. This figure is quoted from the reference [1].

1.3 KOTO Experiment

In this section I describe a basic strategy of KOTO experiment designed to observe $K_L \to \pi^0\nu\bar{\nu}$ decay. Through that, I am going to reveal important roles of the CsI calorimeter which is the main detector of the KOTO experiment.

1.3.1 Introduction of KOTO Experiment

The purpose of KOTO experiment is to measure the branching ratio of the $K_L \to \pi^0\nu\bar{\nu}$ decay. We plan to have two phases of the measurement, Step 1 and Step 2. The goal of Step 1 is to make the first observation of the decay. In Step 2, we plan to measure the branching ratio by accumulating more than 100 decay events. In the following, I will concentrate on the Step 1 experiment.

The experiment is conducted in J-PARC [3] which is the accelerator facility in Tokai village, Japan. Protons are accelerated to 30 GeV and extracted to hit a fixed target. K_L mesons generated at the target are guided to a 2 m-long vacuum decay volume. We observe K_L mesons decaying in that volume. Detailed descriptions for the beam facilities will be given in Chapter 2.

1.3.2 Signature of $K_L \to \pi^0\nu\bar{\nu}$

$K_L \to \pi^0\nu\bar{\nu}$ decay has a unique feature, that is, the observable particles in the final state are only two gammas from π^0, and the π^0 has a transverse momentum (Pt) because of missing neutrinos. Because no other K_L decay mode has such a final

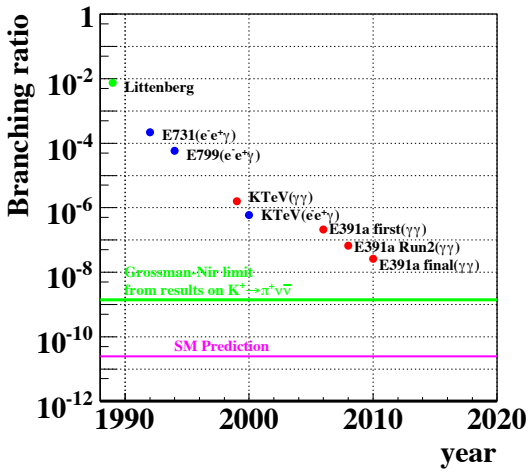

Figure 1.4: History of $K_L \to \pi^0\nu\bar{\nu}$ decay search.

state,[1] this is a signature of $K_L \to \pi^0\nu\bar{\nu}$ decay. We search for this unique feature, 2γ + Pt, by the following steps.

1. Observe two gammas with a calorimeter.

   Two gammas are the sole observable particles in this decay mode. They are observed by the CsI electromagnetic calorimeter which consists of 2716 undoped CsI crystals used in the FNAL KTeV experiment. The CsI calorimeter is located in the downstream of the decay volume. It measures the energies and incident positions of the two gammas.

2. Reconstruct decay vertex.

   The π^0 decay vertex is reconstructed to calculate its Pt, as well as to ensure that the decay occurs within the decay volume. The vertex is calculated from the energies and incident positions of two gammas, which are measured with the CsI calorimeter. Assuming that observed two gammas are produced from a π^0 decay, that is, their invariant mass is equal to π^0 mass, the opening angle between the two gammas (θ) can be calculated by using the conservation law of 4-momentum as

   $$\cos\theta = 1 - \frac{m_{\pi^0}^2}{2E_1E_2}, \tag{1.14}$$

   where m_{π^0} is a mass of π^0, and $E_{1,2}$ are energies of the two gammas. With two more assumptions that the decay vertex is located on the beam axis and is located in upstream of the CsI calorimeter, a position satisfying Eq. (1.14) is

[1] $K_L \to \gamma\gamma$ decay also has only two gammas in its final state, but the Pt of the two gammas is balanced.

decided uniquely in many cases,[2] as shown in Fig. 1.5(a). We require that the Pt, calculated from the reconstructed vertex position, should be greater than 130 MeV/c.

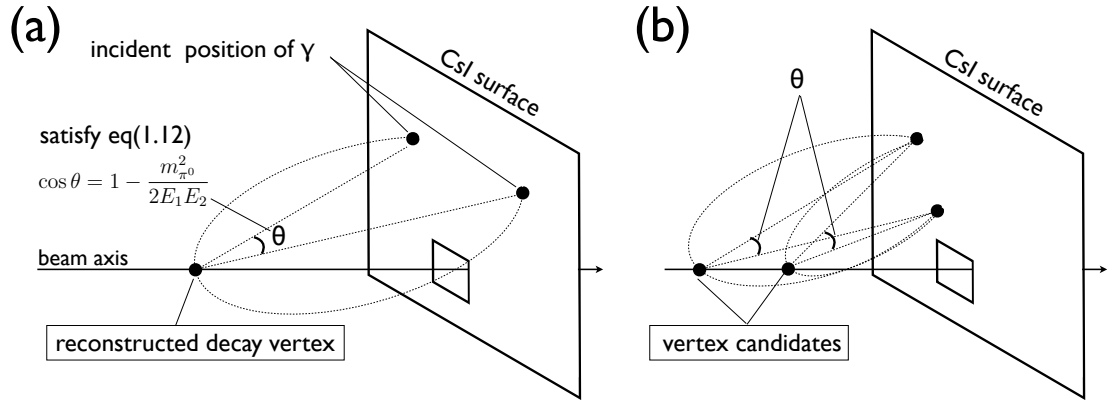

Figure 1.5: Schematic view of the decay vertex reconstruction. (a) The vertex is found on the circle which passes through the two incident positions of gammas, and of which circumferential angle satisfies Eq. (1.14). We define the decay vertex as the intersection point of the circle and the beam axis. There are such points both in upstream and downstream of the CsI calorimeter. We adopt the upstream one. (b) An example of the case in which multi-vertexs exist. We discard such events.

3. Veto extra particles.

   To make sure that there are no observable particles except two gammas, we cover the decay volume with hermetic veto counters as shown in Fig. 1.6. All detectors in the figure except the CsI calorimeter are veto counters.

1.3.3 Backgrounds Suppression

The background events arise from the other K_L decays or neutrons in the beam. Although most of the other K_L decays involve charged particles or extra gammas that can be vetoed, a measurable amount of them escape detection of the veto counters due to the finite efficiency. Those decays are misidentified as the $K_L \to \pi^0\nu\bar{\nu}$ decay if all the particles to be vetoed are missed. The neutrons in the beam can be background sources by interacting with the detector component. Although the CsI calorimeter and the other veto detectors have beam holes to pass the core part of the beam, a small

[2]Sometimes multi-vertexes satisfy Eq. (1.14) as shown in Fig. 1.5(b). In that case, the event is just discarded.

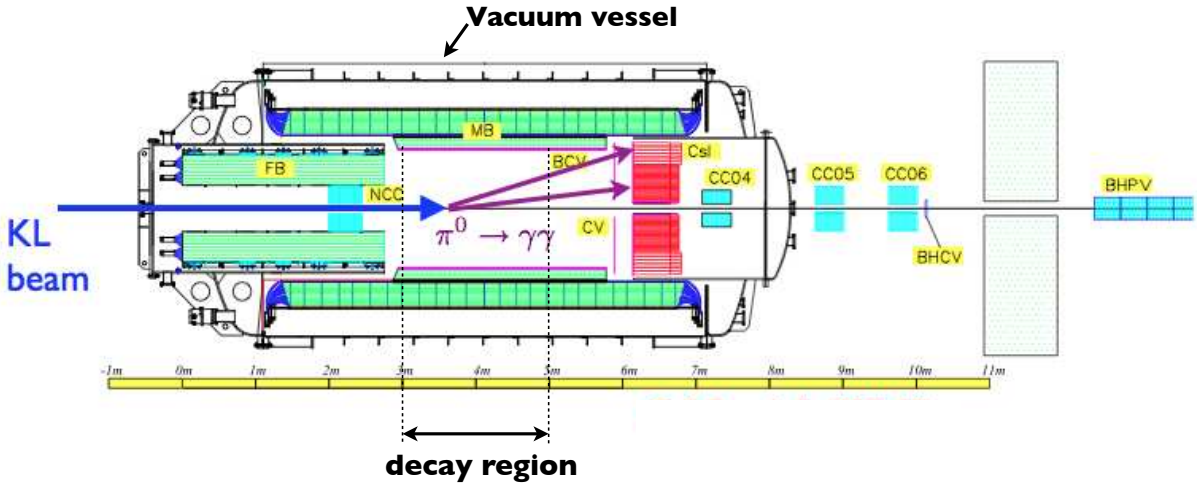

Figure 1.6: The KOTO detector. All detector components except for the CsI calorimeter are veto counters. The 2-m decay volume is also shown.

portion of the beam neutrons spreads over the sizes of the beam holes. They are called halo neutrons. The secondary particles which are generated from the interaction of halo neutrons with the detector component sometimes mimics $K_L \to \pi^0\nu\bar{\nu}$ decay and becomes a background. Some examples of beam-neutron background are shown in Fig. 1.7.

Those backgrounds are suppressed by kinematic cuts and shower shape cuts. The kinematic cuts are based on the energies and incident positions measured by the CsI calorimeter. The cuts are designed to distinguish characteristic distributions of background. The shower shape cuts compares the shape of shower observed in the CsI calorimeter with the shape expected by Monte Carlo simulation. Because the CsI calorimeter consists of crystals with smaller cross-section than Moliere radius, the electromagnetic shower spreads over many crystals and we can observe its shape. Some backgrounds have a hadronic shower or a shower overlapped multi-gammas. Those backgrounds are strongly suppressed by shower shape cuts.

The number of signal events and background events from the $K_L \to \pi^0\pi^0$ decay which are expected to be the largest background are estimated with a Monte Carlo simulation as shown in Table 1.1. The numbers in the table represent for the case of a twelve-months data taking with designed beam intensity (2×10^{14} protons on a production target every 3.3-sec beam cycle). The ratio of the signal and the background events increases from 0.5 to 1.7 before and after applying these cuts. A detailed explanation for the $K_L \to \pi^0\pi^0$ background and the other backgrounds is given in Appendix A. Details for the kinematic cuts and the shower shape cuts are also given in Appendix A. I want to emphasis here the fact that both of kinematics and shower shapes are solely measured by the CsI calorimeter. The performance of the CsI calorimeter thus directly

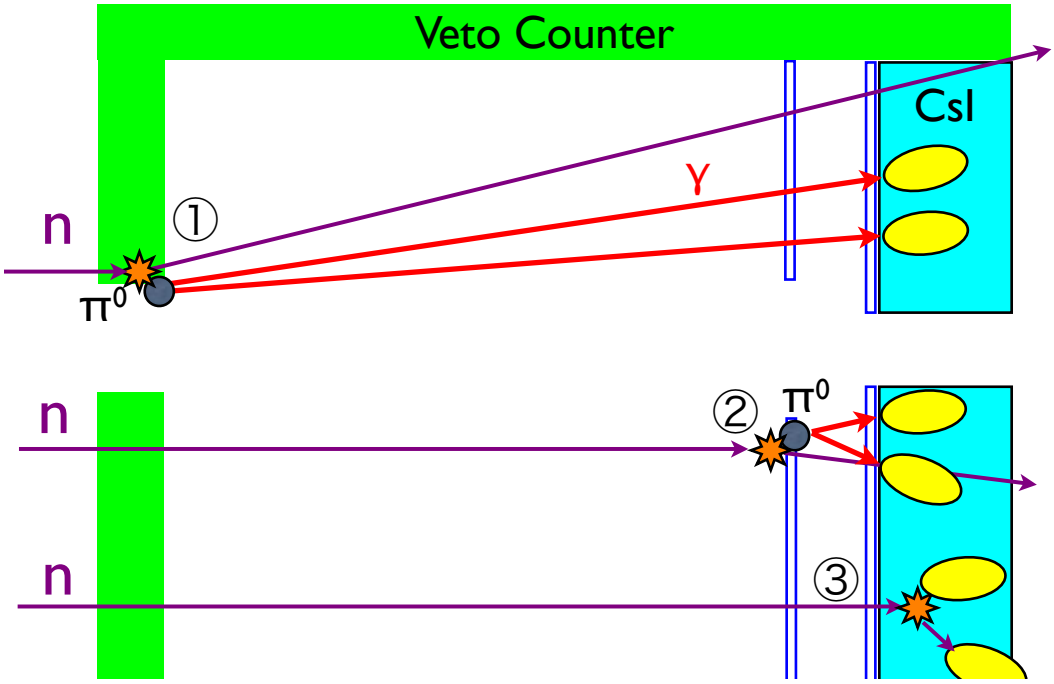

Figure 1.7: Schematic view of neutron backgrounds. Halo neutrons sometimes interact with the detector component near the beam hole. The secondary particles make activities in the CsI calorimeter that mimics the $K_L \to \pi^0\nu\bar{\nu}$ decay.

influences the signal-to-background ratio.

1.4 Engineering Runs in 2012

The CsI calorimeter is the main detector of the KOTO experiment as described in the previous section. The construction of the CsI calorimeter started in 2008 from transferring the CsI crystals from FNAL to J-PARC. All the crystals had been stacked in the KOTO experimental area by February 2011. Although J-PARC had a large earthquake in March 2011, the calorimeter did not suffer a significant damage. After waiting for restoration of accelerator facilities, we conducted engineering runs in February and June in 2012.

These were the first tests to operate the CsI calorimeter in almost the same condition with the physics run. In that time, we had not yet measured a basic performance of the

Table 1.1: The number of signal events and background events from the $K_L \to \pi^0\pi^0$ decay expected in 12-months data taking with designed beam intensity. The number in each column shows the number of events remaining after requiring selection cuts which are shown in the top row. The selection cuts are applied in sequence from the left .

	2γ on CsI	Pt & Z	veto	kinematics	shower shape
$K_L \to \pi^0\nu\bar{\nu}$	42.3	15.8	6.73	3.62	2.99
$K_L \to \pi^0\pi^0$	1.99×10^9	3.34×10^8	12.9	5.46	1.72

calorimeter such as an energy resolution and position resolution.[3] We had not checked the consistency of Monte Carlo simulation for electromagnetic shower shapes on the calorimeter, either. Uncertainties of these issues will directly affect the effectiveness of the kinematic cuts and the shower shape cuts which were introduced in the previous section. One of the main purposes of the engineering runs was to study the shower shape and the resolutions of the CsI calorimeter.

A beam test with a small number of crystals had been carried out [4] while the crystals were still in the process of stacking. The issues listed above, however, were not studied because a clustering process, which is a process to group CsI crystals with finite energy deposits and reconstruct an incident gamma, was not carried out due to a limited number of CsI crystals used in the test.

In the engineering runs, I used electrons which were generated from $K_L \to \pi e\nu$ decays as a reference to study the shower shape and the resolutions. The response of the CsI calorimeter to gammas can be well approximated by the response to electrons, because electrons make electromagnetic showers with almost the same mechanism as gammas. In the engineering runs, the veto counters and the vacuum vessel were not installed yet in the experimental area, and a space upstream of the CsI calorimeter to install them was vacant. In that space, I installed a spectrometer which consisted of three drift chambers and a magnet, to measure momenta and incident positions of electrons. These runs were the last chance to use beam electrons to study the calorimeter, because an installation of the veto counters and the vacuum vessel soon started after the engineering runs and no trackers were available after installing them.

The engineering runs were also considered as a unique opportunity that we could measure both charged particles and gammas. Taking this opportunity, I observed

[3]The KTeV experiment group had already measured those resolutions when they were using the CsI crystals in FNAL. A beam condition, however, was different from that of KOTO experiment and their result cannot directly adopted to KOTO. A typical energy of incident gammas in KTeV experiment was over 10 times larger than that in our experiment. In addition, polar angles of incident gammas in our experiment will be distribute widely up to ~ 30 deg while they were almost ~ 0 degree in KTeV experiment.

$K_L \to \pi^+\pi^-$ and $K_L \to \pi^+\pi^-\pi^0$ decays in order to measure the K_L momentum spectrum. All particles in the final states of those decays can be observed by using the spectrometer and the CsI calorimeter cooperatively, and a momentum of parent K_L can be exclusively reconstructed. The K_L momentum spectrum has been already measured [23], but that measurement had no acceptance in the momentum region higher than 4 GeV/c. My measurement complement the previous work.

1.5 Overview of the Thesis

In this thesis, I studied the following three issues with the data from the engineering runs conducted in 2012.

1. A consistency check for electromagnetic shower shape between a Monte Carlo simulation and the data.
2. A measurement for an energy and position resolution of the CsI calorimeter.
3. A measurement for K_L momentum spectrum.

In this chapter, I have introduced the basic issues about CP symmetry, $K_L \to \pi^0\nu\bar{\nu}$ decay and KOTO experiment, and revealed the motivation of this thesis. I show the result of the engineering runs in the rest of the thesis.

I describe an experimental apparatus and conditions of the engineering runs in Chapter 2. The analysis regarding the CsI calorimeter is described in Chapter 3, while the analysis of the spectrometer is in Chapter 4. I describe an energy calibration of the CsI calorimeter with electrons as a separate chapter in Chapter 5, because this calibration process involves both of the spectrometer and the CsI calorimeter analyses, and also the electron selection criteria which is introduced in that chapter is important in the following chapters. Chapter 6, 7, and 8 are devoted to the measurement of the main three topics listed above, respectively. The impact that this thesis will give on the KOTO physics run is discussed in Chapter 9. Chapter 10 concludes this thesis.

Chapter 2

Apparatus of the Engineering Run

In this chapter, I will describe the experimental apparatus of the engineering runs conducted in February and June of 2012. I will first explain the beam facilities followed by the detectors. The data acquisition systems and run conditions will be also described.

Let us define a coordinate system here. The origin is placed on the K_L beam axis, 21 m downstream of the production target. The z axis is parallel to the K_L beam axis, pointing downstream. The y axis points vertically up, and the x axis points to the direction for the system to be right-handed. Hereafter I will use this coordinate system unless otherwise stated.

2.1 K_L Beam

2.1.1 Primary Proton Beam and Production Target

The Japan Proton Accelerator Research Complex (J-PARC) is a high-intensity proton accelerator facility in Japan. It consists of three accelerators: a linear accelerator (Linac), a 3-GeV Rapid-Cycling Synchrotron (RCS) and a 30-GeV synchrotron (Main Ring), as shown in Fig. 2.1. Protons are accelerated up to 30 GeV through these accelerators before extracted toward a production target in the Hadron Experimental Hall. The production target was a platinum rod with 60 mm in length and 6 mm in diameter. The flux of extracted protons was almost flat for 2.6 seconds, and we took data in this flat duration (spill). The beam was extracted every 6 seconds. Typical

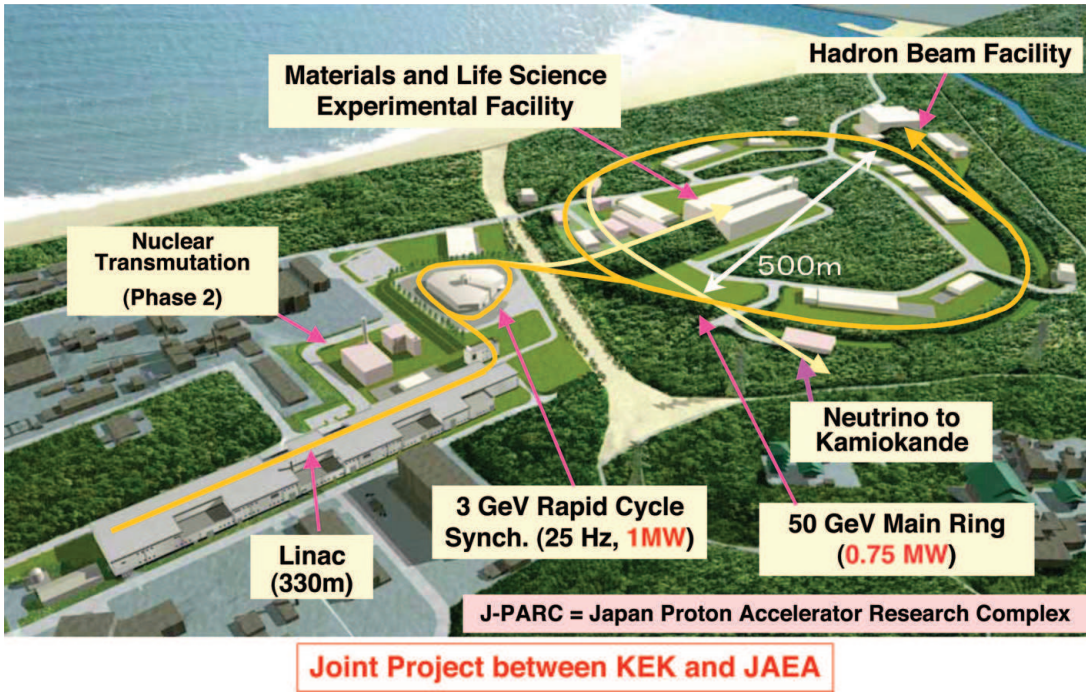

Figure 2.1: Overall view of J-PARC. The KOTO experiment is held in the hadron experimental hall located in the "Hadron Beam Facility". Though the energy of the Main Ring is described as 50 GeV in the figure, protons are currently accelerated up to 30 GeV. This figure is quoted from the reference [2]

beam intensity at the target was 4×10^{12} protons per spill [1].

The experimental hall was designed to deliver the secondary particles from the target to several experiments simultaneously through different beam lines. The layout of the hall in 2012 is shown in Fig. 2.2. The engineering runs were conducted on the KL beam line which is located in the south area of the hall.

2.1.2 K_L Beam Line

The K_L beam line is directed at 16 degrees from the primary proton beam axis. The beam line consists of a gamma absorber, a 2-tesla dipole magnet and two collimators as shown in Fig. 2.3.

Almost all neutral particles generated at the production target decay while passing through the beam line, except gammas, neutrons and K_Ls. The gamma absorber,

[1] With the design value, J-PARC will provide 2×10^{14} protons every 3.3-second beam cycles. In that condition, the target will be a water-cooled nickel disk which is designed to be easy for cooling.

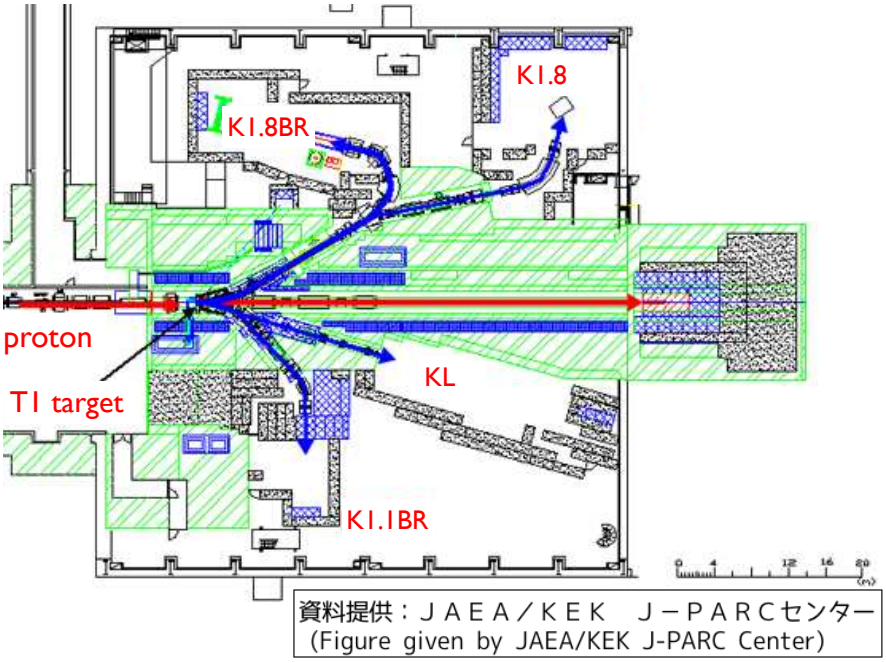

Figure 2.2: Layout of the hadron experimental hall in the engineering runs. This figure is given by the J-PARC Center [3].

which is a 7-cm-thick lead block, reduces the gamma flux in the beam. The dipole magnet swept out charged particles either from the decays in flight or from the target. Thus, the beam includes dominantly neutrons and K_Ls at the exit of the beam line.

The beam profile is shaped into a narrow square by the collimators which are made of iron, and partly embedded tungsten alloys. The collimators are designed carefully to reduce the beam neutrons scattering on its surface, because such scattering produces the halo neutrons which are the background sources of KOTO experiment as already discussed in Section 1.3. The detail design of the collimators is described in [24]. The beam profile after shaping by the collimators is shown in Fig. 2.4, which is simulated by using Geant3. The ratio of halo neutrons to beam core neutrons is well suppressed to the order of 10^{-5}.

The K_L flux after passing through the beam line was already measured in 2010 [23]. The number of K_Ls at the exit of beam line was estimated as 4.19×10^7 K_Ls per 2×10^{14} protons on the target.

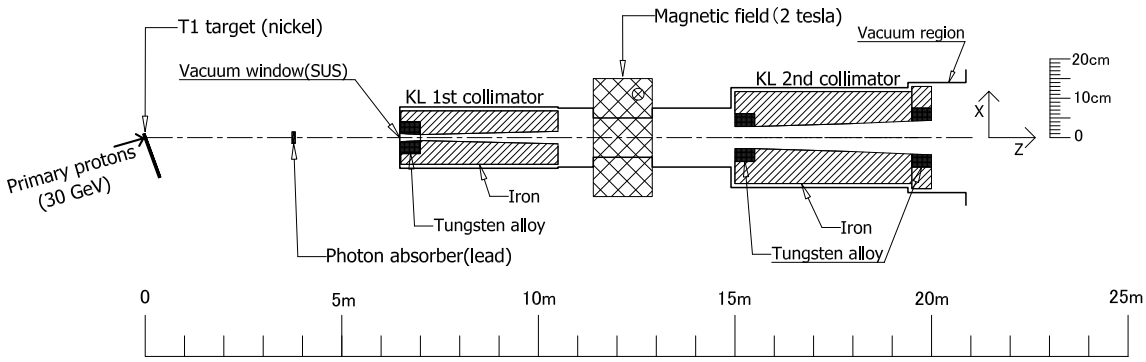

Figure 2.3: Schematic view of K_L beam line. The ruler shows the distance from the production target

2.2 Detectors

The layout of detectors in the engineering runs is shown in Fig. 2.5. There were two detectors: the spectrometer and the CsI calorimeter.

2.2.1 Spectrometer

The spectrometer was used to measure momenta and track paths of charged particles. It consisted of a dipole magnet, three drift chambers and trigger scintillators.

Magnet

A view of the spectrometer magnet is shown in Fig. 2.6. The center position of the magnet was located at z=1600 mm. The iron return yoke of the magnet had a window-frame structure, and the gap between the two poles was 1400 mm in x, 800 mm in y and 800 mm in z directions. Coils were placed in the gap. They were bent up or down at the entrance and exit of the gap, in order not to obstruct paths of incident charged particles. In order to suppress fringe field, 10-cm-thick iron plates, called end guards, were placed on each side of the yoke. The end guard on the upstream side had a 600×300-mm^2 hole, while the one on the downstream side had a 1100×702-mm^2 hole. The magnet was operated with 2400 A of current. The field strength at the center of the magnet was 0.7 Tesla, and its direction was downward.

The magnetic field was measured before installing the magnet in the experimental area. The measured points were arranged in a grid-like pattern. The interval of the

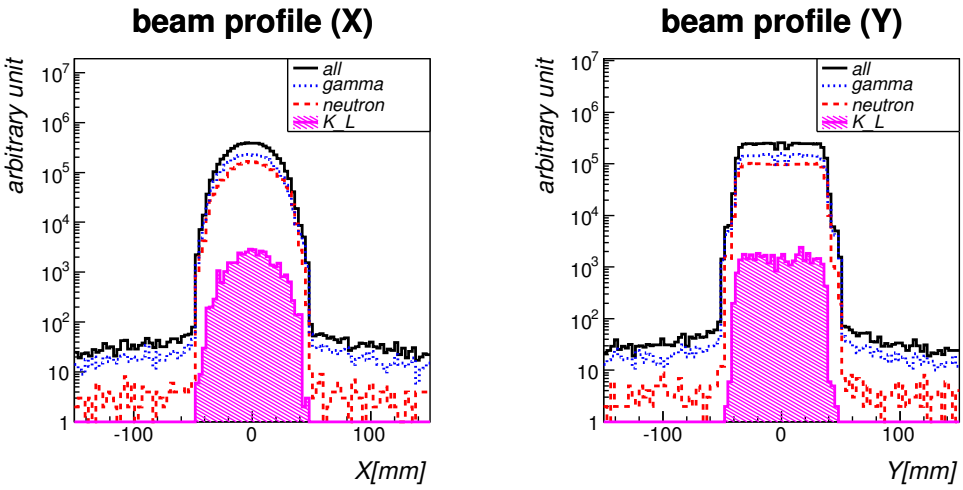

Figure 2.4: Beam profile at Z=0 m simulated using Geant3.

grid points were 60 mm (20, 30 mm) in the x (y, z) direction. The gap between points were interpolated linearly. The measurement was done only for the first quadrant, that is, $x > 0$ and $y > 0$ region. For other quadrant regions, the measured field was appropriately inverted and used. The measurement covered from -1000 mm to +970 mm in the z direction with respect to the center of the magnet. For the field outside of the measured range, I calculated it using ANSYS [25] which is a software for a numerical calculation with a finite element method. The calculated values are shown in Fig. 2.7.

The whole field was scaled by a factor 0.98 to match the K_L mass (= 497.614 MeV/c^2 [26]) measured with $K_L \to \pi^+\pi^-$ analysis, which will be described later in Chapter 8.

Drift chambers

Three drift chambers were used in the spectrometer. We will call them "1st chamber", "2nd chamber" and "3rd chamber", respectively, in the order from the upstream. The 1st chamber was located between the magnet poles, and the other two were placed just downstream of the downstream end-guard. The center positions of the 1st, 2nd, and 3rd chambers were located at z=1576.5 mm, 2640 mm, and 2909 mm, respectively.

All the chambers had four sense-wire planes, y, y', x, and x'. The number and the spacing of the sense wires are summarized in Table 2.1. The y and y' (or x and x') wires were parallel, and staggered by a half of the wire spacing. The y' wires of

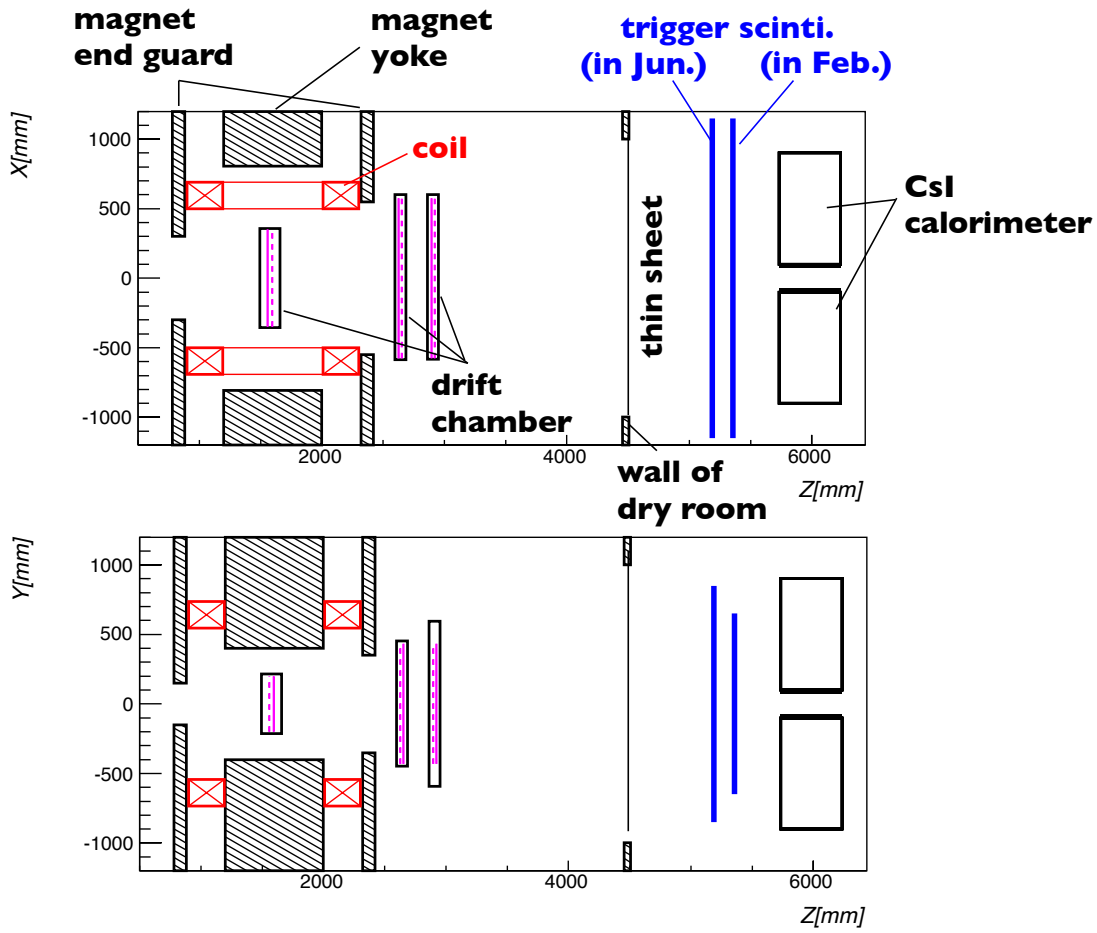

Figure 2.5: Layout of detectors in the engineering runs. The top (bottom) figure shows the view in the x-z (y-z) plane. The CsI calorimeter and the trigger scintillators were placed inside a dry room. The position of the trigger scintillators was different between the February run and the June run.

the 2nd chamber were not active because the readout electronics for them were not functioning.

Field wires were placed around each sense wire to form a hexagonal cell. They were applied negative high voltage in order to form an electric field to drift ionization electrons, which were produced by charged particles passing through the cells, toward the sense wires. Guard wires were placed at the outermost side of the chambers in order to shape the electric field and to reject the electrons produced outside the cells. As for the 1st chamber, the guard wires were also placed at the center of the chamber. The layout of the wires are illustrated in Fig. 2.8. Materials, diameters and applied voltage of the wires are summarized in Table 2.2.

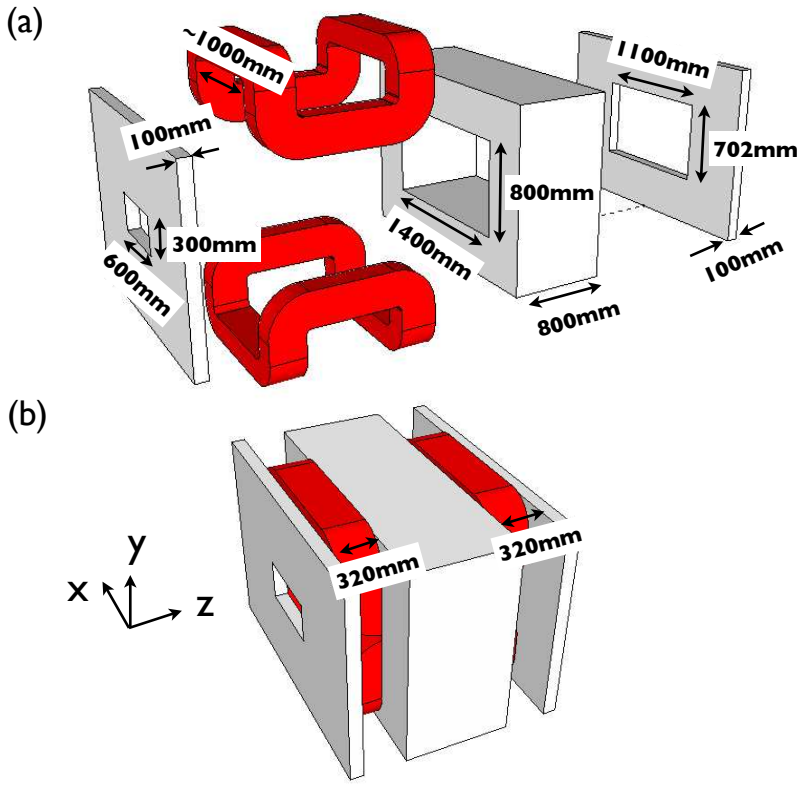

Figure 2.6: (a) Components of the spectrometer magnet. In order from the left, they are the upstream end guard, electric coils, the return yoke, and the downstream end guard. (b) Overview of the magnet unifying the components.

The front and back of each chambers were covered by 25μm polyethylene-terephthalate sheets. The mixture of 50% argon and 50% ethane at atmospheric pressure were used for the chamber gas.

Trigger scintillators

Trigger scintillators were placed just upstream of the CsI calorimeter, at z=535 cm in the February run and at z=519 cm in the June run. The role of the trigger scintillators was to make trigger signals for a data acquisition system and start-signals for TDC modules for drift chambers.

The trigger scintillators consisted of plastic scintillator bars which were 1-cm thick, 5-cm wide and 112-cm long (some bars were 120-cm length) as shown in Fig. 2.9(a). The surface of the bar was coated with TiO_2 reflective paint. Each bar had a 2 $\times$ 4 mm hole along the longer direction. Two wave-length-shifting fibers, Kuraray Y11, were inserted in each hole to transmit the scintillation light out of the bar.

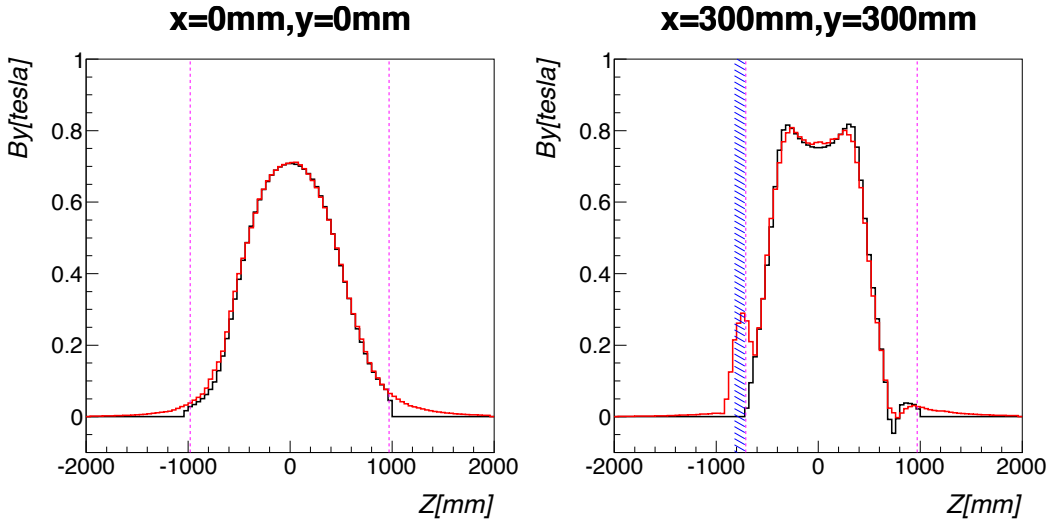

Figure 2.7: The y component of the magnetic field as a function of the z position at (a) x=0 and y=0, and (b) x=300mm and y=300mm. The black histogram shows the measured values while the red histogram shows the values calculated using ANSYS. The area filled with blue color is inside the end guard. The range between purple vertical lines show the measured area.

A group of four, five or six scintillator bars were combined as a module. The fibers in each module were connected to a photomultiplier tube (PMT) with optical cement (Fig. 2.9(b)). Each module was covered by black sheet for light shielding. Twelve modules were stacked as shown in Fig. 2.9(c). Modules with ID=10 and 11 in the figure were not installed in the February run.

We used 2-inch Hamamatsu R329 PMTs for modules with ID=5, 6, 10 and 11, and 2-inch Hamamatsu R329-EGP PMTs [27] for the rest.

Table 2.1: The numbers and spacing of sense wires.

	spacing	# of wires	note
1st chamber	10 mm	(x, x') 70	
		(y, y') 40	
2nd chamber	9 mm	(x, x') 128	
		(y, y') 96	The y' wires were not active
3rd chamber	9 mm	(x, x') 128	
		(y, y') 128	Only 96 wires were active

Table 2.2: Materials, diameters and applied voltages of the chamber wires.

	wire type	materials	diameter	applied voltage
1st chamber	sense	Au-plated W	ϕ 30μm	-
	field	Au-plated BeCu	ϕ 50μm	2700 V
	guard	Au-plated BeCu	ϕ 50μm	0 V
2nd chamber	sense	Au-plated W	ϕ 20μm	-
	field	Au-plated Al	ϕ 100μm	2100 V
	guard	Au-plated Al	ϕ 100μm	1800 V
3rd chamber	sense	Au-plated W	ϕ 20μm	-
	field	Au-plated Al	ϕ 100μm	2100 V
	guard	Au-plated Al	ϕ 100μm	1500 V

2.2.2 CsI Calorimeter

CsI crystals

The CsI electromagnetic calorimeter was placed downstream of the spectrometer. Its upstream surface was located at z=573 cm. The calorimeter had a cylindrical shape with a diameter of 1.9 m and consisted of 2716 pure CsI crystal as illustrated in Fig. 2.10. The inner 1.2×1.2 m^2 region of the calorimeter consisted of 2240 crystals whose size was $2.5 \times 2.5 \times 50$ cm^3, while the outer region consisted of 476 larger crystals whose size was $5.0 \times 5.0 \times 50$ cm^3. A square 20×20 cm^2 beam hole was made at the center of the calorimeter. Each crystal was separately wrapped with 13-μm-thick mylar to optically isolate each other. Some sections of the mylar were aluminized and other sections were painted with black ink. The allocation of these aluminized and black sections had been adjusted individually for each crystal by the KTeV experiment group so that the light yield became uniform along the z direction. The uniformities of light yield along the z direction was within $\pm$5%.

Scintillation light produced in the CsI crystal was detected by a PMT mounted on the downstream surface of each crystal. The small crystals were viewed by 3/4-inch Hamamatsu R5364 PMTs, while the large crystals were viewed by 1.5-inch Hamamatsu R5330 PMTs. An UV transmitting filter was placed on the surface of the PMT to reduce the slow component of scintillation light from the CsI crystal. Each CsI crystal and PMT was optically connected through a transparent silicone called a "cookie". We will not be able to use air cooling for the PMTs in the physics run because the calorimeter will be operated in vacuum. In order to suppress the heat produced in the PMTs, we developed a custom Cockcroft-Walton bases to supply HV to PMTs with small power (60 mW in the CW circuit [28]).

Because readout equipments for the CsI calorimeter was still under preparation, crystals located above y=600 mm and below y=-600 mm were not readout. The silicone

cookies of the crystals in the south side had been damaged by outgas from cables around the calorimeter in a vacuum test which was conducted before the engineering runs. In the February run, those crystals with damaged cookies were read out though the light transmission of their cookies was about a half of usual one. Such crystals were not read out in the June run. The location of active crystals is also shown in Fig. 2.10.

Equipment for monitoring and conditioning

There were several equipments for monitoring or conditioning the CsI calorimeter.

- thermocouples

  Light output from CsI crystal decreases about 1.5% if its temperature increases by 1 Kelvin. The temperatures at the upstream and downstream surfaces of the CsI calorimeter were monitored with 40 thermocouples through the runs. The correction of light output for the temperature shift will be described in Chapter 3.

- cosmic-ray scintillators

  Five plastic scintillators were placed above and below the CsI calorimeter each, to collect cosmic-ray muons to be used for energy calibration of the calorimeter. The five scintillators were arranged along the z direction as shown in Fig. 2.11 to find trajectories of the muons in the y-z view.

- dry room

  The CsI calorimeter was placed in a dry room where the humidity was controlled to be less than 20%, in order to prevent the crystals from deliquescence. The walls of the room were made of steel and heat insulator. A small section of the downstream wall near the beam axis and a 2×2 m^2 section of the upstream wall were removed not to obstruct the paths of incident particles. Those areas were covered with 100-μm-thick black sheets and 7.2×10^3 g/cm^2 moisture prevention sheets.

- CsI cover for earthquake

  The northeast area of Japan suffered a large earthquake in 2011. The CsI calorimeter, which was already installed in the experimental area, was not significantly damaged by the earthquake but the CsI crystals moved at most 5 mm away from its support structure. From that experience, we prepared a cover in front of the calorimeter so that the crystals will not fly out of the support structure even if an earthquake gives them 1G acceleration in the z direction.

The cover is illustrated in Fig. 2.12. The cover was made of two cloths of Teijin Technora MF1500 whose total mass thickness was 0.044 g/cm^2, with a structure made of 3-mm-thick polyvinyl-chloride pipes to form the cover in a parabolic shape. In addition, there were two plates of 2-mm-thick polyethylene on the upstream and downstream side of the pipes to protect the surface of CsI crystals, and the cloths from the edges of the pipes. The center parts of the pipe structure and polyethylene plates were removed in a circular shape with a 200-mm radius to avoid interactions with beam particles.[2]

2.2.3 Other materials

There were some materials in the experimental area which were not directly related to my studies.

- Beam shutter

  A beam shutter made of steel and tungsten was placed around z = 0 m to allow access to the experimental area during the accelerator operation. Its size was 200, 150, and 750 mm in x, y, and z directions, respectively. It was movable along x direction, and opened when the data was taken.

- Charged Veto (CV)

  In the June run, an operation test of plastic scintillator modules, which is called "Charged Veto" or "CV" and will be used as a veto detector for charged particles in KOTO physics run, was conducted in parallel with my measurement. The CV consisted of 3-mm-thick plastic scintillator plate and and a 0.8-mm-thick carbon fiber reinforced plastic (CFRP) plate. Two CV was placed in the dry room, upstream of the trigger scintillators, at z = 477 and 502 cm. In my measurement, these modules were treated as dead materials.

2.3 Data Acquisition System

2.3.1 Readout Electronics

Spectrometer

A signal from each sense wire of drift chambers was amplified by a pre-amplifier (FUJITSU MB43468). The signal was subsequently transmitted through a 4-m twisted pair cable to an Amp-Discri module which had an amplifier (PLESSEY SL560C) and a

[2]In the physics run, another cover made of CFRP is used instead of the cover described here.

comparator (LeCroy MVL407). A differential ECL-level output from the Amp-Discri module was sent to a Time-to-Digital converter modules (TDC) through a 40-m long twisted pair cable. I used two types of TDCs, Repic 32-channel Dr.T for the 1st chamber and GND 64-channel HRTDC for the 2nd and 3rd chambers. Both TDCs were based on TKO-standard [29]. The Dr.T operated as a common stop TDC while HRTDC was a common start TDC. Both the common start and stop signals were made from trigger scintillators. The Dr.T generate information that each channel had a hit or not, as a TTL-level signal. This information was used for trigger decisions.

Raw signals from each trigger scintillator module were amplified by a NIM-standard amplifier module and transmitted through 12-m BNC cables to a discriminator in the module rack where the TDCs for chambers were also placed. The discriminated output was divided into two paths. One was sent to the trigger logic to make the timing of start and stop signals for the TDCs. Another one was sent to the HRTDC input, to later identify which trigger module determines the trigger timing.

If a DAQ trigger, which will be described later in this section, was made, the TDC data was transferred to a buffer on a VME memory module (SMP). The data in the SMP buffer was sent to a Linux PC between spills.

CsI calorimeter

Raw signals from each PMT of the CsI calorimeter were amplified by a pre-amplifier and transmitted to a custom made flash analog-to-digital converter module (FADC).

The FADC modules had filters for shaping input pulses, and ADC chips. The type of the filter was called 10-pole Bessel filter and it was designed to shape the waveform of CsI output to a Gaussian shape with $\sigma \sim 30$ nsec as shown in Fig. 2.13. The ADC chip had the dynamic range of 14 bit to cover up to 1500 MeV, and digitized the input waveform every 8 nsec. With the shaping filter, we can obtain a larger number of sampling points for a signal pulse to increase the accuracy of fitting the waveform.

The digitized data was stored onto its buffer for 4 μsec. If a DAQ trigger, described later in this section, was generated, the digitized data for 512 nsec (= 64 sampling points) was transferred to a memory module [3]. The data on the memory module was sent to a Linux PC farm every spill during a beam interval. This system basically did not have a dead time.

[3] In the physics run, this memory module will provide several selection methods to distinguish $K_L \to \pi^0\nu\bar{\nu}$ decay from backgrounds and suppress the amount of data to store. In the engineering runs, however, we did not use that function.

2.3.2 Trigger

I analyzed $K_L \to \pi^+\pi^-$, $K_L \to \pi^+\pi^-\pi^0$ and $K_L \to \pi e\nu$ decays for this thesis. All these decays have two charged particles in their final states. I designed a trigger to select such final states.

On the trigger scintillators, I allocated four regions, Right-up, Right-down, Left-up, and Left-down, as shown in Fig. 2.14. I required at least two hits on the trigger scintillators, and the two hits located on a diagonal areas each other. Namely, a pair of hits on Right-up and Left-down or a pair of hits on Right-down and Left-up were accepted. I also required at least two hits on y-wire plane of the 1st chamber to ensure that the K_L decayed upstream of the 1st chamber.

The trigger logic diagram is shown in Fig. 2.15. If the trigger scintillators had hits with a diagonal pattern, start and stop signals for the TDC modules were produced as long as the following conditions were satisfied.

- A memory module for the CsI system was not full.
- A "spill gate", which was open during the spill, was on.
- "DAQ ready" flag was on.

The "DAQ ready" flag was turned off when the "TDC start" signals were produced so that the next event will not be accepted until the trigger decision for this event was made. After distributing TDC stop signals, the TDC modules for the 1st chamber returned information of hit channels as TTL signal. The DAQ trigger was requested if there were more than two hits on the y plane of the 1st chamber. Subsequently, TDC data of the spectrometer was transferred to a memory module (named SMP) after waiting for the TDC conversion time (200μsec). The transfer to the SMP took several hundred μsec and dominated the dead time of the DAQ system. The FADC data of the CsI calorimeter was also transferred to the memory module for the CsI system. This process had no dead time. After data was transferred to the SMP, the TDC modules were cleared and "DAQ ready" flag was turned on to accept the next event. If the number of hits on the y plane of the 1st chamber was less than two, the TDC modules were cleared and "DAQ ready" flag was turned on immediately.

2.4 Run

The February run was carried out for about 3 weeks from January to February in 2012, while the June run was carried out for about 3 weeks from June to July of 2012. Because we used the beam for several studies, the data taking for studies described in this thesis was carried out only a half of each beam time.

Table 2.3: Beam Intensity thorough the engineering runs and the number of triggers collected in each period. The term "POT" in the table means the number of protons on target.

	POT / spill	# triggers accepted
Feb. 1 $\sim$ Feb. 9	1.3×10^{12}	7.2×10^{5}
Feb. 10 $\sim$ Feb. 22	3.8×10^{12}	11.5×10^{5}
June 9 $\sim$ June 21	4.1×10^{12}	21.4×10^{5}

The beam intensity gradually changed because the accelerator was still under commissioning. The beam intensity during the runs are written in Table 2.3. I also took the data with the magnet turned off in addition to the normal run, to collect straight charged tracks to align the detectors. Before and after each beam time, we collected cosmic ray muons for several days for an energy calibration of the CsI calorimeter.

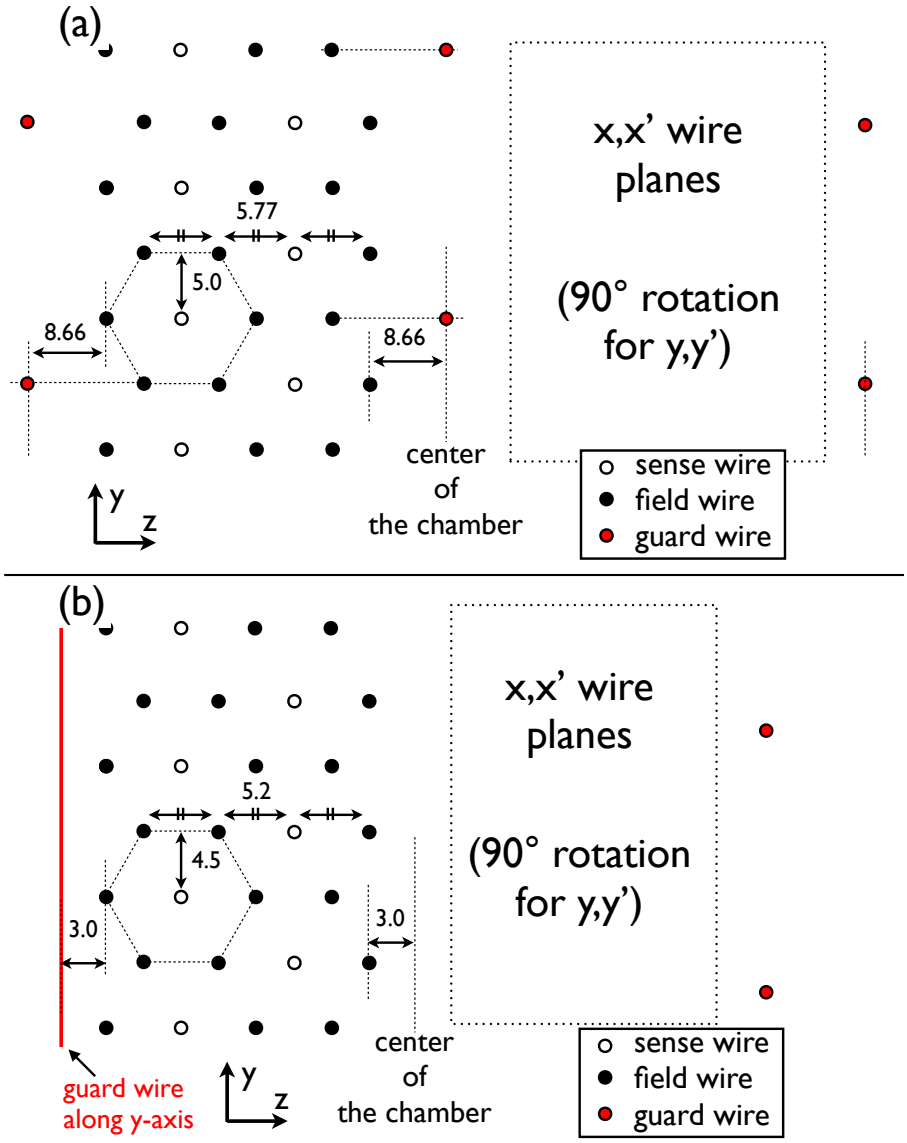

Figure 2.8: Schematic view of wire cells of (a) the 1st chamber and (b) the 2nd and 3rd chambers.

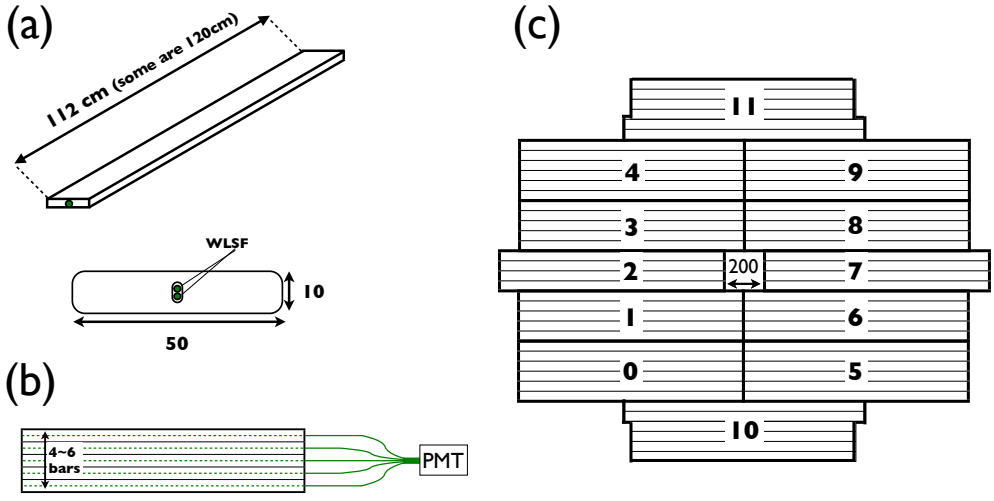

Figure 2.9: (a) Scintillator bar used for the trigger scintillator. (b) A trigger scintillator module consisting of 4∼6 scintillator bars. Scintillation light of each bar is transmited through two wave-length-shifting fibers to PMT. (c) Whole image of trigger scintillators. Twelve modules were stacked in the June run. Modules 10 and 11 were not installed in the February run.

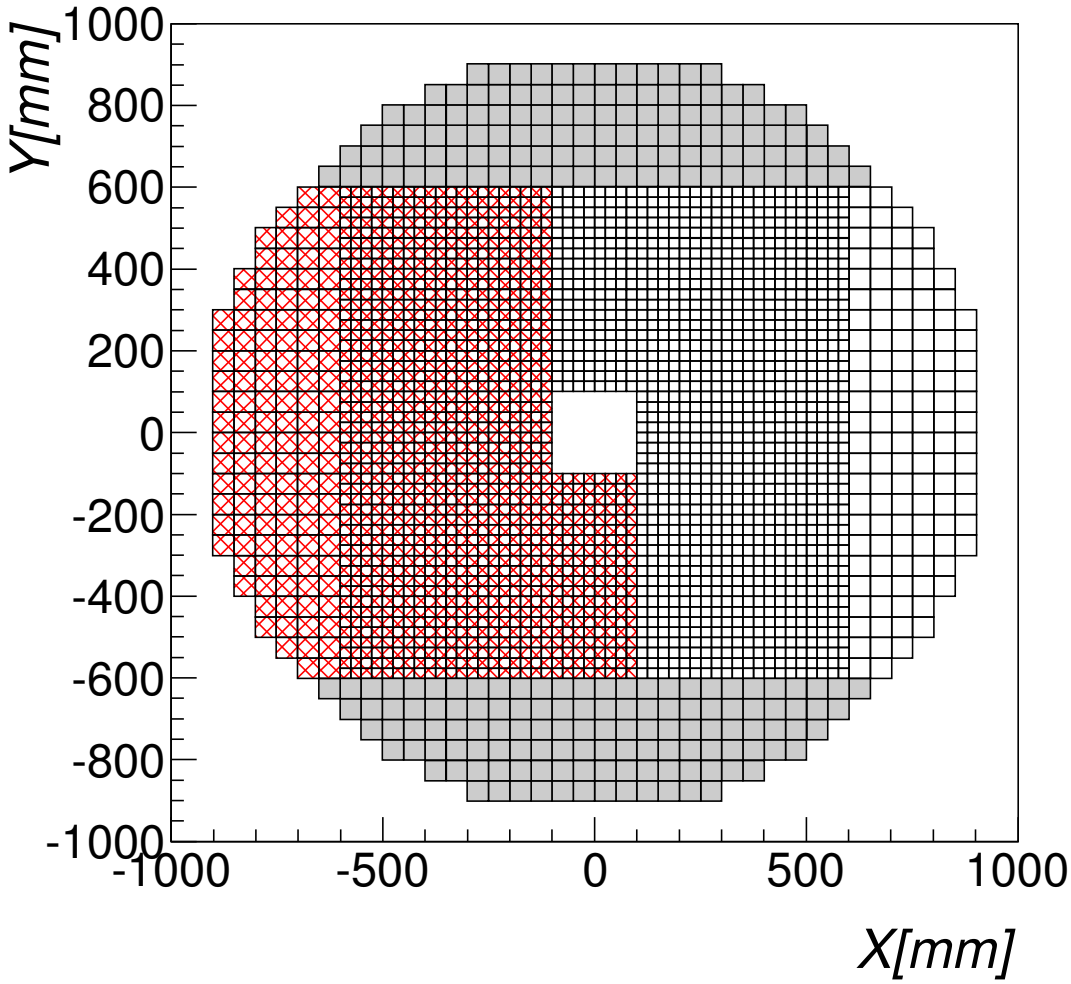

Figure 2.10: Schematic view of the CsI calorimeter. Crystals above 600 mm and below -600 mm, filled with gray in the figure, were not active because the readout equipments were under preparation. Meshed crystals had lower gains in the February run and they were not active in the June run because their silicone cookies were damaged.

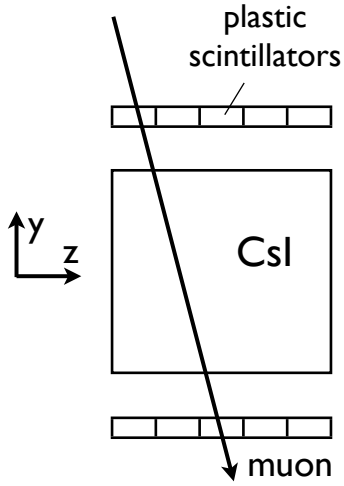

Figure 2.11: Schematic view of cosmic-ray scintillators.

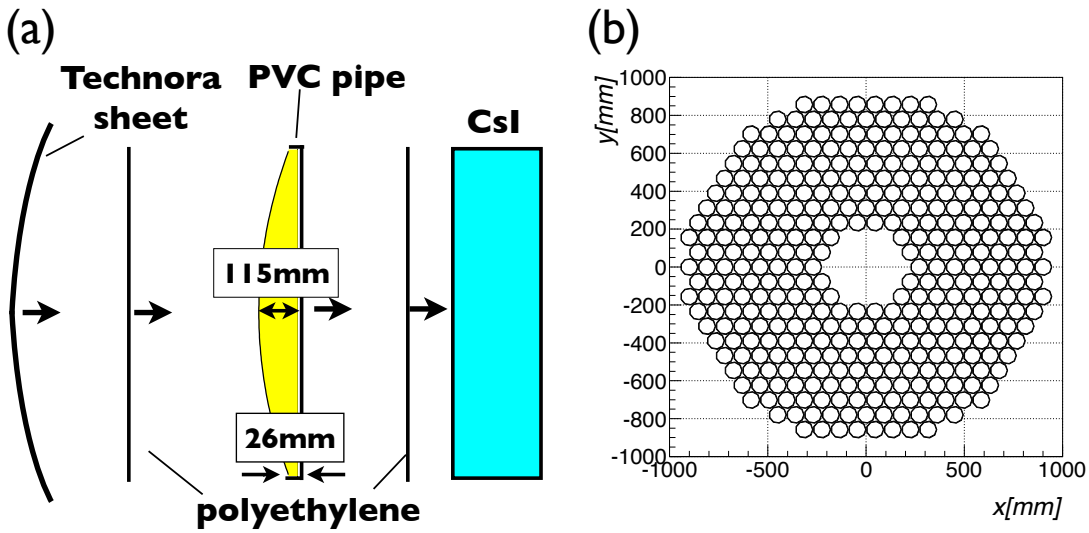

Figure 2.12: (a) Schematic view of CsI cover. (b) Front view of the parabolic shaped polyvinyl-chloride pipes whose side view is shown in yellow in (a).

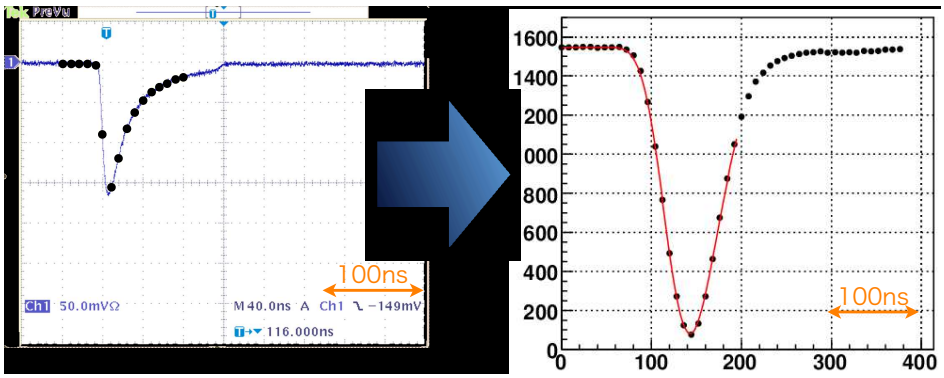

Figure 2.13: A conceptual view of a role of a shaping filter. A raw signal from CsI crystal (a blue line in the left figure) was shaped to approximately Gaussian with a larger width (a red line in the right figure). Black dots shows FADC sampling points. We can obtain more sampling points a pulse due to the shaping filter.

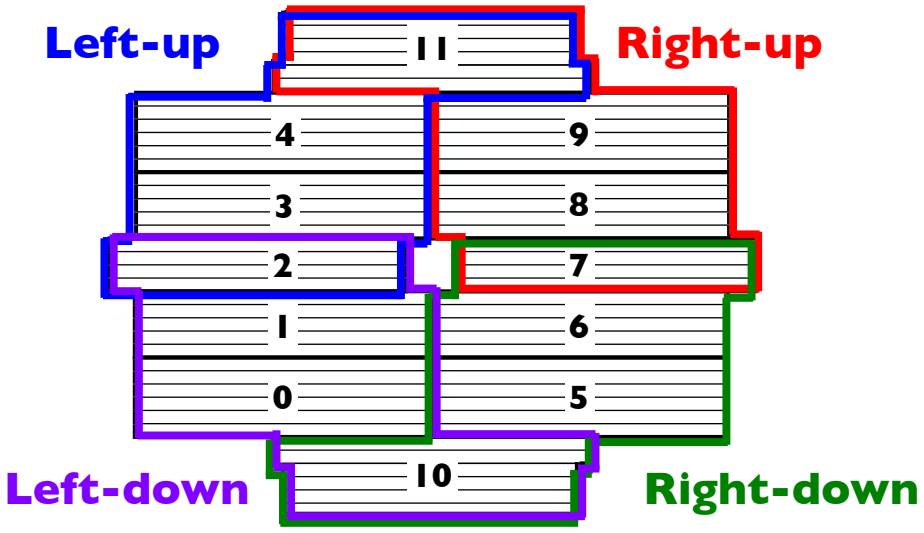

Figure 2.14: Four regions allocated on the trigger scintillators. If Right-up and Left-down regions had hits, or Left-down and Right-up regions had hits, stop and start signals were distributed to TDC modules.

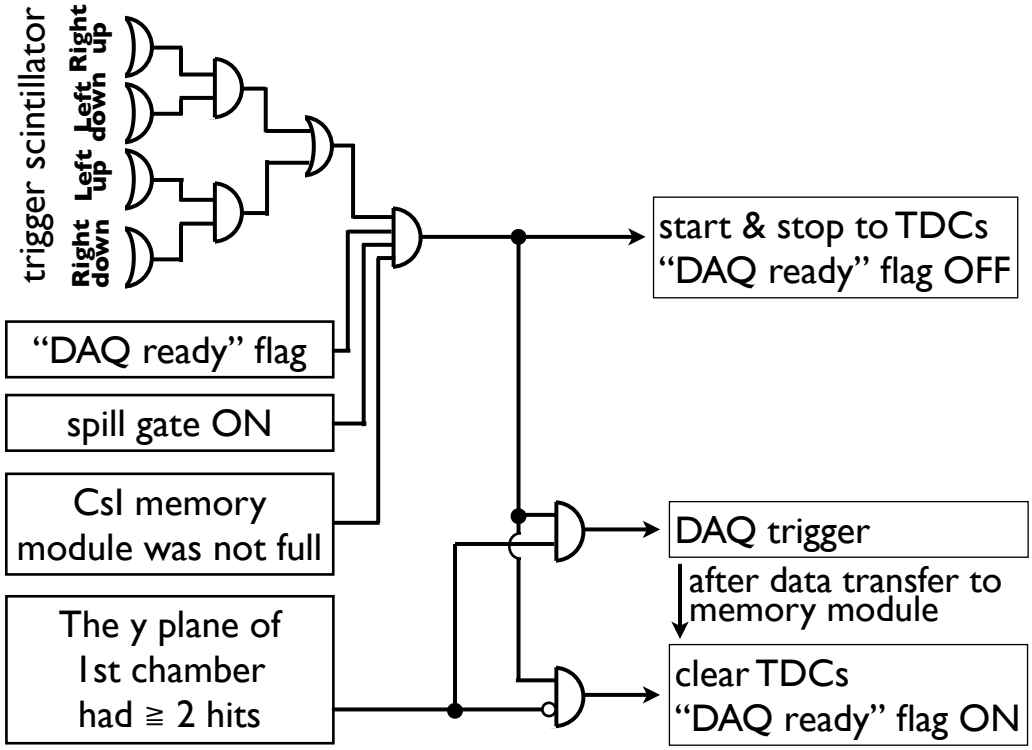

Figure 2.15: Trigger logic.

Chapter 3

The CsI Calorimeter Analysis

In this chapter, I will describe how to reconstruct the energies and positions of gammas (or electrons) hitting the CsI calorimeter based on the waveforms recorded with the FADC modules. This process consisted of the following steps.

1. Integrate the waveform.
2. Convert the integral to an energy deposit.
3. Group the energy deposits of an incident gamma (or electron).
4. Apply corrections for a temporal shift of energy scale.

3.1 Waveform Fitting

The first step of the calorimeter analysis is to calculate the integral of the waveform. A simple method for that is just summing ADC values of the 64 sampling points in the waveform. The summing method, however, is affected by ground noises on every sampling points. In addition, the summation method cannot recognize strange waveforms like two overlapped pulses. For these reasons, I adopted a fitting method to calculate the integral. This method is based on a previous work [4], but slightly modified according to the run condition.

3.1.1 Fitting Function

Because the waveforms were difficult to be parameterized with any given formula, I used an averaged waveform, which was derived from the data, as the fitting function. The averaging of waveforms was separately done for each CsI crystals because

the waveforms were slightly different between CsI crystals. Because the waveforms depended on its height, I prepared averaged waveforms for 11 pulse height sections separately.

There were not many waveforms with large heights in the data, as shown in Fig. 3.1. To collect statistics even in a larger height region, the height sections were arranged at logarithmically equal intervals, as also shown in Fig. 3.1. Namely, the boundaries of the height sections were located at

$$10 \text{ to the power of } \left(\frac{\log_{10}(10000) - \log_{10}(20)}{10} \times (i - 0.5) + \log_{10}(20) \right) \text{[counts]},$$

where $i = \{0, 1, 2, ..., 10\}$. The smallest boundary was located at 14.6 counts, while the largest boundary was located at 13600 counts. These roughly correspond to energy deposits of 1.3 MeV and 1.2 GeV, respectively.

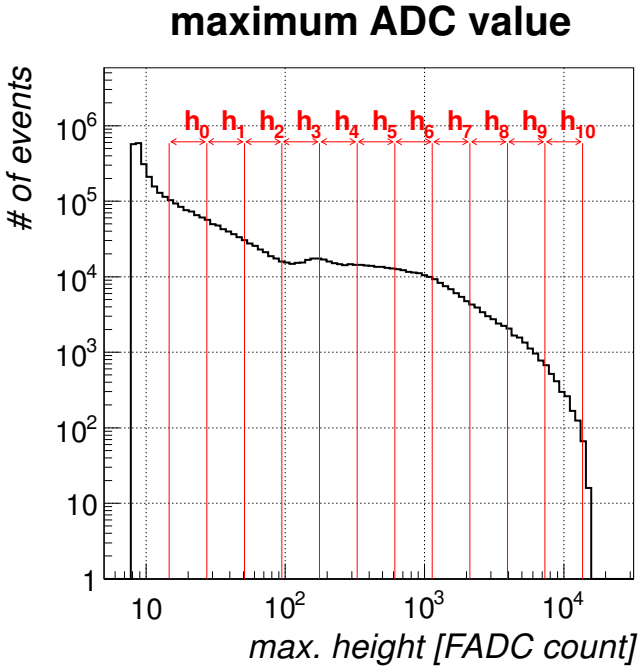

Figure 3.1: Distribution of the maximum ADC value of 64 sampling points. Here, pedestals were subtracted.

The averaging process took the following four steps.

1. A custom asymmetric gaussian $f_{agaus}(t)$ was fitted to each waveform as shown in Fig. 3.2(a), to obtain a rough peak height and peak timing. The $f_{agaus}(t)$ is defined as

$$f_{agaus}(t) \equiv A \times \text{Gaussian}(t, \mu, \sigma(t)) + C, \tag{3.1}$$

where A, μ, and C represent a peak height, a peak timing, and a pedestal, respectively. The $\sigma(t)$ was defined as

$$\sigma(t) = a(t-\mu)^4 + b(t-\mu)^3 + c(t-\mu)^2 + d(t-\mu) + \sigma_0.$$

The C was fixed as the average value of the first nine FADC samples in the fitting. Other parameters were free. The fitting range was restricted within -5 $\sim$ 5 sampling points around the point with the maximum ADC count. A ground noise fluctuation (=2.04 counts) was added as an error to each sampling point.

2. After subtracting the pedestal, the height of the waveform was normalized by the peak height derived at the step 1, as shown in Fig. 3.2(b). In addition, the timing of the waveform was shifted to align the peak timing to be zero.

3. The normalized waveform was interpolated with a cubic spline curve as shown in Fig. 3.2(c). The values on the curve were then sampled every 1 nsec from -176 nsec to 200 nsec.

4. The mean value of many sample waveforms were taken for the each 1-nsec point. A curve interpolating those mean values, shown in Fig. 3.2(d), was the averaged waveform that we wanted to derive. The RMSs of the 1-nsec-sampled values were also calculated to be used later as errors in the fitting process. The average waveform of the i-th height section denotes $f_i^{wf}(t)$ as a function of timing.

The fitting function, F, was obtained by summing two averaged waveforms with logarithmic weights, *i.e.*:

$$F(t,h,\mu,c) = h \times \Big((1-W) f_i^{wf}(t-\mu) + W f_{i+1}^{wf}(t-\mu)\Big) + c, \tag{3.2}$$

where h, μ, and c represent a peak height, a peak timing, and a pedestal, respectively. The i-th and $i+1$-th sections are the two nearest height sections to h. The W is the weight defined as

$$W = \frac{\log(h) - \log 20}{\log 10000 - \log 20} \times 10 - i. \tag{3.3}$$

3.1.2 Integral of the Waveform

The function in Eq. (3.2) was fitted to each waveform with the free parameters, h, μ, and c. The fitting process was iterated twice. In the first iteration, the fit range was restricted to within -160 $\sim$ 40 nsec around the sampling point with the maximum ADC count. The ground noise level, 2.04 counts, was used as an error of each sampling point. In the second iteration, the fit range was updated to -160 $\sim$ 40 nsec around the μ which was obtained from the first iteration. Errors of sampling points were set as the RMSs derived in the step 4 of the averaging process described in the previous subsection.

Instead of numerically integrating the fitting function, look-up tables were used to determine the integral of the waveform. Figure 3.3 shows a ratio of a summation of 64 ADC values to the height which was derived from the fitting. The same plots were made for every CsI crystal, and the mean value in each height (dots in the figure) was stored. After fitting and obtaining a waveform height, we could obtain the integral corresponding to the height by referring these stored values.

3.2 Energy Calibration

An integral of waveform was converted to an energy deposit, by simply multiplying a calibration constant. The calibration constant was derived for each CsI crystal by using cosmic rays.[1]

Cosmic rays were triggered by using cosmic-ray scintillators described in Section 2.2. There were 5 scintillators each above and below the calorimeter as shown in Fig. 2.11. We required that the most upstream counters on the both sides had hits. This requirement limited the paths of cosmic rays to the upstream part of CsI crystals, and suppressed the fluctuation of CsI light output due to a light yield non-uniformity along the z direction.

Figure 3.4 shows a distribution of the waveform integrals of one of the CsI crystals in the cosmic-ray events. Considering the angle dependence of the path length, the integral was multiplied by the cosine of the incident angle. The peak position in the distribution was determined by fitting Landau function. The calibration constant was calculated as the ratio of an expected energy deposit (= 5.63 MeV/cm $\times$ the crystal size) to the peak position.

3.3 γ / Electron Reconstruction

3.3.1 Clustering

Electromagnetic showers on the calorimeter tend to spread over multiple CsI crystals because the Morier radius of CsI is larger than the size of the CsI crystals. We should group energy deposits located close to each other to reconstruct the energy and position of the incident particle. The group is called “cluster”, and the grouping process is called “clustering”.

[1]There was another method using electrons tracked by the spectrometer, that I will introduce later in Chapter 5

The clustering process is illustrated in Fig. 3.5. We picked CsI crystals with more than 3-MeV energy deposits as cluster seeds. We then focused on a cluster seed with the maximum energy deposit. If there were other cluster seeds within a square of 14×14 cm^2 centered on the focused seed, such seeds were linked with the focused seed. The focus was then moved to one of the linked seeds. The other seeds around the focused seed were again searched for and linked with. The process to move the focus and link was iterated until no more seed was linked with. A group of the linked seeds was defined as a cluster. After a cluster was found, we tried to find another cluster from the remaining seeds. The cluster finding was iterated until all the seeds were used.

A cluster energy E_{clus} was defined as the sum of energy deposits of seeds in the cluster. A cluster timing t_{clus} was defined as the mean of the seed timings weighted by their timing resolution. Cluster positions, X_{clus} and Y_{clus}, were calculated as the mean of the positions of the seed weighted by energy deposits. Namely,

$$\begin{aligned} E_{clus} &\equiv \sum_{i}^{seeds} e_i \\ t_{clus} &\equiv \left(\sum_{i}^{seeds} \frac{t_i}{\sigma_t^2} \right) / \left(\sum_{i}^{seeds} \frac{1}{\sigma_t^2} \right) \\ x_{clus} &\equiv \left(\sum_{i}^{seeds} x_i \times e_i \right) / E_{clus} \\ y_{clus} &\equiv \left(\sum_{i}^{seeds} y_i \times e_i \right) / E_{clus} \end{aligned} \tag{3.4}$$

where e_i, t_i, x_i and y_i represent the energy deposit, timing, x and y components of the center position of the i-th seed, respectively. The σ_t is the timing resolution of a crystal measured in a past beam test [4] which is defined as

$$\sigma_t[\text{ns}] = 5/e_i[MeV] \oplus 3.63/\sqrt{e_i[\text{MeV}]} \oplus 0.13. \tag{3.5}$$

Due to a fluctuation of electromagnetic shower development, a part of seeds were sometimes not included in a proper cluster and were observed as a separate cluster. In order to reject such clusters, I required that clusters should have energies more than 20 MeV and more than 1 seed.

Cluster information in Eq. (3.4) are still different from the information of the incident photon. Several corrections are applied as described in the following subsections.

3.3.2 Accidental Hit Rejection

The cluster might include accidental hits. Those hits are excluded by using their timing information, with reference to the method in [30]. A 2-dimensional histogram in Fig. 3.6 shows the timing difference observed in the data between the cluster and the crystals in it, as a function of energy deposits in the crystals. The red lines in the figure represent 5 × RMS of each x bin. I then calculated the ratio of the timing difference to the 5 × RMS for each crystal, *i.e.*:

$$R_i^{time} \equiv \frac{|t_i - t_{clus}|}{5 \times \mathrm{RMS}}, \tag{3.6}$$

where t_i means the timing of the i-th crystal in the cluster. To reject accidental hits, the ratio, R_i^{time}, was required to be less than 1 for every crystal in the cluster. If there were crystals with the $R_i^{time} > 1$, the crystal with the largest R_i was eliminated from the cluster. The clustering process was then repeated again with the remaining crystals, the t_{clus} was newly calculated, and the R_i^{time} was re-calculated with the renewed t_{clus}. This elimination process was iterated until all the crystals in the cluster satisfied $R_i^{time} < 1$.

3.3.3 Energy Reconstruction

The cluster energy defined in Eq. (3.4) was generally smaller than the energy of incident particle. This is because energy deposits in crystals less than 3 MeV were ignored in the clustering process. In order to obtain the incident energy of photon, E_{inc}, we applied an energy correction as

$$E_{inc} = \frac{1}{f_{Ecor}(E_{inc}, \theta)} \times E_{clus}, \tag{3.7}$$

where f_{Ecor} is a correction function described below. The θ represents the incident angle of the photon or the electrons. For electrons, the θ could be measured directly with the spectrometer. In case of photons from $K_L \to \pi^+\pi^-\pi^0$ decays, the θ was calculated from the cluster position and the decay vertex which was reconstructed from $\pi^+\pi^-$ tracks measured with the spectrometer.

Correction function

The form of f_{Ecor} in Eq. (3.7) was studied by using Geant4 simulation. The simulation was run for photons with several energies and incident angles, because f_{Ecor} depends on such kinematics. The simulation was also run for a region of small CsI crystals and for a region of large CsI crystals, separately.

Table 3.1: The values of parameters a, b, c, and d, in Eq. (3.8). They were derived from Monte Carlo simulation.

	for small CsI				for large CsI			
sinθ	a	b	c	d	a	b	c	d
$\sqrt{3}/20\times$ 0	0.992	-0.0573	-0.00366	-117.349	0.988	-0.0205	-0.00525	-10.724
$\sqrt{3}/20\times$ 1	0.996	-0.0613	-0.00223	-122.288	0.988	-0.0206	-0.00507	-8.705
$\sqrt{3}/20\times$ 2	0.968	-0.0319	-0.0129	-50.329	0.989	-0.0215	-0.00474	-13.915
$\sqrt{3}/20\times$ 3	0.987	-0.0523	-0.00530	-96.304	0.987	-0.0204	-0.00542	-4.780
$\sqrt{3}/20\times$ 4	0.988	-0.0539	-0.00534	-100.387	0.987	-0.0203	-0.00576	-7.560
$\sqrt{3}/20\times$ 5	0.967	-0.0324	-0.0136	-38.456	0.987	-0.0206	-0.00580	-1.673
$\sqrt{3}/20\times$ 6	0.966	-0.0329	-0.0138	-34.263	0.988	-0.0228	-0.00520	-4.093
$\sqrt{3}/20\times$ 7	0.965	-0.0334	-0.0142	-28.306	0.989	-0.0245	-0.00477	0.205
$\sqrt{3}/20\times$ 8	0.986	-0.0580	-0.00546	-70.594	1.003	-0.0401	0.00102	-44.58
$\sqrt{3}/20\times$ 9	0.963	-0.0371	-0.0147	-23.422	0.989	-0.0282	-0.00435	-0.225
$\sqrt{3}/20\times$ 10	0.962	-0.0415	-0.0135	-19.867	0.984	-0.0294	-0.00525	0.291

The E_{clus}/E_{inc} distribution for $E_{inc} = 400$ MeV and $\theta = 15$ deg is shown in Fig. 3.7(a) as an example. The mean values of the similar histograms for various E_{inc} and θ are plotted in Fig. 3.7(b).

The f_{Ecor} was derived by fitting the mean values with

$$f_{Ecor}(E_{inc},\theta) = a(\theta) + \frac{b(\theta)}{\sqrt{(E[MeV] - d(\theta))/1000}} + c(\theta)\log((E[MeV] - d(\theta))/1000). \tag{3.8}$$

The values of parameters a, b, c, and d, are summarized in Table 3.1. The f_{Ecor} for a given θ was derived by linearly interpolating the f_{Ecor}s for the two nearest angles in the table.

The f_{Ecor} was prepared for small CsI crystals and for large CsI crystals separately. As for a cluster including both kinds of crystals, the weighted sum of f_{Ecor} for small crystals, f^S_{Ecor}, and f_{Ecor} for large crystals, f^L_{Ecor}, were combined as:

$$f_{Ecor}(E_{inc},\theta) = (1-W)\times f^S_{Ecor}(E_{inc},\theta) + W \times f^L_{Ecor}(E_{inc},\theta). \tag{3.9}$$

The form of the weight W was studied by using Geant4 simulation. As shown in Fig. 3.8, I found that the W can be represented by:

$$W = \begin{cases} \frac{g(E_{clus},\theta)}{-\log(1.5MeV/E_{clus})-\log 2}\log(0.5\frac{E_{\rm large}}{E_{clus}}) + g(E_{clus},\theta) & for\ \frac{E_{\rm large}}{E_{clus}} \le 0.5 \\ \frac{g(E_{clus},\theta)-1}{-\log(1.5MeV/E_{clus})+\log 2}\log(0.5(1-\frac{E_{\rm large}}{E_{clus}})) + g(E_{clus},\theta) & for\ \frac{E_{\rm large}}{E_{clus}} > 0.5 \end{cases}, \tag{3.10}$$

where $g(E_{clus}, \theta)$ was derived for several E_{clus} and θ.

The f_{Ecor} was designed as a function of E_{inc} so far. The E_{inc} is, however, what we want to derive. The observable quantity is E_{clus}. To obtain a proper f_{Ecor} value, an iterative process was used. At first I calculated f_{Ecor} value with assuming $E_{inc} = E_{clus}$ and applied the correction shown by Eq. (3.7). I calculated f_{Ecor} again with the corrected cluster energy in the second iteration. Namely, f_{Ecor} in Eq. (3.7) was approximated as

$$f_{Ecor}(E_{inc}, \theta) \rightarrow f\left(\frac{E_{clus}}{f_{Ecor}(E_{clus}, \theta)}, \theta\right). \tag{3.11}$$

3.3.4 Incident Position Reconstruction

The cluster position defined in Eq. (3.4) tends to locate farther away from the beam center than the true incident position of the photon. This difference is due to the finite length of electromagnetic shower, as illustrated in Fig. 3.9. We applied a correction as

$$\begin{aligned} x_{inc} &= x_{clus} - L\sin\theta\cos\phi \\ y_{inc} &= y_{clus} - L\sin\theta\sin\phi, \end{aligned} \tag{3.12}$$

where θ and ϕ are the incident angle and the azimuthal angle of the incident photon. The L is the length from the incident position to the shower maximum. The L was estimated with a Geant4 simulation as

$$L_\gamma(E_{inc})[cm] = X_0 \times (6.37 + 1.11\log(E_{inc}[GeV])) \tag{3.13}$$

for photons, and

$$L_e(E_{inc})[cm] = L_\gamma(E_{inc}) - X_0 \times (0.796 - 0.091\log(E_{inc}[GeV])) \tag{3.14}$$

for electrons, where X_0 denotes the radiation length of CsI (1.85 cm).

3.3.5 Alternative Method for Position Reconstruction

An alternative method to reconstruct the incident position using the cluster shape information was proposed by E. Iwai [4]. In that method, we calculate the sum of energy deposit in each column (or row) of crystal arrays, as shown in Fig. 3.10. This column (row) energies is regarded as the projected cluster shape to x (y) direction. The x (y) projected shapes are fitted with a fitting function, to determine the incident x (y) position. The fitting function is the expected shape of the projected cluster based on Monte Carlo simulation, as shown in Fig. 3.11. The fitting function is prepared for

every 9 energy sections, 25 polar angle sections and 15 azimuthal angle sections. More details for this method were found in [4]. Hereafter, I will call this method "*shape*" method.

From the Monte Carlo study, the *shape* method is expected to have a better position resolution compared to the current "*COE*" method defined in Eq. (3.4) and Eq. (3.12). In Chapter 7, I will evaluate position resolutions using the *shape* method as well as the *COE* method.

3.4 Correction for Temporal Change

Minimum ionization particles (MIPs) in the beam were used to check the drifting of energy scale of the calorimeter with time. They made a peak in a cluster energy distribution even without any selection cuts, as shown in Fig. 3.12.

The position of the MIP peak changed about 2% during the runs as shown in Fig. 3.13. This drift could be explained by the temperature change of the CsI blocks which was monitored by the thermocouples described in Section 2.2. I found a negative correlation between the MIP peak position and the temperature of the upstream surface of the calorimeter, as shown in Fig. 3.14. I corrected energy deposits in each crystal by -1.4% per Kelvin temperature shift.

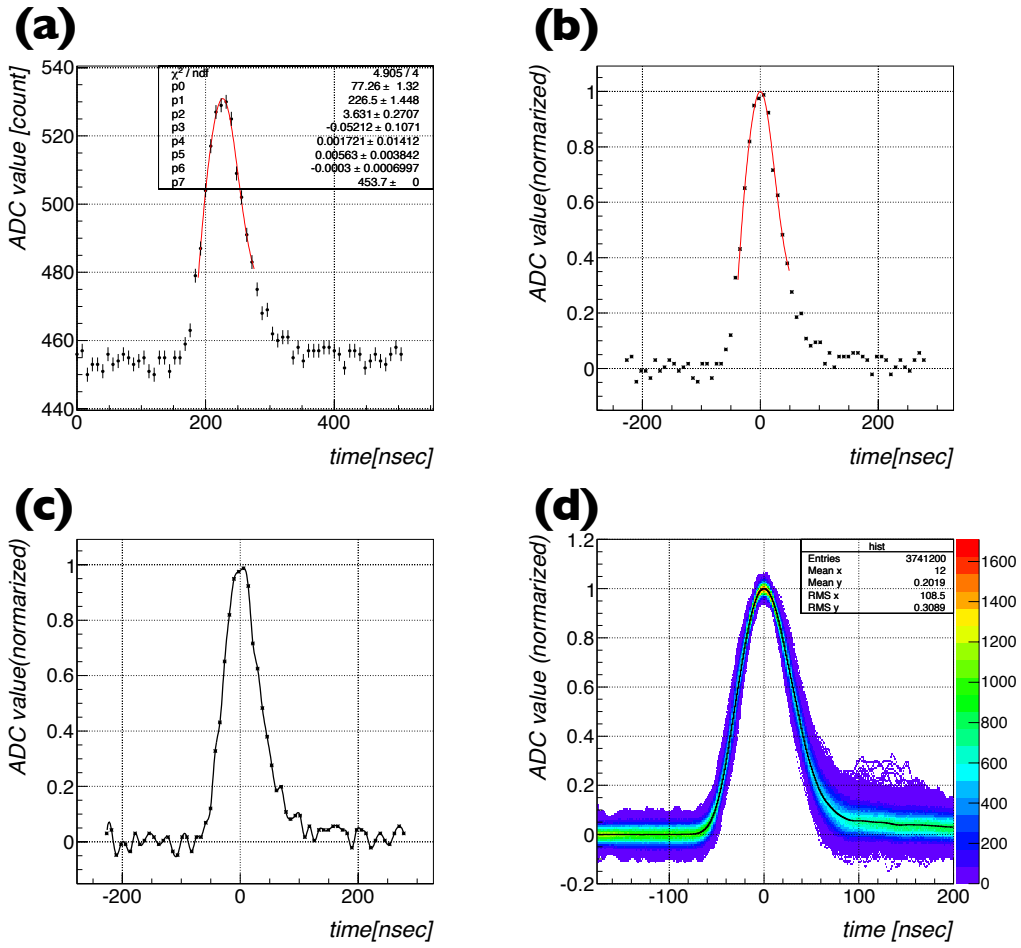

Figure 3.2: Process to derive the average waveform. (a) The function in Eq. (3.1) was fitted to each waveform recorded on the FADC. Black dots show the ADC values and the red line shows the fitting result. (b) Based on the fitting result, the height of the waveform was normalized to 1 and its peak timing was shifted to 0. (c) The normalized waveform was interpolated with a cubic spline curve as drawn by a black line. (d) Values on the spline curve at every 1 nsec filled in a 2-dimentional histogram. Their mean values were calculated, as shown by a black line.

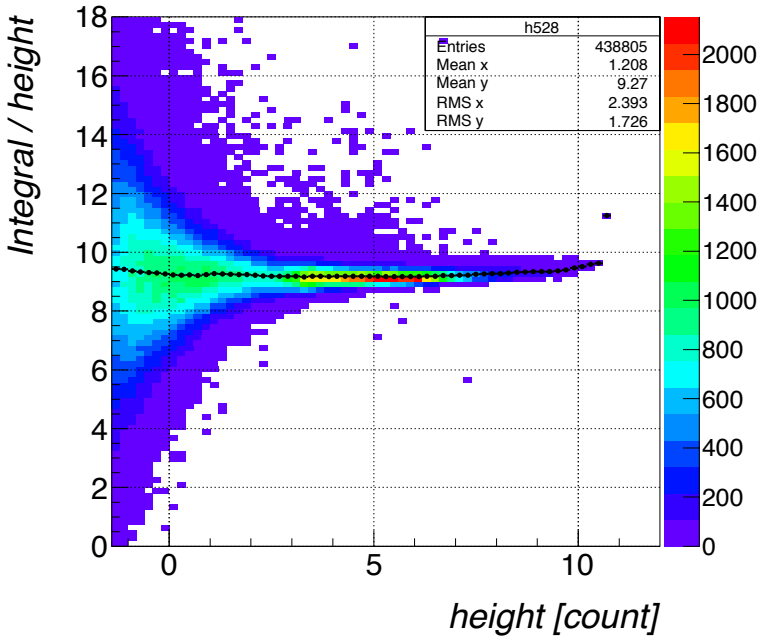

Figure 3.3: The ratio of a summation of 64 ADC values in a waveform divided by the height of the waveform is shown as a function of the height. Black dots represent mean values of the ratio.

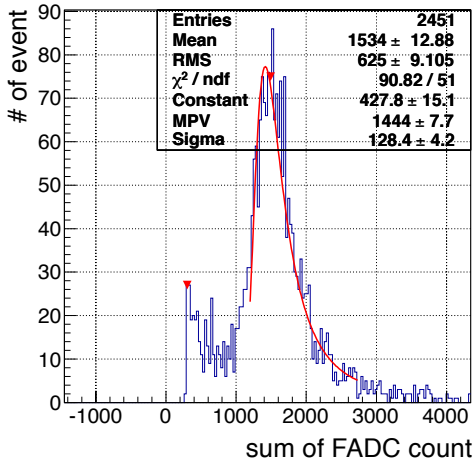

Figure 3.4: The histogram shows the distribution of the integral of waveform for the cosmic-ray events. The peak position was determined by fitting Landau function as shown in the red line.

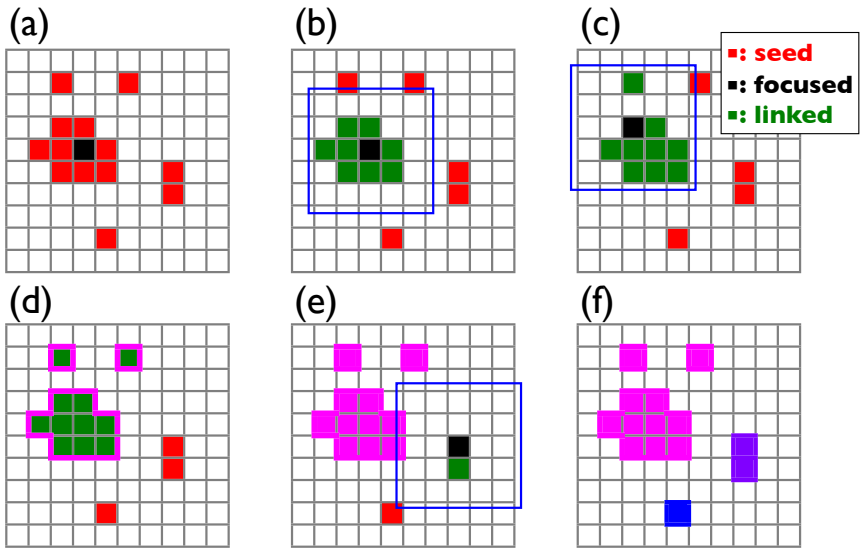

Figure 3.5: Illustration of the clustering process. (a) The CsI crystals with energy deposits more than 3 MeV are shown in red. They are defined as cluster seeds. The black block represents the seed with the maximum energy deposit. First we focused on the black block. (b) The 14×14 cm^2 square, drawn with blue line, is placed around the focused block. The seeds which were located in the square are linked with the focused seed. The linked crystals are filled with green. (c) We then move the focus to one of the linked crystals and seek the seed in the square centered on the focused block. (d) The process in (c) is iterated until no more seeds can be linked. The group of the linked crystals is defined as "cluster". (e) The processes (a)$\sim$(d) are iterated for the remaining seeds. (f) In this example, three clusters are finally found (Each of them are shown in magenta, purple and blue, respectively).

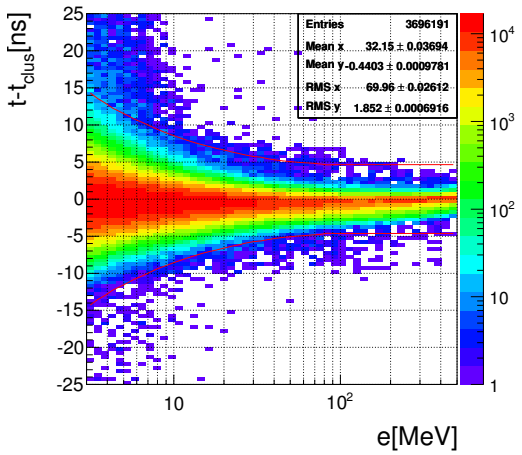

Figure 3.6: Timing difference between the custer and the crystals in it, $t - t_{clus}$, as a function of energy deposits in the crystals. A 2-dimensional histogram shows the data, and red lines show the 5× RMS of each x bin.

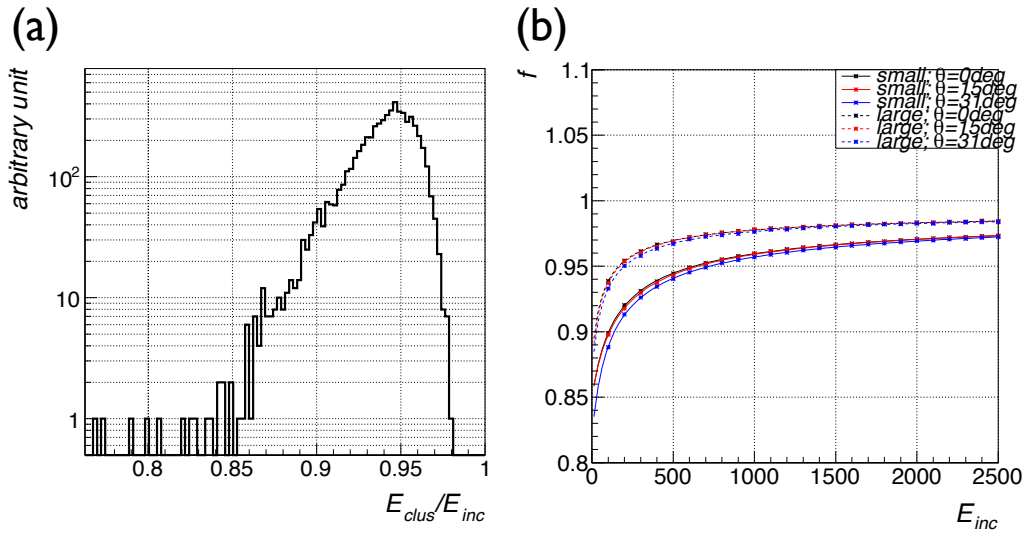

Figure 3.7: (a) Distribution of E_{clus}/E_{inc} in the case of $E_{inc} = 400$ MeV and $\theta = 15$ deg. (b) The f_{Ecor} for several θs are shown as a function of E_{inc}.

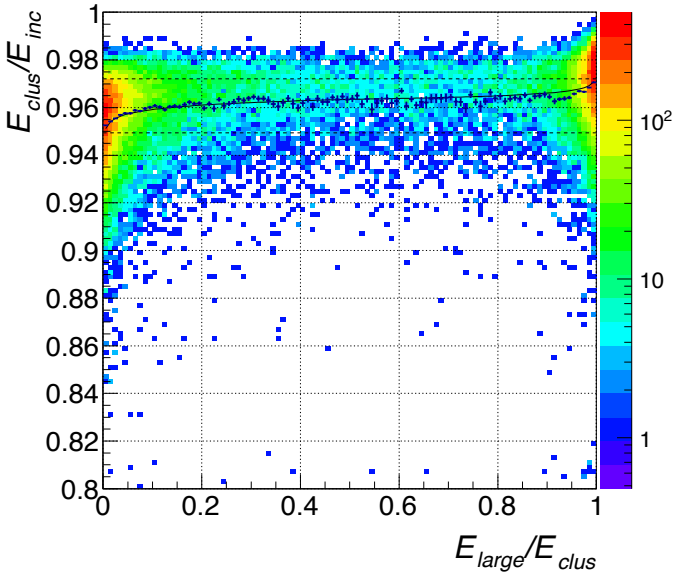

Figure 3.8: The E_{clus}/E_{inc} is shown as a function of the ratio of total energy in large CsI crystals to a cluster energy. The $E_{inc} = 600$ MeV and $\theta = 15$ deg. The black solid line shows f_{Ecor} in Eq. (3.9), and the lower (upper) dashed line shows f^S_{Ecor} (f^L_{Ecor}).

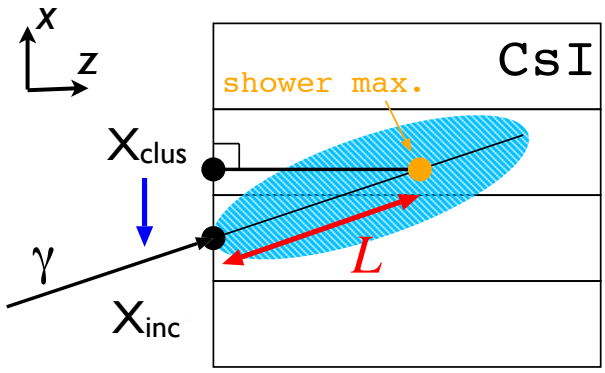

Figure 3.9: Schematic view of the correction for cluster position. Due to the finite length of shower, the center-of-energy position (x_{clus}) is different from the incident position of photon (x_{inc}).

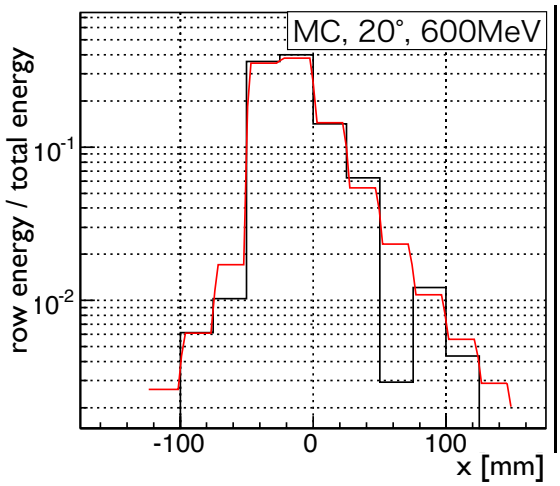

Figure 3.10: An example of the *shape* method. The black histogram shows the projected cluster shape to the x direction, and the red line shows the fitting function. This figure is quoted from the reference [4].

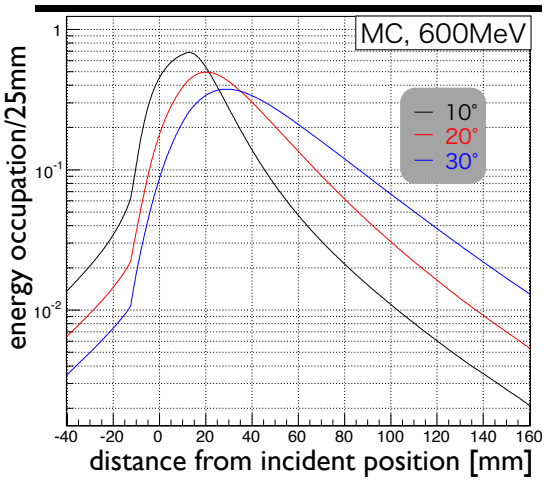

Figure 3.11: Fitting functions used in the *shape* method. The fitting functions are prepared for various photon kinematics. The functions in the figure are for the photon with 600 MeV energy and with 10- (black), 20- (red), and 30- (blue) degree incident angle. This figure is quoted from the reference [4].

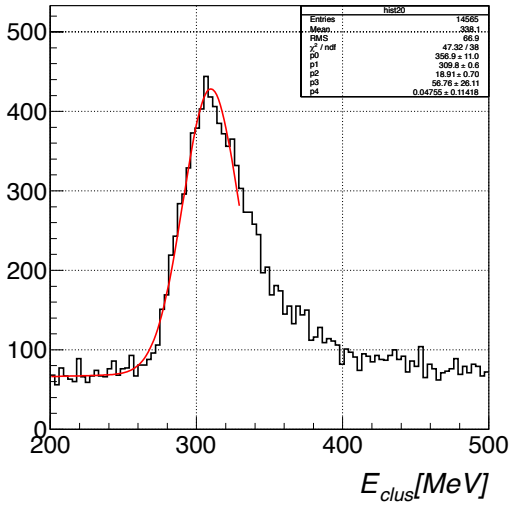

Figure 3.12: Cluster energy distribution in a data file (corresponding to ∼20-minute data taking). The MIP peak was located around 300 MeV. The peak position was determined by fitting a Gaussian + a straight line as shown by the red line.

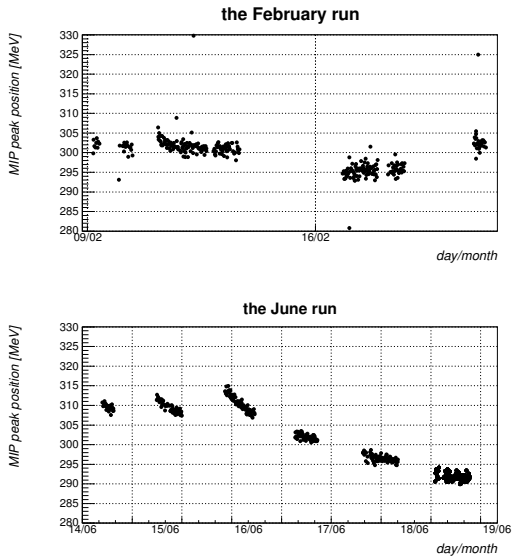

Figure 3.13: Drifting of MIP peak position with time observed in the February run (top) and in the June run (bottom).

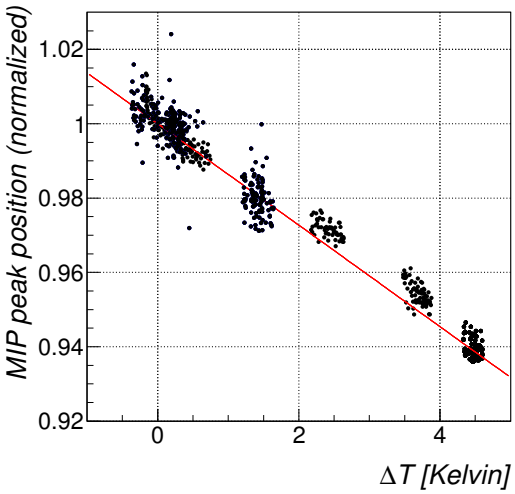

Figure 3.14: Relation between the MIP peak position and the temperature shift, ΔT. The MIP peak position was normalized by the value at the beginning of the run. The red line shows the slope of -1.4%/Kelvin.

Chapter 4

The Spectrometer Analysis

The $K_L \to \pi e \nu$ decays will be used to study the performance of the CsI calorimeter in Chapter 6 and Chapter 7. The $K_L \to \pi^+\pi^-$ and $K_L \to \pi^+\pi^-\pi^0$ decays will be used to measure the K_L momentum spectrum in Chapter 8. In the final state of any of the three decays, there are two charged particles, and both of them are reconstructed by using the spectrometer.

In this chapter, I will first describe the analysis of the spectrometer to reconstruct the two charged tracks. Subsequently, I will explain some corrections to increase the tracking accuracy. In the final section, I will estimate the spectrometer performance.

Alignment for the drift chambers and the trigger scintillators was important, because a large systematic errors will arise if the alignment is inadequate. I will explain that in Appendix C.

4.1 Reconstruction of Two Charged Tracks

4.1.1 Drift Chamber Analysis

I reconstructed the hit positions on the drift chambers from their TDC data.

TDC calibration

TDC data T[count] of each wire of the drift chambers was converted to a drift time $t_{\rm drift}$[nsec] assuming a simple linear correlation:

$$t_{\rm drift} = a \times T - t_0, \tag{4.1}$$

where a [nsec /count] represents a conversion factor and t_0 [nsec] represents an offset. The a for each TDC channel was measured with a clock generator before the runs started. It was typically 0.7 [nsec/count] for Repic-Dr.T, and 0.05 [nsec/count] for GND-HRTDC.

The t_0 for each wire was determined from the data. To select events which did not include accidental hits or noises, I defined "hit cluster". A particle could pass through $2 \sim 4$ successive wire cells in x and x' (or y and y') planes, as illustrated in Fig. 4.1. Such successive hits were grouped as a "hit cluster" and considered to be made by one incident particle. If there were 5∼8 successive hit wires, those were divided into two hit clusters with 4 hit wires as shown in Fig. 4.2. If there were more than 8 successive hit wires, those hits were ignored. As for the y plane of the 2nd chamber, where the y' plane was not active due to a shortage of readout electronics, a single hit was treated as a hit cluster. In order to derive the t_0s, I required that there were only two hit clusters in every wire plane. Figure 4.3 shows a typical $t_{\rm drift}$ distribution assuming $t_0 = 0$. I fitted a linear function to the rising edge of the distribution, and sought for a timing where a value on the linear function was equal to be a half of the maximum height of the distribution. The timing was set as t_0.

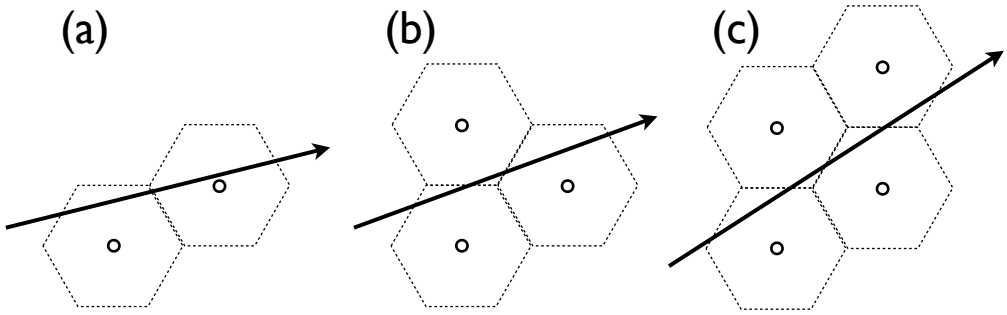

Figure 4.1: Hit patterns that a charged particle can make. The arrow represents a track of a charged particle and the circles represent hit sense wires. The 2∼4 hit wires with the patterns in the figures and their flipped patterns were grouped as a hit cluster.

X-T function

The drift time was converted to a drift length by using an X-T function $f_{XT}(t_{\rm drift})$. The f_{XT} was derived from the data. I selected events in which each wire plane had just two hit clusters. The f_{XT} was derived by integrating the drift time distribution, $g(t_{\rm drift})$, as

$$f_{XT}(t_{\rm drift}) = \frac{h}{2}\frac{\int_{\rm min}^{t_{\rm drift}} g(t)dt}{\int_{\rm min}^{\rm max} g(t)dt}, \tag{4.2}$$

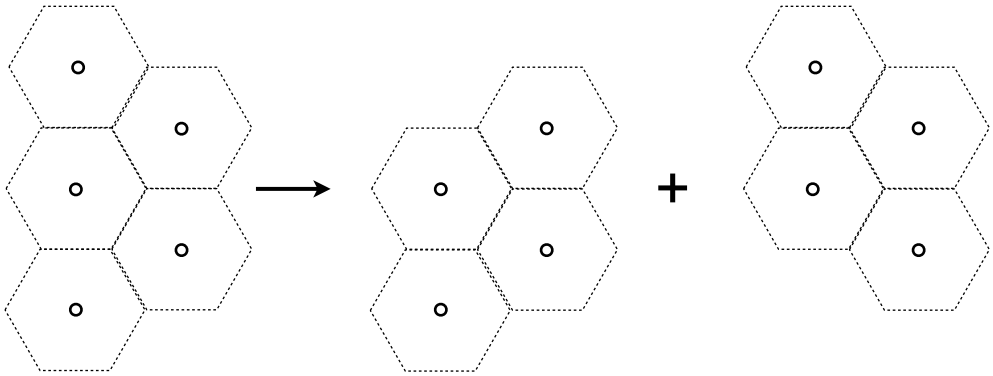

Figure 4.2: More than 4 successive hit cells was divided into two hit clusters.

where h is the spacing of the sense wires. The f_{XT} was prepared for each wire plane separately. An example of f_{XT} is shown in Fig. 4.4.

4.1.2 Track Candidate Selection

Because every chamber had multiple hits, many combinations of such hits were conceivable. We had to select one of the combinations corresponding to the two charged particles.

First of all, I picked a hit cluster in xx' (or yy') planes from each of three chambers. These three hit clusters were a candidate to form a track in the x (or y) direction. For y-track candidates, I required that the three hit clusters were located on a straight line, as

$$|y_2 - \{\frac{y_3 - y_1}{z_3 - z_1}(z_2 - z_1) + y_1\}| < 3\sigma, \tag{4.3}$$

where y_i and z_i represent y and z positions of the hit cluster on the i-th chamber, which was defined as an average position of the hit wires in the hit cluster. The σ was calculated according to the error propagation by assuming that errors on the y-positions were $h/\sqrt{12}$, where h is the gap of sense wires, and the z-position error was zero.

Next, I made a combination of 2 x-track candidates and 2 y-track candidates as a candidate of two charged tracks. I required some conditions for angles of those track candidates. Before explaining the conditions, let me introduce the notation to denote

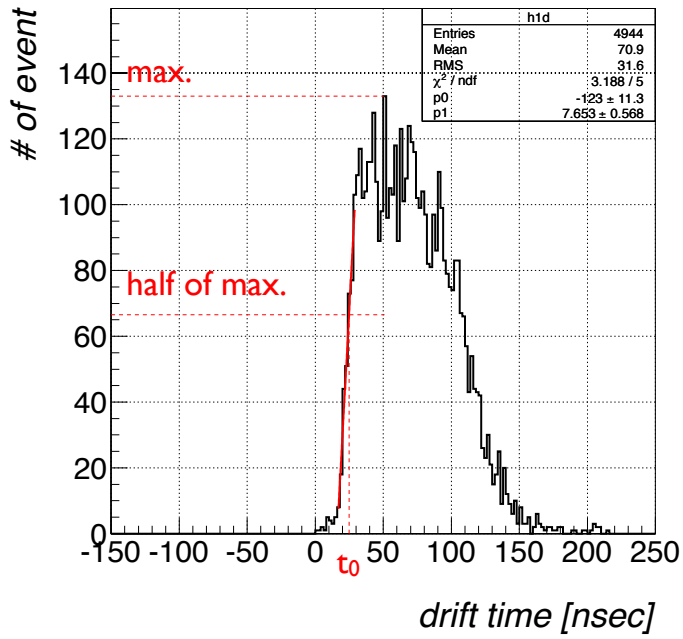

Figure 4.3: Drift time distribution of a given wire. The rising edge was fitted with a linear function as shown in solid line.

the angle,

$$\begin{aligned} \theta_{ij}^{\mathrm{xR(L)}} &= \arctan \frac{x_j^{\mathrm{R(L)}} - x_i^{\mathrm{R(L)}}}{z_j^{\mathrm{R(L)}} - z_i^{\mathrm{R(L)}}} \\ \theta_{ij}^{\mathrm{yD(U)}} &= \arctan \frac{y_j^{\mathrm{D(U)}} - y_i^{\mathrm{D(U)}}}{z_j^{\mathrm{D(U)}} - z_i^{\mathrm{D(U)}}}, \end{aligned} \tag{4.4}$$

where x_i and y_i mean x and y positons of hit clusters on the i-th chamber. The superscript R (or L) represent that, on the 1st chamber, the hit cluster of the track was located right (left) of the other track . Similarly, the superscripts for y direction, D and U, represent *Down* and *Up*, respectively. This notation is illustrated in Fig. 4.5. I rejected the two-track candidates which satisfied any of the following conditions.

1. The two tracks had the same curvature directions.

$$\left(\theta_{12}^{\mathrm{xR}} - \theta_{23}^{\mathrm{xR}}\right) \times \left(\theta_{12}^{\mathrm{xL}} - \theta_{23}^{\mathrm{xL}}\right) > 3\sigma.$$

2. The two tracks could not intersect at upstream of the 1st chamber.

$$\theta_{12}^{\mathrm{xR}} - \theta_{23}^{\mathrm{xR}} > 3\sigma \text{ and } \theta_{12}^{\mathrm{xR}} - \theta_{12}^{\mathrm{xL}} > 3\sigma$$

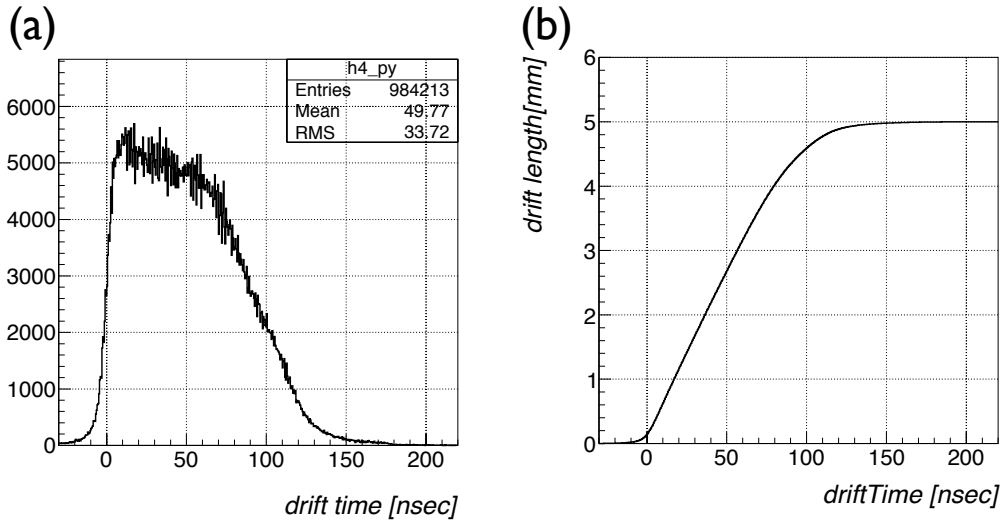

Figure 4.4: (a) Drift time distribution g(t) of x-wire plane of the 1st chamber. (b) The XT function, f_{XT} . It was obtained by integrating g(t).

for x hit clusters, or,

$$\theta_{12}^{\mathrm{yD}} - \theta_{12}^{\mathrm{yU}} > 3\sigma$$

for y hit clusters.

In each of the conditions, the error σ was calculated from errors of the positions of hit clusters by using the error propagation.

4.1.3 Track Path Reconstruction

Track paths were reconstructed for every remaining candidate of two charged tracks.

Tracking method

I used the tracking method based on [31, 32]. I will introduce only the essence of the method here.

In general, x and y positions of any curved track path, x_{path} and y_{path}, can be described

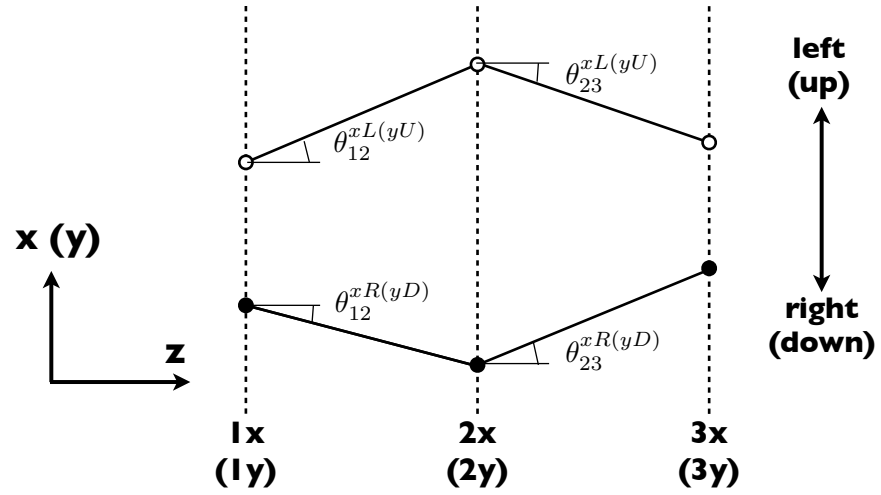

Figure 4.5: Schematic view of $\theta_{ij}^{xR(L)}, \theta_{ij}^{yU(D)}$ defined in Eq. (4.4). White and black circles represent the positions of hit clusters.

as a function of z position, as

$$\begin{aligned} x_{\rm path}(z) &= x_{\rm path}(0) + x'_{\rm path}(0)z + \int_0^z dz \int_0^{z'} dz\ x''_{\rm path}(z) \\ y_{\rm path}(z) &= y_{\rm path}(0) + y'_{\rm path}(0)z + \int_0^z dz \int_0^{z'} dz\ y''_{\rm path}(z), \end{aligned} \tag{4.5}$$

where the prime ($'$) indicates the differential to z. We cannot derive the track path from these equations, because $x''_{\rm path}(z)$ and $y''_{\rm path}(z)$ in the right-hand side are unknown.

In this tracking method, the equations are modified as

$$\begin{aligned} x_{\rm path}(z) &= x_{\rm path}(0) + x'_{\rm path}(0)z + \frac{1}{p}\int_0^z dz \int_0^{z'} dz\ px''_{\rm path}(z) \\ y_{\rm path}(z) &= y_{\rm path}(0) + y'_{\rm path}(0)z + \frac{1}{p}\int_0^z dz \int_0^{z'} dz\ py''_{\rm path}(z), \end{aligned} \tag{4.6}$$

where the p is the momentum of the charged particle. Because now we consider the charged particles moving in the magnetic field, the p is a constant. Although the $px''_{\rm path}(z)$ and $py''_{\rm path}(z)$ are still unknown, they can be estimated by using the known magnetic field and the roughly-estimated $x'_{\rm path}(z)$ and $y'_{\rm path}(z)$, as described

in Appendix D.1. On the assumption that those double-integrals were given, the five unknown parameters, $x_{\rm path}(0)$, $y_{\rm path}(0)$, $x'_{\rm path}(0)$, $y'_{\rm path}(0)$ and p^{-1}, were determined by fitting $x_{\rm path}(z)$ and $y_{\rm path}(z)$ to the positions measured with drift chambers. The estimation of the double-integrals were then updated with the fit result, and the fitting was repeated again. The parameters and the double integrals converged after iterating this process 6 times.

In each iteration of the fitting, the parameters were determined to minimize the χ^2 which was defined as

$$\chi^2 \equiv \sum_{i}^{\text{x wire plane}} \frac{(X_i - x_{\rm path}(Z_i))^2}{\sigma_{di}^2} + \sum_{i}^{\text{y wire plane}} \frac{(Y_i - y_{\rm path}(Z_i))^2}{\sigma_{di}^2}, \tag{4.7}$$

where X_i (Y_i, Z_i) represents x (y, z) position of a hit on the i-th wire plane, and σ_{di} is the resolution of the drift length for the hit.[1] The σ_d was set to 300 μm in all hits in the beginning, and updated later after evaluating the position resolutions of the wire planes which will be described later in Section 4.3.1. The X_i (or Y_i) was calculated using f_{XT} of Eq. (4.2), as

$$X(\text{ or } Y) = s \times \frac{f_{XT}(t_{\rm drift})}{\cos\theta} + \text{wire position}, \tag{4.8}$$

where the θ is the track angle projected to the x-z (or y-z) plane. In the first iteration of the fitting, the $\cos\theta$ was tentatively set to ∞, or the first term was ignored. From the second iteration, the θ was set to the value obtained from the previous iteration. The s is $+1$ or -1, to represent the side of the wire that the track passed through. If the track passed through the left (above) side of x (y) wire, $s = +1$, otherwise $s = -1$. In order to recognize the passed side, I used "sum of distances" which is described in the following subsection.

In the case that a hit cluster included 3 or 4 hit wires, I used only two of them for the fitting. I also used the "sum of distances" for selecting the two wires.

To reject tracks with bad combinations, I required that the χ^2 defined in Eq. (4.7) should be less than 10. This cut value was determined based on a Monte Carlo simulation so that the efficiency for correct track candidates were 99%.

Sum of distance

Although the drift chamber can measure the distance between a wire and a track path, it cannot tell which side of the wire the track passed through. If each of x and x' sense wire has a hit, there are four possible paths as shown in Fig. 4.6.

[1] The parameters to minimize the χ^2 can be solved without any numerical solution, as described in Appendix D.1.2. Thus, this tracking method generally takes less computing time than methods with numerical calculation.

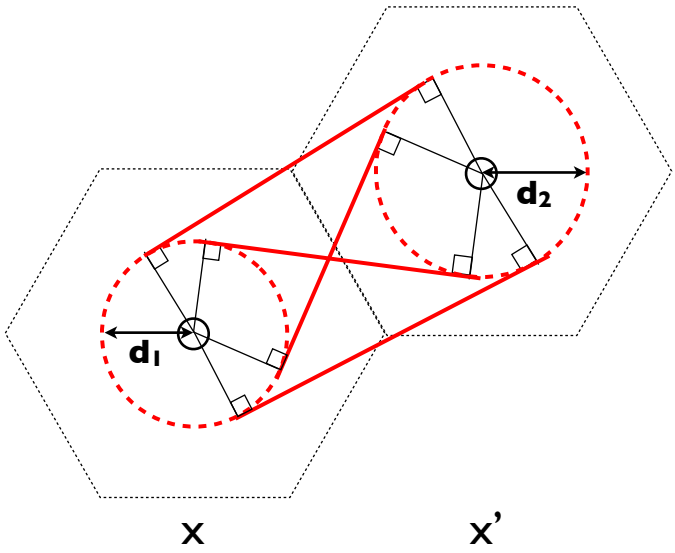

Figure 4.6: Schematic view of the ambiguity. White circles represent x and x' sense wires. For drift lengths of x and x' wires d_1 and d_2, there are four possible track paths which correspond to common tangent lines as shown in red solid lines.

In order to solve this ambiguity, I calculated the "sum of distances (SOD)". Defining the drift length of x (or x') wire as d (d'), the SOD_{obs} was defined as

$$SOD_{obs} \equiv -s \times d + s' \times d', \tag{4.9}$$

where s (and s') is $+1$ or -1 as used in Eq. (4.8)[2]. There are 4 combinations of s and s' which correspond to the 4 common tangent lines in Fig. 4.6.

As illustrated in Fig. 4.7, the expected value of the sum of distances, SOD_{exp}, can be calculated from the track angle as

$$SOD_{exp} = h \sin\left(\theta + s_{wire} \times 30^\circ\right) \tag{4.10}$$

where h is the space of sense wires[3] and θ is the incident angle projected on the x-z (or y-z) plane. The s_{wire} is $+1$ or -1. If the x (y) wire is located on the left (or upper) side of the x' (y') wire, s_{wire} is positive, and *vice versa*.

In order to determine s and s' in the fitting of the tracking process, I used ΔSOD which was defined as

$$\Delta SOD \equiv SOD_{obs} - SOD_{exp}. \tag{4.11}$$

In the first iteration of the fitting, s and s' are assumed as 0. From the second iteration, SOD_{exp} was calculated with the θ obtained in the previous iteration. The combination

[2] Equation (4.9) becomes $SOD_{obs} = d + d'$ if $s = -1$ and $s = +1$. That is why I call this quantity "sum of distances".

[3] It is equal to the distance between the closest x and x' wire.

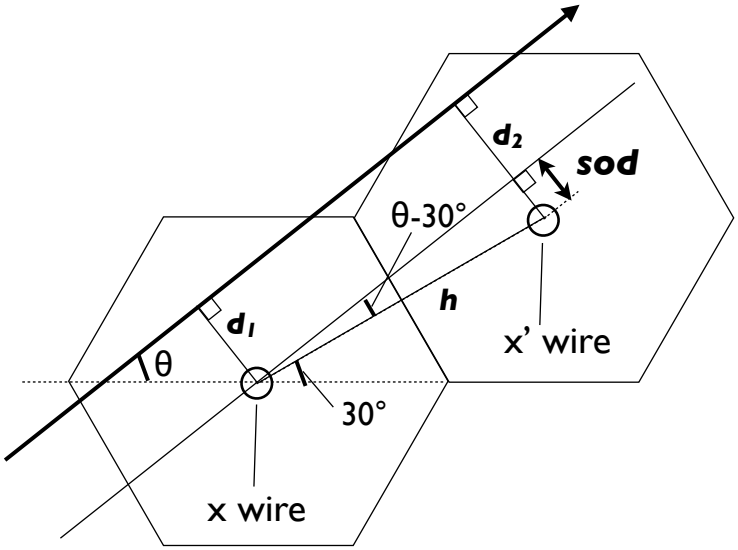

Figure 4.7: Schematic view of SOD.. Because $s = s' = 1$ and $s_{wire} = -1$ in this example, SOD_{obs} in Eq. (4.9) becomes $d' - d$ and SOD_{exp} in Eq. (4.10) becomes $h \sin(\theta - 30^\circ)$. Both are consistent with "SOD" in the figure.

of s and s' which made $|\Delta SOD|$ minimum was adopted. As for the y plane of the 2nd chamber where y' plane was nonactive and SOD_{obs} could not be calculated, I selected the s which made the hit position defined in Eq. (4.8) closer to the track path which was derived from the previous iteration.

If a hit cluster included more than two wires, only two wires were used for the fitting in the tracking process. In that case, the SODs were calculated for every combination of x and x' (or y and y') wires, and the one with the minimum $|\Delta SOD|$ was adopted.

Determination of two track paths

After the track path reconstruction, the matching with trigger scintillators was checked for each candidate. I extrapolated two reconstructed tracks to the surface of the trigger scintillators, and required that both of the extrapolated positions were located within one of the hit scintillators or within 2 cm from the edge of them. In case that two hit scintillators were channel 2 and channel 7, the event was discarded because both of the scintillators were located at y=0 and we cannot match tracks in the x and y views.

To select the most appropriate candidate, I used the minimum distance of the two tracks, $L_{\min}$, to evaluate the goodness of the candidate. If two tracks were produced from a K_L decay, the two tracks should intersect at the decay vertex and $L_{\min}$ should

be nearly equal to zero. The candidate which made the $L_{\min}$ minimum was adopted as the correct two tracks in the event. Figure 4.8 shows the distribution of minimum $L_{\min}$. To ensure the quality of the two tracks, I required that the minimum $L_{\min}$ was less than 50 mm. This requirement reduced the acceptance by 4.3 % for the data, and 2.7 % for Monte Carlo simulation. I also required that the two track paths are more than 5 mm away from the massive materials in the experimental area, such as frame structures of the drift chambers, the components of the magnet, and components of the beam shutter. The events which did not satisfy these requirements were discarded.

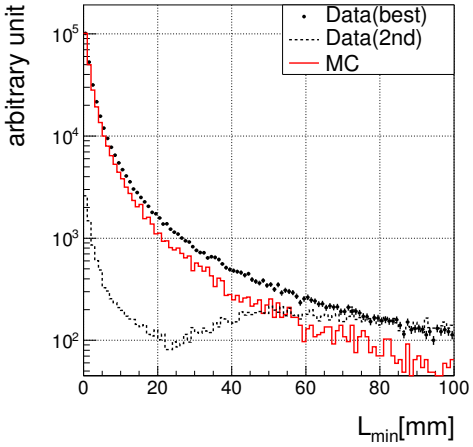

Figure 4.8: The L_{min} distribution. The black dots and the dashed line show the L_{min}s of the best candidate and the second best candidate for the data, respectively, and the red line shows the best candidate for the Monte Carlo simulation.

4.2 Improvements on Tracking Quality

In this section, I will introduce some updates and corrections to improve the tracking quality.

4.2.1 X-T Function

The X-T function f_{XT} which was defined as Eq. (4.2), was updated using the tracking result. The updated function was determined to minimize the ΔSOD which was defined in Eq. (4.11). I defined a χ^2 as

$$\chi^2 \equiv \sum_{event} (\Delta SOD)^2 . \tag{4.12}$$

where the summation was taken over events. With Eq. (4.9) and Eq. (4.11), it can be written as

$$\chi^2 = \sum_{event} \left(-s \times f_{XT}(t) + s' \times f'_{XT}(t') - SOD_{exp}\right)^2 , \tag{4.13}$$

where prime ($'$) indicates the value for x' plane.

The shape of the old X-T function, $f_{XT}^{\rm old}$ (Eq. (4.2)), was well expressed with a polynomial function except the regions near the sense wire and near the edge of the wire cell. I therefore parameterized the updated X-T function as

$$\begin{aligned} f_{XT}(t; t_{5\%} < t < t_{95\%}) &= f_{\rm pol5}(t) \\ f_{XT}(t; t < t_{5\%}) &= \frac{f_{\rm pol5}(t_{5\%})}{f_{XT}^{\rm old}(t_{5\%})} \times f_{XT}^{\rm old}(t) \\ f_{XT}(t; t > t_{95\%}) &= \left(f_{XT}^{\rm old}(t) - f_{XT}^{\rm old}(t_{95\%})\right) \frac{h/2 - f_{\rm pol5}(t_{95\%})}{h/2 - f_{XT}^{\rm old}(t_{95\%})} + f_{\rm pol5}(t_{95\%}), \end{aligned} \tag{4.14}$$

where h is the spacing of sense wires, and the $t_{5\%}$ and $t_{95\%}$ are the timings where the f_{XT} value becomes 5% and 95% of $h/2$, respectively. The $f_{\rm pol5}(t)$ represents polynomial function of fifth degree, *i.e.*:

$$f_{\rm pol5}(t) \equiv \sum_{i=1}^{5} \left(a_i(t - a_0)\right)^i . \tag{4.15}$$

In other words, I used an old X-T function with appropriately scaling at the regions where $f_{XT} \sim 0$ and $f_{XT} \sim h/2$, and used a fifth polynomial function in other ranges.

The 10 parameters of f_{XT} and f'_{XT}, $a_i (i = 0 \sim 5)$ in Eq. (4.15), were determined by minimizing the χ^2 in Eq. (4.13) for each xx' or yy' wire plane pair of each chamber. The ΔSODs and the f_{XT} before and after the minimization are shown in Fig. 4.9.

As for the y plane of the 2nd chamber, where we cannot calculate the SOD because the y' plane was inactive, the X-T function was updated with another method. I reconstructed the tracks without using the y plane of the 2nd chamber. The distance between the tracks and hit wires at the y plane of the 2nd chamber is shown in Fig. 4.10 as a function of the TDC times of the hit wires. The X-T function was determined by fitting the function in Eq. (4.14) to this plot.

4.2.2 Drift Time

I applyed two corrections to the drift time of the chambers.

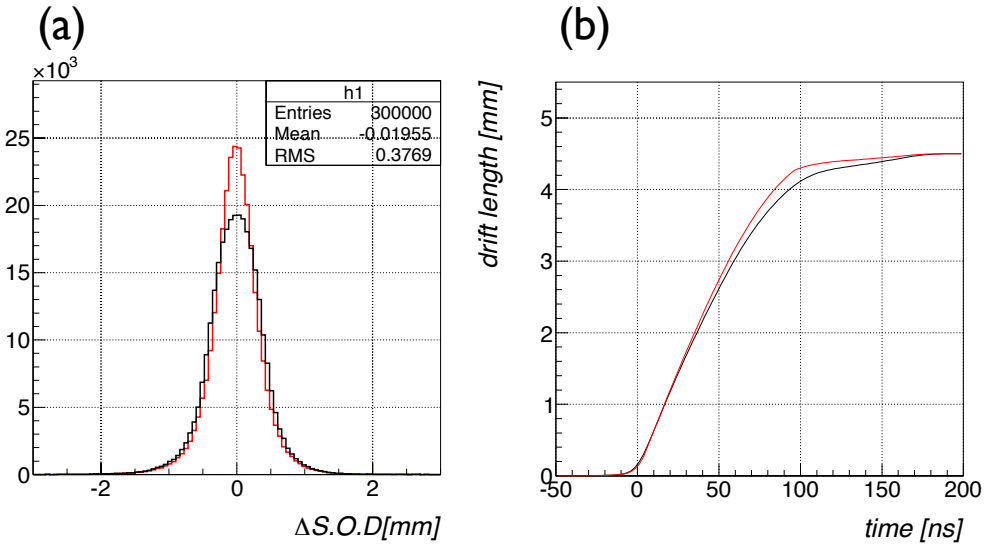

Figure 4.9: (a) The ΔSOD distribution of the x plane of the 2nd chamber calculated with old f_{XT} (black histogram) and with updated f_{XT} (red histogram). (b) The old $f_{XT}(t)$ (black line) and the updated $f_{XT}(t)$ (red line) of the x plane of the 2nd chamber.

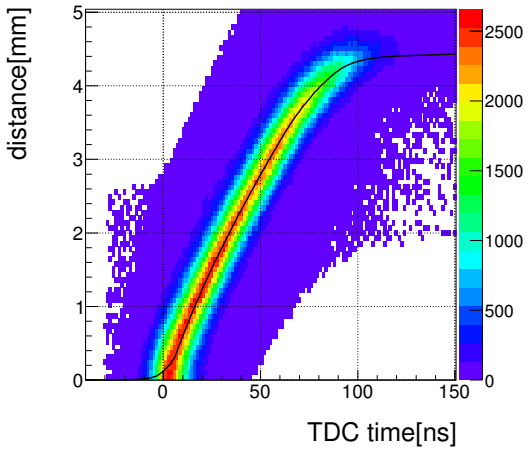

Figure 4.10: Histogram showing the distance of positions between the tracks and hit wires at the y plane of the 2nd chamber. The black line shows the updated X-T function.

Table 4.1: Propagation velocities in sense wires.

	propagation velocity[mm/nsec]
1st chamber	313 ± 15
2nd chamber	225 ± 4
3rd chamber	208 ± 3

- Propagation time in sense wire

  It took a finite time to transmit signal pulses through the sense wires to the PreAmps mounted on one side of the chambers. Consequently, the observed drift time was different from the true value due to the propagation time in the wire. By approximating that the drift velocity is constant in the wire cell, the drift length differed due to this effect as

$$d \rightarrow d_{modif} \equiv d + \delta d = d + \frac{L_{wire}}{V_{wire}} \times V_{drift}, \tag{4.16}$$

  where δd denotes the difference due to the propagation time in wire, L_{wire} and V_{wire} represent the propagation length and velocity, respectively. The V_{drift} represents the average drift velocity and was estimated to be 50 μm/nsec. In order to study this difference, I used ΔSOD defined in Eq. (4.11). Modifying the drift length as Eq. (4.16), the ΔSOD was also modified as

$$\begin{aligned} \Delta SOD \rightarrow \Delta SOD_{modif} &\equiv -s \times (d_{modif}) + s' \times (d'_{modif}) - SOD_{exp} \\ &= \Delta SOD + (s' - s)\frac{L_{wire}}{V_{wire}} \times V_{drift}. \end{aligned} \tag{4.17}$$

  By requiring $s' \neq s$,

$$(-s) \times \Delta SOD_{modif} = (-s) \times \Delta SOD + 2\frac{L_{wire}}{V_{wire}} \times V_{drift}. \tag{4.18}$$

  Thus, the $(-s) \times \Delta SOD$ observed in the data should include the component proportional to the propagation length L_{wire}. The dependence of ΔSOD upon the L_{wire} is shown in Fig. 4.11 (The kink in the plot of yy' wire plane is due to a propagation time in a trigger scintillator which is described in a following subsection). The propagation velocities of each chamber were then derived from the slopes of the plots for x-planes which corresponded to $2V_{drift}/V_{wire}$. They were estimated by linear fitting as summarized in Table 4.1.

  The drift time, t_{drift}, was corrected as

$$t_{drift} \rightarrow t_{drift} - L_{wire}/V_{wire}. \tag{4.19}$$

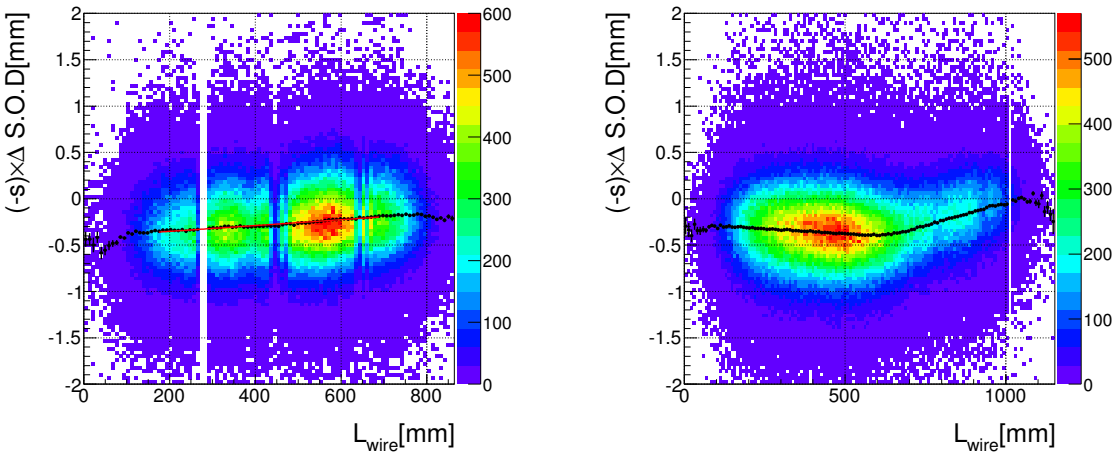

Figure 4.11: Dependence of ΔSOD multiplied $(-s)$ upon the propagation length in wire, L_{wire}. Here I required $s \neq s'$. The left and the right plots show the dependence in x plane and y plane of the 3rd chamber, respectively. The red line in the left plot shows a fit result with a linear function.

- Propagation time in the trigger scintillator

  A scintillation light generated in a trigger scintillator took a finite propagation time to reach a PMT. Similarly to the propagation time in wire, this effect was also observed as the dependence of the ΔSOD with $s \neq s'$ upon the propagation length, as shown in Fig. 4.12. I determined the propagation velocity of the scintillation light as 23.3 ± 0.1 cm/nsec, by linear fitting with the plots for the y planes. The drift time was then corrected as

  $$t_{drift} \rightarrow t_{drift} + L_{scinti}/V_{scinti}, \tag{4.20}$$

  where V_{scinti} and L_{scinti} represent the propagation velocity and length in the scintillator, respectively.

After these corrections were applied, TDC offsets of each wire which were determined in Section 4.1.1 were derived again with the corrected drift time.

Stability of trigger timing

The mean value of the ΔSOD drifted through the run time as shown in Fig. 4.13(a). Because the shift was common to all the chambers, this shift should be caused by the trigger signal. I set an offset for trigger timing for each data file corresponding to about 20 minutes data taking so that the mean value of the ΔSOD of all the wire planes became zero as shown in Fig. 4.13(b).

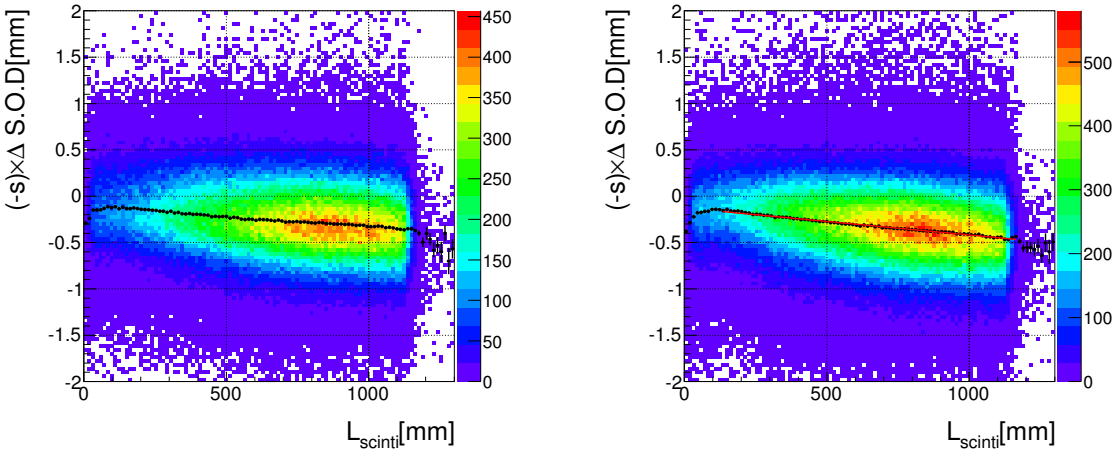

Figure 4.12: Dependence of ΔSOD multiplied $(-s)$ upon the propagation length in the trigger scintillator. Here I required $s \neq s'$. The left and the right plots show the dependence observed in the x plane and y plane of the 3rd chamber, respectively. The red line in the right plot shows a fit result with a linear function.

(a) (b)

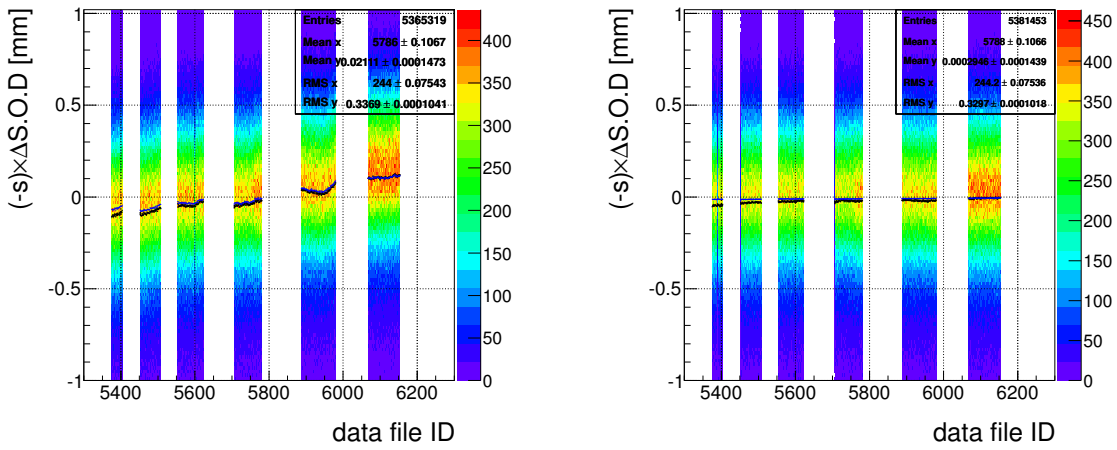

Figure 4.13: (a) Temporal shift of the ΔSOD multiplied $(-s)$ with requiring $s \neq s'$. The 2-dimensional histogram shows the $(-s) \times \Delta SOD$ observed in the x wire plane of the 2nd chamber, and the black line shows its mean value. The blue line shows a mean value of the $(-s) \times \Delta SOD$ in the y wire plane of the 3rd chamber. (b) Plots in (a) after applying the correction for the shift.

4.3 Performance Evaluation

The performance of the spectrometer is evaluated in this section. First, the fluctuation of the drift lengths measured with the drift chambers will be derived from the data. Subsequently, the momentum resolution and the incident position resolution of the spectrometer will be evaluated from the Monte Carlo simulation, by using the drift-length fluctuation as the Monte Carlo input.

4.3.1 Fluctuation of Drift Length

The drift lengths measured with the drift chambers were fluctuated by several sources, for example, the diffusion of the drift electrons. The difference of the measured drift length from its true value was described as δd. I used the ΔSOD defined in Eq. (4.11) to derive the distribution of δd. By assuming that the error on the SOD_{exp} is negligible, the ΔSOD is related to the δd as

$$\Delta SOD = -s\delta d + s'\delta d', \tag{4.21}$$

where s is $+1$ or -1 as in Eq. (4.8), and a quantity with a prime mark (') indicates that it is a value related to the x' wire plane. By requiring $s \neq s'$, we obtain

$$(-s) \times \Delta SOD = \delta d + \delta d'. \tag{4.22}$$

Figure 4.14(a) shows this $(-s)\times\Delta SOD$ observed in the data. Because the distribution was not a Gaussian, the distribution of δd is not expected to be a Gaussian either. Besides, a correlation was found between two ΔSODs of different wire planes, as shown in Fig. 4.14(b).

To reproduce these features of the ΔSOD, I assumed that the δd had two component as

$$\delta d = \delta d_{int} + \delta d_{com}. \tag{4.23}$$

The first component, δd_{int}, describes a fluctuation intrinsic to each wire plane, such as the diffusion of drift electrons or an inaccuracy of the X-T function. The second component, δd_{com}, describes a fluctuation common to all wire planes, such as the timing fluctuation of the trigger signal. The δd_{com} explains the correlation in Fig. 4.14(b). The distribution of δd is then expressed as

$$f(\delta d) = [f_{int} * f_{com}](\delta d), \tag{4.24}$$

where f_{int} and f_{com} represent the distributions of δd_{int} and δd_{com} respectively, and the operator "*" means a convolution, *i.e.*:

$$[f_{int} * f_{com}](x) = \int_{-\infty}^{\infty} f_{int}(x') f_{com}(x - x')dx'. \tag{4.25}$$

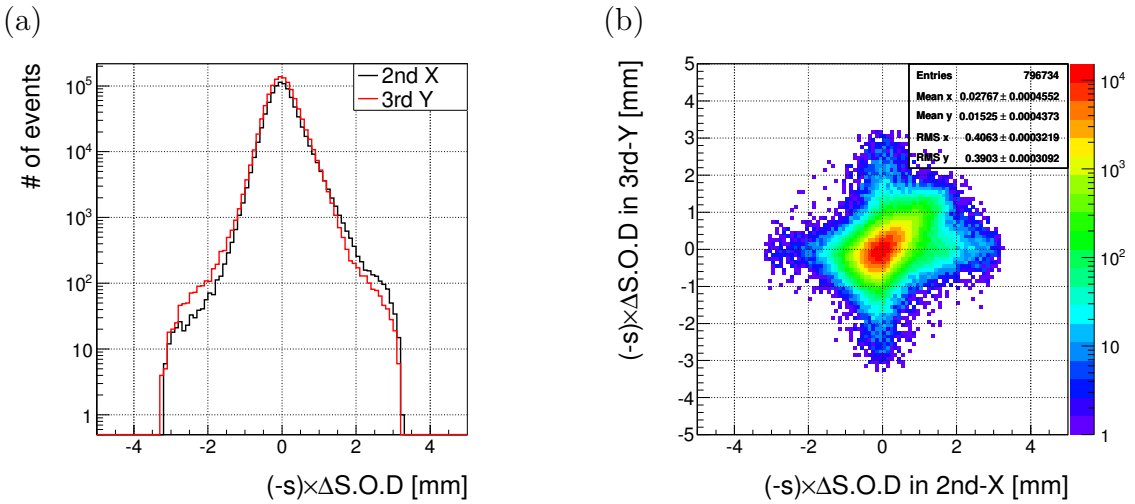

Figure 4.14: (a)The distributions of $(-s) \times \Delta SOD$ observed in the data, which corresponded to $\delta d + \delta d'$ as described in Eq. (4.22). Here I required $s \times s' = -1$. The black and the red histograms show the distributions observed in x wire planes of the 2nd and 3rd chambers, respectively. (b) Correlation of the ΔSODs between the different wire planes.

I reconstructed the forms of f_{int} and f_{com} separately with following steps. First, I took the difference between two ΔSODs to eliminate the contribution from the d_{com}. Because there were two charged tracks in each event, there were two ΔSODs in each wire plane. By subtracting one of the two ΔSODs from the other and requiring $s \neq s'$, the common fluctuation was canceled and we could obtain the contribution from the δd_{int} only, as

$$\begin{aligned} \Delta(\Delta SOD) &\equiv s^{(1)}\Delta SOD^{(1)} - s^{(2)}\Delta SOD^{(2)} \\ &= -\left(\delta d_{int}^{(1)} + \delta d_{int}^{(1)'} + 2\delta d_{com}\right) + \left(\delta d_{int}^{(2)} + \delta d_{int}^{(2)'} - 2\delta d_{com}\right) \\ &= -\delta d_{int}^{(1)} - \delta d_{int}^{(1)'} + \delta d_{int}^{(2)} + \delta d_{int}^{(2)'}, \end{aligned} \tag{4.26}$$

where superscripts (1) and (2) represent the track ID. Describing the convolution of two f_{int} as

$$F_{int}(x) = [f_{int} * f_{int}](x), \tag{4.27}$$

the distribution of $\Delta(\Delta SOD)$ is expressed as the convolution of $F_{int}(x)$ and $F_{int}(-x)$. The $\Delta(\Delta SOD)$ observed in the data is shown in Fig. 4.15(a). It was fitted well with a triple Gaussian f_{tgaus} which is defined as

$$\begin{aligned} f_{tgaus}(x) &= \frac{1 - A_2 - A_3}{\sqrt{2\pi}\sigma_1} \exp\left(-\frac{(x-\mu)^2}{2\sigma_1^2}\right) \\ &\quad + \frac{A_2}{\sqrt{2\pi}\sigma_2} \exp\left(-\frac{(x-\mu)^2}{2\sigma_2^2}\right) + \frac{A_3}{\sqrt{2\pi}\sigma_3} \exp\left(-\frac{(x-\mu)^2}{2\sigma_3^2}\right). \end{aligned} \tag{4.28}$$

I assumed that the $f_{int}(x)$ also could be expressed with the triple Gaussian. The F_{int} is then expressed as

$$F_{int}(x) = [f_{tgaus} * f_{tgaus}](x), \tag{4.29}$$

and the $\Delta(\Delta SOD)$ distribution is expressed as

$$f_{\Delta\Delta}(x) \equiv N \times [F_{int} * F_{int}](x), \tag{4.30}$$

where N is a normalization factor. The $f_{\Delta\Delta}(x)$ is calculable numerically. The $f_{\Delta\Delta}(x)$ was fitted to the observed $\Delta(\Delta SOD)$ distribution to determine the parameter set ($N, A_2, A_3, \mu, \sigma_1, \sigma_2$ and σ_3). The fit result and the obtained $f_{int}(x)$ are shown in Fig. 4.15(a) and (b).

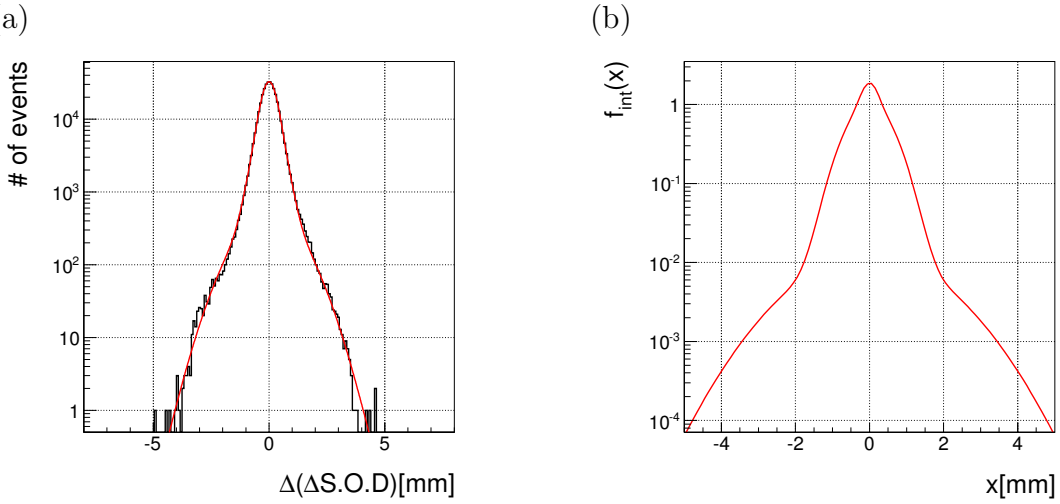

Figure 4.15: (a) The $\Delta(\Delta SOD)$ distribution defined in Eq. (4.26). The black histogram shows the data of x-plane of the 2nd chamber. The red line shows the best fit of $f_{\Delta\Delta}(x)$ which was defined in Eq. (4.30). (b) The f_{int} derived from the fitting.

Next I derived the f_{com}. Requiring $s \neq s'$, Eq. (4.21) was rewritten as

$$(-s) \times \Delta SOD = \delta d_{int} + \delta d'_{int} + 2\delta d_{com}. \tag{4.31}$$

Therefore, the distribution of the $(-s) \times \Delta SOD$ was expressed with the following function,

$$f_{\Delta}(x) = \int dx' [f_{int} * f_{int}](x') f_{com}(\frac{x - x'}{2}). \tag{4.32}$$

The f_{int} was already derived as the triple Gaussian, and consequently $[f_{int} * f_{int}]$ is calculable. The f_{com} was derived by unfolding the contribution of the $[f_{int} * f_{int}]$ from the measured $(-s) \times \Delta SOD$ distribution, by using *TUnfold* in *ROOT* library [33,34] which provides a function to solve unfolding problems.An example of the distributions of $(-s) \times \Delta SOD$ was already shown in Fig. 4.14(a). The $[f_{int} * f_{int}]$ and the derived

$f_{com}(x)$ are shown in Fig. 4.16(a). The average of the derived f_{com}s of all wire planes is shown in Fig. 4.16(b). It was parameterized with three Gaussians, *i.e.*:

$$f_{com}(x) = \sum_{i=0}^{2} A_i \exp\left(\frac{(x-\mu_i)^2}{2\sigma_i^2}\right). \tag{4.33}$$

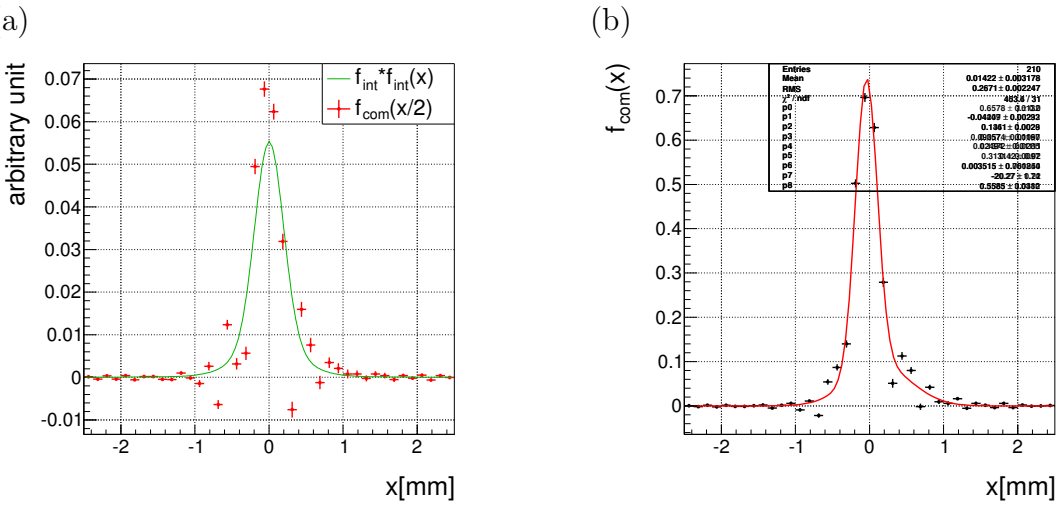

Figure 4.16: (a) The $[f_{int} * f_{int}](x)$ (green) and $f_{com}(x/2)$ (red), which appeared in Eq. (4.32), for an x wire plane of the 2nd chamber. (b) An average of the f_{com}s derived from all wire planes (black) and its fit result with three Gaussians (red).

The RMS of the derived f_{com} was 0.165 mm in the February run and 0.222 mm in the June run, and those of the derived f_{int} are summarized in Table 4.2. The performance of the 1st chamber in the February run was worse than that in the June run because the voltage supplied to the preAmps of the 1st chamber was set lower than usual to suppress observed noises in the February run. A quadratic sum of the f_{int} RMS for each wire plane and the f_{com} RMS is also shown in Table 4.2 and 4.3. It corresponded to the position resolution of the wire plane, and used as the σ_d in Eq. (4.7) to calculate the χ^2 of the track in the tracking process.

4.3.2 Momentum Resolution and Incident Position Resolution

The track position resolution at the CsI calorimeter z position and the momentum resolution of the spectrometer were derived from the Monte Carlo simulation. Hit positions on the chambers were fluctuated with the f_{int} and f_{com} derived above. Details of the Monte Carlo simulation are described in Appendix B.

Table 4.2: An RMS of the f_{int} and σ_d (= (RMS of f_{int}) $\oplus$ (RMS of f_{com})) for each wire plane in the February run.

(The February Run)

chamber	wire plane	RMS of f_{int}[mm]	σ_d[mm]
1st	x	0.467	0.495
	y	0.462	0.490
2nd	x	0.248	0.298
	y	-	-
3rd	x	0.292	0.335
	y	0.265	0.312

Table 4.3: An RMS of the f_{int} and σ_d (= (RMS of f_{int}) $\oplus$ (RMS of f_{com})) for each wire plane in the June run.

(The June Run)

chamber	wire plane	RMS of f_{int}[mm]	σ_d[mm]
1st	x	0.179	0.285
	y	0.182	0.287
2nd	x	0.218	0.311
	y	-	-
3rd	x	0.207	0.303
	y	0.208	0.304

In the simulation, charged tracks were reconstructed with the same procedure as the data. The reconstructed momentum and incident positions to the calorimeter were compared to the Monte Carlo true values, as shown in Fig. 4.17. The resolutions were evaluated from the width of these distributions. The momentum resolution σ_p is

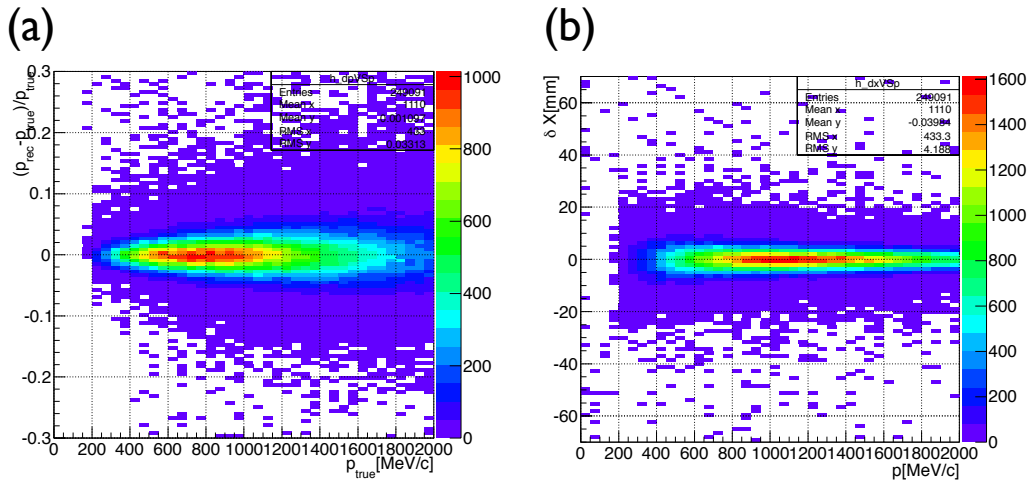

Figure 4.17: Residuals between the reconstructed value and the Monte Carlo true value for the momentum (a) and the incident position (b).

expressed as

$$\begin{aligned} \frac{\sigma_p(p)}{p} &\equiv a_p \oplus b_p \times p[GeV/c] \\ &= (1.347 \pm 0.011^{+0.101}_{-0.038})\% \oplus (2.618 \pm 0.007^{+0.039}_{-0.017})\% \times p[GeV/c] \end{aligned} \quad (4.34)$$

for the February run and

$$\frac{\sigma_p(p)}{p} = (1.286 \pm 0.010^{+0.101}_{-0.038})\% \oplus (1.981 \pm 0.007^{+0.039}_{-0.017})\% \times p[GeV/c] \quad (4.35)$$

for the June run, where p represents a momentum. The first error of each parameter was derived from Monte Carlo statistics, while the second error shows the systematic uncertainty which is described in the next section. The incident position resolutions

for x direction, σ_x, and for y direction, σ_y, were expressed as

$$\begin{aligned}
\sigma_x(p)[\mathrm{mm}] &\equiv a_x \oplus \frac{b_x}{p[GeV/c]} \\
&= (3.089 \pm 0.009^{+0.297}_{-0.036}) \oplus \frac{(2.009 \pm 0.013^{+0.175}_{-0.049})}{p[GeV/c]} \\
\sigma_y(p)[\mathrm{mm}] &\equiv a_y \oplus \frac{b_y}{p[GeV/c]} \\
&= (1.056 \pm 0.008^{+0.143}_{-0.064}) \oplus \frac{(2.377 \pm 0.007^{+0.090}_{-0.060})}{p[GeV]}
\end{aligned} \tag{4.36}$$

for the February run and

$$\begin{aligned}
\sigma_x(p)[\mathrm{mm}] &= (2.368 \pm 0.011^{+0.297}_{-0.036}) \oplus \frac{(2.017 \pm 0.011^{+0.175}_{-0.049})}{p[GeV/c]} \\
\sigma_y(p)[\mathrm{mm}] &= (0.6604 \pm 0.025^{+0.143}_{-0.064}) \oplus \frac{(2.02 \pm 0.01^{+0.090}_{-0.060})}{p[GeV]}
\end{aligned} \tag{4.37}$$

for the June run. Due to the worse position resolutions of the chambers, the spectrometer resolutions in the February run were worse than those in the June run. These functions for the June run are shown in Fig. 4.18.

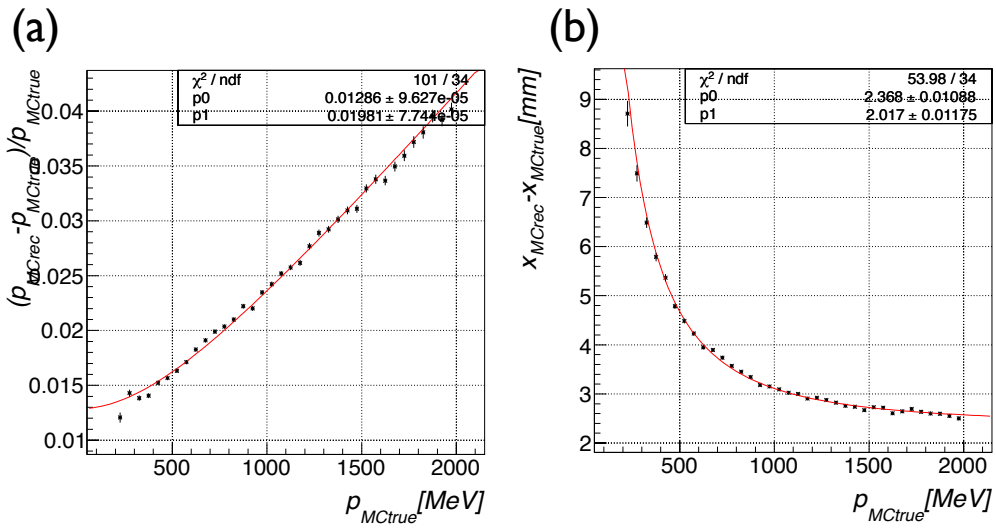

Figure 4.18: Resolution functions of the momentum (a) and the incident position (b) described in Eq. (4.35) and Eq. (4.37).

Table 4.4: Systematic uncertainty of the momentum resolution (σ_p/p) and the x and y position resolutions (σ_x and σ_y) of the spectrometer. The parameters, $a_{p\ (x,y)}$ and $b_{p\ (x,y)}$, are defined in Eq. (4.35) for σ_p/p, in Eq. (4.37) for σ_x and σ_y.

	σ_p/p[%]		σ_x[mm]		σ_y[mm]	
	a_p	b_p	a_x	b_x	a_y	b_y
magnet						
resolution	+0.005	0	+0.002	0	+0.003	-0.001
	0	-0.006	0	-0.003	-0.001	-0.001
direction	+0.004	+0.002	+0.001	0	0	0.008
	-0	-0.006	-0.001	0	-0.004	0
offset	+0.018	+0.004	+0.001	+0.009	0.002	0.018
	0	-0.014	-0.002	0	-0.005	0
asymmetry	+0.101	0	+0	+0.137	0	0.002
	-0	-0.007	-0.041	-0	-0.003	0
ANSYS	+0.004	0	+0.004	+0.012	0.001	0
	0	-0.004	-0.004	0	-0.001	-0.001
multi. scat. model	+0	+0.020	+0.037	+0.041	+0.034	+0
	-0.004	-0.003	-0.007	-0.048	-0.063	-0.057
chamber alignment						
1st chamber	+0.013	0	+0.028	+0.028	+0.181	+0.014
	0	-0.014	-0.015	-0.008	-0.003	-0.006
2nd chamber	+0.013	0	+0.005	+0.002	+0.001	0
	0	-0.014	0	-0.009	0	-0.001
3rd chamber	+0.014	0	+0.009	+0.009	+0.004	+0.002
	0	-0.015	-0.004	-0.009	-0.003	-0.002
total	+0.105	+0.020	+0.048	+0.146	+0.184	+0.024
	-0.004	-0.031	-0.045	-0.050	-0.064	-0.057

4.3.3 Uncertainties of the Resolutions

Table 4.4 shows the systematic uncertainties of the parameters (a and b) of the momentum resolution and the position resolution of the spectrometer. All items in the table were quadratically summed. In the following, I will explain the source of each uncertainty.

Accuracy of magnetic field measurement

As described in Section 2.2.1, I measured the magnetic field of the spectrometer magnet in the $X > 0$ and $Y > 0$ region. In addition, the field was measured for several points at $X = 0$ and $Y < 0$, and also at $Y = 0$ and $X < 0$, to study the systematic uncertainty related to the measurement. The measured region is illustrated in Fig 4.19.

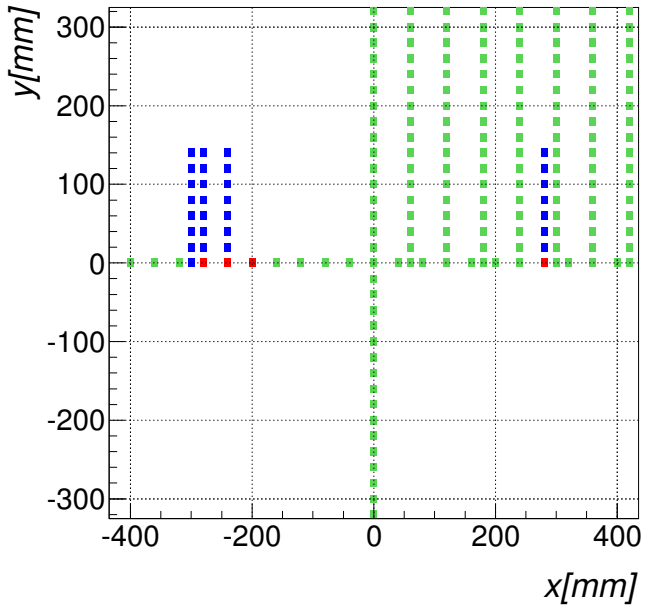

Figure 4.19: Points where the magentic field was measured are illustrated. Some red points shows points where the measurement was done twice. Some points near the dent of the upstream end guard around $X = -300$ mm were measured in addition, which are illustrated as blue points.

- Resolution of the measuring instrument

  The field measurement was done twice for some points shown in red in Fig 4.19. Figure 4.20 shows the difference of those two measurements. The resolution of the measuring instrument was estimated as 4.7 Gauss, from the RMS of the difference divided by $\sqrt{2}$.

  To study the effect of this uncertainty on the spectrometer resolution, the magnetic field of every measured points was fluctuated randomly in the simulation with a Gaussian with $\sigma = 4.7$ Gauss. I tested 9 patterns of the fluctuations. The parameters of the resolution, a and b, were estimated for each pattern. The

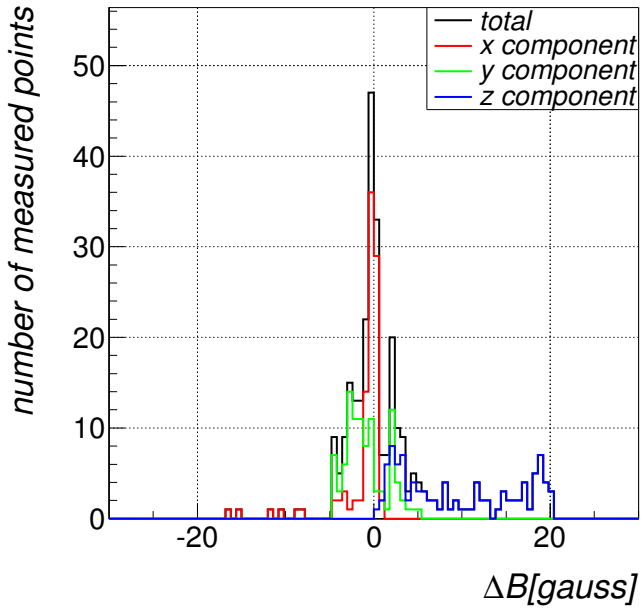

Figure 4.20: Differences of the magnetic field between two measurements. The red, green, and blue histograms show the differences of x, y, and z components of the field, and the black histogram shows the sum of those 3 histograms.

mean ± RMS of the 9 trials was adopted as the systematic error of the parameter which is shown in the "resolution" items in Table 4.4.

- Direction of the measured field.

  Because the magnet had almost symmetric configuration in both vertical and horizontal directions, it was expected that the x and z component of the magnetic field on the z axis should be zero. The measured values, however, were not zero and they had correlation with the y component of the field, as shown in Fig. 4.21(a, b). This indicates that the direction of the measured field was misaligned. Assuming that the direction misalignment was small enough, the real field, B'_x, B'_y and B'_z, can be expressed with the measured field, B_x, B_y and B_z, as

$$\begin{pmatrix} B'_x \\ B'_y \\ B'_z \end{pmatrix} = \begin{pmatrix} 1 & -\theta_z & \theta_y \\ \theta_z & 1 & -\theta_x \\ -\theta_y & \theta_x & 1 \end{pmatrix} \begin{pmatrix} B_x \\ B_y \\ B_z \end{pmatrix} \tag{4.38}$$

  where θ_x, θ_y, and θ_z represent the rotation angles around x, y, and z axis.

  By fitting a linear function to the scattered plots in Fig. 4.21(a, b), θ_x and θ_z

were derived from the slope of the linear function as 0.022 and -0.0016 rad, respectively. The θ_y was determined by using the measurement points at $x = 0$ and $y \neq 0$ where B'_x should be zero. The θ_y corresponded to the slope of $(B_x - \theta_z B_y)$ vs B_z plot which is shown in Fig. 4.21(c). It was estimated as $\theta_y = -0.00308$. The measured field was corrected with these rotational angles.

The scattered plots in Fig. 4.21 have parabola shapes. As described in the next topic, this shape is related to the offset of the magnetic field. An ambiguity to determine the $\theta_{x(y,z)}$ arose due to this parabola shape. To evaluate the effect of this ambiguity on the estimation of the spectrometer resolutions, I did linear fittings separately for the one side and the other side of the parabola, as shown in the blue lines in Fig. 4.21. The rotational angles derived from the fittings denote $\theta^U_{x(y,z)}$ and $\theta^D_{x(y,z)}$. I ran the simulation with using $\theta^U_{x(y,z)}$ or $\theta^D_{x(y,z)}$ for a correction instead of $\theta_{x(y,z)}$. As a result, the parameters of the resolution formula were changed as shown in the "direction" items in Table 4.4. I adopted these changes as the systematic errors.

(a) B_x VS B_y (b) B_z VS B_y (c)$(B_x - \theta_z B_y)$ VS B_z

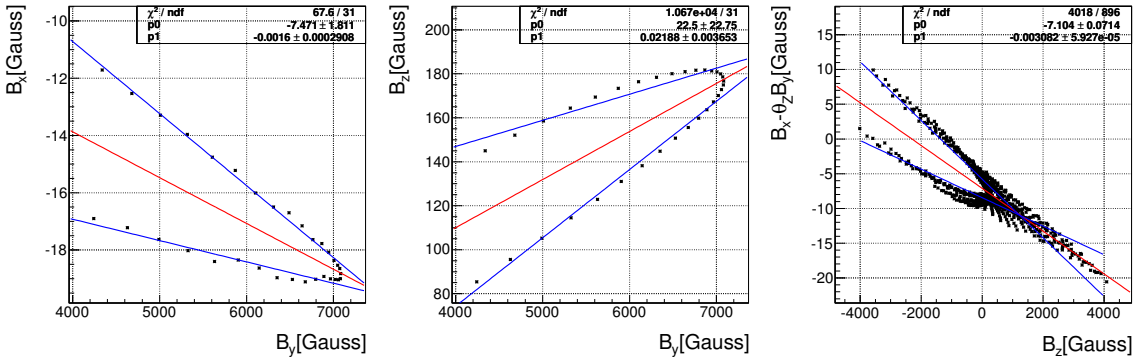

Figure 4.21: Correlations between the components of the magnetic field. (a) The x vs y components on the z axis. (b) The z vs y components on the z axis. (c) The x vs z component at x=0. The red line in each plot shows the result of linear fit with using all points. Blue lines are also linear fit results, but using only the points above or below the red line.

- Offset of the measured field.

  As shown in Fig. 4.22, the B_x values and the B_z values on the z-axis had non-zero values which depended on z position, although they were expected to be zero from the symmetrical shape of the magnet. This was a source of the parabola shape which was described in the previous topic. Each side of the parabola corresponded to values in $z > 0$ and $z < 0$ region.

  The source of this dependence is still unknown. I assumed that the field had a

(a) B_x VS Z (b) B_z VS Z

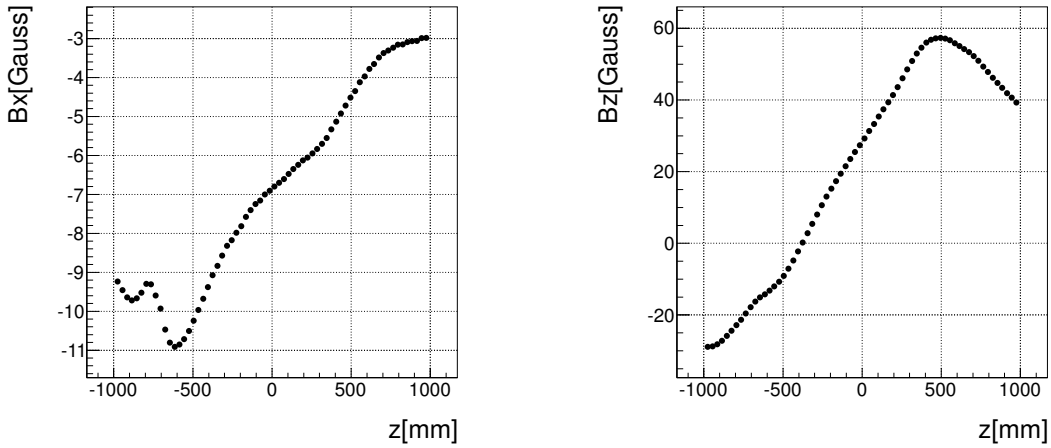

Figure 4.22: The x component (a) and z component (b) of the magnetic field on the z-axis. They had unknown dependence on z position.

z-depended offset, and estimated the uncertainty of the spectrometer resolutions due to such offset. I assumed three types of the offset forms:

1. The z-depended offset. The B_x and B_z values shown in Fig. 4.22 were used as the offset for each z position.
2. A constant offset of -7.5 Gauss for x component, and 22.5 Gauss for z component. These values are corresponding to the components at the center of the magnet.
3. No offset.

With these offsets, the parameters of the resolution changed as shown in the "offset" items in Table 4.4. I adopted these changes as systematic uncertainties.

- Asymmetry along vertical and horizontal directions.

  I measured the magnetic field only in the first quadrant, that is, $X > 0$ and $Y > 0$ region. For other quadrant region, the measured field was appropriately inverted assuming the symmetry along both in vertical and horizontal directions.

  I checked the symmetry along the vertical direction by comparing the y components of the field, B_y, at $Y > 0$ and $X = 0$ with those at $Y < 0$ and $X = 0$. Similarly, the symmetry along horizontal direction was checked by comparing B_y at $X < 0$ and $Y = 0$ with those at $X > 0$ and $Y = 0$. As shown in Fig. 4.23, the asymmetry of the field was less than 2% around the center of the magnet and tended to be larger around the end guards. A region surrounded by the magenta line in the figure had a relatively large asymmetry because there was a 10×10-cm dent on the upstream end guard. Instead of inverting the filed of

1st quadrant, the field was additionally measured for a region around the dent which is shown in Fig. 4.19 with blue points.

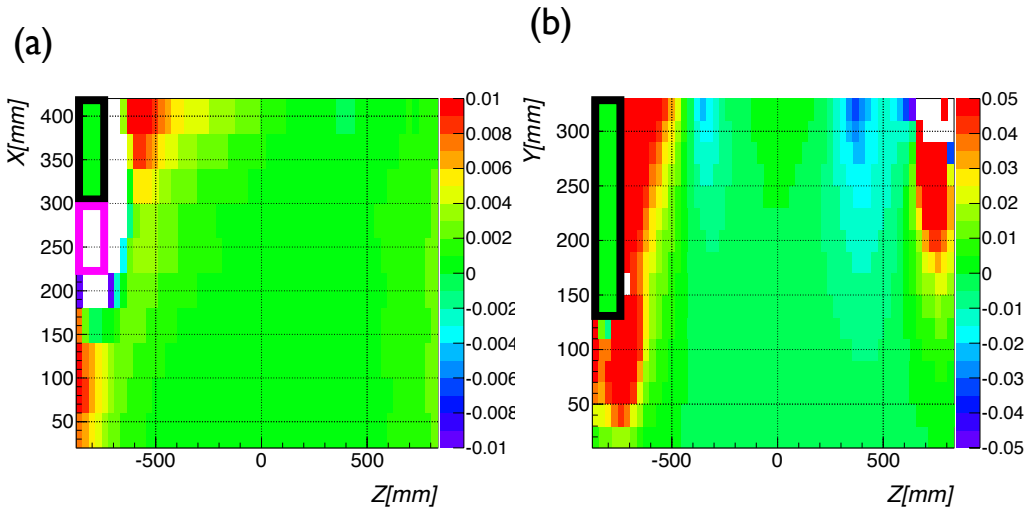

Figure 4.23: (a) Horizontal asymmetry of the y component of the magnetic field, or, $(B_y(-x,0,z) - B_y(x,0,z))/B_y(x,0,z)$. (b) Horizontal asymmetry, or, $(B_y(0,-y,z) - B_y(0,y,z))/B_y(0,y,z)$. The region surrounded by the black line had no measured data because of the end guard. The field was additionally measured around the region surrounded by the magenta line

To evaluate the uncertainty due to this asymmetry, I assumed that a magnetic field at all points in $X < 0$ (or $Y < 0$) region had the same rate of the asymmetry in Fig. 4.23(a) (or (b)). With and without such assumption, the parameters of the resolution changed as shown in the "asymmetry" items in Table 4.4. I adopted those changes as systematic uncertainties. This is the largest source of uncertainty for the parameter a in σ_p/p: $+0.099\%$, and also for the parameter b in σ_x: $+0.126$ mm.

Consistency of ANSYS simulation for magnetic field

As described in Section 2.2.1, the field value calculated with ANSYS was used in the range outside the measurement. The consistency between the ANSYS calculation and the measurement was checked by comparing the values around the center of the magnet where the calculated value and the measured value both existed. The comparison was executed for points within $-200 < x < 200$ mm, $-200 < y < 200$ mm, and $-400 < z < 400$ mm with respect to the center position of the magnet. The RMS of the difference between the ANSYS calculation and the measurement was less than 4 %.

I changed the scale of the values calculated by ANSYS by this difference, ±4%, in the simulation. The parameters of the resolution changed as shown in the "ANSYS" items in Table 4.4. I adopted those changes as systematic uncertainties.

Uncertainty of multiple scattering models

I used the *G4UrbanMscModel95* model to simulate multiple scattering. Geant4 9.5 supports other models, *G4GoudsmitSaundersonMscModel* and *G4WentzelVIModel*. I ran the simulation with these two models. The parameters of the resolutions changed as shown in the "multi. scat. model" items in Table 4.4. I adopted those changes as the systematic uncertainties.

Drift chamber alignment

As described in Appendix C, the position displacements of the drift chambers were represented with the parallel translation δ_{ia} and the rotation θ_{ia} (where the subscript $i = 1, 2, 3$ represents the 1st, 2nd and 3rd chamber in order, and the subscript $a = x, y, z$ represents the direction to translate or the axis to rotate around). Their values and errors were estimated as shown in Table C.1.

To estimate the effect of the chamber displacement on the spectrometer resolutions, the translations and rotations in the simulation were fluctuated randomly within their errors. When the values of the 1st chamber were fluctuated, the corresponding values of the 2nd and 3rd chambers were also modified, because the displacement of the 2nd and 3rd chambers were derived with assuming that the position of the 1st chamber was correct. Similarly, when the values of the 3rd chamber were fluctuated the corresponding values of the 2nd chamber were modified.

I prepared 9 patterns of the fluctuation for each component. The parameters of the resolution were estimated for each pattern, and the mean ± RMS of the 9 trials was calculated. The square sum of the mean ± RMS of all the component was adopted as the systematic error of the parameter. They are shown in the "chamber alignment" items in Table 4.4. These are dominant uncertainties for the parameters of σ_x and σ_y.

Chapter 5

CsI Energy Calibration with Electrons

The energy calibration of the CsI calorimeter was performed by using cosmic rays, as described in Section 3.2. A calibration with using electromagnetic showers is, however, preferable because there is nonuniformity of light output along the z direction of CsI crystal and consequently CsI outputs made by cosmic rays are different from those made by electromagnetic showers.

In this chapter, I will derive calibration factors again with electrons which were tracked by the spectrometer. I will explain the selection criteria for electrons in the first section. The method to determine the calibration factors is given next. If a nonlinearity of the FADC exists, the calibration performance will become worse. The nonlinearity was checked and corrected for in the third section. The accuracy of the calibration factors is estimated in the last section.

5.1 Electron Selection

Electrons were identified by using both the CsI calorimeter information and the spectrometer information cooperatively.

5.1.1 Matching Tracks and Clusters

The tracks which were reconstructed with the spectrometer were related to the clusters observed in the CsI calorimeter according to their positions. If the track position extrapolated to the calorimeter was located within 100 mm of a cluster position, the track was associated with the cluster. To avoid mis-associating, I required that there

were no other clusters within 100 mm of the track position. The distributions of the distances to the nearest and the second nearest clusters from the track position are shown in Fig. 5.1.

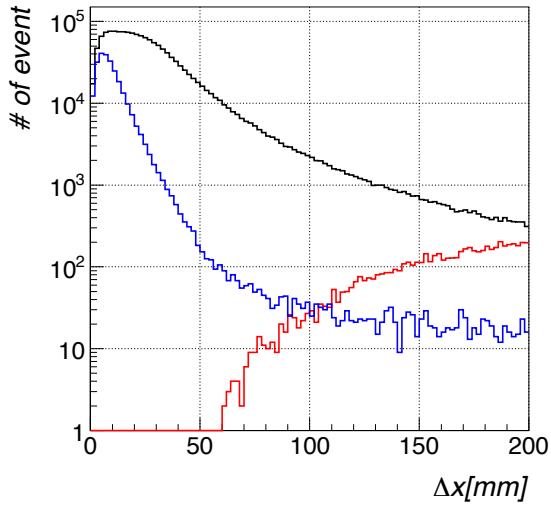

Figure 5.1: Distance between the incident position of charged particles tracked with the spectrometer and the cluster position. The black line shows the distance to the nearest cluster, and the red line shows that to the second nearest. The blue line shows the distance to the nearest cluster after applying the electron selection cuts described in the following section.

5.1.2 E_{CsI}/E^{vis}_{spec} Ratio

Because electrons made electromagnetic showers and deposited almost all of their energies on the CsI calorimeter, the ratio of the energy measured by the CsI calorimeter, E_{CsI}, to the momentum measured with the spectrometer, p_{spec}, had a clear peak centered at 1. This was a signature of electrons. To be more precise, the E_{CsI} differed from p_{spec} by energy deposits in materials in front of the CsI calorimeter such as the trigger scintillators, the CsI covers, and air. The total amount of such energy deposits, $E^{\rm material}_{dep}$, was 8.0 MeV based on the Monte Carlo simulation. As for positrons, the energy deposits also differed by the positron mass because the energy equivalent to their mass was deposited in the calorimeter through annihilation. I defined the visible energy measured with the spectrometer, E^{vis}_{spec}, as

$$E^{vis}_{spec} = \sqrt{m_e^2 + p^2_{spec}} + Q \times m_e - E^{\rm material}_{dep}, \tag{5.1}$$

where m_e denotes the electron mass and Q represents a sign of the charge of the track. The E_{CsI}/E^{vis}_{spec} ratio is shown in Fig. 5.2. A clear peak made by electrons was found

around $E_{CsI}/E^{vis}_{spec} = 1$. The events with the $E_{CsI}/E^{vis}_{spec} < 0.8$ in the figure were considered to be made dominantly by pions and muons from K_L decays. We need further selection cuts to suppress their contamination to the electron peak.

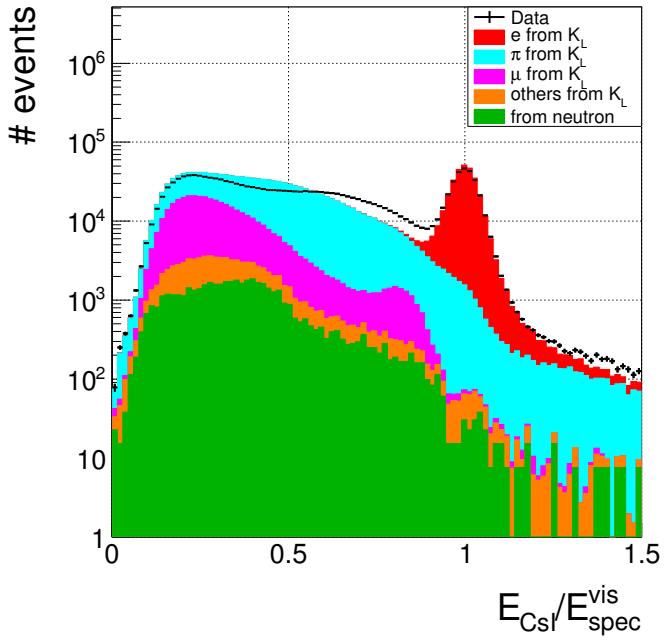

Figure 5.2: Ratio of the E_{CsI} to the E^{vis}_{spec}. The black dots shows the measured data, while the histograms shows the expectation from the Monte Carlo simulation. The colors represent kinds of incident particles. The red, light blue, and magenta show electrons, pions, and muons generated from K_L decays, respectively. The yellow shows particles generated from K_L hadronic interactions or from decays of K_L daughter particles. The green shows particles generated from neutron interactions.

5.1.3 Selection Cuts

I applied selection cuts as follows, to identify the electrons and to guarantee the data quality.

1. FADC range cut.

   To avoid an overflow from the range of the FADC (14-bits), I required the maximum FADC count of every waveforms in the cluster to be less than 15000 counts.

2. CsI fiducial region cut.

   To ensure that electromagnetic showers did not leak from the effective area of the calorimeter, I allocated an *edge* region and a *fiducial* region on the calorimeter

as shown in Fig. 5.3. I required that the both positions measured with the calorimeter and the spectrometer were located within the fiducial region.

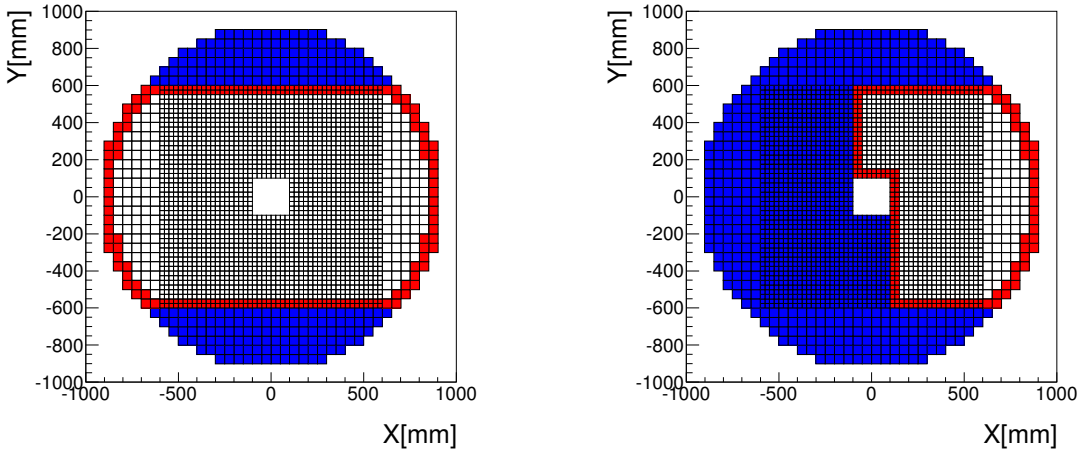

Figure 5.3: Region allocation of the CsI calorimeter. The condition in the February run and the June run are shown in (a) and (b), separately. The white area shows the fiducial region, while the red shows the edge region. The blue filled blocks are inactive crystals.

3. The k_{+-0} cut.

   To suppress the contamination from $K_L \to \pi^+\pi^-\pi^0$ decays, I introduced a parameter called k_{+-0} which was used in the KTeV experiment [35]. It was defined as

$$k_{+-0} = \frac{\left(m_{K_L}^2 - m_{+-}^2 - m_{\pi^0}^2\right)^2 - 4m_{+-}^0 m_{\pi^0}^2 - 4m_{K_L}^2 p_t^2}{4\left(m_{+-}^2 + p_t^2\right)}, \tag{5.2}$$

   where m_{K_L} and m_{π^0} are the masses of K_L and π^0, respectively. The m_{+-} and the p_t represent the invariant mass and the transverse momentum of the system of two charged particles, respectively.

   The physical meaning of the k_{+-0} is that the square of the longitudinal momentum of the π^0 from the $K_L \to \pi^+\pi^-\pi^0$ decay along K_L flight direction in a frame where the $\pi^+\pi^-$ pair has no longitudinal momentum. If the two charged particles did not come from the $K_L \to \pi^+\pi^-\pi^0$ decay, k_{+-0} tend to be negative as shown in Fig. 5.4(a). I required that the k_{+-0} was less than -9000 MeV^2.

4. Shape χ^2 cut.

   To evaluate a cluster shape on the calorimeter, the KOTO experiment uses a variable called "shape χ^2". This value is calculated by comparing the observed energy deposit in each crystal with its expectation derived from a Monte Carlo

simulation. If the cluster is made from a normal electromagnetic shower, the shape χ^2 becomes $\sim$1. The details of the shape χ^2 is described in Appendix A.1.2.

The distribution of the shape χ^2 is shown in Fig. 5.4(b). Clusters made by electrons tend to have smaller shape χ^2 values than the clusters made by other particles. I required the shape χ^2 to be less than 2.5.

5. Cluster size cut.

   The pions and muons often passed through the calorimeter as MIPs. In such a case, energy deposits were made on only a few CsI crystals, as shown in Fig. 5.4(c). I required the number of crystals in the cluster to be > 5.

6. E_{CsI}/E^{vis}_{spec} cut.

   The distribution of the E_{CsI}/E^{vis}_{spec} ratio after applying all the cuts above is shown in Fig. 5.4(d). I required $0.8 < E_{CsI}/E^{vis}_{spec} < 1.2$.

The number of electron candidates passing through all the selection cuts was 2.2×10^5. The energy distribution is shown in Fig. 5.5.

5.2 Calibration Using Electrons

Energies of electrons incident on the CsI calorimeter, E_{inc}, were reconstructed as shown in Eq. (3.4) and Eq. (3.7). By making the calibration constants visible, the E_{inc} was rewritten as

$$E_{inc} = \frac{1}{f_{Ecor}} \sum_i c_i \times I_i, \tag{5.3}$$

where c_i and I_i represent the calibration constant and the waveform integral of the i-th crystal respectively, and f_{Ecor} is the correction function defined in Eq. (3.8).

To determine the calibration constants, I defined χ^2 as

$$\chi^2 = \sum_{events} \left(\frac{E_{inc} - E^{vis}_{spec}}{\sigma_{spec} \oplus \sigma_{CsI}} \right)^2, \tag{5.4}$$

where σ_{spec} and σ_{CsI} represent the momentum resolution of the spectrometer and the energy resolution of the calorimeter, respectively. The summation was taken over all electron events. The σ_{spec} was derived as Eq. (4.35) in Section 4.3. The σ_{CsI} was assumed to be the KOTO design value,

$$\frac{\sigma_{CsI}}{E} = 1\% \oplus \frac{2\%}{\sqrt{E[GeV]}}. \tag{5.5}$$

The set $\{c_i\}$ was determined to make the χ^2 minimum. In such case, a partial differentiation of the χ^2 to a given c_j should be zero, *i.e.*:

$$\begin{aligned}\frac{\partial\chi^2}{\partial c_j} &= \sum_{events}\frac{2I_j}{f_{Ecor}\times\left(\sigma^2_{spec}+\sigma^2_{CsI}\right)}\left(\frac{1}{f_{Ecor}}\sum_i c_i\times I_i - E^{vis}_{spec}\right)\\ &= \sum_i c_i\times\left(\sum_{events}\frac{2I_jI_i}{f^2_{Ecor}\times\left(\sigma^2_{spec}+\sigma^2_{CsI}\right)}\right) - \sum_{events}\frac{2I_jE^{vis}_{spec}}{f_{Ecor}\left(\sigma^2_{spec}+\sigma^2_{CsI}\right)}\\ &= 0. \end{aligned} \tag{5.6}$$

This equation exists for all the active CsI crystals. All these equations are linear combinations of the set of $\{c_i\}$. I solved them by using Gaussian elimination, and obtained optimal values of $\{c_i\}$.

The width of E_{CsI}/E^{vis}_{spec} distribution became narrower after the χ^2 minimization as shown in Fig. 5.6. The difference of the new calibration constants from the old calibration constants derived from the cosmic-ray analysis is shown in Fig. 5.7. The new constants of crystals in the *edge* region defined in Fig. 5.3 were largely different from the old constants. This difference was due to shower leaking out of the CsI calorimeter. For the crystals in the edge region, I kept using old calibration constants.

5.3 Nonlinearity Correction

I found that the mean value of the E_{CsI}/E^{vis}_{spec} of electrons depended on the maximum waveform height of all crystals in the cluster, as shown in Fig. 5.8. This suggested that there was nonlinearity of the FADC, that is, waveform integrals recorded with the FADC did not keep a linear correlation with energy deposits in crystals.

An existence of the nonlinearity was also confirmed with a laboratorial test where known pulses generated by a function generator were injected to the FADC. The saturation of waveform heights recorded on the FADC were found in the test as shown in Fig. 5.9(a). The ratio of waveform integrals on the FADC to input also changed according to the pulse height as shown in Fig. 5.9(b).

Because the nonlinearity depends on the pulse shape, we do not use the result of the laboratorial test for the correction for the nonlinearity effect. Instead, I made the correction function from the observed data shown in Fig. 5.8. The mean value was calculated for every x-bin of the 2-dimensional histograms in the figure, and a line interpolating those mean values linearly was used as the tentative correction function denoting f^{tmp}_{nonL}. Here, the events was divided into two data sets. In one data set, the maximum energy deposit was located on a small crystal, and in the other set it was located on a large crystal. The tentative correction function was derived separately for each data set, to use for the correction for small crystals and for large crystals.

The energy in each crystal was corrected by using the correction function as

$$e \rightarrow e' = e \times \left(1 - f_{nonL}^{tmp}(h)\right), \tag{5.7}$$

where e and h represent the energy and the waveform height of the crystal. The plots like Fig. 5.8 were drawn again with corrected energies, and the mean value for each x-bin was calculated. The f_{nonL}^{tmp} was modified by the mean values. This process was iterated 4 times, and the f_{nonL}^{tmp} was converged as shown in the black line in Fig. 5.10. Finally, the tentative function f_{nonL}^{tmp} were parameterized as a smooth function f_{nonL} which is defined as

$$\begin{aligned} f_{nonL}(h; h < \mu) &= 0 \\ f_{nonL}(h; h >= \mu) &= A \times \left(\exp[-\frac{(h-\mu)^2}{2\sigma^2}] - 1 \right), \end{aligned} \tag{5.8}$$

where the h denotes the maximum waveform height in the cluster. The parameters A, μ and σ were estimated as

$$\begin{aligned} A &= 0.134, \\ \mu &= 3.33 \times 10^3 [\text{counts}], \\ \sigma &= 5.6 \times 10^3 [\text{counts}], \end{aligned}$$

for small crystals, and

$$\begin{aligned} A &= 0.058, \\ \mu &= 3.4 \times 10^3 [\text{counts}], \\ \sigma &= 5.3 \times 10^3 [\text{counts}], \end{aligned}$$

for large crystals. The function form is shown in the red lines in Fig. 5.10.

The dependence on the maximum height disappeared after the nonlinearity was corrected with the f_{nonL}s, as shown in Fig. 5.11. The calibration process explained in the previous section was executed before and after this derivation of the correction function.

5.4 Accuracy

To check the accuracy of the calibration, I divided the data into two parts, events with $n < 5$ and $n \geq 5$ where n represents the lowest digit of the serial event number. I did the calibration for each data set, and compared the derived calibration constants each other as shown in Fig. 5.12. Evaluating the difference of the calibration constants between the two data sets with Gaussian fit and dividing by $\sqrt{2}$, the accuracy of calibration constants was estimated as 0.669±0.016 %.

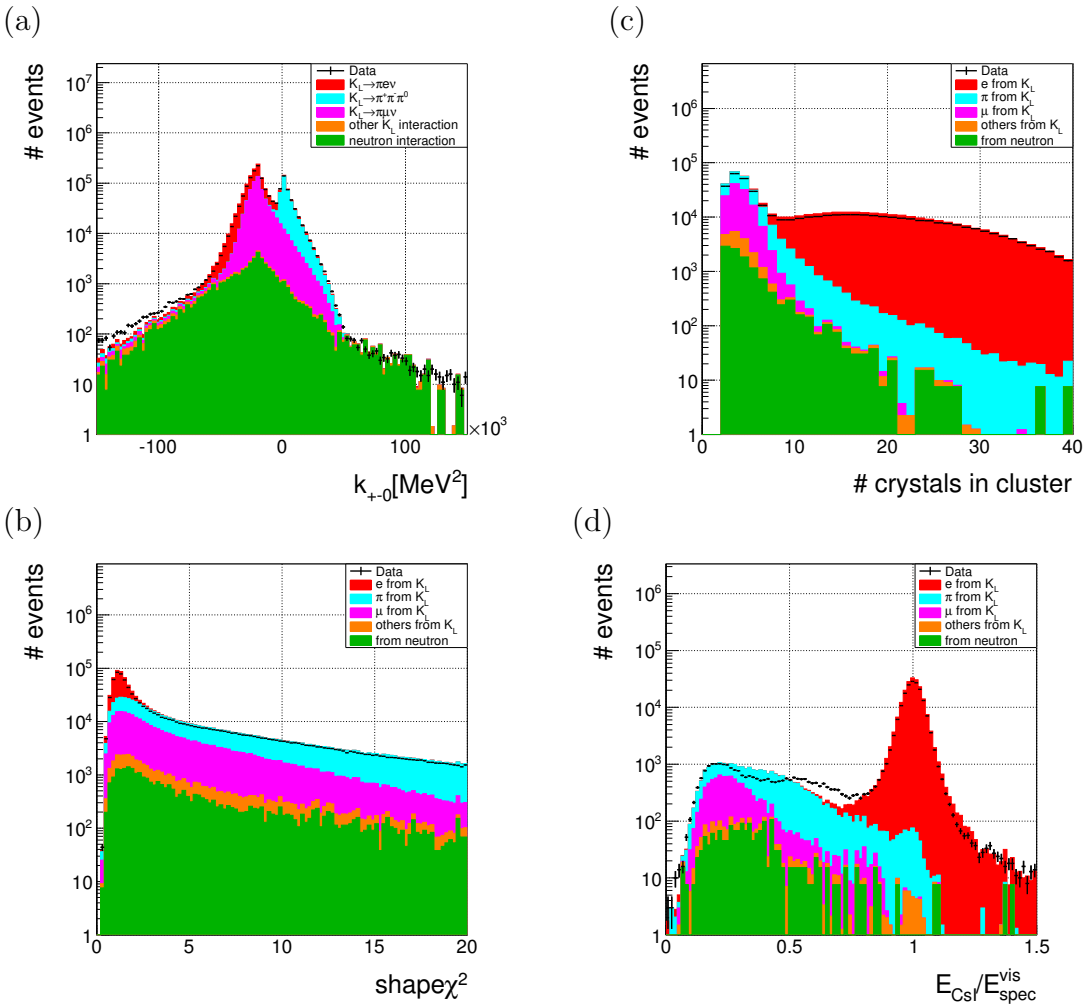

Figure 5.4: (a) The k_{+-0} distribution. (b) The shape χ^2 distribution. (c) Distribution of number of crystals in each cluster. (d)The E_{CsI}/E^{vis}_{spec} distribution. The black dots show the data, while the filled histograms show the estimation from the Monte Carlo simulation. The color difference in (a) represents the decay mode. The red, light blue, and magenta show $K_L \to \pi e \nu$, $K_L \to \pi^+\pi^-\pi^0$, and $K_L \to \pi\mu\nu$ decay, respectively. The yellow and green show the hadronic interaction of K_L's and neutrons, respectively. In other plots, colors represent types of incident particles. the red, light blue, and magenta show electrons, pions, and muons generated from K_L decays. The yellow show particles generated from K_L hadronic interactions or decays of K_L daughter particles. The green shows particles generated from hadronic interactions of neutrons.

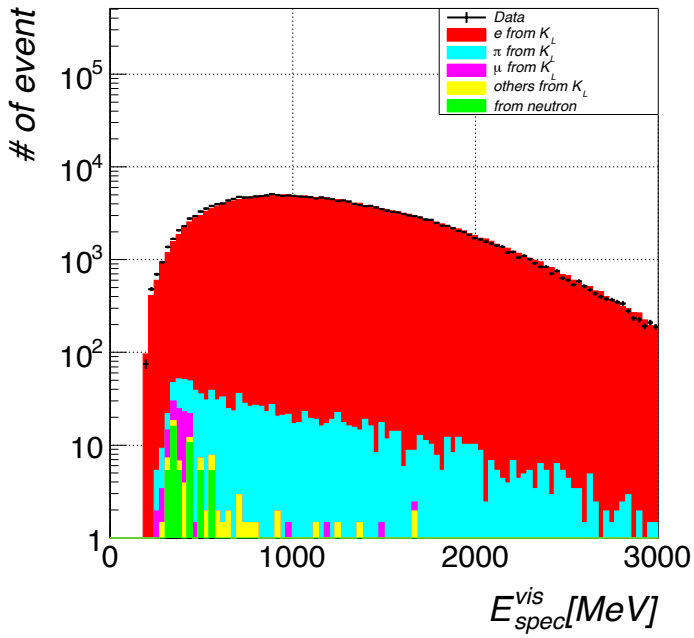

Figure 5.5: The E^{vis}_{spec} distribution after applying all the selection cuts. The black dots shows the measured data with statistic errors. Colors represent types of incident particles. the red, light blue, and magenta show electrons, pions, and muons generated from K_L decays. The yellow show particles generated from K_L hadronic interactions or decays of K_L daughter particles. The green shows particles generated from hadronic interactions of neutrons.

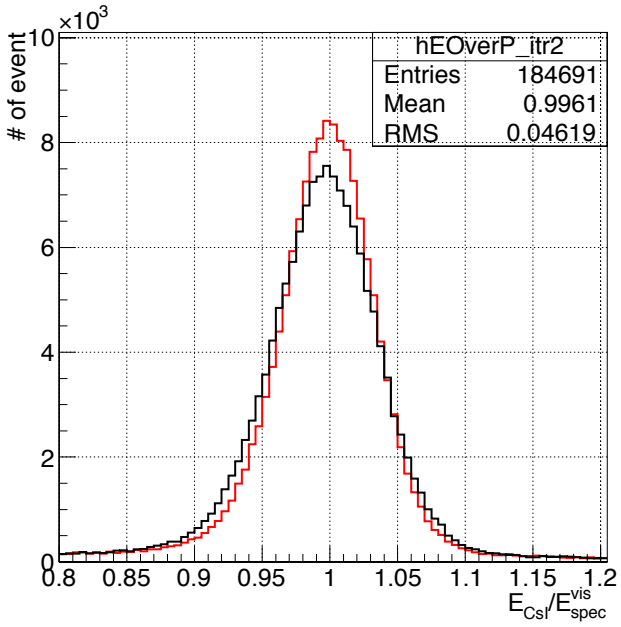

Figure 5.6: The E_{CsI}/E^{vis}_{spec} distribution before the χ^2 minimization (black) and after the χ^2 minimization (red).

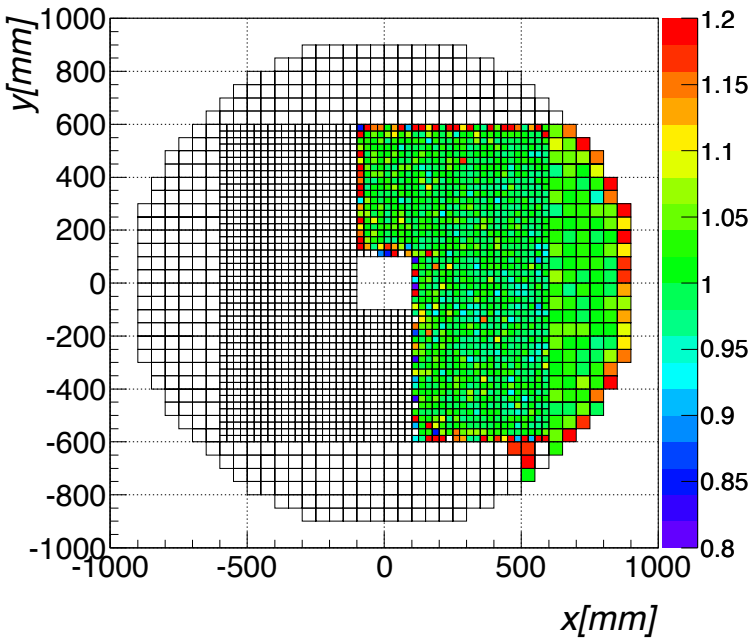

Figure 5.7: The ratio of the calibration constants after the calibration to those before the calibration in the June run.

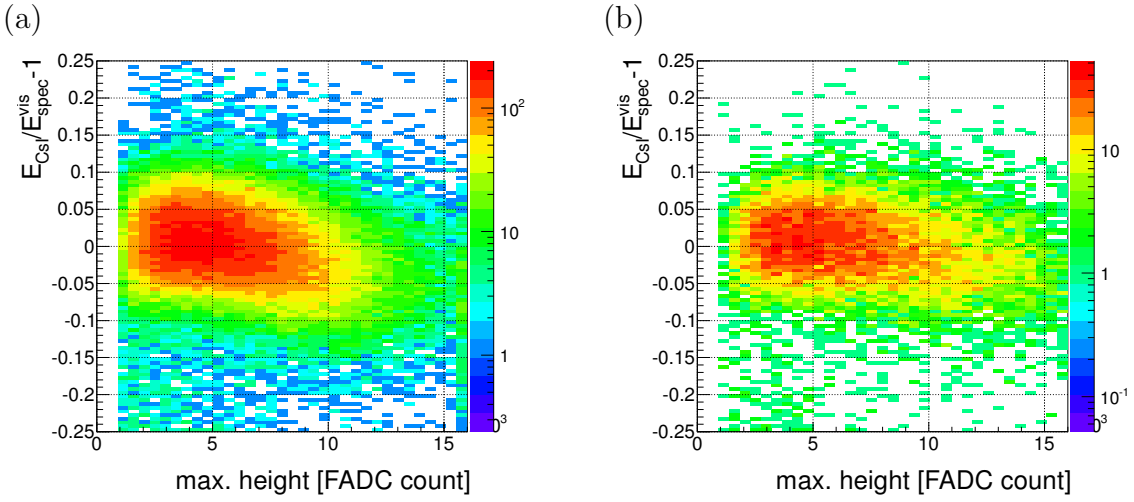

Figure 5.8: (a) Dependence of the $E_{CsI}/E^{vis}_{spec} - 1$ on the maximum height of the waveforms in the cluster. The left (right) plot shows the events in which the maximum energy deposit was located on the small (large) crystal. (b) Nonlinearity after applying the correction.

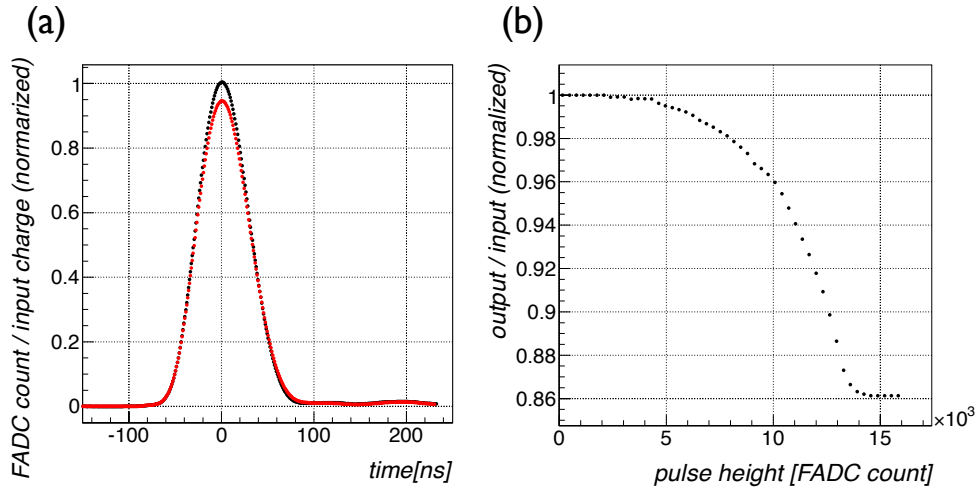

Figure 5.9: (a) Waveform shapes recorded on the FADC in the laboratorial test. The black dots show the waveform when a height of input pulse was 50 mV (corresponding to $\sim$ 125 MeV energy deposit), while the red dots show the waveform with 280 mV input (corresponding to $\sim$ 700 MeV). (b) Ratio between output and input charge as a function of the output pulse height.

(a) for small crystal

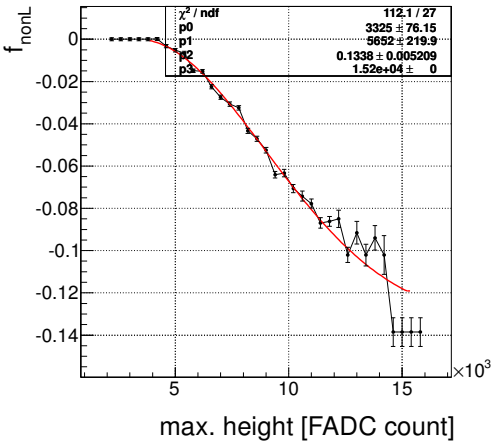

(b) for large crystal

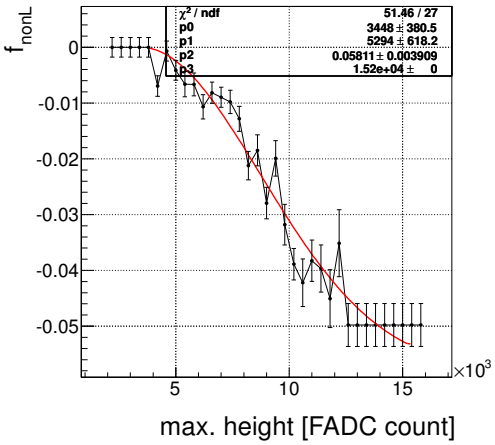

Figure 5.10: The correction function for nonlinearity. The red line shows f_{nonL} defined in Eq. (5.8). The black line shows the tentative correction function f^{tmp}_{nonL}. The functions for small crystals is shown in (a) and for large crystals in (b).

(a)

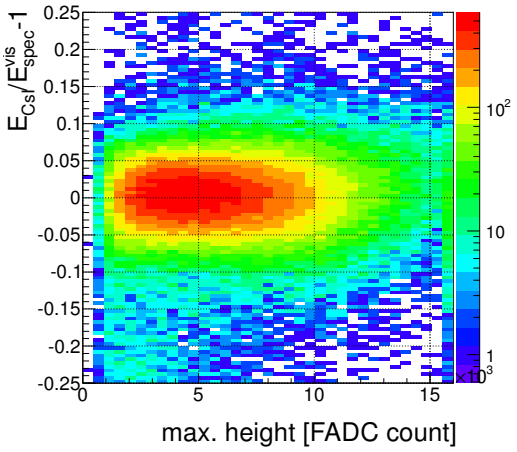

(b)

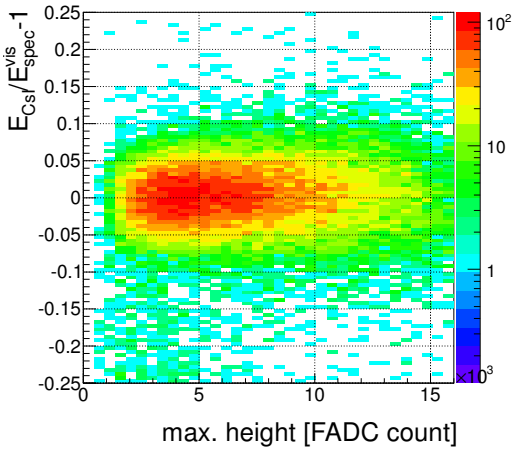

Figure 5.11: Dependence of the $E_{CsI}/E^{vis}_{spec} - 1$ on the maximum height of the waveforms in the cluster after applying the nonlinearity correction. The left (right) plot shows the events in which the maximum energy deposit was located on the small (large) crystal.

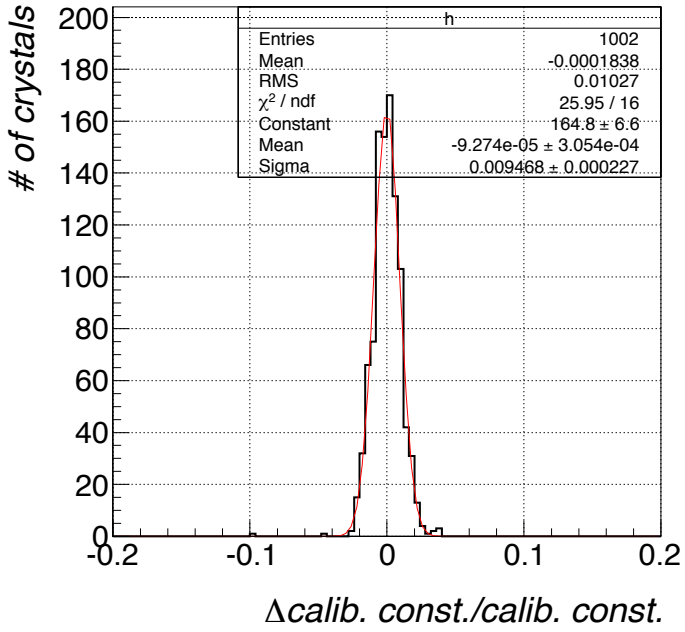

Figure 5.12: The black histogram shows the difference of the calibration constants between the two data sets. The red line shows the best fit with Gaussian.

Chapter 6

The Shower Shape Study

In this chapter, I will describe the study for the shower shape made in the CsI calorimeter. The importance of this study will be explained in the first section. The data selection used for the study will be described in the second section. A consistency between the data and the Monte Carlo will be checked for variables related to the shower shape in Section 6.3. Several conditions for the Monte Carlo will be tested in Section 6.4. The studies in this chapter will be summarized in the last section.

6.1 Motivation

The crystals used in the KOTO CsI calorimeter have smaller sizes than Moliere radius. It enables us to obtain the information of shower shapes which is useful to suppress some background events. In particular, the suppression of the "fusion" $K_L \to \pi^0\pi^0$ background, whose details are described in Appendix A.2.1, is important. In this background, two of four photons generated from the π^0s hit the CsI calorimeter close to each other and their showers overlap so that they are recognized as one cluster. Without the shower shape information, the expectation of this background is 1.4 times larger than that of the signal events even after applying all the other cuts. By applying selection cuts for the shower shape information, the number of this background is reduced to 1/5 of the signal events.

To reject such backgrounds with strange shower shapes, a shape χ^2 method was developed in the KOTO experiment which was already introduced in Section 5.1 and whose detail is described in Appendix A.1.2. This method compares the observed energy deposit in each crystal in the cluster with its expectation derived from a Monte Carlo simulation. The difference is quantified as "shape χ^2". The number of crystals in the cluster and a cluster RMS which is defined in Eq. (A.4) are also useful to distinguish such backgrounds.

The effectiveness of the selection cuts for the shape χ^2, the number of crystals, and the cluster RMS were estimated based on the Monte Carlo studies. The consistency of shower shape between the data and the Monte Carlo is, however, not fully studied yet. In this chapter, I compare these variables observed in the data with those expected from the Monte Carlo simulation, and study the source of the differences between them.

6.2 Data Selection

To study the shower shape, I used electrons from the $K_L \to \pi e \nu$ decays. Because the fundamental processes of electron interaction in the calorimeter is the same as photons, the property of the shower shape is expected to be the same between electrons and photons.

I used the June data because the spectrometer performance was better in the June run than in the February run as described in Section 4.3.

Electron events were selected with the selection cuts listed below.

1. FADC range cut,
2. CsI fidutial region cut,
3. $k_{+-0} <$ -9000 MeV^2,
4. the number of crystals in the cluster > 5,
5. shape $\chi^2 < 5$.

These cuts were almost the same as those used in the calibration process described in Chapter 5, except that the shape χ^2 cut was loosened. In addition, the cluster energy E_{clus} was required to be $600 < E_{clus} < 1800$ MeV whose lower limit was set to reject the events from MIPs. The E_{CsI}/E^{vis}_{spec} was required to be $0.8 < E_{CsI}/E^{vis}_{spec} < 1.2$. The cluster was rejected if it included any large crystal.

6.3 Data/MC Difference

The shape χ^2 distributions observed in the data and the Monte Carlo are shown in Fig. 6.1. The peak position in the data was lower than the position in the Monte Carlo simulation.

Finite differences were also found in the distribution of the number of crystals in the cluster, and the distribution of the cluster RMS, as shown in Fig. 6.2(a) and (b),

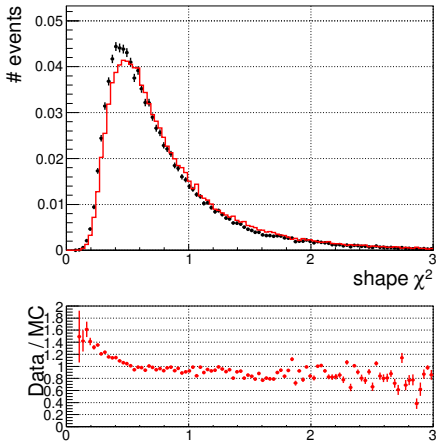

Figure 6.1: (Top) Shape χ^2 distribution obtained from the data (black dots) and from the Monte Carlo simulation (red histogram). (Bottom) The ratio of the data to the Monte Carlo expectation.

respectively. Mean values of the both distributions observed in the data were larger than those in the Monte Carlo. These differences indicate that the electromagnetic shower spread more widely in the data than in the Monte Carlo. To see the spread of the shower more directly, I grouped the crystals as follows. At first I calculated the total energy deposit in each row and each column of crystal arrays. The "center crystal" is then defined as the crystal at the intersection of the row and column with the maximum energy deposit.[1] The crystals were then grouped according to the distance from the center crystal as shown in Fig. 6.3(a). Figure 6.3(b) shows the total energy deposit in each group. Energy deposit in the center crystal observed in the data was about 3% lower than the Monte Carlo expectation, while energy deposits in the outer region in the data were $\sim 5\%$ larger than the Monte Carlo expectation.

6.4 Monte Carlo Conditions

In the default Monte Carlo, the shower in the calorimeter was simulated by using the QGSP_BERT physics list in Geant4 9.5-patch01, where the electromagnetic process is defined in the *G4EmStandardPhysics* class [36]. In the simulation, there were inaccuracies for the reproducibiliy of the CsI configurations, and also there were uncertainties for models for the electromagnetic processes used in Geant4. I estimated the effects of such inaccuracies and uncertainties on the shower shapes, by changing the Monte Carlo conditions. To study these effects efficiently, the showers in the simulation were

[1] This "center crystal" is the same one defined in the explanation for the shape χ^2 method in Appendix A.1.2.

(a) The number of crystals (b) Cluster RMS

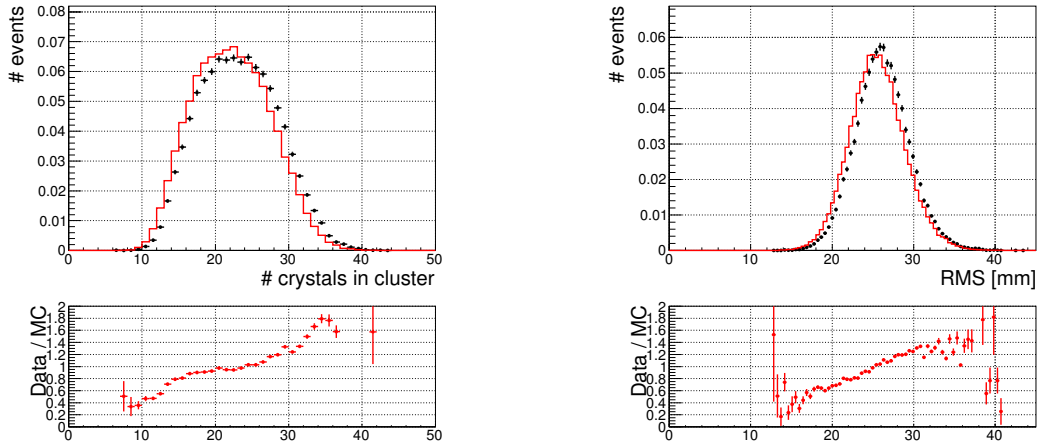

Figure 6.2: (Top) The distribution of the number of crystals in the cluster (a), and the cluster RMS (b). The black dots show the data, while the red histogram shows the Monte Carlo estimation. (Bottom) The ratio of the data to the Monte Carlo estimation.

(a) (b)

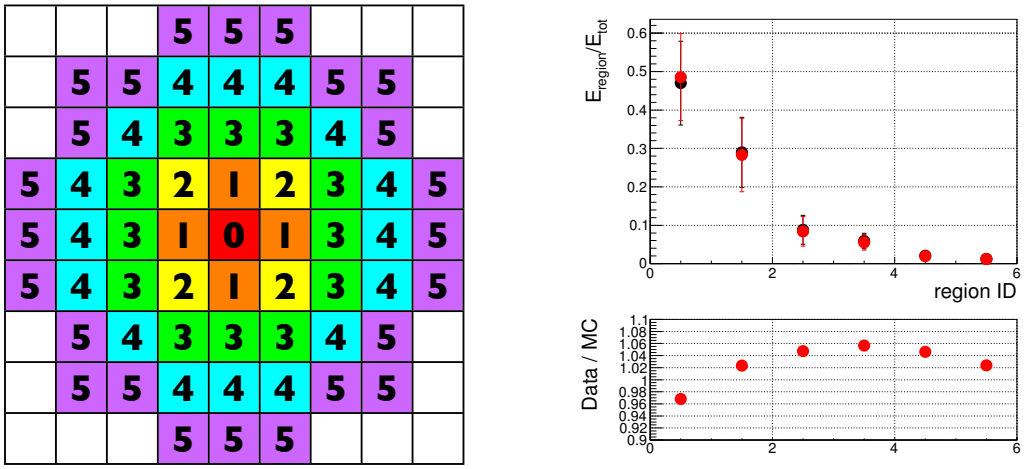

Figure 6.3: (a) Allocation of region ID. The red block represents the "center crystal" defined in the body text, and is allocated ID=0. (Top of (b)) The energy deposit in each region defined in (a) with normalized by the total energy deposit in the cluster. The black and red dots in the top figure show the data and the Monte Carlo expectation, respectively. (Bottom of (b)) Ratio of the data to the Monte Carlo expectation.

produced by generating positrons at the CsI surface with the energies and the incident angles according to the observed distribution in the data. To quantify the differences of the shower shapes, I monitored the average number of crystals in the cluster, the peak position of the shape χ^2 distribution, and the mean value of the cluster RMS. The ratio of each value observed in the data to the simulated estimation was calculated. I also monitored the χ^2 of the distribution between the data and the Monte Carlo simulation, for the distribution of the number of crystals, the shape χ^2, and the cluster RMS. The definition of the χ^2 between two distributions is based on the reference [37], which is implemented in the ROOT library.

6.4.1 Calorimeter Configuration

The CsI calorimeter used in the simulation, which was prepared in the KOTO shared library, has partly inaccurate configurations as listed below. I tested the effects of these inaccuracies on the shower shape, by changing the Monte Carlo conditions.

1. The gap between the crystals are assumed as 50 μm for small crystals and 100 μm for large crystals in the default simulation. The real gaps are unknown although they are guaranteed to be less than 200 μm.

   The shower was simulated by assuming the gaps as 0 μm, and also assuming as 200 μm. The results are shown in Fig. 6.5. The effect of the gaps is too small to explain the data – Monte Carlo inconsistency.

2. The cross-sectional sizes are assumed as 2.5-cm square for small crystals and 5.0-cm square for large crystals in the simulation. The sizes of the real crystals were measured by the KTeV experiment group. The sizes of the small crystals are distributed from 2.49 to 2.52 cm and its average is 2.51 cm, as shown in Fig. 6.4.

   I simulated the showers by assuming that the small crystal size is 24.7, 24.85, and 25.1 mm, and also by assuming that the sizes were randomly distributed as shown in Fig. 6.4. The results are shown in Fig. 6.6. The shower shape did not change.

3. All the crystal lengths are assumed as 50 cm in the simulation. The lengths of the real crystals are not identical. Because we stacked the crystals so that their downstream surface became even, the upstream surface of the crystals were uneven and there were at most 4 mm bumps.

   To reproduce such irregularity of the upstream surface, I fluctuated the z positions of crystals with a Gaussian with $\sigma = 2$ mm in the simulation. The result is shown in Fig. 6.7 in green dots. Almost no differences were observed.

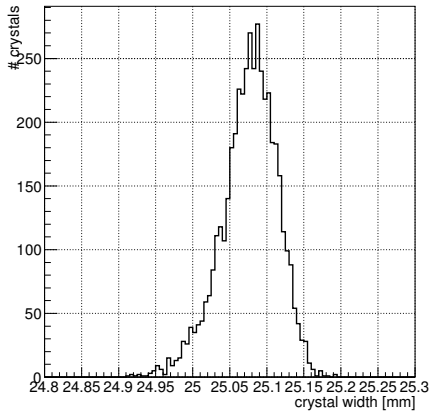

Figure 6.4: Distribution of the width of the small CsI crystals measured by the KTeV group.

4. Mylar sheet covering the surface of every crystal is ignored in the simulation. I set a 20-μm-thick Mylar around each crystal, which is about 1.3 times thicker than the real ones. The result is shown in Fig. 6.7 in blue dots. Almost no differences were observed.

In summary, none of the CsI configuration inaccuracies tested above has a large effect on the shower shape to explain the data – Monte Carlo inconsistency.

6.4.2 Model for Physics Process in Geant4

I tested several models to calculate electromagnetic processes in Geant4 package.

- Electromagnetic physics constructor

  Several sets of models for electromagnetic processes are prepared in Geant4 as electromagnetic physics constructor classes. The default class used in QGSP_BERT is "G4EmStandardPhysics". Instead of the default class, I simulated the showers with using the "G4EmStandardPhysics_option3" (denoting STD3), "G4EmLivermorePhysics" (LM), "G4EmLivermorePolarizedPhysics" (LMP), and "G4EmPenelopePhysics" (PEN). The results are shown in Fig. 6.8. Although the consistency of the shape χ^2 between the data and the Monte Carlo slightly improved with these constructors, there was still a finite difference.

- Multiple scattering model

  A "G4UrbanMscModel95" model is used to calculate multiple scatterings for electrons in all the electromagnetic constructors tested above. Besides this

model, Geant4 provides "G4GoudsmitSaundersonMscModel", and also "G4WentzelVIModel" which is used for multiple scatterings of muons or hadrons. I simulated the shower shapes with using these multiple scattering models. The results are shown in Fig. 6.9. The inconsistency of shape χ^2 peak value was improved by using G4GoudsmitSaundersonMscModel, but inconsistencies of the number of crystals in the cluster or the cluster RMS were rather large. No models for multiple scattering explained the inconsistency between the data and the Monte Carlo.

- Geant4 version

  I used the Geant4 of version 4 9.5-patch01 (denoted by G951) for the simulation as a default. I also simulated with the Geant4 9.4-patch04 (G944) and Geant4 9.6-patch02 (G962). The results are shown in Fig. 6.10. The data - Monte Carlo consistency of all variables improved with using G944.

The improvement by changing the Geant4 version from G951 to G944 was the largest among all of the effects tested in this section.

Difference of the Geant4 versions

One of the difference of electromagnetic processes between G944 and the later versions is a model for the bremsstrahlung. The "G4eBremsstrahlungModel" is used in G944 for the bremsstrahlung from electrons, while the "G4SeltzerBergerModel" is used in G951 and the later version [38]. If the "G4eBremsstrahlungModel" is used in G951, the data – Monte Carlo consistency also improved, as also shown in Fig. 6.10 with orange dots.

The difference of the cross-section of the bremsstrahlung process between the two models is shown in Fig. 6.11. The cross-section in the "G4eBremsstrahlungModel" for electrons with < 10 MeV energy is larger than that in the "G4SeltzerBergerModel". Consequently, the larger number of low energy photons are produced in an electromagnetic shower with the "G4eBremsstrahlungModel", as shown in Fig. 6.12(a). Such low energy photons tend to have large angles from the direction of the incident particle as shown in Fig. 6.12(b), and make the shower shape wider, as observed in the data.

6.5 Summary of Studies in This Chapter

The distributions of variables related to the shower shape information, that is, the shape χ^2, the number of crystals in the cluster, and the cluster RMS, were inconsistent between the data and the Monte Carlo simulation. The electromagnetic shower observed in the data spread more widely than the Monte Carlo expectation.

(a) Ratio of mean values

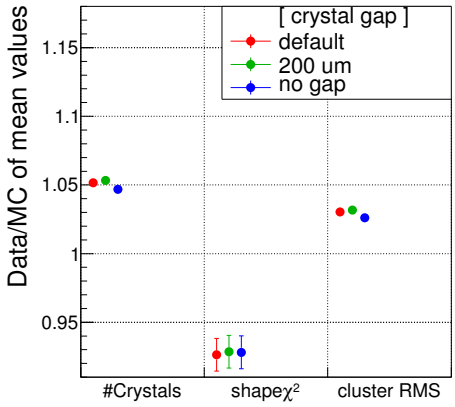

(b) χ^2/NDF

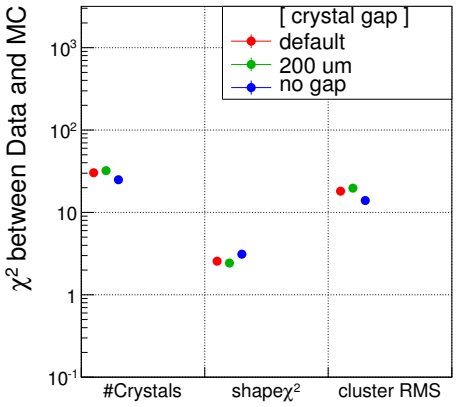

Figure 6.5: Results of the shower shape simulation with the different crystal gaps. The red, green, and blue dots show the default gap (=50 μm), 200 μm, and no gap, respectively. (a) The ratios of the data to the simulation for the mean number of crystals, the peak position of the shape χ^2, and the mean of the cluster RMS. (b) The χ^2/NDF between the data and the Monte Carlo for the distributions of the number of crystals, the shape χ^2, and the cluster RMS.

(a) Ratio of mean values

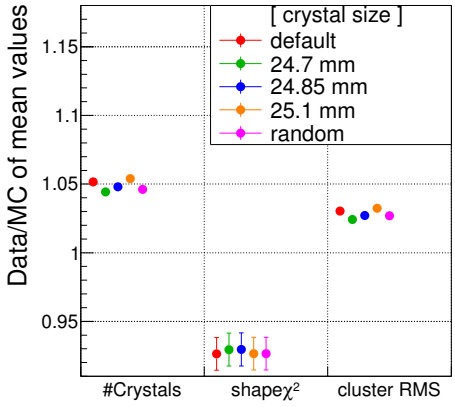

(b) χ^2/NDF

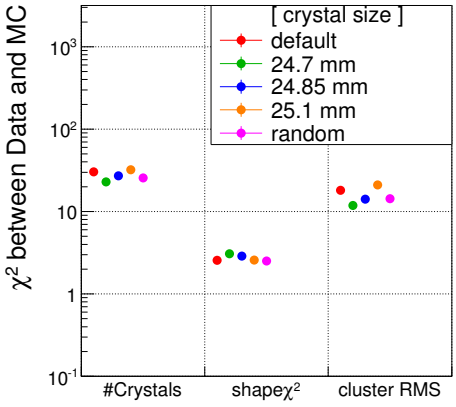

Figure 6.6: Results of the shower shape simulation with different crystal sizes. The meanings of the x and y axes in (a) and (b) are the same as for Fig. 6.5. The red, green, blue, and orange dots show the default size (=25 mm), 24.7 mm, 24.85 mm, and 25.1 mm, respectively. The sizes were randomly fluctuated in the simulation shown in magenta.

(a) Ratio of mean values (b) χ^2/NDF

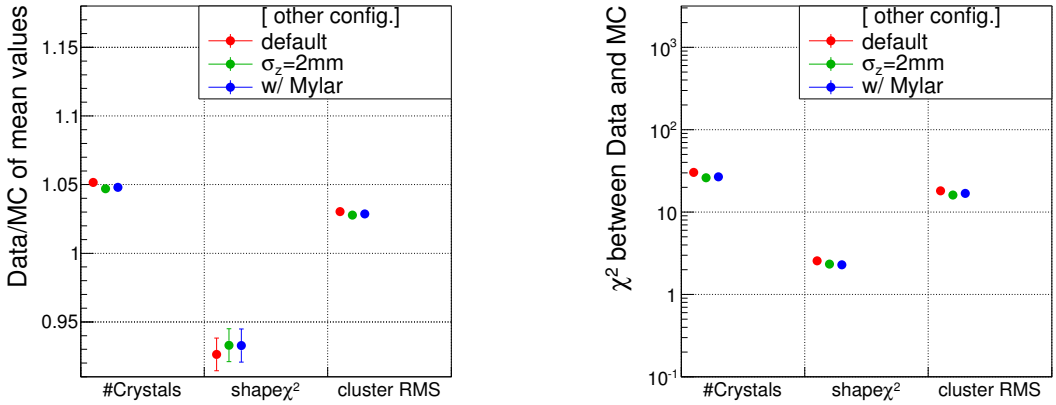

Figure 6.7: Results of the shower shape simulation with the default condition (red), with the irregularity of the CsI upstream surface (green), and with 20-μm-thick Mylars (blue). The meanings of the x and y axes in (a) and (b) are the same as for Fig. 6.5.

(a) Ratio of mean values (b) χ^2/NDF

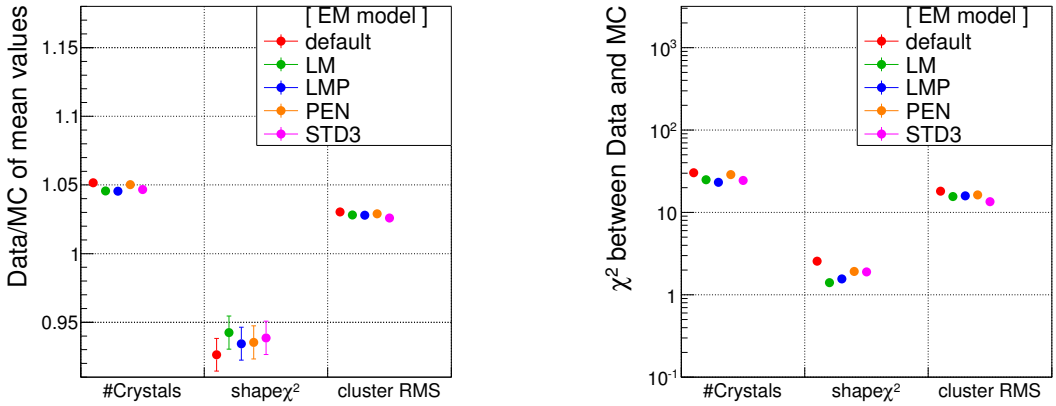

Figure 6.8: Results of the shower shape simulation with five different electromagnetic constructors. The meanings of the x and y axes in (a) and (b) are the same as for Fig. 6.5. The red, green, blue, orange and magenta dots show the defult, LM, LMP, PEN and STD3 constructors, respectively.

(a) Ratio of mean values

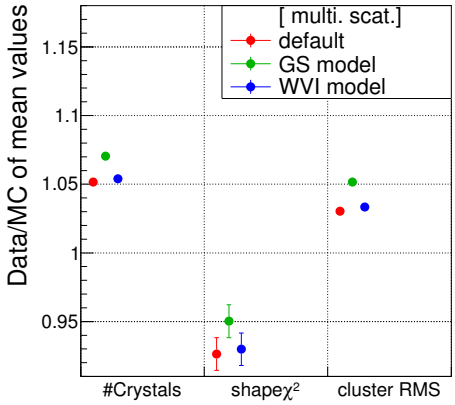

(b) χ^2/NDF

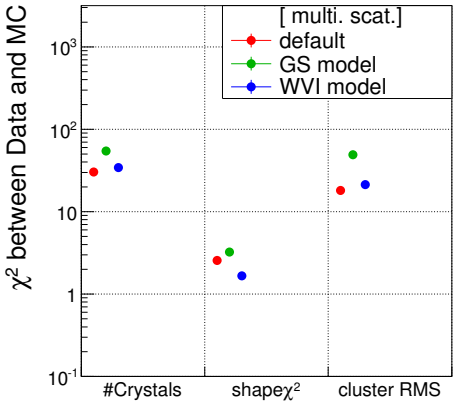

Figure 6.9: Results of the shower shape simulation with three differenct multiple scattering models. The meanings of the x and y axes in (a) and (b) are the same as for Fig. 6.5. The red, green, blue dots show the defult model (G4UrbanMscModel95), G4GoudsmitSaundersonMscModel, and G4WentzelVIModel, respectively.

(a) Ratio of mean values

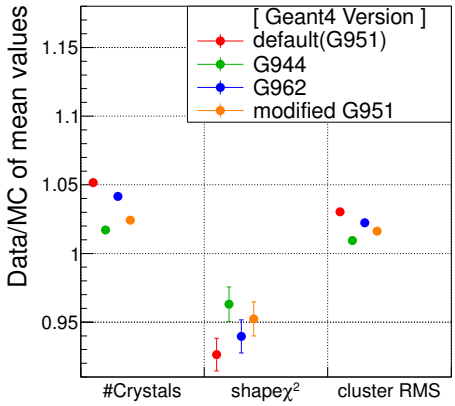

(b) χ^2/NDF

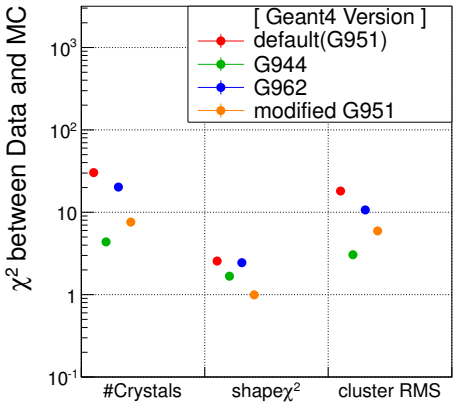

Figure 6.10: Results of the shower shape simulation with the different Geant4 versions. The meanings of the x and y axes in (a) and (b) are the same as for Fig. 6.5. The red, green, blue dots show the G951, G944, G962 versions, respectively. The orange dots show the G951 but the bremsstrahlung model for electrons was changed to "G4eBremsstrahlungModel".

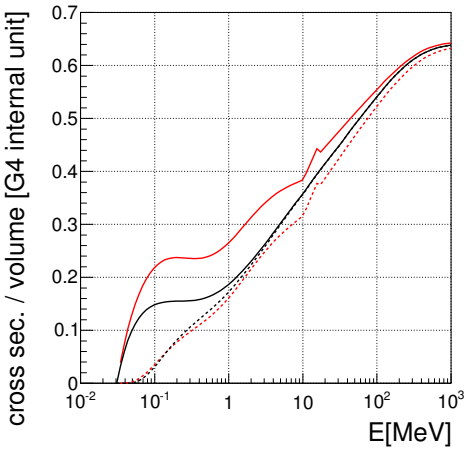

Figure 6.11: Cross-section of the bremsstrahlung process used in the Geant4 based simulation. The black (red) solid line shows the cross-section for electrons in version G951 (G944), and the dashed line shows that for positrons.

(a) (b)

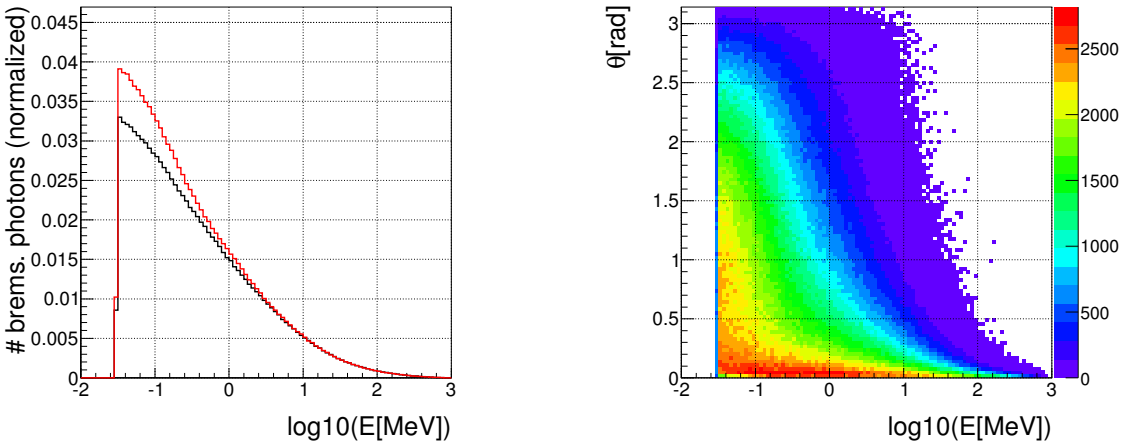

Figure 6.12: Kinematics of the bremsstrahlung photons in electromagnetic showers made by 900 MeV photons. (a) Energies of the bremsstrahlung photons made with G951 (black) and G944 (red). (b) Relation between the energies of the photons and their angles from the direction of the incident particle.

I searched for the source of the inconsistency. I tested several CsI configurations in the simulation, and also tested several models for the physics processes prepared in Geant4. Relatively large improvement was shown when changing Geant4 version from G4 9.5 to G4 9.4, and I found that the improvement mainly arose due to a model used to simulate the bremsstrahlung process for electrons.

Figure 6.13(a)$\sim$(c) show the distributions of the shape χ^2, the number of crystals in the cluster, and the cluster RMS simulated by using a Monte Carlo which was based on G4 9.5 although the bremsstrahlung process was simulated by using the "G4eBremsstrahlungModel" which is the model used in G4 9.4. The other electromagnetic processes were calculated by using the "G4EmLivermorePhysics" electromagnetic constructor, and the Mylar sheet around the CsI crystals and the irregularity of the CsI upstream surface were included in the simulation. Energy deposit in each of the crystal groups which were defined in Fig. 6.3(a) was also shown in Fig. 6.13(d). Even though the consistency between the data and the Monte Carlo were improved in all the plots, there were still finite differences. The effect of the difference on the KOTO physics run will be discussed in Chapter 9.

(a) Shape χ^2

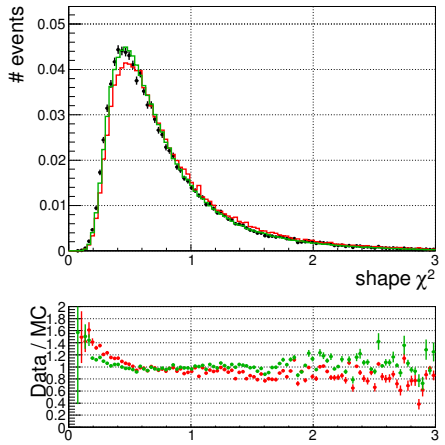

(b) The number of crystals

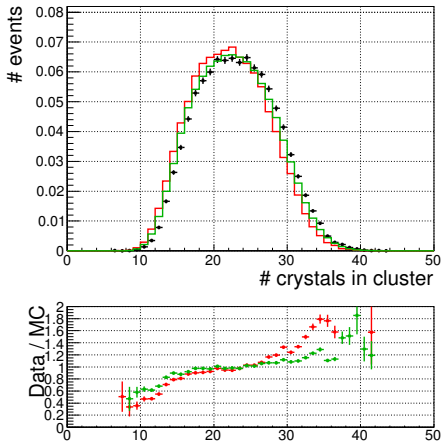

(c) Cluster RMS

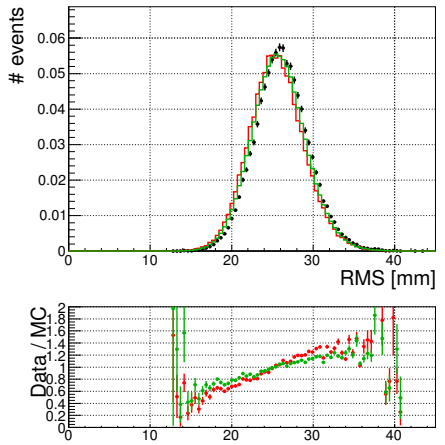

(d) Energy deposit in each region

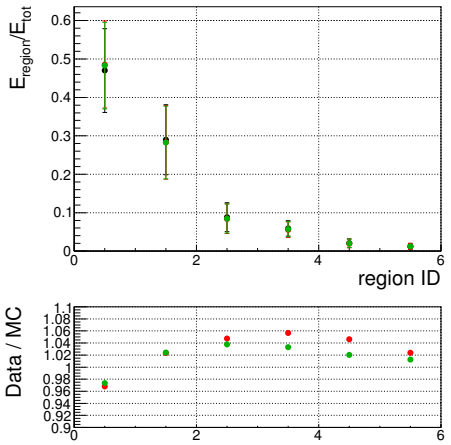

Figure 6.13: (a) Shape χ^2. (b) The number of crystals. (c) Cluster RMS. (d) Energy deposit in each crystal region (the region allocation is defined in Fig. 6.4(a)). The black dots show the data and the red and green histograms show the default and the modified Monte Carlo simulation. The ratio of the data to the Monte Carlo are also shown.

Chapter 7

Resolutions of CsI Calorimeter

The energy resolution and position resolution of the CsI calorimeter directly influence the efficiency of the kinematic cuts in the KOTO physics run. This chapter presents a measurement of the energy and position resolutions of the CsI calorimeter with momentum-analyzed electrons.

7.1 Data Selection

7.1.1 Data Set

I used the June data to derive the energy and position resolutions of the CsI calorimeter, because the spectroemter performance was better in the June run than in the February run as described in Section 4.3.

In order to study the effect of the crystal size on the resolutions, I calculated the ratio of energy deposits in small crystals to the total deposit in the cluster, and divided the data into two subsets according to the ratio. The data with the ratio greater than 0.9 was named small-crystal data subset, while the data with the ratio less than 0.1 was named large-crystal data subset. The resolutions were derived for each subsets individually.

7.1.2 Event Selection

Electron events were selected with the same selection cut set as the calibration process described in Chapter 5, that is,

1. FADC range cut,

2. CsI fidutial region cut,
3. $k_{+-0} <$ -9000 MeV^2,
4. shape $\chi^2 < 2.5$,
5. the number of crystals in the cluster > 5.

To avoid a part of the shower leaking out of the active CsI region, I required an additional cut. If the cluster includes crystals in the edge region which was defined in Fig. 5.7, I required the total energy deposits in such crystals to be less than 1% of the cluster energy.

7.2 Resolutions

The energy resolution and the position resolution were derived using the electron events selected in the previous section.

7.2.1 Energy Resolution

The energy resolution of the calorimeter was determined from the width of the E_{CsI}/E^{vis}_{spec}. The width was evaluated with a Gaussian fit for every 50 MeV E^{vis}_{spec} region, as shown in Fig. 7.1(a). The width of E_{CsI}/E^{vis}_{spec} is shown in Fig. 7.1(b) as a function of energy.

Fluctuations from other sources

The E_{CsI}/E^{vis}_{spec} width is determined by the energy resolution of the CsI calorimeter, the momentum resolution of the spectrometer, and the fluctuation of energy deposits in the materials upstream of the CsI calorimeter.

The momentum resolution of the spectrometer was already estimated in Chapter 4.3 as Eq. (4.35). The energy deposits in the materials were estimated with Monte Calro simulation as shown in Fig. 7.2(a). The RMS of the energy deposit distribution was parameterized as a function of the momentum of the incident electrons p_e as

$$\sigma_{mat}/p_e = \frac{(0.335 \pm 0.003)\,\%}{\sqrt{p_e[GeV]}} \oplus \frac{(0.559 \pm 0.002)\,\%}{p_e[GeV]}. \tag{7.1}$$

The function was shown in Fig. 7.2(b).

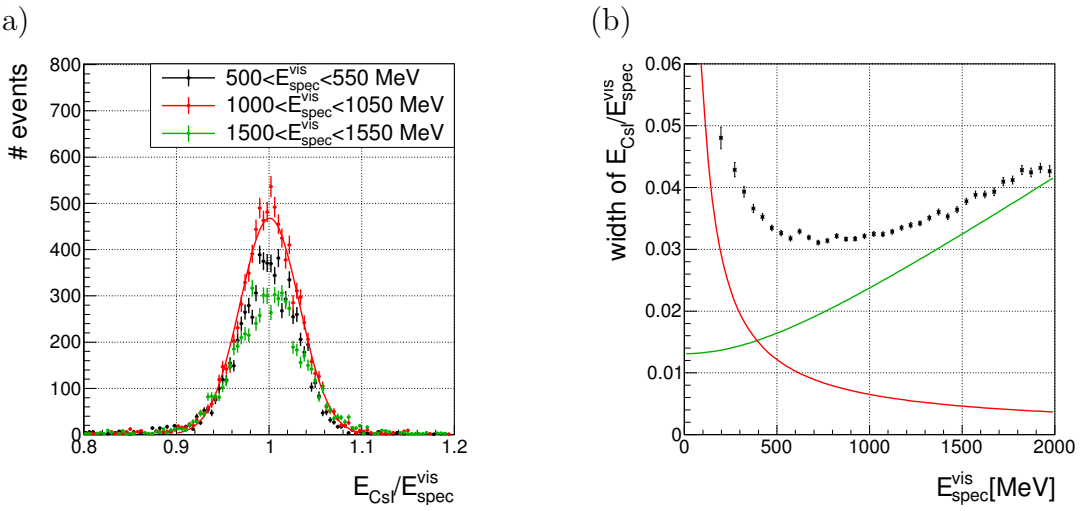

Figure 7.1: (a) Distribution of the E_{CsI}/E^{vis}_{spec}. The colors represent different energy region: 500∼550 MeV (black), 1000∼1050 MeV (red) and 1500∼1550 MeV (green). (b) Width of the E_{CsI}/E^{vis}_{spec} as a function of electron energy. The momentum resolution of the spectrometer (green line) and the energy fluctuation due to the materials upstream of the CsI calorimeter (red line) are also shown.

Energy resolution of the CsI calorimeter

The contributions from the spectrometer and the material were quadratically subtracted from the E_{CsI}/E^{vis}_{spec} width. The remaining width was fitted with a function of general expression of energy resolution, *i.e.*:

$$\frac{\sigma_E}{E} = p_1 \oplus \frac{p_2}{\sqrt{E[\mathrm{GeV}]}} \oplus \frac{p_3}{E[\mathrm{GeV}]}. \tag{7.2}$$

The fitted parameters are

$$p_1 = (0.66 \pm 0.12 \pm 0.51)\%,\ p_2 = (1.81 \pm 0.04 \pm 0.02)\%,\ p_3 = (0 \pm 0.15 \pm 0.00)\% \tag{7.3}$$

for the small-crystal data subset, and

$$p_1 = (1.71 \pm 0.11 \pm 0.13)\%,\ p_2 = (1.31 \pm 0.10 \pm 0.01)\%,\ p_3 = (0 \pm 0.44 \pm 0.00)\% \tag{7.4}$$

for the large-crystal data subset, where the first error of each parameter is a statistic error, and the second error is a systematic error of which derivation is described in the next section. The covariances between the parameters are shown in Table 7.1. The fitting result for the small-crystal data subset and for large-crystal data subset are shown in Fig. 7.3(a) and (b), respectively. The fitting error of the function, shown

(a) (b)

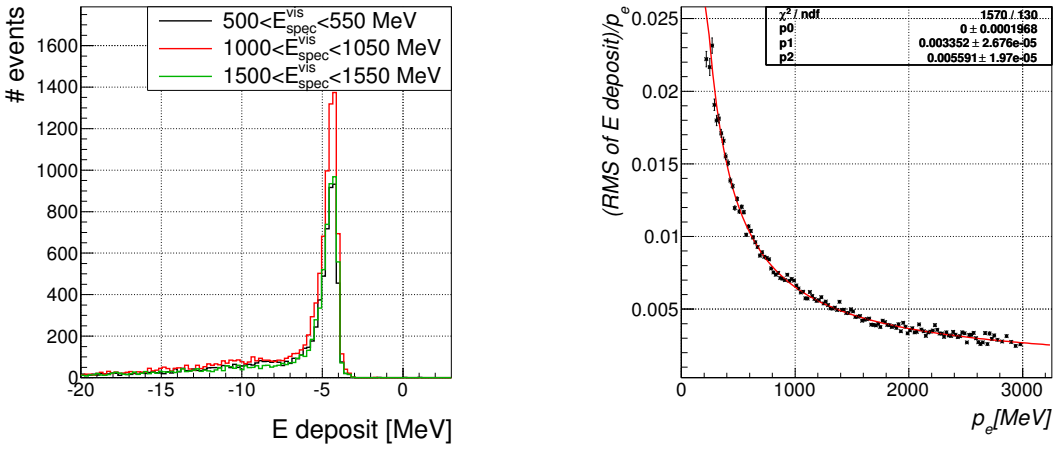

Figure 7.2: (a) Energy deposits by the electrons in the materials located upstream of the CsI calorimeter, estimated with the Monte Carlo simulation. Colors represent different E^{vis}_{spec} regions: 500 $\sim$ 550 MeV (black), 1000 $\sim$ 1050 MeV (red) and 1500 $\sim$ 1550 MeV(green). (b) RMS of the energy deposit as a function of momentum. The black dots show the measured data, and the red line shows the function defined in Eq. (7.1).

Table 7.1: Covariance between the parameters of energy resolution function.

	$\mathrm{cov}(p_1, p_2)$	$\mathrm{cov}(p_1, p_3)$	$\mathrm{cov}(p_2, p_3)$
for *small* subset	-6.53×10^{-9}	2.03×10^{-12}	-3.31×10^{-11}
for *large* subset	-1.51×10^{-5}	1.31×10^{-5}	-3.23×10^{-5}

in the green area in the plot, was calculated from the fitting errors of the parameters and the covariances, as described in Appendix D.2.

The result of the small-crystal data subset was consistent with the Monte Calro estimation within its error. As for the result of the large-crystal data subset, the constant term was 1.4% larger than the Monte Calro estimation. The effect of this difference on the KOTO physics run will be discussed in Chapter 9.

Consistency of energy correction

A cluster energy was corrected to an incident energy of electron with the correction function f_{Ecor} defined in Eq. (3.7). To confirm the consistency of this correction, a difference of the center value of the E_{CsI}/E^{vis}_{spec} distribution from 1 was checked. In this study I used whole data set, without separating the data into the small- and large-crystal data subsets. The difference are shown in Fig. 7.4 as a function of the incident energy or a function of the incident angle, which are the parameters of the

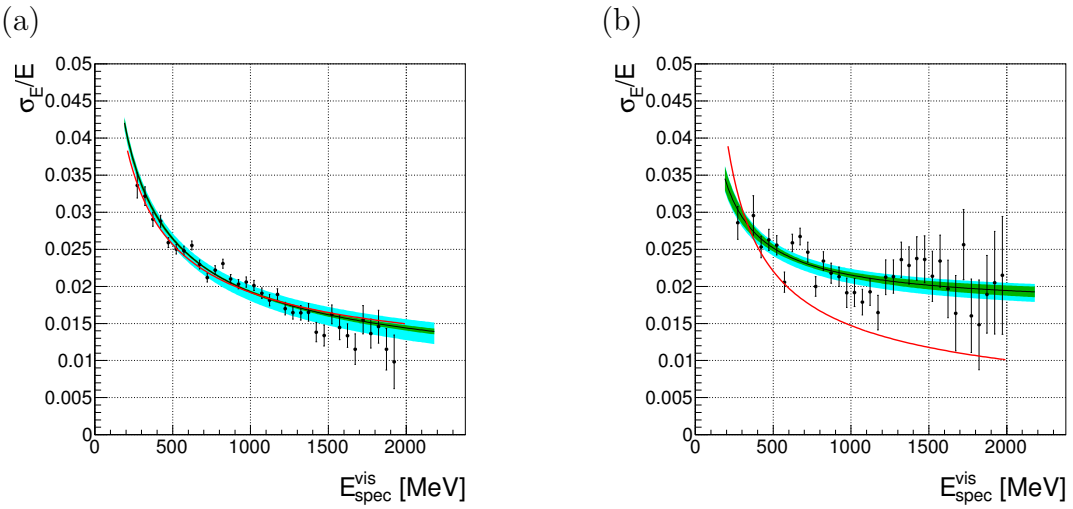

Figure 7.3: Energy resolutions of the CsI calorimeter obtained from the small-crystal data subset (a) and the large-crystal data subset (b). The black dots show the measured data, and the black line shows the best fit with the resolution function defined in Eq. (7.2). The green-filled (light blue-filled) area shows $\pm 1\sigma$ deviation of fitting (systematic) error. The red line shows the expectation from the Monte Carlo simulation.

correction function. The difference was smaller than 1/5 of the energy resolution given in Eq. (7.3) at any energies or angles, and it was considered to have no significant effect on the physics run.

7.2.2 Position Resolution

The data set used to determine the position resolution had an additional electron selection cut:

$$|E_{CsI}/E^{vis}_{spec} - 1| < 3\frac{\sigma_{E^{vis}_{spec}}}{E^{vis}_{spec}}, \tag{7.5}$$

where σ_E/E was derived in the previous subsection.

The x and y position resolutions were determined from the difference of the incident position measured with the CsI calorimeter from that measured with the spectrometer. The distribution of those differences, Δx and Δy, in some energy regions are shown in Fig. 7.5(a). The width of $\Delta x(\Delta y)$ distribution was evaluated with a Gaussian fit for every 50 MeV E^{vis}_{spec} region. The evaluated width is shown in Fig. 7.5(b) as a function of energy.

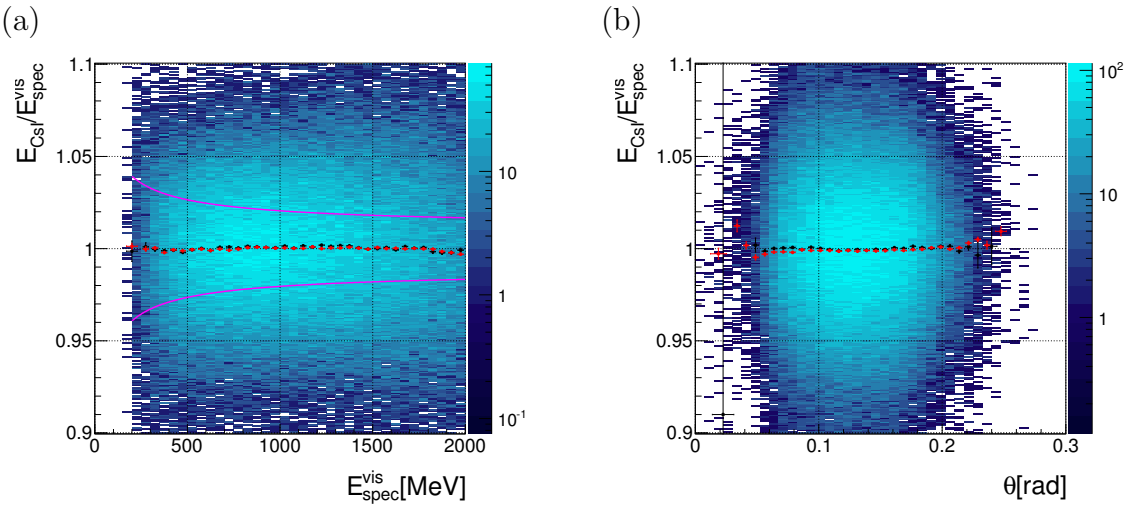

Figure 7.4: Dependence of E_{CsI}/E^{vis}_{spec} on energy (a) and incident angle (b). Each black (red) dot shows the center values of each x bin, observed in the data (simulation). The magenta lines in (a) represent $\pm 1\sigma$ deviation of the energy resolution for the small crystals given in Eq. (7.3).

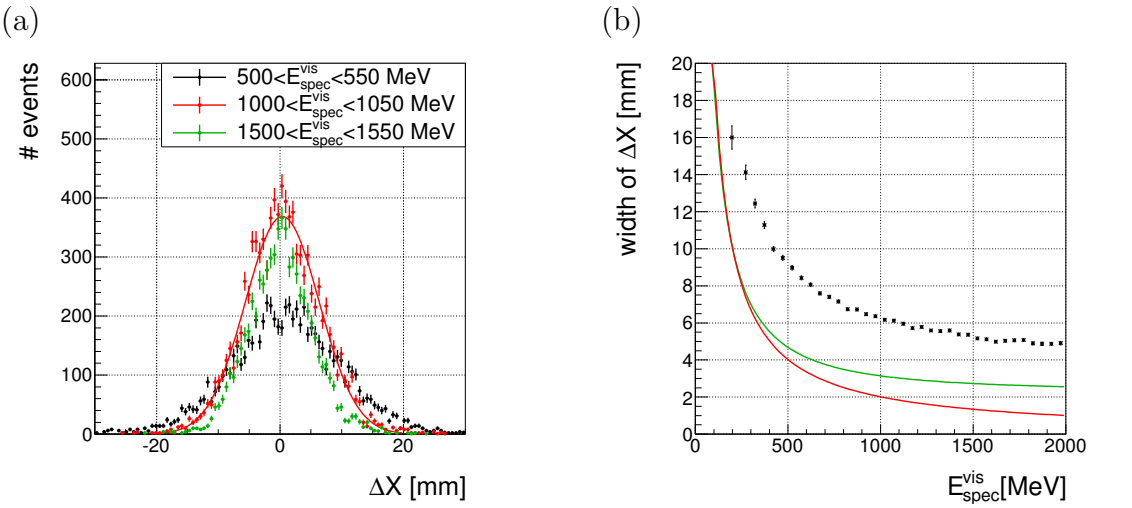

Figure 7.5: (a) Distribution of the difference between x positions measured with the CsI calorimeter and the spectrometer ($= \Delta x$). The colors show different E^{vis}_{spec} ranges: 500 $\sim$ 550 MeV (black), 1000 $\sim$ 1050 MeV (red), and 1500 $\sim$ 1550 MeV (green). (b) Width of Δx as a function of electron energy. The position resolution of the spectrometer (green line) and the position fluctuation due to the materials upstream of the CsI calorimeter (red line) are also shown.

Fluctuations from other sources

The position resolution of the spectrometer was already estimated in Chapter 4.3 as Eq. (4.37). The position fluctuation due to multiple scattering in the materials were estimated with Monte Calro simulation as shown in Fig. 7.6(a). The RMS of the position displacement was parameterized as a function of the electron momentum p_e as

$$\sigma_{mat}[\mathrm{mm}] = \frac{2.012 \pm 0.002}{p_e[GeV]}, \tag{7.6}$$

as shown in Fig. 7.6(b).

(a) (b)

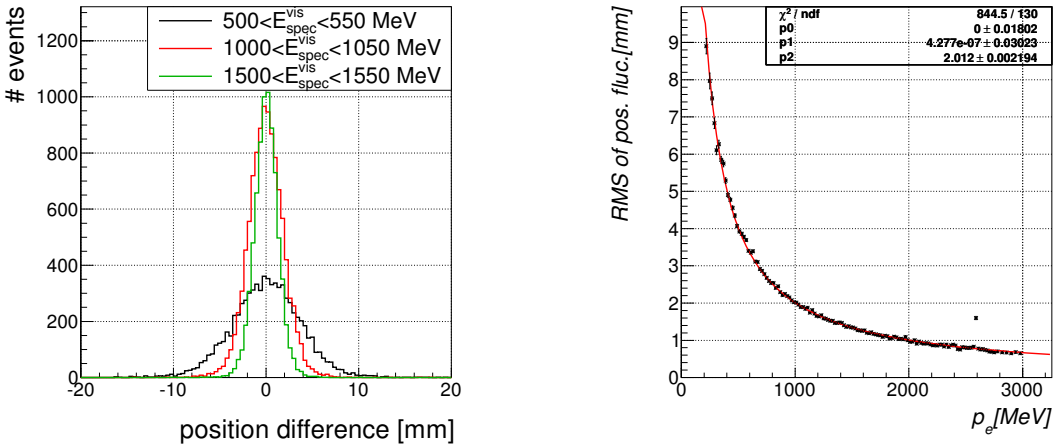

Figure 7.6: (a) Position displacement due to the materials located upstream of the CsI calorimeter, estimated with the Monte Carlo simulation. Colors represent different E^{vis}_{spec} regions: 500 $\sim$ 550MeV (black), 1000 $\sim$ 1050MeV (red) and 1500 $\sim$ 1550 MeV(green). (b) RMS of the position displacement as a function of momentum. The black dots show the measured data, and the red line shows the function defined in Eq. (7.6).

Position resolution of the CsI calorimeter

The contributions from the spectrometer and the material were quadratically subtracted from the Δx (or Δy) width. The remaining width was fitted with a position resolution function which was defined as

$$\sigma[mm] = p_1 \oplus \frac{p_2}{\sqrt{E[\mathrm{GeV}]}}. \tag{7.7}$$

The fitting result is shown in Fig. 7.7. The fitted parameters are

$$\begin{aligned} p_1 &= 1.52 \pm 0.14 \pm 0.39, \quad p_2 = 4.18 \pm 0.06 \pm 0.35 \quad \text{for } \Delta \text{ x} \\ p_1 &= 2.37 \pm 0.08 \pm 0.27, \quad p_2 = 3.72 \pm 0.06 \pm 0.61 \quad \text{for } \Delta \text{ y} \end{aligned} \tag{7.8}$$

Table 7.2: Covariances between the parameters of the position resolution function.

	direction	$\mathrm{cov}(p_1, p_2)$
for small-crystal	X	-7.52×10^{-3}
	Y	-4.21×10^{-3}
for large-crystal	X	-4.04×10^{-2}
	Y	-4.41×10^{-2}

for the small crystals, and

$$\begin{array}{llll} p_1 = 5.39 \pm 0.18 \pm 0.12, & p_2 = 4.09 \pm 0.24 \pm 0.41 & \text{for } \Delta\mathrm{x} \\ p_1 = 6.87 \pm 0.17 \pm 0.06, & p_2 = 3.93 \pm 0.29 \pm 0.68 & \text{for } \Delta\mathrm{y} \end{array} \tag{7.9}$$

for the large crystals, where the first error of each parameter represents statistic error, and the second error is the systematic error of which derivation is described in the next section. The covariances of the parameters were estimated as shown in Table 7.2. These parameter errors and the covariances were used to calculate the error of the fitting function, as described in Appendix D.2.

For the large crystals, the y resolution was ∼1.5 mm larger than the x resolution. This difference was reproduced in the Monte Calro simulation, and is explained by the dependence of the position resolution on the azimuthal angle. If the direction of incident electron has a finite polar angle, the numbers of rows and columns of crystals that its electromagnetic shower spread over changes due to the azimuthal angle of the electron direction. Because the cluster position was reconstructed with the *COE* method defined in Eq. (3.4), the x (or y) position resolution depended on the number of rows (columns) of crystals. When the azimuthal angle is near zero or π ($\pi/2$ or $3\pi/2$), the number of rows (columns) became minimum and the x (y) resolution became worst. Because only the large crystals on the north side of the CsI calorimeter were read out in the June run, the azimuthal angle of incident electrons were peaked at 0 degree. Subsequently the x resolution were better than the y resolution.

This explanation was confirmed with a Monte Carlo simulation. In the simulation, photons with a flat E distribution ($1.1 < E < 1.8GeV$), a flat azimuthal angle distribution, and a fixed polar angle (10 degree) were injected to a large crystal area of the CsI calorimeter. The resolution of reconstructed cluster position had a dependence on the azimuthal angle as shown in Fig. 7.8. The measured x and y resolutions are also shown in the figure.

Position Reconstruction Method with Cluster Shape Information

Besides the current "*COE*" method for a position reconstruction, an alternative method using cluster shape information (called "*shape*" method) was proposed, as described

(a) σ_x for small-crystal

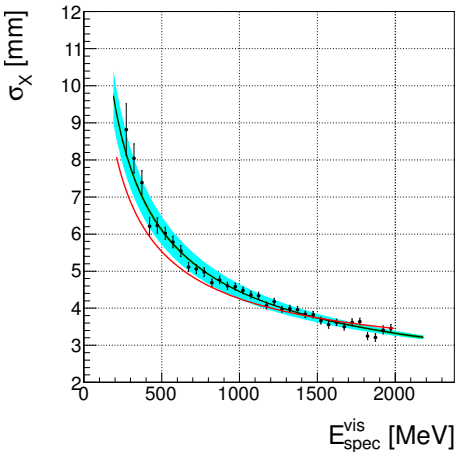

(b) σ_y for small-crystal

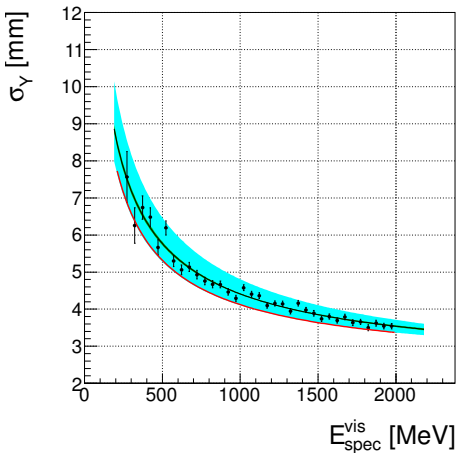

(c) σ_x for large-crystal

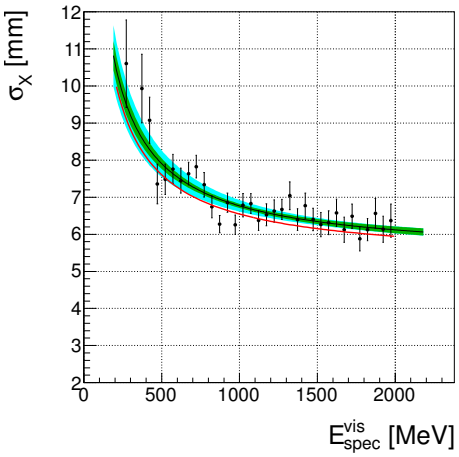

(d) σ_y for large-crystal

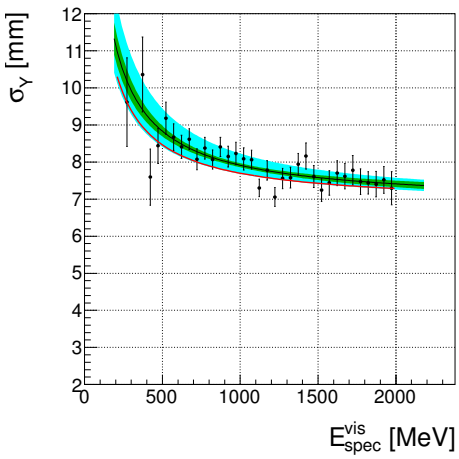

Figure 7.7: Position resolutions of the CsI calorimeter. Plots (a) and (b) show the x and y resolutions obtained from the small-crystal data subset, and plots (c) and (d) show those obtained from the large-crystal data subset, respectively. The black line shows the best fit with the resolution function defined in Eq. (7.7). The green-filled (light blue-filled) area shows $\pm 1\sigma$ deviation of fitting (systematic) error. The red line shows the expectation of the Monte Carlo simulation.

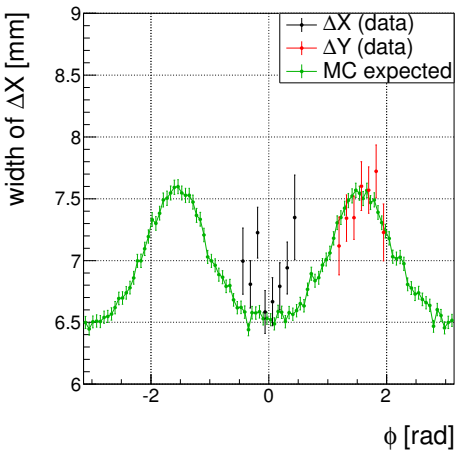

Figure 7.8: Azimuthal angle (ϕ) dependence of the position resolution of the CsI calorimeter. The black dots show the measured σ_X as a function of ϕ. The red dots show the measured σ_Y, but ϕ was calculated as the angle from not x-axis but y-axis. The green dots show the expectation from a Monte Carlo simulation.

in Section 3.3.5. I evaluated the x and y position resolution with the *shape* method as shown in Fig. 7.9, with the same procedure described so far. The difference of x and y resolutions, or, the dependence on azimuthal angle discussed above, was reduced with this method. Also, the constant term of the resolution was improved.

The improvement of the constant term was explained by resolving the localization of cluster position. A cluster position derived with the current *COE* method tended to be localized at the center position of the crystal with the maximum energy deposit. The $\Delta x(\Delta y)$ strongly correlated with the incident x (y) position in the crystal as the result, as shown in Fig. 7.10(a). This correlation was one of the main sources of the constant term, in particular for large crystals. The *shape* method resolved this localization as shown in Fig. 7.10(b), and improved the position resolution.

Consistency of Position Correction

The cluster position was corrected to the electron incident position with the function defined in Eq. (3.12). The consistency of the correction was tested by checking the discrepancy of the mean value of the Δx (or Δy) from zero. In this study I used whole data set, without separating the data into the small- and large-crystal data subsets.

The dependence of the mean value of the Δx on the electron energy is plotted in Fig. 7.11(a). The difference of Δx from zero was smaller than 1/5 of the position resolution in any energy range.

(a) small-crystal data subset

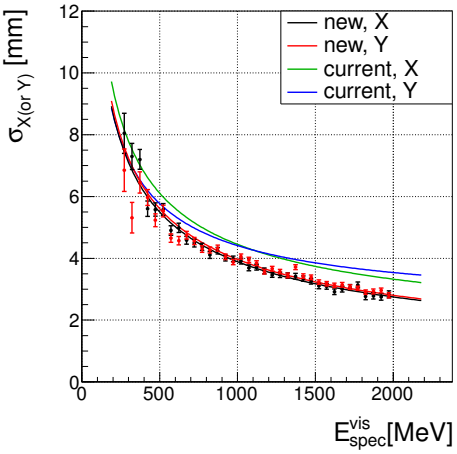

(b) large-crystal data subset

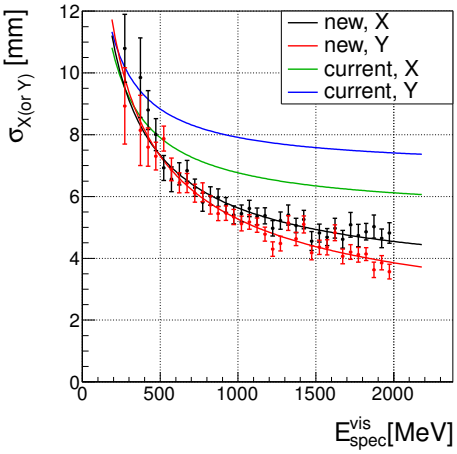

Figure 7.9: Position resolution with the *shape* position reconstruction method obtained from the small-crystal data subset (a) and from the large-crystal data subset (b). The black (red) dots show the measured data for x (y) resolution, and the black (red) line shows the best fit of the resolution function. Resolutions for x (or y) obtained by the current method are also shown in the green (blue) line.

(a)

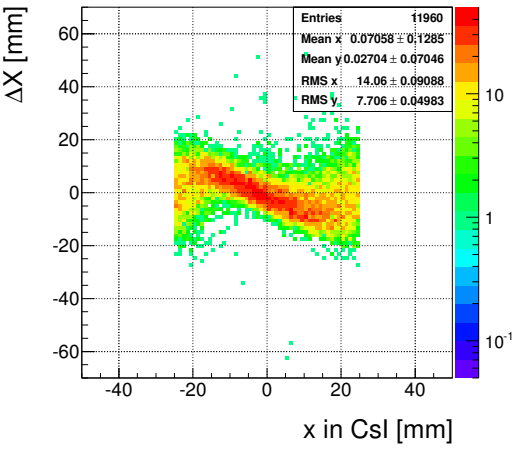

(b)

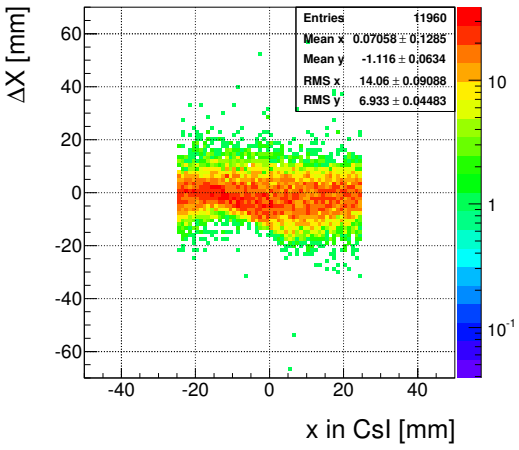

Figure 7.10: Dependence of the Δx on the x incident position in the crystal. The dependence shown in (a) was derived with the *COE* method, while that in (b) was derived with the *shape* method. Both plots were made by using the large-crystal data subset.

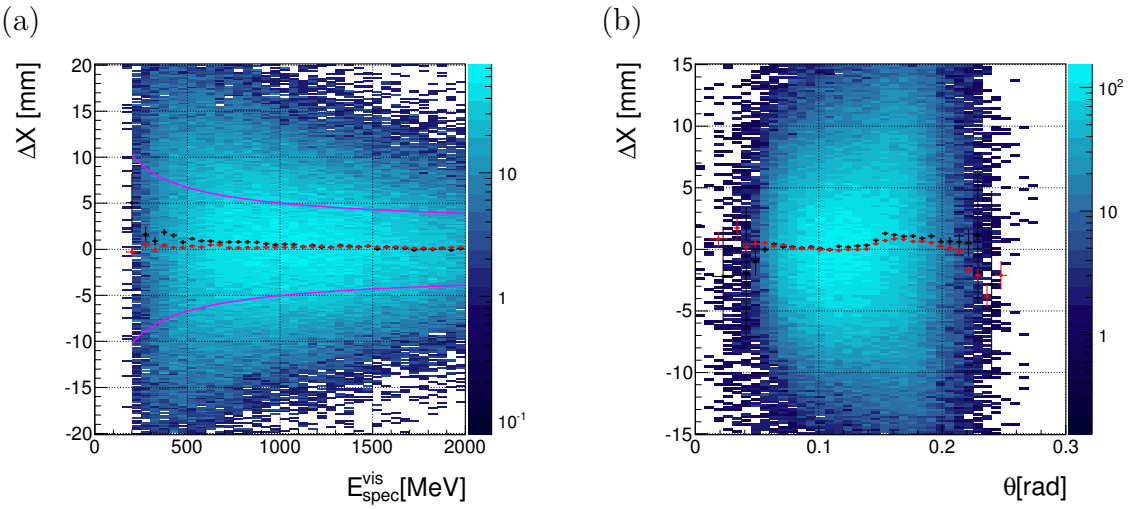

Figure 7.11: Dependence of ΔX on energy (a) and incident angle (b). The black (red) dots show the center values of every x bin observed in the data (simulation). The magenta lines in (a) represent $\pm 1\sigma$ deviation of the position resolution for the small crystals given in Eq. (7.7)

The dependence on the incident angle θ is plotted in Fig. 7.11(b). There was about a 1 mm difference around $\theta = 0.15$ rad. This difference was reproduced in the Monte Calro estimation. Based on the Monte Calro study, this discrepancy was considered to occur at the boundary of the small and large crystals. This could be seen more clearly as the x position dependence of the Δx, as shown in Fig. 7.12. The discrepancy of the Δx from zero was about 4 mm at 500 mm $\sim$ the boundary(= 600 mm).[1] This discrepancy arose from calculating the cluster position by using the *COE* method, and was resolved by using the *shape* method as shown in Fig. 7.12 in red.

7.3 Systematic Uncertainties

I separately estimated the systematic uncertainties related to three contributions: the spectrometer resolution, the materials located upstream of the CsI calorimeter, and the width of E_{CsI}/E^{vis}_{spec} or ΔX.

[1]The zigzag structure found in outside the boundary was due to the localization of the cluster position shown in Fig. 7.10

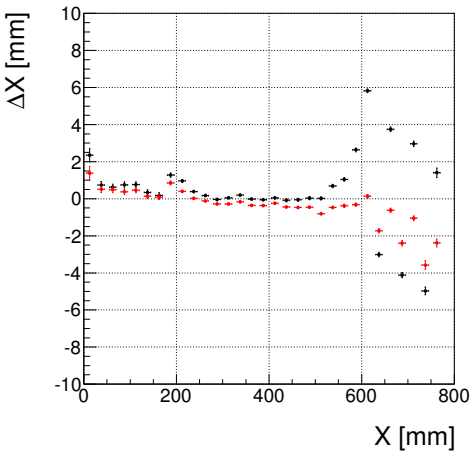

Figure 7.12: Dependence of ΔX on x incident position. The black (red) dots were derived with using the *COE* (*shape*) method for position reconstruction.

7.3.1 Uncertainties of Spectrometer Resolution

The uncertainties of the spectrometer resolutions were already estimated in Chapter 4.3, as shown in Eq. (4.35) and Eq. (4.37). The error due to Monte Calro statistics, which was separately described in Eq. (4.35) or Eq. (4.37), was treated as a part of the systematic errors for the calorimeter resolutions.

7.3.2 Uncertainties due to Materials

The fluctuation of electron energies and incident positions due to the materials located upstream of the calorimeter was estimated with Monte Calro simulation. I considered two kinds of sources for the systematic uncertainties: the amount of the materials, and the physics models of electromagnetic process in Geant4.

Amount of materials

Table 7.3 shows the materials, expected energy deposits in them, and energy and position fluctuations due to them estimated from the Monte Carlo simulation. The CsI cover occupied about a half of the total amount of materials, and it was a dominant source of the energy fluctuation. The CsI cover was considered to have the worst reproducibility of the configuration in the simulation, because its structure was relatively complicated than other materials. The inaccuracy of the amount of material of

Table 7.3: Materials upstream of the CsI calorimeter. The average energy deposits in them, and energy and position fluctuations due to them estimated from the Monte Carlo are also shown.

name	ene. dep. [MeV]	ene. fluc. [%]	pos. fluc. [mm]
air	0.35	0.03	1.02
window of dry room	0.06	0.01	0.94
CV	1.83	0.18	2.05
trigger scinti.	2.24	0.21	1.64
CsI cover	3.36	0.69	0.92

the CsI cover in the simulation is conservatively estimated to be less than 10 %.

I increased and decreased 10% of the amount of material of the CsI cover in the simulation. To be conservative, I also changed the amount of materials of the CV and the trigger scintillators at the same rate. With these changes, the fluctuations of energies and incident positions varied as shown in Fig. 7.13. I summed the variations of the fluctuations quadratically, and assigned the systematic uncertainties based on the summed variation as shown with black lines in the figure.

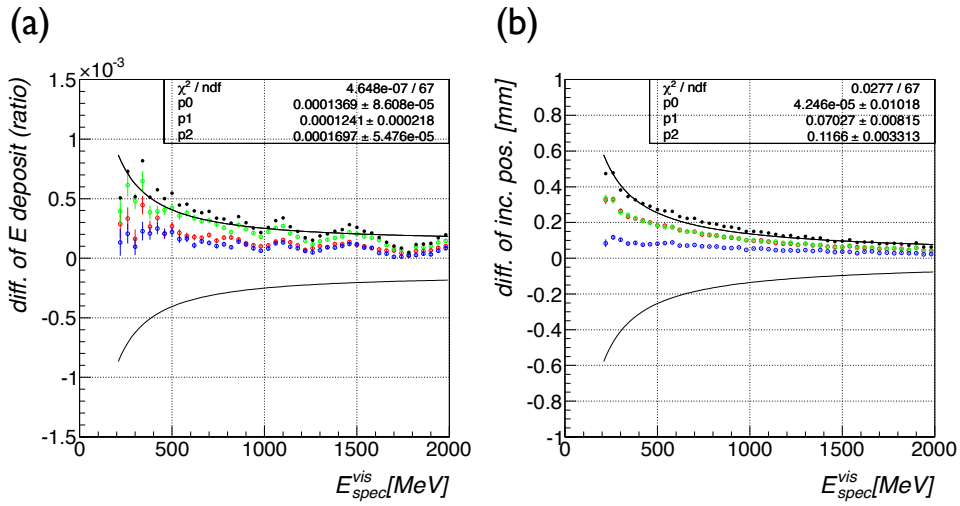

Figure 7.13: Differences of energy fluctuation (a) and incident position fluctuation (b) from default value by changing the amount of materials upstream of the CsI calorimeter. The red, green, and blue dots show the differences by changing the amount of materials of the CV, the trigger scintillators, and the CsI cover by 10 %, respectively. The black dots show the quadratic sum of the differences of the three cases. The black line shows the systematic uncertainty I adopted.

Dependence on physics models

There are several physics models for electromagnetic processes in Geant4 [36]. I simulated interactions in the materials by using those models individually. The differences between the models were less than 0.05% for the energy resolution and 0.02 mm for the position resolution in all energy range, as shown in Fig. 7.14. I assigned the systematic uncertainty as shown with black lines in the figures.

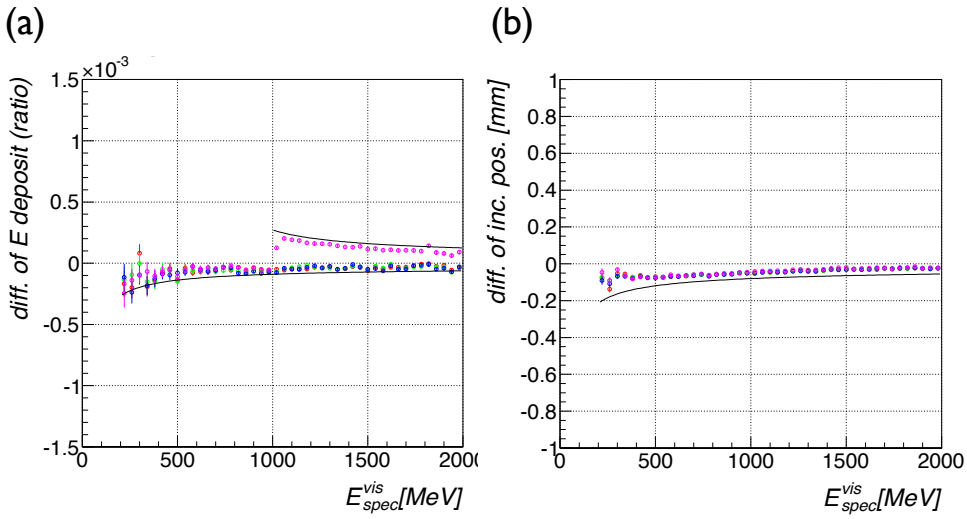

Figure 7.14: Differences of energy fluctuation (a) and incident position fluctuation (b) from the default value when the different physics models of electromagnetic process were used in the simulation. The colors show the different models: G4EmStandardPhysicsModel_Option3 (red), G4EmLivermorePhysicsModel (green), G4EmLivermorePolarPhysicsModel (blue), and G4EmPenelopePhysicsModel (magenta). The default model was G4EmStandardPhysicsModel. The black lines show the systematic uncertainties I adopted.

7.3.3 Uncertainties for the Widths of E_{CsI}/E^{vis}_{spec} and ΔX Distributions

There remained some non-electron events even after applying the electron selection cuts. Those backgrounds events could distort the estimation for the widths of E_{CsI}/E^{vis}_{spec} and ΔX.

To evaluate the effect of those backgrounds, I estimated the widths using the Monte Calro simulation with and without the backgrounds. The differences of the widths between the two cases are shown in Fig. 7.15. Finite differences were found in the

E_{CsI}/E^{vis}_{spec} width and the ΔX width. Here I iterated the Monte Calro simulation by 20 times by changing its random seed. The mean value and RMS value of the 20 trials are shown in red circles and their error bars in the figure. I assigned the mean ± RMS as the systematic uncertainties.

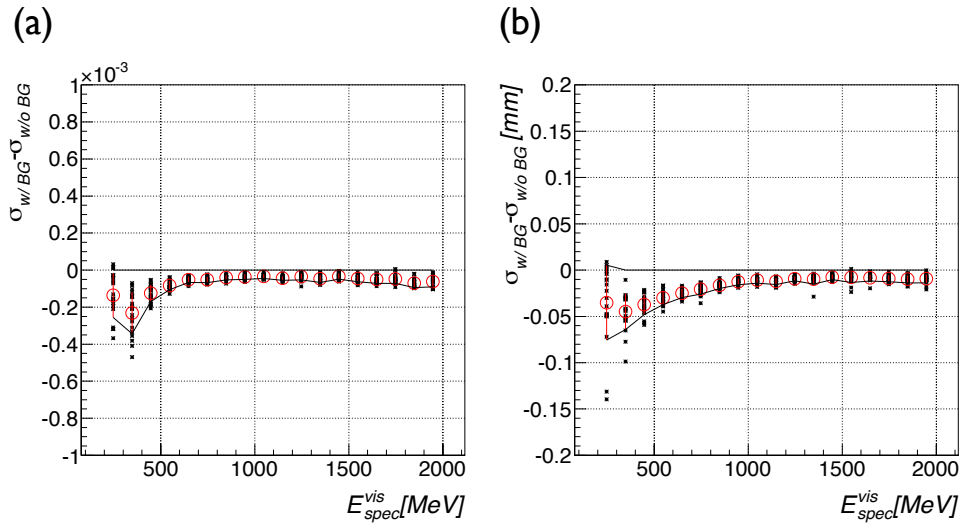

Figure 7.15: Difference of E_{CsI}/E^{vis}_{spec} width (a) and ΔX width (b) with and without background events. The simulation was iterated 20 times. The 20 black points in each x value correspond to the 20 iterations, and the red circles show the average of them. The black lines represent the systematic errors I adopted.

The background level in the E_{CsI}/E^{vis}_{spec} plot was different between the data and the Monte Calro simulation. To make the background level comparable between the data and the Monte Calro, I loosened the shape χ^2 cut value from 2.5 to 4.05 in the Monte Calro simulation as shown in Fig. 7.16. The differences of the estimated widths before and after changing the cut value were evaluated as shown in Fig. 7.17. The both widths became slightly wider after loosening the cut value. Here I iterated the Monte Calro simulation by 20 times by changing its random seed. The mean value and RMS value of the 20 trials are shown in red circles and their error bars in the figure. I assigned the mean ± RMS as the systematic uncertainties.

7.3.4 Uncertainty in Total

I will explain how the systematic errors for the energy and position resolution were calculated from the uncertainties for the three contributions estimated so far.

I describe the case of the energy resolution obtained from the small-crystal data subset, as an example. Figure 7.18 shows the three contributions to the energy resolution,

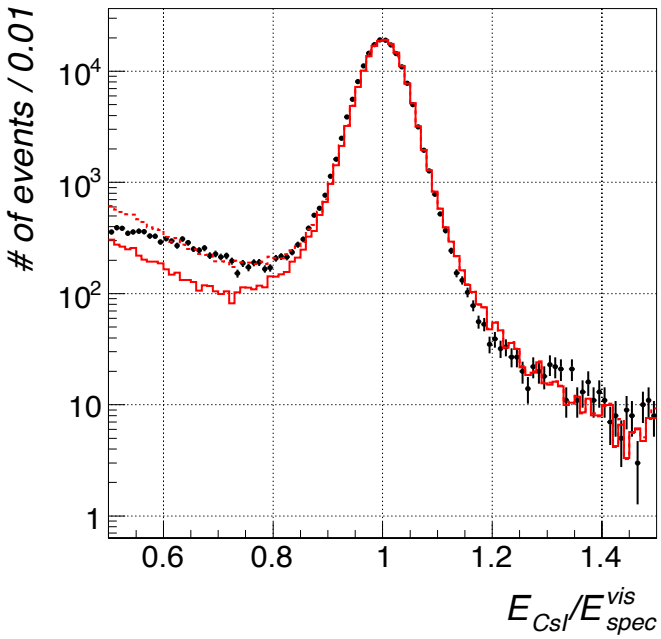

Figure 7.16: The E_{CsI}/E^{vis}_{spec} distribution. The black dots show the data and the red solid-lined histogram shows the default Monte Calro simulation. The red dashed-lined histogram shows the Monte Calro simulation with a loose cut value for shape χ^2. The histograms are scaled so that their peak heights are consistent with that of the data.

i.e: the spectrometer resolution (shown in the solid lines), the energy fluctuation due to materials (the dashed lines), and the measured width of E_{CsI}/E^{vis}_{spec} (the circles), with their systematic errors. The black circles and lines in the figure include no systematic uncertainties, while the red (green) colored circles and lines in the figure include systematic uncertainties which make the estimation for the energy resolution larger (smaller).

As described in the previous section, I derived the energy resolution by quadratically subtracting the contributions of the spectrometer and the materials from the width of E_{CsI}/E^{vis}_{spec}. In other words, the widths shown by the black solid line and dashed line in Fig. 7.18 were quadratically subtracted from the width shown by black circles in the same figure. I did the subtraction process for two more cases: subtraction of the widths shown by the two red lines from the width shown by the red circles, or subtraction of the widths shown by the two green lines from the width shown by the green circles in the figure. We then obtained three estimations for the resolution as shown in the dots in Fig. 7.19. These dots were individually fitted with the energy resolution function (Eq. (7.2)). The fit results were shown in the lines in the figure. The differences of the estimation shown by the red and green lines from the estimation shown by the black line were considered as the systematic errors of the energy resolution of the CsI

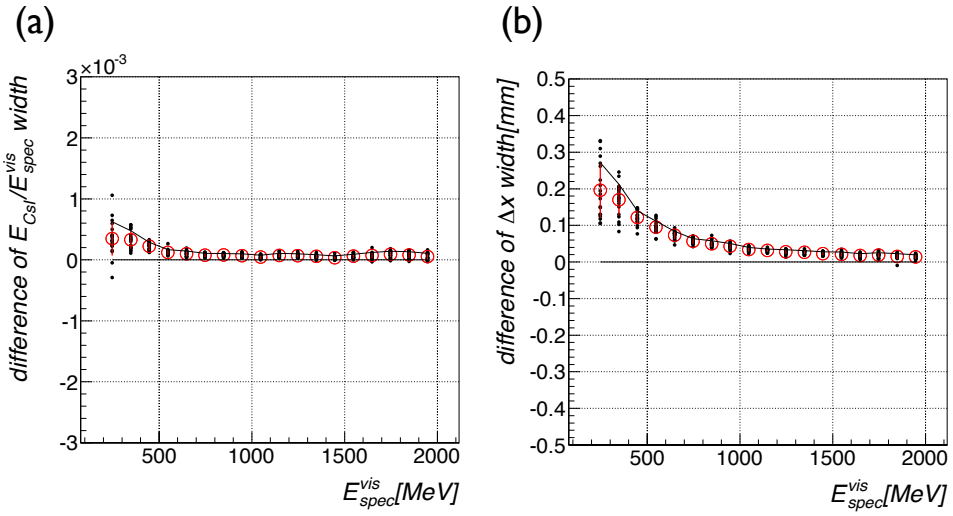

Figure 7.17: Differences of E_{CsI}/E^{vis}_{spec} width (a) and ΔX width (b) before and after loosening shape χ^2 cut value. The simulation was iterated 20 times. The 20 black points in each x value correspond to the 20 iterations, and the red circles show the average of them. The black lines represent the systematic errors I adopted.

calorimeter. The fitted parameters are shown in Table 7.4.

Similarly I estimated the systematic uncertainties for the other resolutions: the energy resolution for large-crystal data set (described in Eq. (7.3)) and the position resolutions for small-crystal and large-crystal data set (described in Eq. (7.8, 7.9)). The results are summarized in Table 7.4.

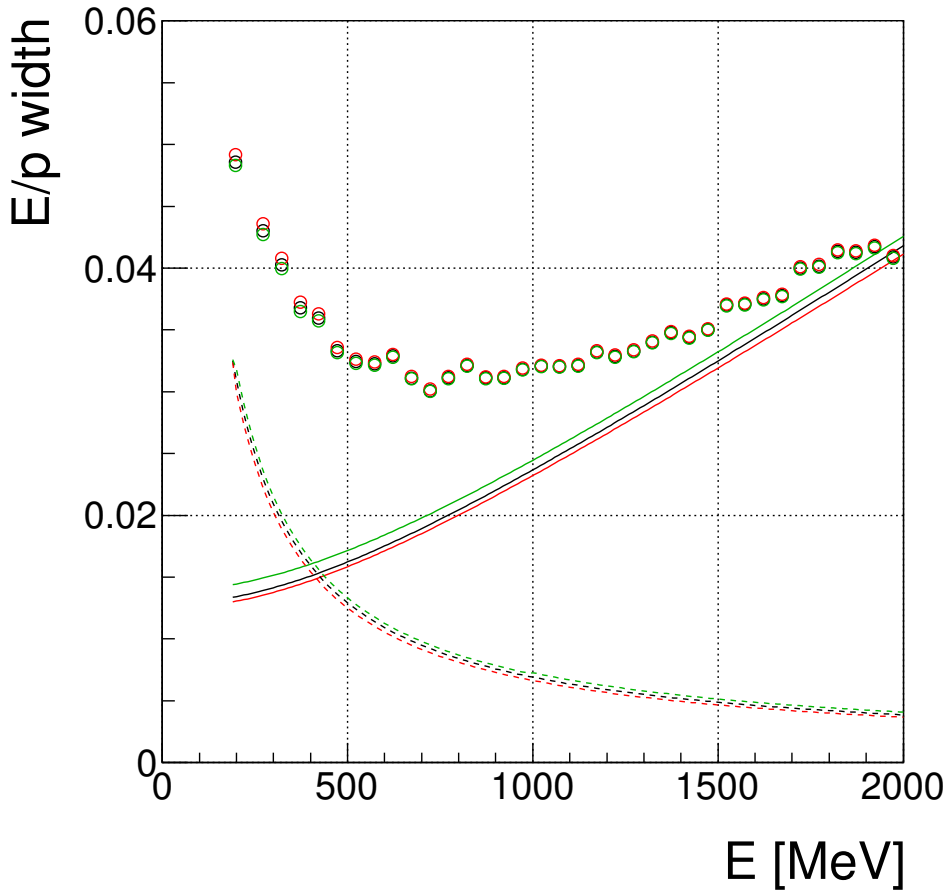

Figure 7.18: Three contributions for the energy resolution. Contributions of the spectrometer, the materials, and the width of E_{CsI}/E^{vis}_{spec} are shown as the solid line, the dashed line, and the circles, respectively. The circles and lines colored in black include no systematic uncertainties, while the red (green) plots include the systematic uncertainties which make the estimation for energy resolution larger (smaller).

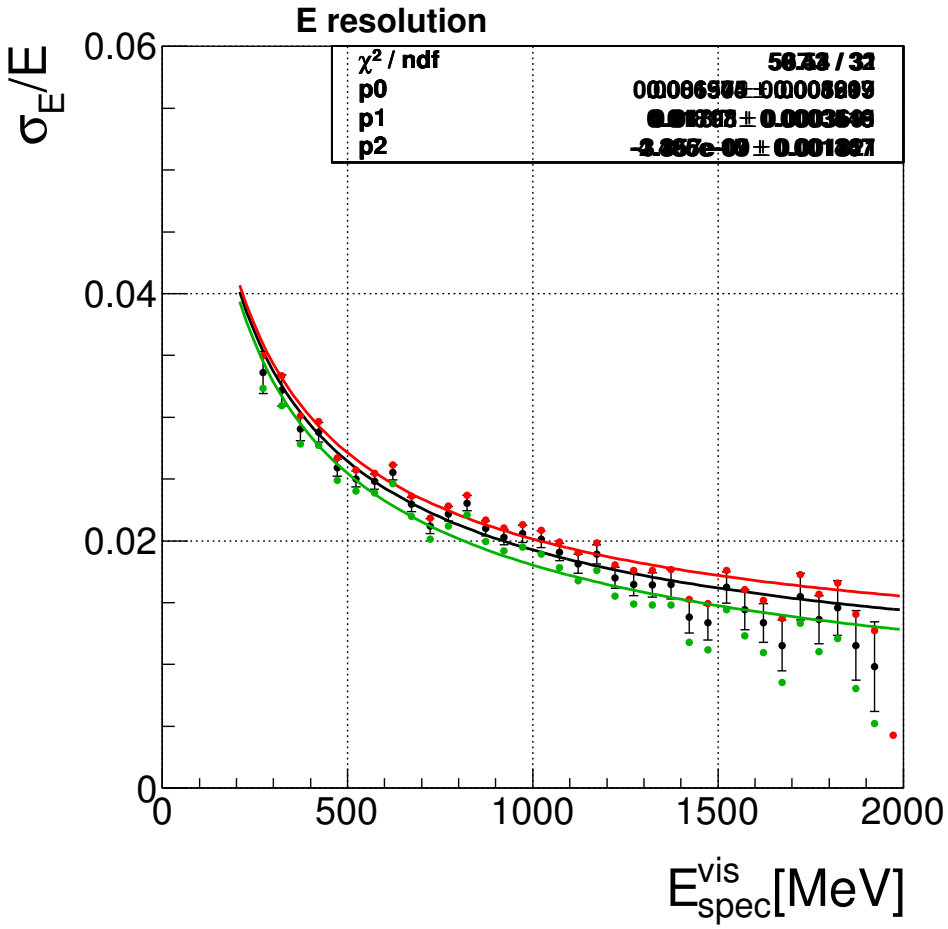

Figure 7.19: Energy resolution of the calorimeter. The black, red, and green dots were derived by using the black, red, and green plots in Fig. 7.18. The lines show fitting results with the function in Eq. (7.2).

Table 7.4: Systematic errors for parameters of the resolution functions. The "default" column shows the estimation without the systematic uncertainties, while the "larger" ("smaller") column shows the estimation with the systematic uncertainties which makes the estimation larger (smaller).

• Parameters for the energy resolution function defined in Eq. (7.2)

	defulat			larger			smaller		
	p_1	p_2	p_3	p_1	p_2	p_3	p_1	p_2	p_3
for small-crystal	0.66	1.81	0	0.87	1.82	0	0.15	1.79	0
for large-crystal	1.71	1.31	0	1.80	1.32	0	1.58	1.30	0

• Parameters for the x position resolution function defined in Eq. (7.7)

	defulat		larger		smaller	
	p_1	p_2	p_1	p_2	p_1	p_2
for small-crystal	1.52	4.18	1.13	4.51	1.81	3.83
for large-crystal	5.39	4.09	5.28	4.47	5.51	3.68

• Parameters for the y position resolution function defined in Eq. (7.7)

	defulat		larger		smaller	
	p_1	p_2	p_1	p_2	p_1	p_2
for small-crystal	2.37	3.72	2.10	4.33	2.41	3.32
for large-crystal	6.87	3.93	6.81	4.61	6.86	3.47

Chapter 8

Measurement of K_L Momentum Spectrum

In this chapter, I will describe the measurement the K_L momentum spectrum by using $K_L \to \pi^+\pi^-$ and $K_L \to \pi^+\pi^-\pi^0$ decays. Both decays can be reconstructed exclusively using the CsI calorimeter and the spectrometer.

First I will introduce the previous measurement of the K_L momentum spectrum and reveal its problems. Next, I will explain the event reconstruction for each decay. The momentum distribution of the reconstructed K_L should be deformed from the momentum spectrum of the beam, because of detection efficiencies of the decays and a smearing effect due to detector resolutions. I will describe corrections for these effects in the third section. In the last section, the systematic errors will be estimated.

8.1 Previous Work

The momentum spectrum of the K_L beam was already measured in 2010 [5]. The spectrum is shown in Fig. 8.1(a). The measurement, however, did not have a sensitivity to the K_L with momentum higher than 4 GeV/c (Fig. 8.1(b)). The tail shape of the spectrum had a relatively large uncertainty as the result. In addition, the specific function form of K_L momentum spectrum was assumed to derive the spectrum from the observed K_L momentum distribution. Due to such an assumption, there was some bias in the result.

The measurement described in this chapter is a cross check for the previous measurement. It has a higher acceptance in the higher momentum region and it does not assume any function form for the momentum spectrum.

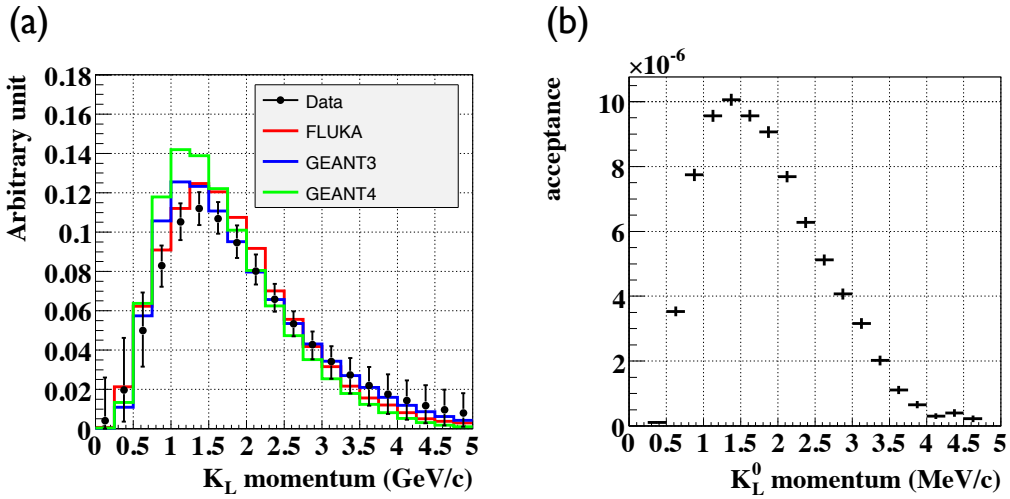

Figure 8.1: (a) Momentum spectrum previously measured (black dots) and the Monte Carlo estimations with different simulator (colored histograms). (b) Signal acceptance in the measurement. Both plots are from reference [5].

8.2 K_L Reconstruction

In this section I will describe the identification of the $K_L \to \pi^+\pi^-$ and $K_L \to \pi^+\pi^-\pi^0$ decays and the reconstruction of the K_L momentum. I used the June data for the analysis of the $K_L \to \pi^+\pi^-$ decay while the February data was used for the analysis of the $K_L \to \pi^+\pi^-\pi^0$ decay.

8.2.1 $K_L \to \pi^+\pi^-$ Analysis

Particles in the final state of the $K_L \to \pi^+\pi^-$ decay are π^+ and π^-. Their momenta $\vec{p}_{\pi^+}$ and $\vec{p}_{\pi^-}$ were measured with the spectrometer. The K_L momentum $\vec{p}_{K_L}$ was obtained by adding the two pion momenta, as

$$\vec{p}_{K_L} = \vec{p}_{\pi^+} + \vec{p}_{\pi^-}. \tag{8.1}$$

The decay vertex $\vec{r}_{vtx}$ was reconstructed from the intersection of the two tracks. The $K_L \to \pi^+\pi^-$ decay events were thus fully reconstructed with the spectrometer information only.

Event selection

I required two kinematic selections to identify the decay.

1. Square of the transverse momentum of $\pi^+\pi^-$

   From Eq. (8.1), the square of the transverse momentum of $\pi^+\pi^-$ perpendicular to the K_L direction should be zero. This value, denoted by p_t^2, was calculated as

$$p_t^2 = (\vec{p}_{\pi^+} + \vec{p}_{\pi^-})^2 \left[1 - \left(\frac{\vec{p}_{\pi^+} + \vec{p}_{\pi^-}}{|\vec{p}_{\pi^+} + \vec{p}_{\pi^-}|} \cdot \vec{d}_{K_L}\right)^2\right], \tag{8.2}$$

   where the $\vec{d}_{K_L}$ represents the unit vector pointing to the K_L direction. The direction from the center of the production target to the decay vertex was used as the $\vec{d}_{K_L}$;

$$\vec{d}_{K_L} = \frac{\vec{r}_{vtx} - (0, 0, -21\text{m})}{|\vec{r}_{vtx} - (0, 0, -21\text{m})|}. \tag{8.3}$$

   The distribution of the observed p_t^2 is shown in Fig. 8.2(a). I required the p_t^2 to be less than 50 MeV$^2/c^2$.

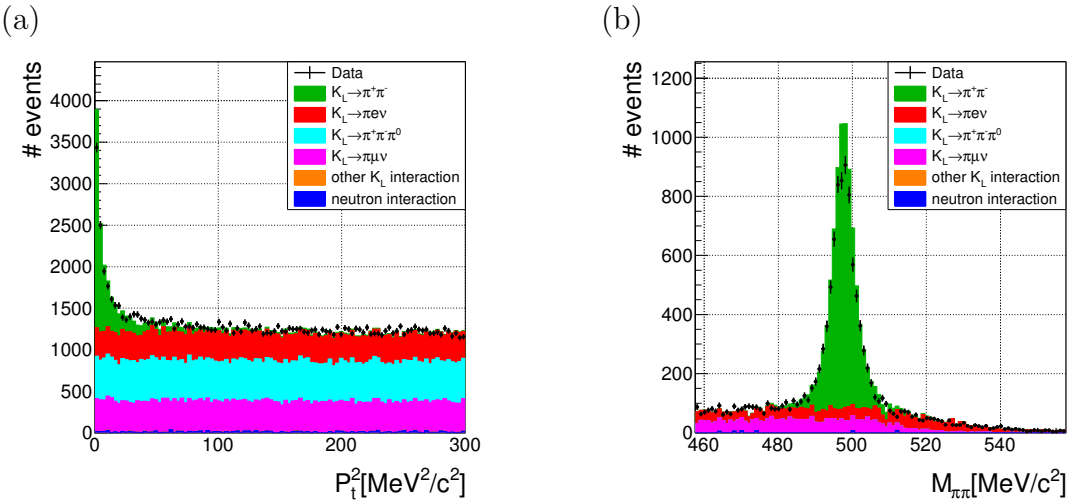

Figure 8.2: (a) Distribution of p_t^2 of the two charged particles which is defined in Eq. (8.2). (b) Distribution of the invariant mass of the two charged particles assuming that they are π^+ and π^-. In both figures, the black dots show the measured data. The histograms show the expectations from the Monte Carlo simulation, and their colors represent the sources of the events: $K_L \to \pi^+\pi^-$ (green), $K_L \to \pi e\nu$ (red), $K_L \to \pi^+\pi^-\pi^0$ (cyan), $K_L \to \pi\mu\nu$ (magenta), other K_L interaction (orange) and beam-neutron interaction (blue).

2. Invariant mass of $\pi^+\pi^-$

   The invariant mass of two charged particles $M_{\pi\pi}$ was reconstructed with assuming that the particles have the π^+ mass (139.57018 MeV/c^2). The distribution of the invariant mass is shown in Fig. 8.2(b). The $K_L \to \pi^+\pi^-$ decay events

have a peak at the K_L mass (497.614 MeV/c^2). I required the invariant mass was equal to the K_L mass within 30 MeV/c^2.

Background subtraction

A contamination from the $K_L \to \pi e\nu$ and the $K_L \to \pi\mu\nu$ decay events still remained even after applying the selection cuts. One possible way to further suppress those backgrounds is using the calorimeter information. Electrons from the $K_L \to \pi e\nu$ decays make electromagnetic showers in the CsI calorimeter, and those showers can be distinguished from the activity of pions from the $K_L \to \pi^+\pi^-$ decays by using the electron selection criteria introduced in Chapter 5. However, I avoided using the calorimeter information because of the reasons listed below.

1. The contamination from the $K_L \to \pi\mu\nu$ decay events was difficult to suppress, because both pions and muons often interacted with the calorimeter as MIPs.
2. Hadron interactions of pions in the calorimeter are difficult to reproduce in the Monte Carlo simulation.
3. A geometrical acceptance is lost by requiring the activity in the calorimeter, because the effective area of the trigger scintillator was larger than that of the calorimeter. In particular, the south side of the calorimeter was not active in the June run.

Instead of introducing further selection cuts, the background contribution was estimated by using the Monte Carlo simulation and subtracted from the data. In the simulation, the K_Ls were generated with a momentum spectrum distributed uniformly from 0 to 10 GeV/c, to obtain a sufficient statistics even in a high momentum region. The events were then weighted so that the momentum spectrum became consistent with that measured in the previous work. The momentum spectrum and the beam profile of neutrons were determined based on an independent simulation with Geant3 [24]. Details about the Monte Carlo simulation is described in Appendix B.

The amount of background contamination was determined by fitting the probability density function (PDF) of the backgrounds to the p_t^2 distribution of the data. For the K_L background, the histogram of the p_t^2 distribution obtained from the simulation was used as the PDF. For neutrons, the PDF was assumed as a parabolic function as shown in Fig. 8.3. Its parameters were determined by fitting the p_t^2 distribution in the simulation, by requiring the invariant mass cut.

The data was divided into 100 MeV/c regions in the reconstructed K_L momentum. The PDF for the p_t^2 distribution from the K_L background was prepared for each momentum region, while the shape of the PDF for the neutron background was common to all the regions. The K_L and neutron PDFs were combined based on the ratio of the numbers

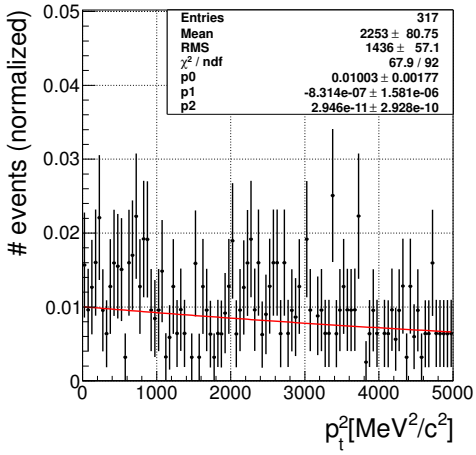

Figure 8.3: Monte Carlo expectaion of the p_t^2 distribution of the neutrons. The neutron PDF was obtained by fitting a parabolic function to this plot, as shown in the red line.

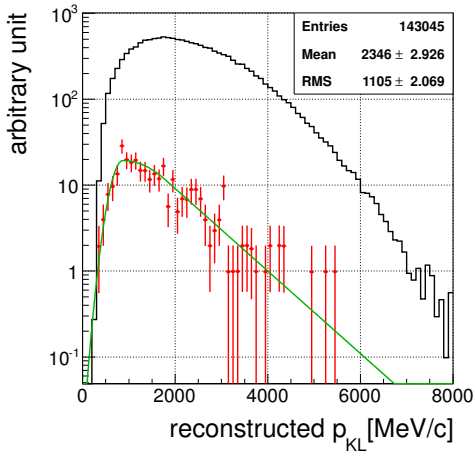

Figure 8.4: Monte Carlo expectation of the numbers of background events from K_L (black histogram) and neutrons (red crosses) as a function of reconstructed K_L momentum. Here, I required $p_t^2 < 5000$ MeV$^2/c^2$ and $|M_{\pi\pi} - M_{K_L}| < 30$ MeV$/c^2$. The absolute value of the y axis was arbitrary, but the relative scale of the two background was retained. The green line shows a function used to estimate the number of neutrons in each momentum.

of expected events in each momentum region which is shown in Fig. 8.4. Because of a small statistics of the Monte Carlo, the number of the neutrons in each region was determined by assuming the distribution shown in a green line in the figure.

The PDF was fitted to the data in $2000 < p_t^2 < 5000$ MeV$^2/c^2$ range as shown in Fig. 8.5. The PDF shape at $p_t^2 < 1500$ MeV$^2/c^2$ was approximated as a linear function to determine the number of the background events in the signal region, as also shown in Fig. 8.5 in a green line. The K_L momentum distribution after subtracting the backgrounds is shown in Fig. 8.6.

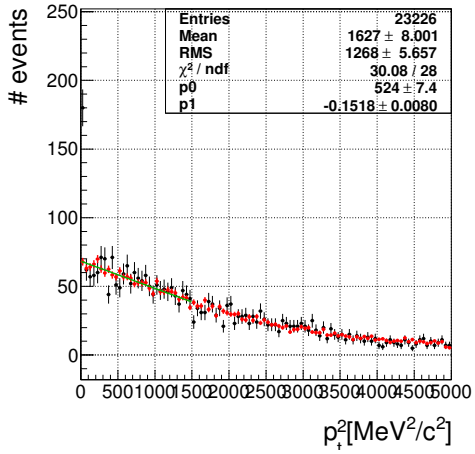

Figure 8.5: An example of the PDF fitting. The black dots show the p_t^2 distribution observed in the data in $600 < p_{K_L} < 700$ MeV/c range. The red dots show the PDF of the backgrounds. The PDF shape at $p_t^2 < 1500$ MeV$^2/c^2$ was approximated as a linear function which is shown in green.

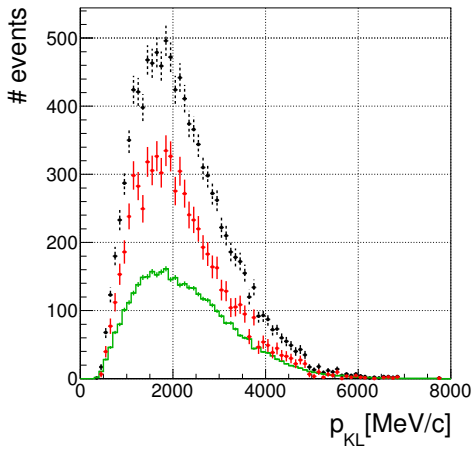

Figure 8.6: The number of events in the signal region as a function of K_L momentum. The black dots show all the events observed in the data, while the green histogram shows the expected number of background contamination in it. The red dots show the remaining events after subtracting the backgrounds.

8.2.2 $K_L \to \pi^+\pi^-\pi^0$ Analysis

There are two charged pions, and two gammas from π^0 in the final state of $K_L \to \pi^+\pi^-\pi^0$ decay. The momenta of the pions $\vec{p}_{\pi^+}$ and $\vec{p}_{\pi^-}$ and the decay vertex position $\vec{r}_{vtx}$ were measured with the spectrometer. The energies of the two gammas E_1 and E_2 and their incident positions $\vec{r}_1$ and $\vec{r}_2$ were measured with the CsI calorimeter. The momenta of the two gammas $\vec{p}_{\gamma 1}$ and $\vec{p}_{\gamma 2}$ were then calculated as

$$\vec{p}_{\gamma i} = E_i\,(\vec{r}_i - \vec{r}_{vtx}) \quad (i = 1, 2). \tag{8.4}$$

The momentum of K_L was calculated as

$$\vec{p}_{K_L} = \vec{p}_{\gamma 1} + \vec{p}_{\gamma 2} + \vec{p}_{\pi^+} + \vec{p}_{\pi^-} \tag{8.5}$$

The $K_L \to \pi^+\pi^-\pi^0$ decay was thus fully reconstructed.

Event selection

I required some conditions to identify the decay.

1. Number of clusters.

   Because there are 4 particles in the final state, I required 4 clusters in the CsI calorimeter with energy > 50 MeV.

2. Track association to the cluster.

   If the cluster position was located within 100 mm around the incident position of charged tracks measured with the spectrometer, the cluster was regarded as a charged pion and associated with the track. If any of the following conditions were satisfied, such events were discarded.

   - There were no associated cluster for at least one of the tracks.
   - There were 2 or more clusters associated with one track.
   - There was a cluster associated with both tracks.

3. CsI fiducial region.

   Clusters which were not associated with any tracks were regarded as gammas, called gamma clusters. To suppress electromagnetic showers leaking out of the active region of the CsI calorimeter, the positions of the gamma clusters were required to be located within the fiducial region which was defined in Fig. 5.3(a). In addition, if a gamma cluster includes crystals located in the edge region which was also defined in Fig. 5.3(a), the total energy deposit in such crystals was required to be less than 10 % of the total energy deposit in the cluster.

4. Invariant mass of 2 γs ($M_{\gamma\gamma}$).

   I required that the invariant mass of the 2 γs should be equal to the π^0 mass (134.9766 MeV/c^2) within 25 MeV/c^2. As shown in Fig. 8.7(a), almost all the contributions from the K_L decays except the $K_L \to \pi^+\pi^-\pi^0$ decay were rejected with this requirement.

5. The k_{+-0}.

   As already shown in Chapter 5.1, the k_{+-0} defined in Eq. (5.2) tends to be positive if the decay mode is $K_L \to \pi^+\pi^-\pi^0$. Figure 8.7 (b) shows the observed

k_{+-0} distribution. To reject charged tracks with mis-reconstructed momenta, the k_{+-0} was required to be greater than -20000 MeV^2.

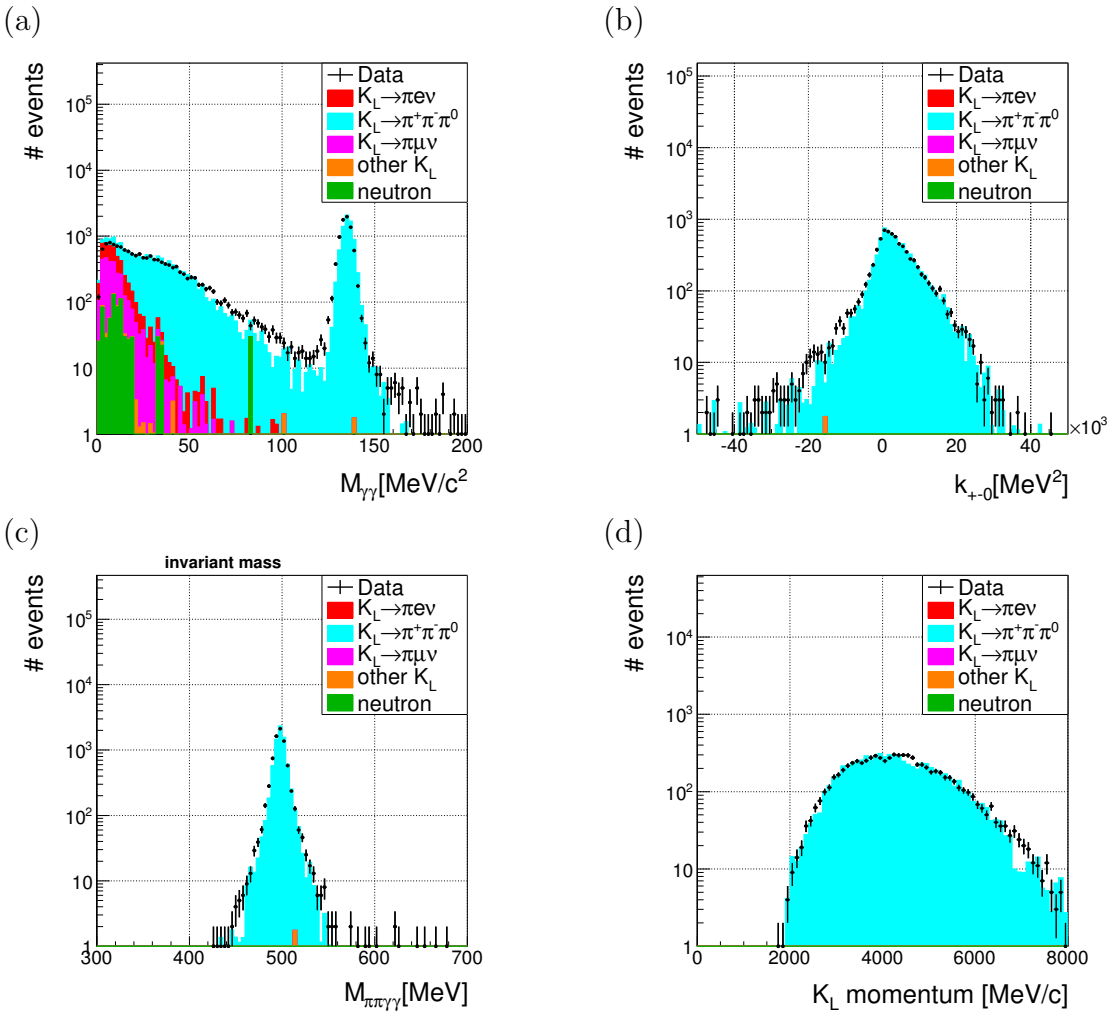

Figure 8.7: (a) The invariant mass of 2 gammas. (b) The k_{+-0} distribution. (c) The invariant mass of 4 particles. (d) The observed K_L momentum distribution. The black dots shows the data with statistical errors. The histograms shows estimations from Monte Calro simulation. Their colors represent origins of the events: the $K_L \to \pi e\nu$ decay (red), the $K_L \to \pi^+\pi^-\pi^0$ decay (cyan), $K_L \to \pi\mu\nu$ decay (magenta), other K_L interactions (orange), and the beam neutrons (green).

6. Invariant mass of 4 particles ($M_{\pi\pi\gamma\gamma}$).

   Figure 8.7(c) shows the invariant mass of all 4 particles by assuming that the charged particles were pions. I required that the mass should be equal to the K_L mass (497.614 MeVc^2) within 50 MeV/c^2.

Backgrounds from other K_L decays were well suppressed to the negligible level with these selections. There remained 7552 events after these selection cuts. The reconstructed K_L momentum distribution of those events is shown in Fig. 8.7(d).

8.3 K_L momentum spectrum

The reconstructed K_L momentum distributions in the previous section, shown in Fig. 8.6 and Fig. 8.7(d), were different from the momentum spectrum of the K_L beam, because they were smeared due to the resolution of K_L momentum measurement, and also because the probability to observe the K_L depended on its momentum. In this section, I describe the correction for the smearing effect and the observation probability.

8.3.1 Unfolding

The resolution for the K_L momentum was estimated with the Monte Carlo simulation, and represented as the 2-dimensional histogram shown in Fig. 8.8, which is called a migration matrix. The x axis of the migration matrix shows the Monte Carlo true value of the K_L momentum while the y axis shows the momentum smeared due to the detector resolution. We have to *unfold*, or, correct for the smearing effect due to the resolution. The unfolding process was done by using *TUnfold* class [34] which is prepared in the *ROOT* library [33]. This class provides a function to solve the unfolding problem.

The unfolded K_L momentum distributions are shown in Fig. 8.9.

8.3.2 Observation Probability

Probability that the K_L was observed through the $K_L \to \pi^+\pi^-$ or the $K_L \to \pi^+\pi^-\pi^0$ analysis was determined by four factors: the branching ratio of the decay, the probability to decay before the spectrometer, The geometrical acceptance of the detector, and the efficiency of the selection cuts. This observation probability, Prob_{obs}, was defined as

$$\mathrm{Prob}_{obs} = \frac{\text{number of observed } K_L}{\text{number of } K_L \text{ at the beam exit (or } Z = -1\mathrm{m})}. \tag{8.6}$$

The observation probability was estimated with the Monte Calro as a function of the K_L momentum, as shown in Fig. 8.10. The $K_L \to \pi^+\pi^-$ decay analysis covered a wide momentum region, while the $K_L \to \pi^+\pi^-\pi^0$ decay analysis had a high sensitivity in high momentum region.

(a) (b)

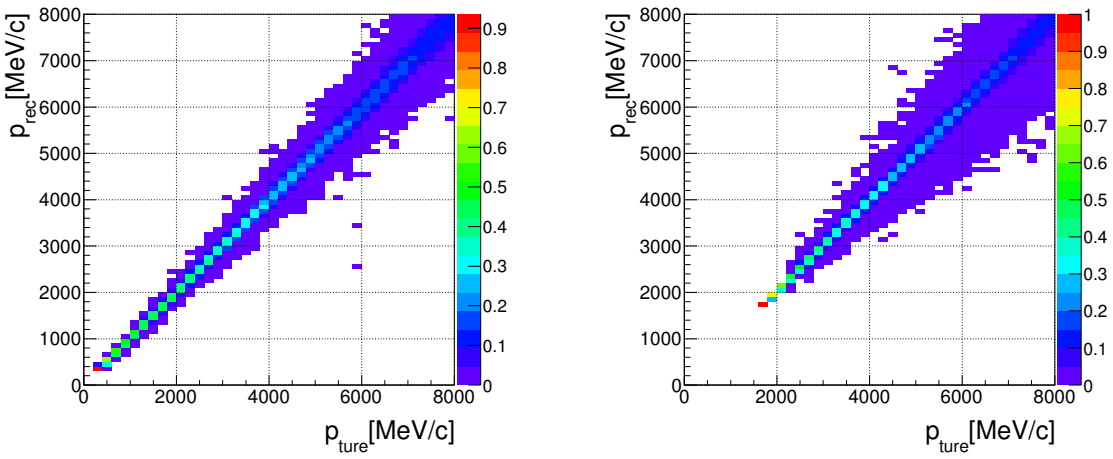

Figure 8.8: Migration matrices for the $K_L \to \pi^+\pi^-$ decay (a) and the $K_L \to \pi^+\pi^-\pi^0$ decay (b) which show the relation between the reconstructed K_L momentum (p_{rec}) and its Monte Calro true value (p_{true}).

(a) (b)

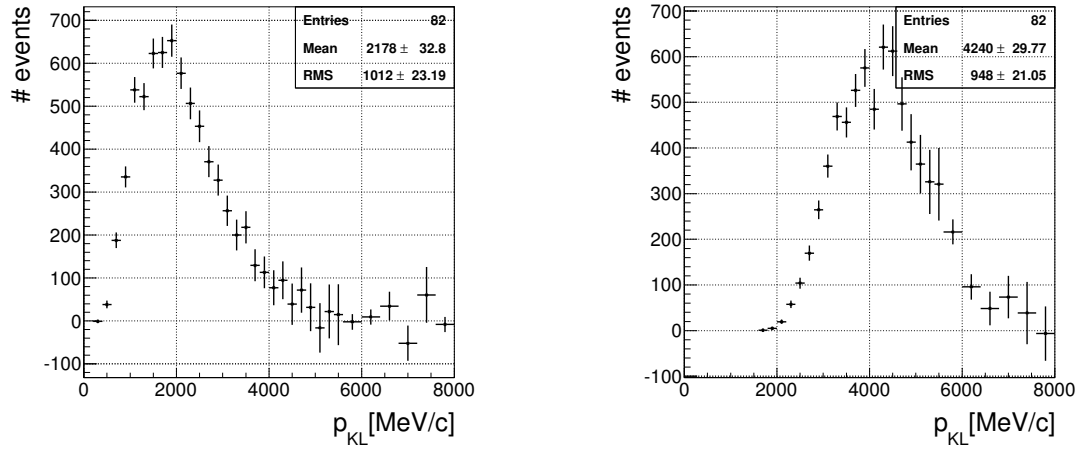

Figure 8.9: Unfolded K_L momentum spectrums observed in the $K_L \to \pi^+\pi^-$ analysis (a) and in the $K_L \to \pi^+\pi^-\pi^0$ analysis (b).

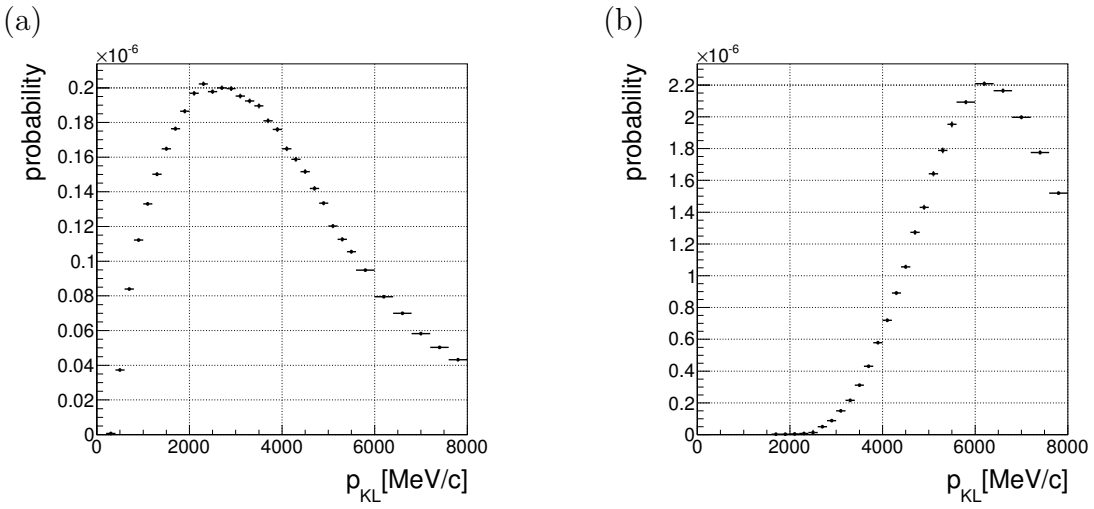

Figure 8.10: Observation probability of $K_L \to \pi^+\pi^-$ decay (a) and $K_L \to \pi^+\pi^-\pi^0$ decay (b) as a function of K_L momentum.

8.3.3 Result

The K_L momentum spectrum at the beam exit was obtained by dividing the unfolded momentum distribution by the observation probability. Two spectrums obtained from the $K_L \to \pi^+\pi^-$ analysis and the $K_L \to \pi^+\pi^-\pi^0$ analysis were scaled to minimize the chi-square between them. The average of the two histograms was calculated with weighting the bin errors. The result is shown in Fig. 8.11.

To test the previous work [5], the result was fitted with the function used in that work which was defined as

$$f(p_{K_L}) = A \cdot \exp\left(-\frac{(p_{K_L}[\mathrm{GeV}] - \mu)^2}{2\,(\sigma(p_{K_L}))^2}\right), \tag{8.7}$$

where p_{K_L} represents the momentum of K_L, and

$$\sigma(p_{K_L}) = a\,(1 - (b + cp_{K_L}[\mathrm{GeV}]) \cdot (p_{K_L}[\mathrm{GeV}] - \mu))\,. \tag{8.8}$$

The fitting result is also shown in Fig. 8.11(b). The fit χ^2/NDF was 25.6/28. This function well described the obtained K_L momentum spectrum. The parameter errors and the covariances between them are shown in Table 8.1 and Table 8.2. The error of the fitting function, also shown in the dashed lines in the figure, were calculated with the errors and covariances of the parameters. Details of the error calculation is described in Appendix D.3.

The spectrum measured in the previous work is also shown in Fig. 8.11(b) in a blue line. The spectrums were consistent with each other within 1-sigma deviation in a

Table 8.1: Parameters and their errors of Eq. (8.7) obtained by fitting the data.

parameter	A	μ	a	b	c
value	1	1.393	0.797	-0.299	0.0178
error	$\pm$0.026	$\pm$0.035	$\pm$0.031	$\pm$0.048	$\pm$0.0060

Table 8.2: Covariances between parameters of Eq. (8.7) obtained by fitting the data.

parameter	A	μ	a	b	c
A	0.000693161	-0.000341346	-0.000561413	-0.000582277	5.14247e-05
μ	-	0.00121924	0.000602337	0.00125762	-0.000157314
a	-	-	0.000991683	0.00130622	-0.000133764
b	-	-	-	0.00226127	-0.000271999
c	-	-	-	-	3.55324e-05

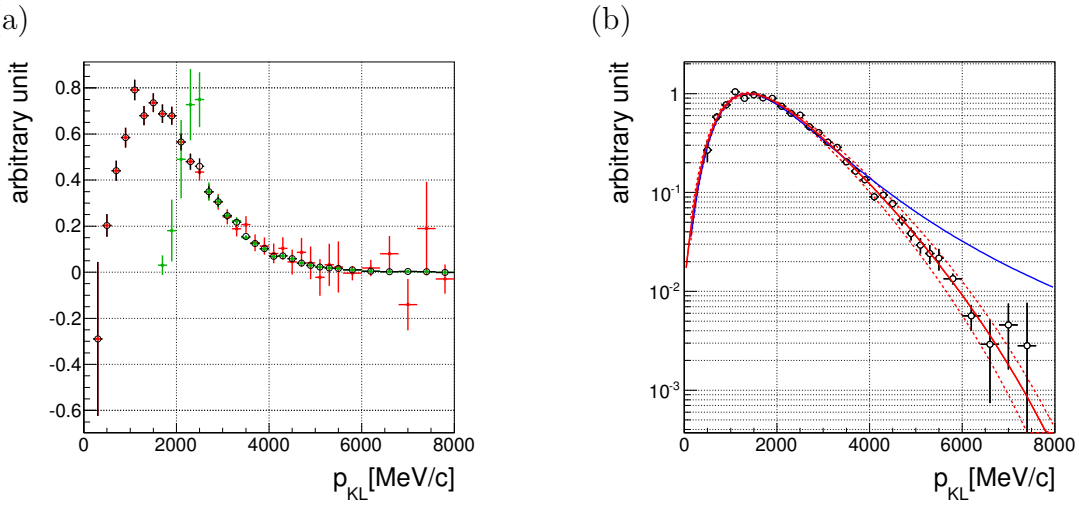

Figure 8.11: The K_L momentum spectrum at the beam exit derived from the data, shown in linear scale (a) and in log scale (b). The red and green dots in (a) show the spectrum obtained from $K_L \to \pi^+\pi^-$ decay and that from $K_L \to \pi^+\pi^-\pi^0$ decay, respectively. The black circles in both (a) and (b) show the combined result. In (b), the best fit with Eq. (8.7) is shown in the red solid line and its $\pm 1\sigma$ deviation are shown in the red dashed lines. The blue line in (b) shows the result of the previous measurement.

momentum region below 4 GeV. In the higher momentum region, the previous work overestimated the number of K_Ls.

8.4 Systematic Uncertainties

The systematic uncertainties of the K_L momentum spectrum is described in this section. I estimated uncertainties related to the background estimation, the resolution of K_L momentum, and the cut effectiveness.

8.4.1 Uncertainties for Background Estimation

To reconstruct the K_L momentum spectrum, I assumed that there is no background contamination in the observed K_L momentum distributions (Fig. 8.6 and Fig. 8.7(d)). I estimated the uncertainties related to the background estimation.

$K_L \to \pi^+\pi^-$ analysis

1. Shape of the p_t^2 PDF for K_L backgrounds.

   The PDF of the p_t^2 distribution for K_L backgrounds was made from the Monte Carlo by assuming the K_L momentum spectrum measured in the previous work. To study a sensitivity of the PDF shape to the momentum spectrum shape, I tested another PDF which is made by assuming the spectrum obtained in this measurement, and also a PDF made by assuming the spectrum with a triangle shape as shown in Fig. 8.12(a). This changed the observed K_L momentum distribution as Fig. 8.12(b). Even if the triangle shape is used, the change was smaller than the statistical fluctuation in almost all momentum range. Although a relatively large difference was found around the 4000 GeV/c, it had almost no effect on the final result because the $K_L \to \pi^+\pi^-\pi^0$ analysis dominantly determined the spectrum shape in that range.

2. Shape of the p_t^2 PDF for the beam neutrons.

   The p_t^2 PDF shape of the neutron backgrounds was assumed as a parabolic function. It had a large uncertainty because of a small amount of the Monte Carlo statistics. The parameters of the function was determined from the p_t^2 distribution observed in the Monte Carlo, with requiring $|M_{\pi\pi} - M_{K_L}| < 30$ MeV/c^2 . To study this uncertainty, I tested a variety of PDFs made with requiring other conditions:

   - $|M_{\pi\pi} - M_{K_L}| < 45$ MeV/c^2

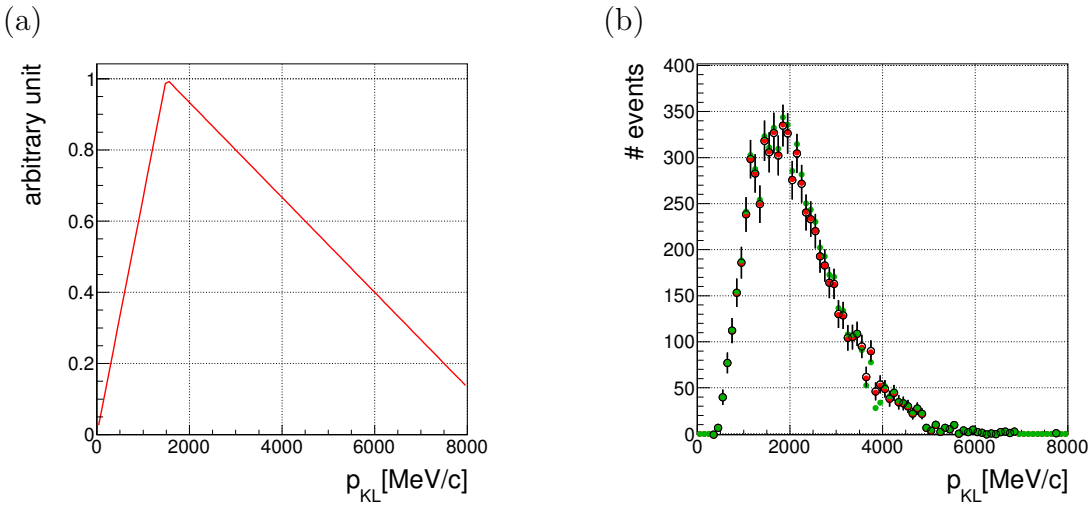

Figure 8.12: (a) Triangle K_L momentum spectrum shapes used to study the systematic uncertainties. (b) The K_L momentum distributions with three types of the K_L PDFs. The PDFs were made by assuming the K_L momentum spectrum measured in the previous work (black), measured in this thesis (red) and the triangle spectrum (green).

- $|M_{\pi\pi} - M_{K_L}| < 60$ MeV/c^2
- $|M_{\pi\pi} - M_{K_L}| < 60$ MeV/c^2 and $p_{K_L} < 1000$ MeV/c
- $|M_{\pi\pi} - M_{K_L}| < 60$ MeV/c^2 and $1000 < p_{K_L} < 2000$ MeV/c
- $|M_{\pi\pi} - M_{K_L}| < 60$ MeV/c^2 and $p_{K_L} > 2000$ MeV/c.

In addition to a parabolic function, the PDF with a linear function form was also tested. Differences of the observed K_L momentum distribution by changing the PDFs were much smaller than the statistical errors, as shown in Fig. 8.13.

3. The number of the beam neutron backgrounds.

   The neutron flux was estimated based on the Geant3 simulation, but that number has an uncertainty due to an inaccuracy of simulation for hadronic interactions. The z vertex distribution observed in the data agreed with this expected flux, but the $M_{\pi\pi}$ distribution claimed the neutron flux should be 1.5 times larger than expected, as shown in Fig. 8.14.

   I changed the neutron flux to be $\times 3$ or $\times 1/3$ of the Geant3 expectation, and studied the effect on the momentum spectrum measurement. The difference of the observed K_L momentum distribution due to the flux ambiguity was much smaller than statistical fluctuation, as show in Fig. 8.15.

4. Approximation of the p_t^2 PDF around the signal region

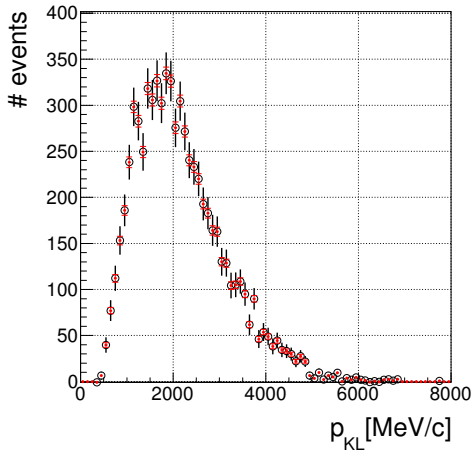

Figure 8.13: The K_L momentum distribution with the default condition and its statistic errors are shown in the black dots and error bars. The fluctuation by changing the neutron PDFs is shown in the red error bars.

(a) Z vertex distribution

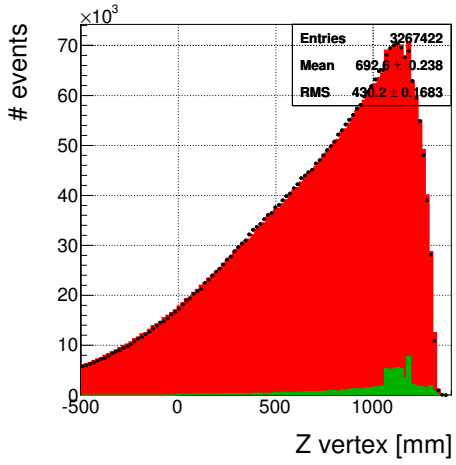

(b) $M_{\pi\pi}$ distribution

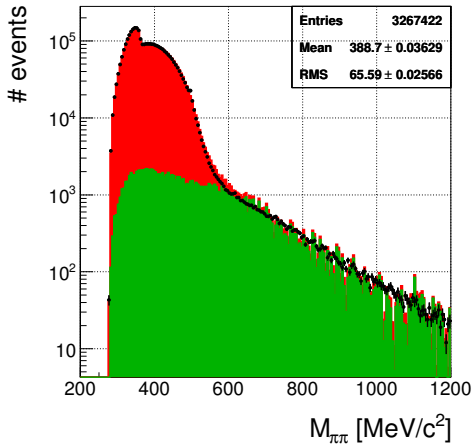

Figure 8.14: (a) Z position of the decay vertex. (b) The $M_{\pi\pi}$ distribution. The black dots show the data, while red and green histograms show the Monte Carlo expectation from K_L and beam neutrons. To reproduce the tail shape, the neutron events was scaled by factor 1.5 in (b).

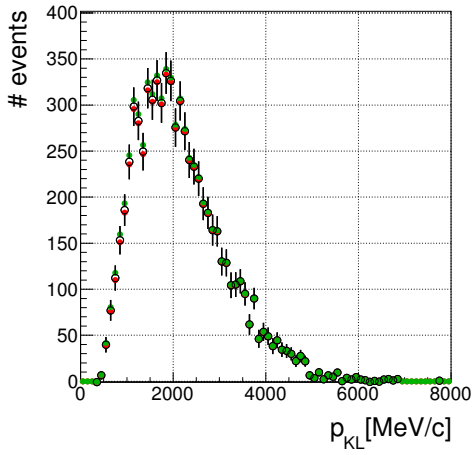

Figure 8.15: The K_L momentum distribution derived with scaling the expected number of neutron events by 0.333 (red), 1 (black), 3 (green).

To estimate the number of backgrounds events in the signal region, I approximated the PDF of the p_t^2 distribution near the signal region as a linear function as shown in the green line in Fig. 8.5. Its parameters were determined by fitting the function to the PDF in the range of $p_t^2 < 1500$ MeV$^2/c^2$. To study the uncertainty related to this approximation, I changed the fitting range from 800 to 2000 MeV$^2/c^2$, and also changed the function form to a parabolic function. The difference of the K_L momentum distribution due to these change was much smaller than the statistical errors, as shown in Fig. 8.16

$K_L \to \pi^+\pi^-\pi^0$ analysis

1. Other K_L decays and beam neutrons.

   After applying all the selection cuts, the number of events from the K_L decays other than the $K_L \to \pi^+\pi^-\pi^0$ decays was estimated to be 1.28 by using the Monte Carlo simulation. Because this number was $\sim$ 6000 times smaller than that from the $K_L \to \pi^+\pi^-\pi^0$ decays, its contribution to the measurement result was negligible.

   The number of events from the beam neutrons after applying all the selection cuts was estimated as 0 with the Monte Carlo. The Monte Carlo statistics, however, was insufficient, as small as 3 % of the data. To enhance the neutron events, I removed the cut on the invariant mass of four particles ($M_{\pi\pi\gamma\gamma}$ cut) and the k_{+-0} cut. Although it made neutron events 10 times larger, the invariant mass cut for two photons ($M_{\gamma\gamma}$ cut) rejected all the events. (The $M_{\gamma\gamma}$ distribution from neutrons without the k_{+-0} and $M_{\pi\pi\gamma\gamma}$ cuts were already shown in

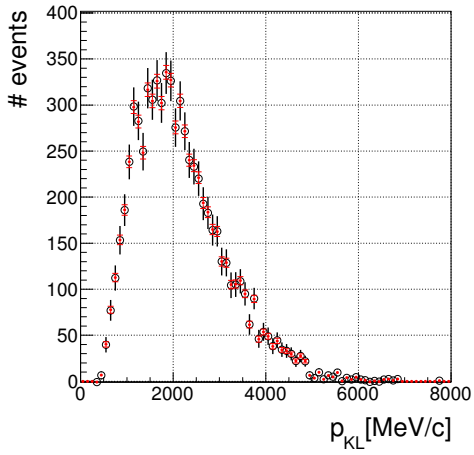

Figure 8.16: The K_L momentum distribution with the default condition and its statistic errors are shown in the black dots and error bars. The fluctuation by changing the method of approximation of the PDF around the signal region is shown in the red error bars.

Fig. 8.7(a)). I therefore decided that the neutron contribution to the measurement was negligible.

2. Mis-reconstructed $K_L \to \pi^+\pi^-\pi^0$ decays.

   There were events where the $M_{\gamma\gamma}$ was less than 100 MeV/c^2 in both the data and the Monte Carlo simulation as shown in Fig. 8.17(a). From the Monte Carlo study, I found that in such events one of the two photons did not hit the calorimeter but the hadronic shower from the pion in the calorimeter mimicked two clusters. Because the hadronic interactions are involved, the number of such events was not consistent between the data and the Monte Carlo.

   To estimate the number of such events contaminating the signal region, I fitted an exponential function to the data in the range of $60 < M_{\gamma\gamma} < 100$ MeV/c^2, and extrapolated the function to the signal region, as shown in the black line in Fig. 8.17(a). The expectation was 126 events.

   To study the effect of these contamination on the measurement, I subtracted 126 events from the observed K_L momentum distribution. The momentum distribution of 126 events was assumed to be the same as that of the events in $60 < M_{\gamma\gamma} < 100$ MeV/c^2, which is shown in Fig. 8.17(b). The 126 events were generated randomly according to this distribution and were subtracted. I tested 200 patterns of the random generation. The change of the K_L momentum distribution due to this subtraction was smaller than the statistical errors, as shown in Fig. 8.18.

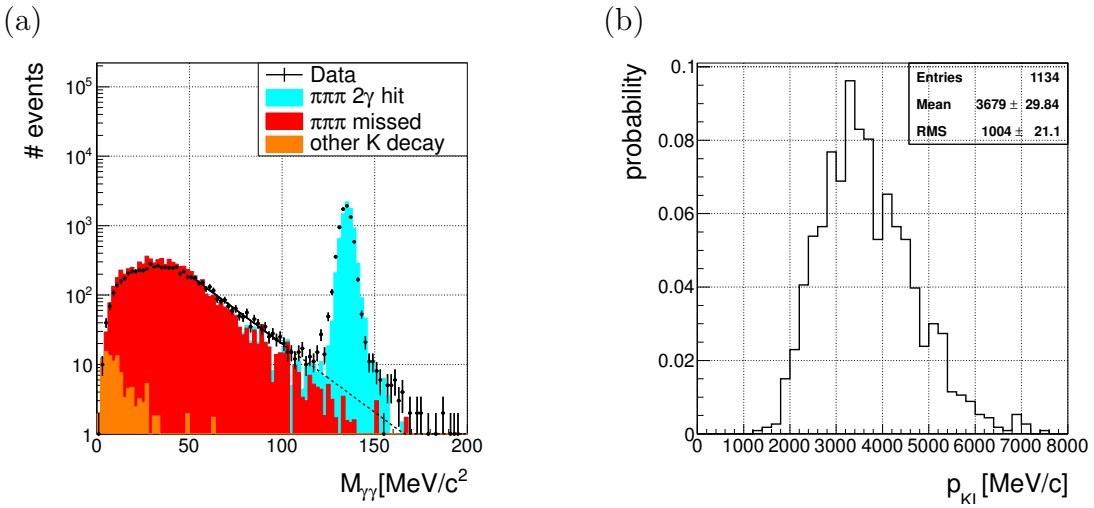

Figure 8.17: (a)The $M_{\gamma\gamma}$ from the $K_L \to \pi^+\pi^-\pi^0$ decay. The black dots show the data. The cyan and red histograms show the Monte Carlo expectation from the $K_L \to \pi^+\pi^-\pi^0$ decays. I required that both of the two photons from π^0 hit the CsI calorimeter for the cyan histogram, while I required for the red histogram that at least one photon did not hit. The orange histogram shows the events from the other K_L decays. (b) Reconstructed momentum distribution of events with $60 < M_{\gamma\gamma} < 100$ MeV/c^2.

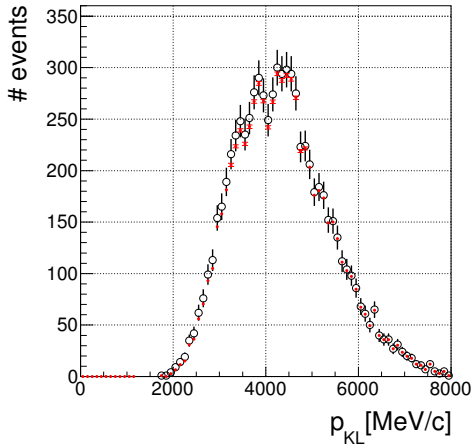

Figure 8.18: The K_L momentum distribution with and without subtracting the contribution from the mis-reconstructed $K_L \to \pi^+\pi^-\pi^0$ events. The distribution without the subtraction and its statistical errors are shown in the black circles and error bars. The red dots show the distirbution with the subtraction, and their error bars show the fluctuation of the 200 patterns of the random generation.

8.4.2 Uncertainties due to Resolution for K_L Momentum

The resolution of K_L momentum, σ_{pK}, was determined by the momentum resolution of the spectrometer, σ_p/p, and the energy and position resolutions of the CsI calorimeter, σ_E/E and σ_X. Although these resolutions were estimated in Chapter 4 or measured in Chapter 7, finite errors were assigned to the evaluation as described in Eq. (4.35), Eq. (7.3), Eq. (7.8), and Eq. (7.9). These errors gave an ambiguity to the σ_{pK}. To study the relation of the σ_{pK} to the σ_p/p, σ_E/E, and σ_X, I did a toy Monte Carlo simulation. In the simulation, the Monte Carlo true value of the momentum of the pion from the $K_L \to \pi^+\pi^-$ decay or $K_L \to \pi^+\pi^-\pi^0$ decay was smeared in two patterns: smeared with σ_p/p, or with σ_p/p plus its error. Similarly, the photon energy in $K_L \to \pi^+\pi^-\pi^0$ decay was smeared by σ_E/E or by σ_E/E plus its error, and the photon hit position was smeared by σ_X or by σ_X plus its error. The K_L momentum was calculated using those smeared values. The difference of the σ_{pK} due to adding the errors is shown in Fig. 8.19. I then derived the migration matrix by additionally smearing the reconstructed K_L momentum according to this σ_{pk} difference. The K_L momentum distribution unfolded with these migration matrix is shown in Fig. 8.20. The difference is smaller than the statistical fluctuation.

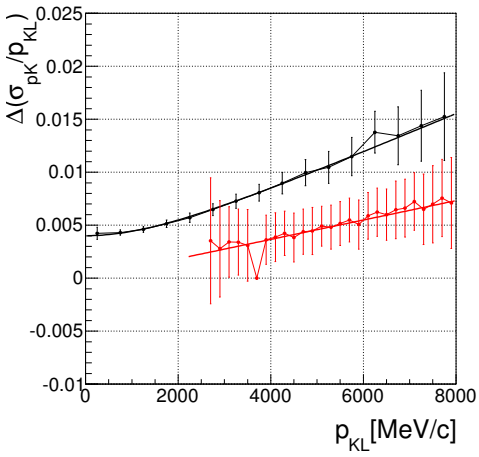

Figure 8.19: Change in K_L momentum resolution due to the worsening of the spectrometer and calorimeter resolutions by 1σ. The black and red show the $K_L \to \pi^+\pi^-$ decay and the $K_L \to \pi^+\pi^-\pi^0$ decay, respectively.

8.4.3 Uncertainties due to Cut Effectiveness

The difference of the effectiveness of the kinematic cuts between the data and the Monte Carlo expectation is one of the uncertainties of the observation probability.

- The $K_L \to \pi^+\pi^-$ analysis

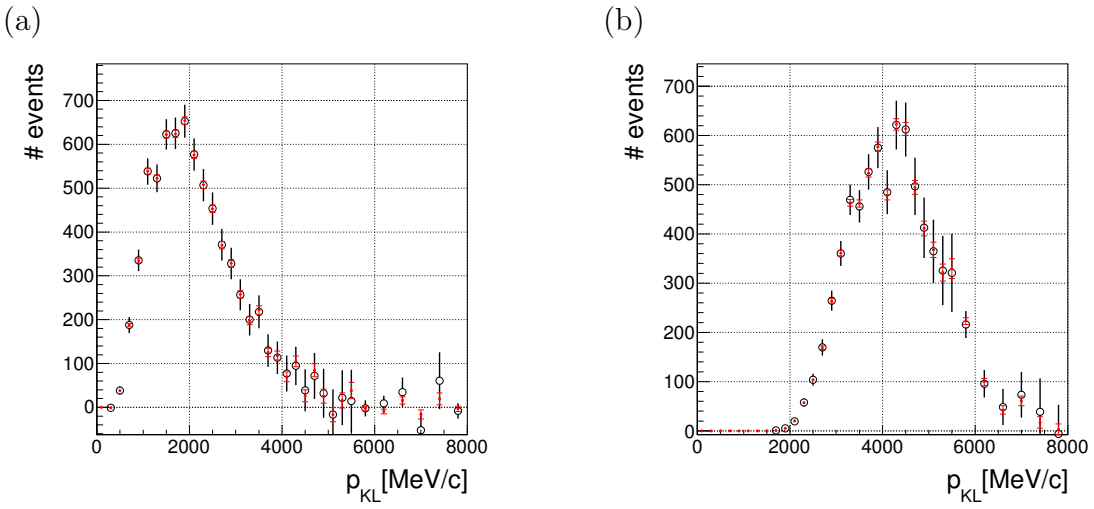

Figure 8.20: The red dots show the unfolded K_L momentum distribution using the migration matrix with additionally smearing by the σ_{pK} uncertainty. Their error bars show the fluctuation by changing the smearing pattern. The black circles show the distribution without smearing, and their error bars show the statistic errors. (a)The $K_L \to \pi^+\pi^-$ decays. (b)The $K_L \to \pi^+\pi^-\pi^0$ decays.

In the $K_L \to \pi^+\pi^-$ analysis, two kinematic selection cuts were applied as described in Section 8.2.1, that is, the invariant mass cut ($M_{\pi\pi}$ cut) and the square of transverse momentum cut (p_t^2 cut) of the two charged particles.

I changed each cut value to be $\times 2$ or $\times 1/2$ of the default value. The reconstructed K_L momentum distribution and the observation probability with the different p_t^2 cut values are shown in Fig. 8.21(a) and (b). Although there are large changes in these plots, the K_L momentum distribution divided by the observation probability changed within the statistical errors as shown in the Fig. 8.22.

- The $K_L \to \pi^+\pi^-\pi^0$ analysis

  In the $K_L \to \pi^+\pi^-\pi^0$ analysis, six kinematic conditions were applied as enumerated in Section 8.2.2 "Event selection".

  The uncertainties of the first condition (the number of clusters) and the second condition (track association) mainly come from the pion showers in the CsI calorimeter, because they were made by hadronic interactions which were difficult to reproduce in the Monte Carlo. To study the pion interaction in the CsI calorimeter, I used the $K_L \to \pi e\nu$ decays. I collected events where two charged tracks hit the CsI calorimeter and one of the tracks was identified as electrons by using the selection criteria introduced in Chapter 5. Because electrons dominantly came from the $K_L \to \pi e\nu$ decays, the other track was identified as pions. By using these pion samples, the probability that a pion makes two clusters

(a) (b)

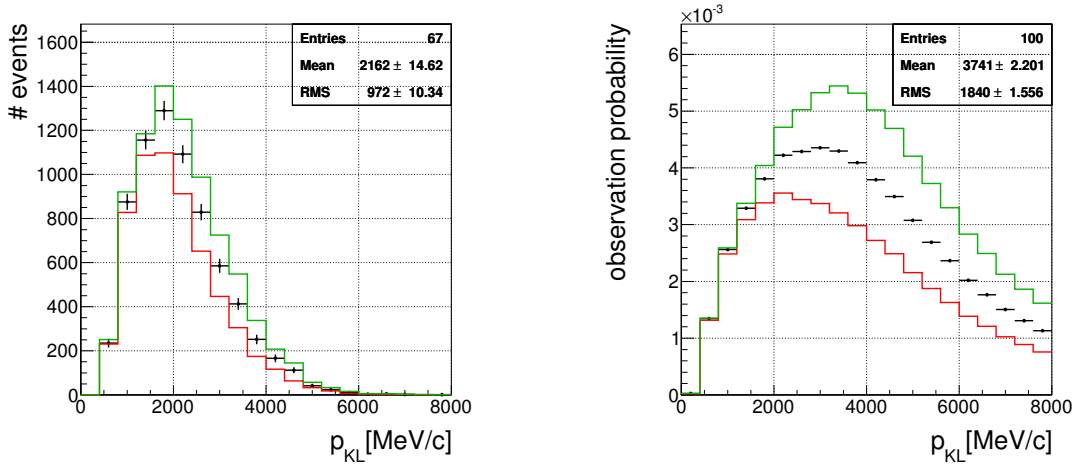

Figure 8.21: (a) The K_L momentum distributions and (b) the observation probability, with the different p_t^2 cut values. The black histgram shows the distribution with the default cut value ($p_t^2 < 50$ MeV$^2/c^2$) and its statistic error, while the red and green histograms show the distribution with $p_t^2 < 25$ MeV$^2/c^2$ and < 100 MeV$^2/c^2$, respectively.

(a) Changing p_t^2 cut value. (b) Changing $M_{\pi\pi}$ cut value.

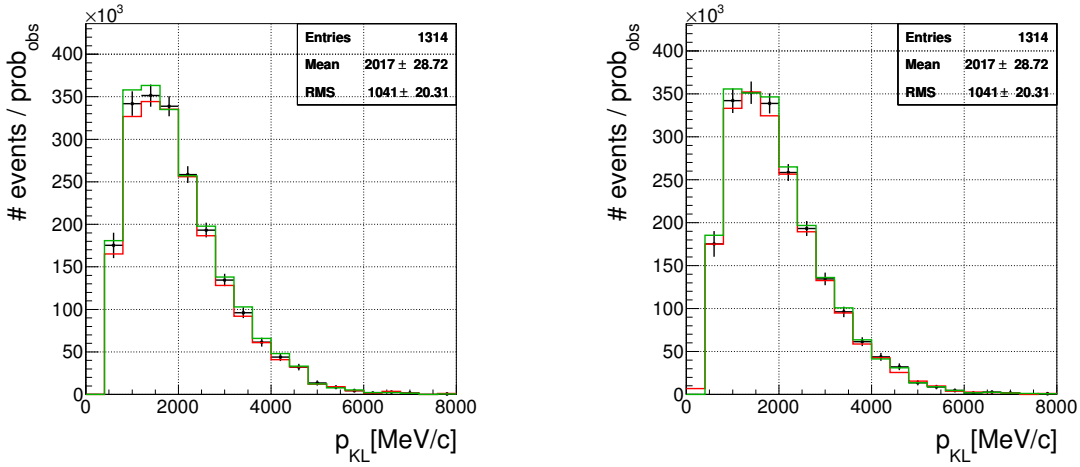

Figure 8.22: The K_L momentum distributions divided by the observation probability, with the different p_t^2 cut values (a) and with the different $M_{\pi\pi}$ cut value (b). The black histgram shows the distribution with the default cut value ($p_t^2 < 50$ MeV$^2/c^2$ or $-M_{\pi\pi} - M_{K_L}| < 30MeV/c^2$). The red and green histograms show the distribution with $\times 1/2$ and $\times 2$ of the default cut values.

whose energy are larger than 50 MeV, and the distance between the two clusters is greater than 100 mm, was estimated as the function of the pion momentum, as shown in Fig. 8.23(a). The probability that the pion tracks associated with a single cluster was also estimated as shown in Fig. 8.23(b). The ratio of these probabilities of the data to those of the simulation was defined as a weight of the pion track. I then calculated the observation probability for the $K_L \to \pi^+\pi^-\pi^0$ decay again, with assigning the weight to each of the two pion tracks and counting the event as the multiplication of those two weights. The observation probability was changed with the weight as shown in Fig. 8.24. Although the absolute scale of the probability was changed, the momentum spectrum did not change.

(a) Condition for the number of cluster. (b) Condition for the track association.

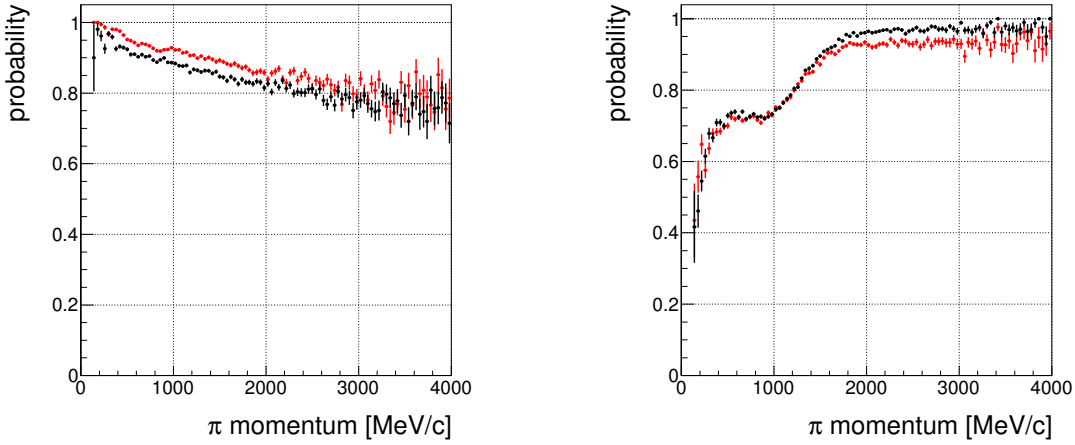

Figure 8.23: Probability that a pion satisfies the first condition (a) and the second condition (b) of the $K_L \to \pi^+\pi^-\pi^0$ kinematic cuts, as a function of the pion momentum. The black dots show the data, and the red dots shows the Monte Carlo simulaiton.

The third conditions (CsI fiducial region) was related to an electromagnetic process and the uncertainty from this condition was negligible compared to the first and the second conditions.

To estimate uncertainties of $M_{\gamma\gamma}$, k_{+-0}, and $M_{\pi\pi\gamma\gamma}$ cuts, the number of events were compared before and after applying the cuts. The data set was divided into 5 K_L momentum sections, and the comparison was taken for each section. For the $M_{\gamma\gamma}$ cut, there were contributions from background events from the misreconstructed $K_L \to \pi^+\pi^-\pi^0$ decays. The number of such backgrounds were estimated by assuming that those events distributed exponentially, as shown in Fig. 8.25. The cut efficiency was calculated as

$$\frac{N_{obs}^{\text{center}} - N_{BG}^{\text{center}}}{N_{obs}^{\text{wide}} - N_{BG}^{\text{wide}}}, \tag{8.9}$$

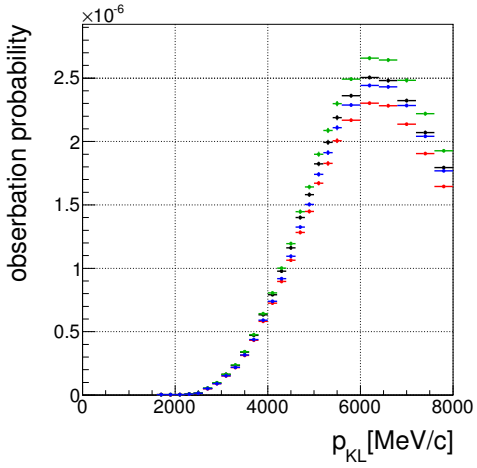

Figure 8.24: Observation probability for the $K_L \to \pi^+\pi^-\pi^0$ decay. In the black histogram, the uncertainty of the first and the second conditions of the kinematic cuts are not considered. In the colored histograms, the uncertainties of only the first (red), only the second (green) or both conditions (blue) were considered.

where N_{obs} and N_{BG} represent the number of observed events and the estimation of the background events, respectively. The superscript "center" means the numbers in the range of $|M_{\gamma\gamma} - M_{\pi^0}(= 134.9766\text{MeV}/c^2)| < 25$ MeV/c^2, while "wide" means in the range of $70 < M_{\gamma\gamma} < 200$ MeV/c^2. For the k_{+-0} cut and the $M_{\pi\pi\gamma\gamma}$ cut, the cut efficiencies were calculated as

$$\frac{(\text{the number of observed events after applying cut})}{(\text{the number of observed events before applying cut})}. \tag{8.10}$$

Figure 8.26 shows the efficiencies of the $M_{\gamma\gamma}$, k_{+-0} and $M_{\pi\pi\gamma\gamma}$ cuts in each momentum region. The difference of the efficiency between the data and the Monte Carlo was less than 2% for any cut and for any momentum region.

8.4.4 Uncertainties in Total

The K_L momentum spectrum was derived separately with including each uncertainty source described above. The fluctuation of the derived spectrum were then quadratically summed, and adopted as a systematic uncertainty of the spectrum as shown in Fig. 8.27(a). The ratio of the systematic uncertainty to the statistic error is shown in Fig. 8.27(b). The systematic uncertainties are comparable or smaller than the statistic errors, except for $p < 500$ MeV/c region. Table 8.3 summarizes the contribution from each uncertainty source at the K_L momentum = 1.7 GeV/c and 5.1 GeV/c.

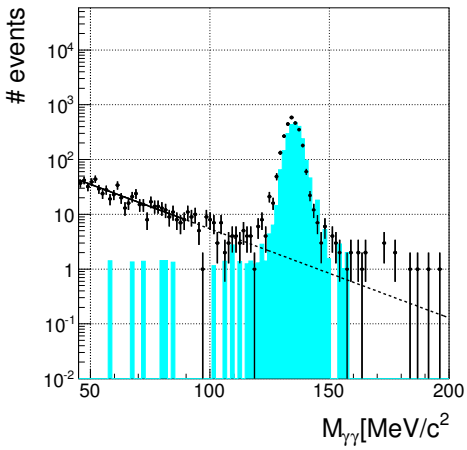

Figure 8.25: An example of an estimation of cut efficiency for the $M_{\gamma\gamma}$ cut. The dots and histogram show the $M_{\gamma\gamma}$ distribution in the data and the simulation where the K_L momentum is in the range of $4 \sim 5$ GeV/c. The data in $45 < M_{\gamma\gamma} < 90\mathrm{MeV}/c^2$ was fitted with an exponential function as shown in the solid line, and the function was extrapolated as shown in the dashed line, to estimate the number of background events in the signal region.

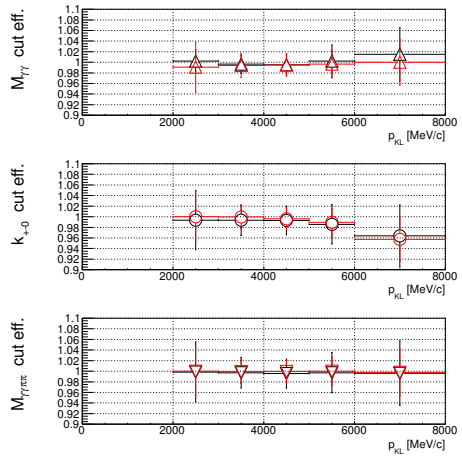

Figure 8.26: Cut efficiencies for $M_{\gamma\gamma}$ cut (top), k_{+-0} cut (middle), and $M_{\pi\pi\gamma\gamma}$ cut (bottom). The black markers show the data, while the red markers show the Monte Carlo expectation.

Table 8.3: Uncertainties of the K_L momentum spectrum at p_{K_L} = 1.7 GeV/c and 5.1 GeV/c, where the p_{K_L} represent K momentum. The spectrum heights at those momenta are also shown in the last row.

uncertainty source		at p_{K_L} = 1.7 GeV/c	at p_{K_L} = 5.1 GeV/c
$K_L \to \pi^+\pi^-$	background estimation	0.007	0.0007
	resolution for p_{K_L}	0.015	0.0014
	cut efficiency	0.044	0.0010
$K_L \to \pi^+\pi^-\pi^0$	background estimation	0.005	0.0017
	resolution for p_{K_L}	0.012	0.0015
	cut efficiency	0.009	0.0003
total of sys. err.		0.050	0.0031
stat. err.		0.053	0.0052
spectrum height		0.907	0.0293

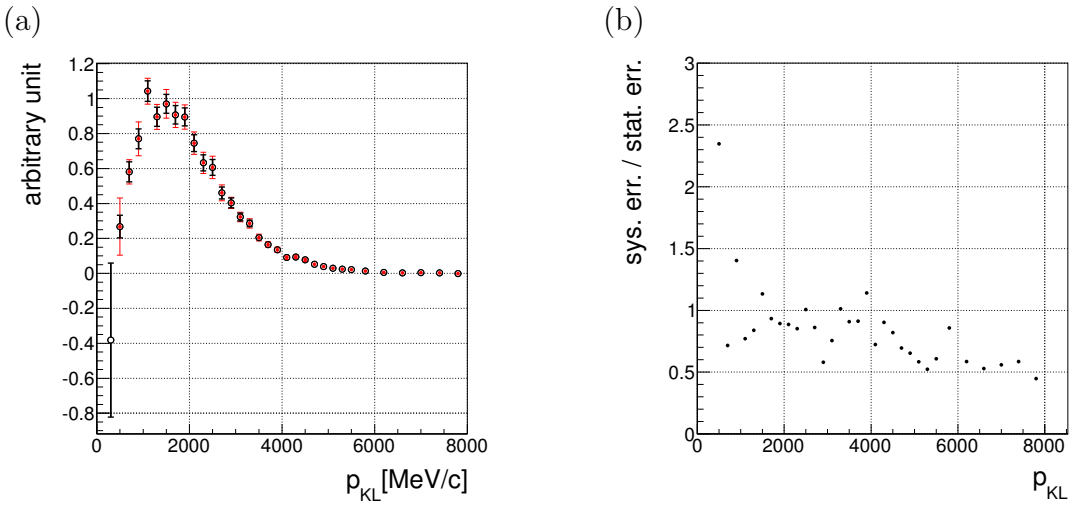

Figure 8.27: (a) TheK_L momentum spectrum with statistical errors (black error bars) and with statistic and systematic errors (red error bars). (b) The ratio of the systematic error to the statistical errors.

Chapter 9

Discussion

In this chapter, I will discuss the impact of my studies on the KOTO physics run.

9.1 Shower Shape Study

As described In Chapter 6, there were inconsistencies between the data and the Monte Carlo in the distributions of the shape χ^2, the number of the crystals in the cluster, and the cluster RMS. I modified the bremsstrahlung model used in the Geant4 simulaiton from the default G4SeltzerBergerModel to the G4eBremsstrahlungModel, to improve the Data – Monte Carlo consistency. In this section, I will discuss how the inconsistencies influence the signal efficiency of the shower shape cuts for the KOTO physics run, and also discuss the effect of the Monte Carlo modification. In this study, I assume that the responses of the calorimeter to photons and electrons are similar.

9.1.1 Cluster RMS and the Number of Crystals

First I studied the efficiencies of the cuts applied to the cluster RMS and the number of crystals. The electron data used in Chapter 6 was also used in this study. Because these cut variables depend on the energy of the incident electrons as shown in Figure 9.1, I divided the data into 100 MeV/c regions in the electron energy, and studied each region. The cut efficiency with a given cut value was estimated by integrating and normalizing the distributions of the cut variables, as

$$P^{cut}_{RMS}(x) = \frac{\int_0^x f_{RMS}(x')dx'}{\int_0^\infty f_{RMS}(x')dx'} \tag{9.1}$$

for the cluster RMS, and

$$P^{cut}_{nCsI}(x) = \frac{\int_0^x f_{nCsI}(x')dx'}{\int_0^\infty f_{nCsI}(x')dx'}, \tag{9.2}$$

for the number of crystals, where the x is the cut value and the f_{RMS} and f_{nCsI} represent the distributions of the cluster RMS and the number of crystals. Here, the events with larger values than the cut values are rejected. The $P^{cut}_{RMS}(x)$ and $P^{cut}_{nCsI}(x)$ for the events with $600 < E_e < 700$ MeV/c^2, where the E_e represents the electron energy, are shown for the data and the Monte Carlo simulations in Fig. 9.2(a) and (b). As shown in Fig. 9.3(a, b), the difference between the data and the default Monte Carlo was at most 12 %, while difference between the data and the modified Monte Carlo was 6 %. The differences in the different energy regions are shown in Fig. 9.4. In all the energy regions, the differences of the modified Monte Carlo from the data were about a half of those of the default Monte Carlo.

(a) Cluster RMS (b) The number of crystals in a cluster

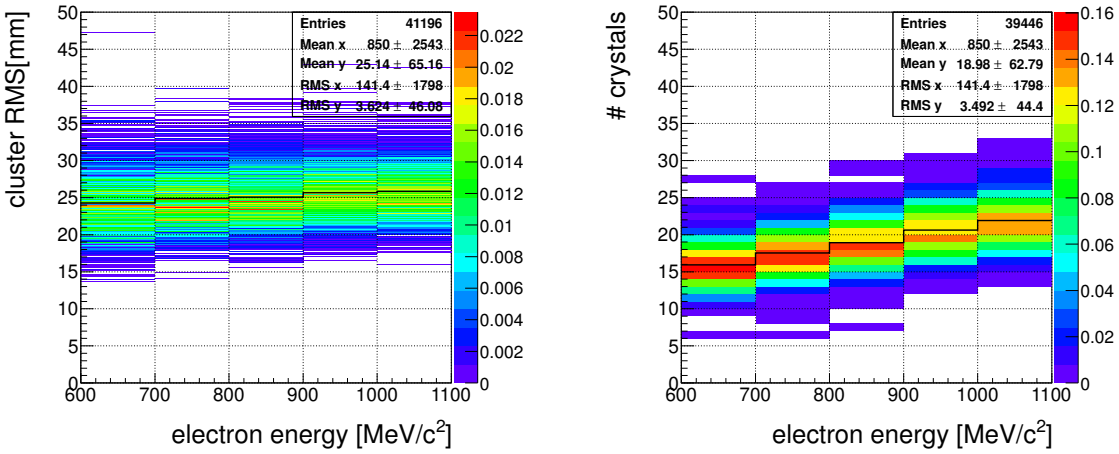

Figure 9.1: Cluster RMS (a) and the number of crystals (b) as a function of the incident electron energy. The histogram shows the number of events observed in the data, which are scaled so that the integral in each x bin is equal to 1. The black line in each x bin shows the mean value in the bin.

9.1.2 Shape χ^2

To study the shape χ^2, the electron data was selected by the same selection cut set used in Chapter 6 except that the shape χ^2 cut was removed. Because no dependence on the incident electron energy was observed in the shape χ^2 distribution as shown in Fig. 9.5, I did not divide the data by the energy. The amount of the background contamination was estimated from the events with $0.5 < E_{CsI}/E^{vis}_{spec} < 0.7$ and subtracted as shown in Fig. 9.6.

(a) Cluster RMS

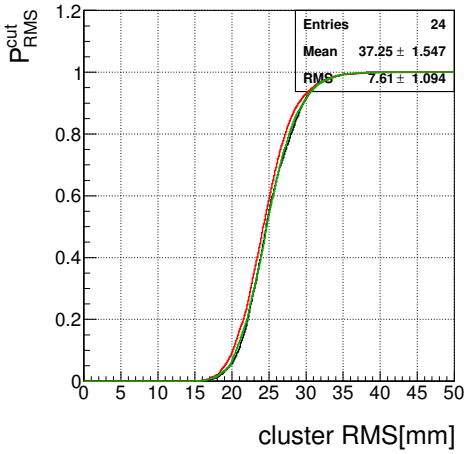

(b) The number of crystals in a cluster

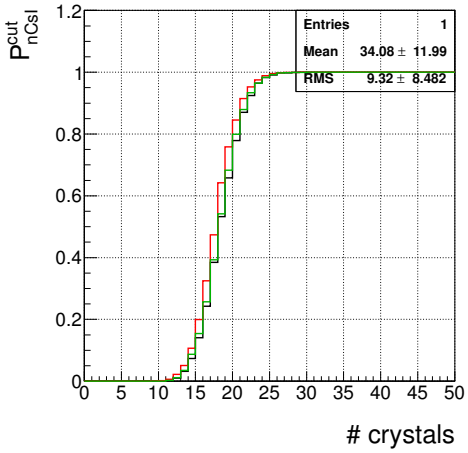

Figure 9.2: Cut efficiency of the cluster RMS (a) and the number of crystals (b). The x axis shows the cut values. The black, red, and green lines are derived from the data, the default Monte Carlo, and the modified Monte Carlo simulation, respectively.

(a)

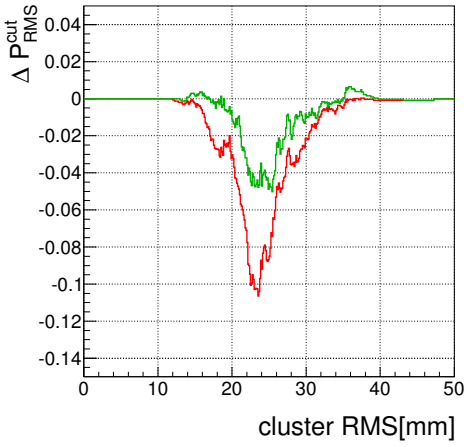

(b)

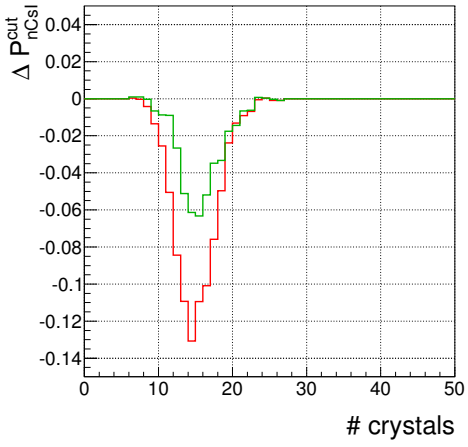

Figure 9.3: Difference of the cut efficiency between the data and the Monte Carlo simulation for the cluster RMS (a) and the number of crystals (b). The x axis shows the cut value. The red (green) line shows the difference of the data from the default (modified) Monte Carlo.

(a) Cluster RMS (b) The number of crystals in a cluster

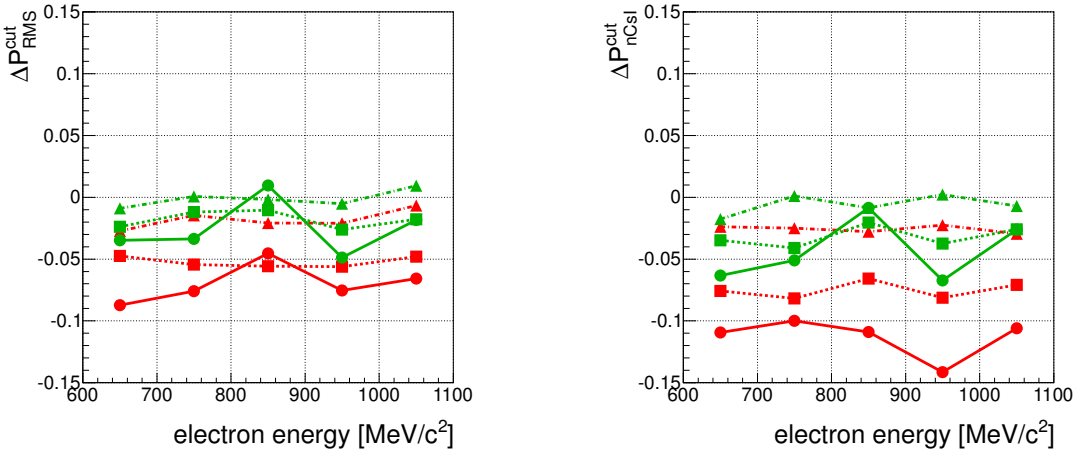

Figure 9.4: Difference of the cut efficiencies between the data and the Monte Carlo simulation for the cluster RMS (a) and the number of crystals (b), in each energy region. The red (green) graphs show the differences between the data and the default (modified) Monte Carlo. The dots, squares, triangles show the differences of the efficiency at the cut values where the effciencies observed in the data are 50, 70, and 90 %, respectively.

The cut efficiency for the shape χ^2 was calculated from the shape χ^2 distribution f_{shape} as

$$P^{cut}_{shape}(x) = \frac{\int_0^x f_{shape}(x')dx'}{\int_0^{10} f_{shape}(x')dx'}, \tag{9.3}$$

where I assumed that the events with large shape χ^2 are dominantly from the backgrounds, and restricted the integral range in $0 <$ shape $\chi^2 < 10$. The cut efficiency in the data and the Monte Carlo, and those differences are shown in Fig. 9.7 and Fig. 9.8. The differences from the data are at most 4 % and 2% in the default and the modified Monte Carlo, respectively.

9.2 Resolutions of the CsI Calorimeter

As described in Section 1.3.2, all the kinematic information of the $K_L \to \pi^0\nu\bar{\nu}$ events and backgrounds are solely obtained from the CsI calorimeter. Therefore, the efficiency of kinematic selection cuts, which is described in Appendix A.1, depends on the energy and position resolution of the calorimeter. To study this dependence, I used a toy Monte Carlo simulation in which all particles hitting any detector were stopped on its surface, without simulating the interaction with the detector component. Energies and positions of photons stopping at the CsI calorimeter was then smeared by a given

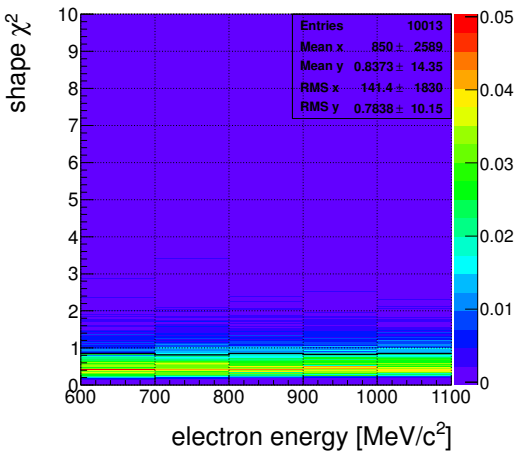

Figure 9.5: Energy dependence of the shape χ^2.

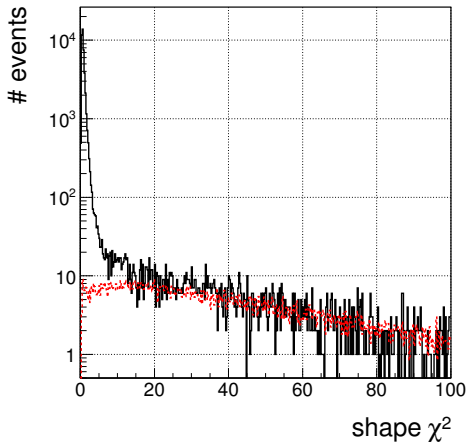

Figure 9.6: Shape χ^2 distribution of the events with $0.9 < E_{CsI}/E^{vis}_{spec} < 1.1$ (black histogram) and $0.5 < E_{CsI}/E^{vis}_{spec} < 0.7$ (red histogram). The red histogram is scaled so that the integral from 50 to 100 is equal to that of the black histogram.

(a)

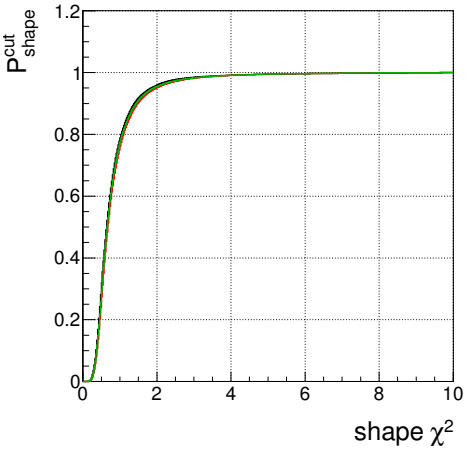

Figure 9.7: (a) Cut efficiency of the shape χ^2. The black, red, green histograms show the data, the default Monte Carlo, and the modified Monte Carlo, respectively.

(b)

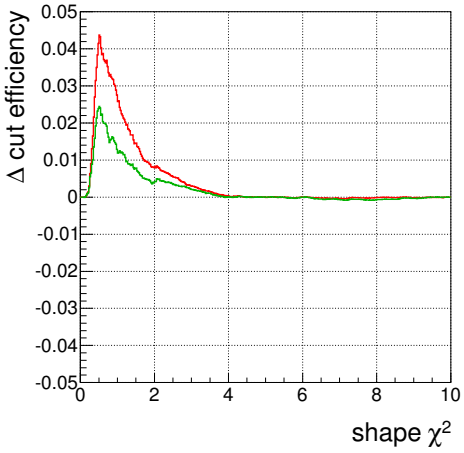

Figure 9.8: (b) Difference of the cut efficiency of the shape χ^2 between the data and the Monte Carlo. The red (green) histogram shows the difference of the data from the default (modified) Monte Carlo.

resolution. The particles stopping at the veto detectors were ignored to study the influences of the CsI calorimeter resolution alone.

In this section, I will first describe how the CsI resolutions affect the π^0 reconstruction in the $K_L \to \pi^0\nu\bar{\nu}$ decay. I will then show the influence of the resolution measurement described in Chapter 7 on the KOTO physics run.

In this study, the standard coordinate system of the KOTO experiment is used. The directions of the x, y, and z axis in the system are the same as the system used in this thesis. The origin is located on the upstream surface of the "Front Barrel" which is the most upstream veto counter in the KOTO detector. In this coordinate system, the upstream surface of the CsI Calorimeter is located at z = 6.148 m.

9.2.1 π^0 Kinematics for Signal Events

Let us study the π^0 reconstruction in the $K_L \to \pi^0\nu\bar{\nu}$ decay to understand how the CsI calorimeter performance influences the kinematic variables. Even if the CsI calorimeter has infinitely accurate resolutions for photon energy and incident position, the uncertainties of the π^0 kinematics arise from the size of the beam profile, because the x and y positions of the π^0 vertex are unknown in the reconstruction process, and we assume that the π^0 vertex is located on the beam axis. The differences of the reconstructed π^0 Pt and the z vertex from their Monte Carlo true values are shown in Fig. 9.9 as a function of the z vertex, where no smearing effects due to the energy and position resolution of the calorimeter are included. To simulate the calorimeter resolution effect, I defined an energy resolution function as

$$\frac{\sigma_E}{E}(E) = a_E \oplus \frac{b_E}{\sqrt{E[GeV]}}, \tag{9.4}$$

and a resolution function for the incident position as

$$\sigma_X(E) = a_X \oplus \frac{b_X}{\sqrt{E[GeV]}}, \tag{9.5}$$

where E represents the photon energy. The energies and positions of the photons hitting the CsI calorimeter were then smeared with these resolution functions. The parameters a_E and b_E (or a_X and b_X) were changed from 0 to 9 % (0 to 9 mm). When one of the parameters were changed, the other parameters were set to 0. Fluctuations of the Pt and the z position due to the smearing are shown in Fig. 9.10. The Pt resolution is dominated by the uncertainty due to the finite beam size, while the z position resolution strongly depends on the energy resolution of the CsI calorimeter. The z vertex dependence of the π^0 Pt resolution and the z vertex resolution are shown in Fig. 9.11, where $b_E = 2\%$ and $a_E = a_X = b_X = 0$. The z position resolution becomes wider for upstream decays.

(a) Pt (b) Z position of decay vertex

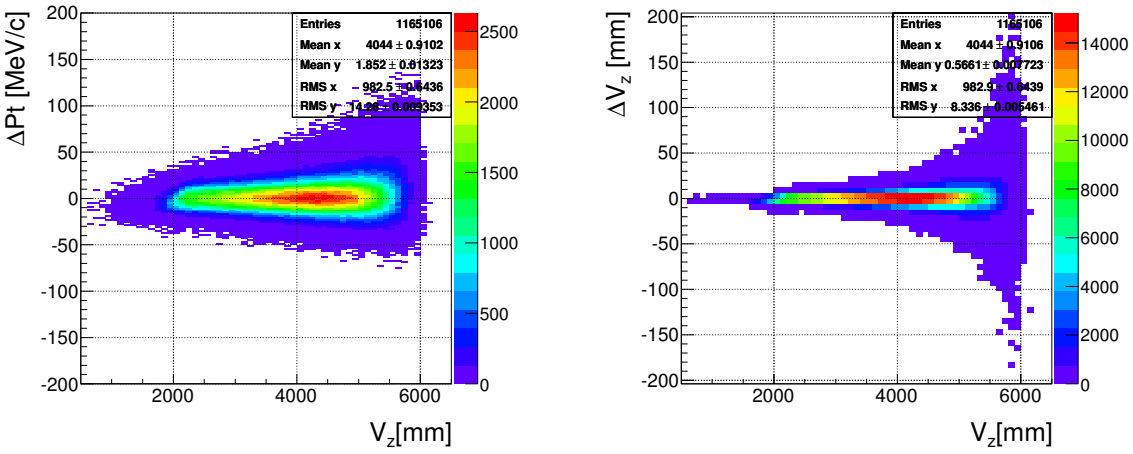

Figure 9.9: Differences of the reconstructed π^0 Pt (a) and the z position of the decay vertex (b) from their Monte Carlo true values as a function of decay z position. Here, the photon energy and incident position are not smeared. The differences come from the uncertainty of x and y positions of the decay vertex due to the finite beam size.

(a) Pt (b) Z position of decay vertex

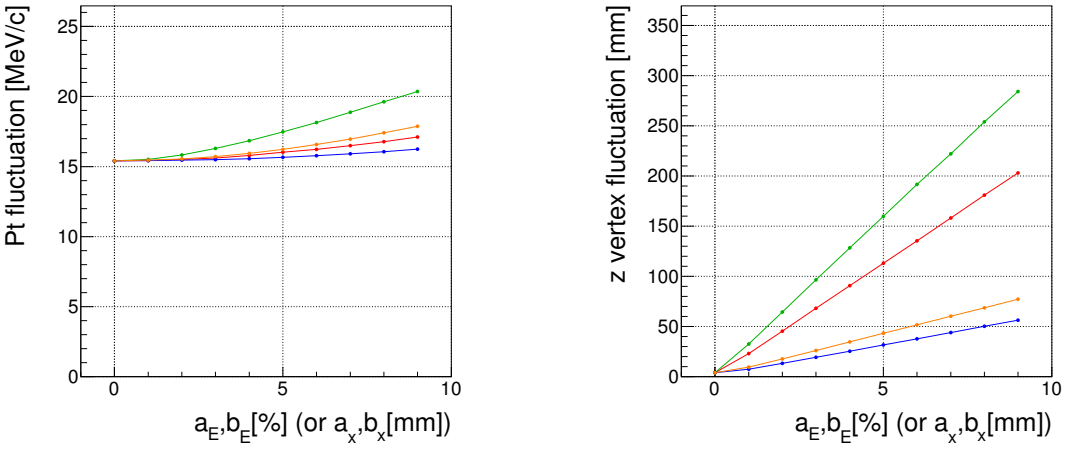

Figure 9.10: RMS of the differences of the reconstructed π^0 Pt (a) and the z vertex (b) from their Monte Carlo true values V.S. the parameters of the resolution functions. The dependence on a_E, b_E, a_X, and b_X are shown in red, green, blue, and orange lines, respectively.

(a) Pt (b) Z position of decay vertex

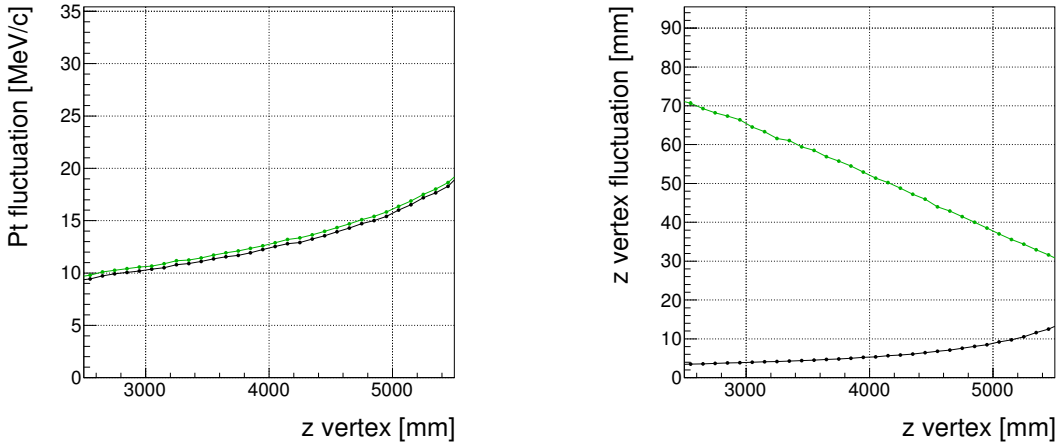

Figure 9.11: RMS of the differences of the reconstructed π^0 Pt (a) and the z vertex (b) from their Monte Carlo true values, as a function of z position of the vertex. The black line shows the fluctuation with no smearing, while the green line shows that with the smearing based on the energy and position resolution for the small crystals described in Eq. (9.6).

9.2.2 The Influence on the Physics RUN

The measurements in Chapter 7 determined the parameters as

$$a_E = (0.66 \pm 0.52)\%, \quad (9.6)$$
$$b_E = (1.81 \pm 0.04)\%, \quad (9.7)$$
$$a_X = (1.99 \pm 0.23)\text{mm}, \quad (9.8)$$
$$b_X = (3.95 \pm 0.35)\text{mm} \quad (9.9)$$

for the small crystals, and

$$a_E = (1.71 \pm 0.17)\%, \quad (9.10)$$
$$b_E = (1.31 \pm 0.10)\%, \quad (9.11)$$
$$a_X = (6.17 \pm 0.18)\text{mm}, \quad (9.12)$$
$$b_X = (4.01 \pm 0.40)\text{mm} \quad (9.13)$$

for the large crystals. The a_X and b_X were calculated as

$$a_X = \sqrt{\frac{(p_1^x)^2 + (p_1^y)^2}{2}},\ b_X = \sqrt{\frac{(p_2^x)^2 + (p_2^y)^2}{2}}, \quad (9.14)$$

where $p_1^{x(y)}$ and $p_2^{x(y)}$ represent parameters p_1 and p_2 of x (y) position resolution in Eq. (7.8) and Eq. (7.9). The parameters expected from the Monte Carlo simulation

Table 9.1: Parameters of the resolution function. The measured values, the values expected from the Monte Carlo simulation, the KOTO design values are shown.

	crystal area	a_E [%]	b_E [%]	a_X [mm]	b_X [mm]
measured values	(small)	0.66 ± 0.52	1.81 ± 0.04	1.99 ± 0.23	3.95 ± 0.35
	(large)	1.71 ± 0.17	1.31 ± 0.10	6.17 ± 0.18	4.01 ± 0.40
MC expectation	(small)	0.86	1.72	2.35	3.56
	(large)	0.00	1.56	5.27	3.90
KOTO design values	(small & large)	1	2	0	5

are shown in Table 9.1. The KOTO design values of the calorimeter performance are also shown in the table. In the preparation period of the KOTO experiment, we estimated the number of the signal and background events by assuming this design values.

In the following, I will study the changes of the background estimations due to the uncertainties of the measured parameters, and also due to the difference between the measured parameters and the Monte Carlo expected parameters or the KOTO design values.

Background expectation

Among the K_L backgrounds expected in the KOTO experiment, the kinematic cuts are important in particular for the "odd-pair" $K_L \to \pi^0\pi^0$ background and the $K_L \to \pi^+\pi^-\pi^0$ background. The odd-pair $K_L \to \pi^0\pi^0$ background is a kind of background events from the $K_L \to \pi^0\pi^0$ decay, where two photons from *different* π^0s hit the CsI calorimeter. The reconstructed decay vertex is incorrect in this background, and consequently the kinematics of the two photons are reconstructed incorrectly. The cut for the product of the photon energy and incident angle (E-θ cut), and the cut for the ratio of two photon energies (E ratio cut) strongly suppress this background. The $K_L \to \pi^+\pi^-\pi^0$ background is strongly suppressed by requiring the π^0 Pt to be > 130 MeV/c, because the momentum of the π^0 generated in this decay mode is kinematically limited to be less than 133 MeV/c. The number of the signal events, the odd-pair $K_L \to \pi^0\pi^0$ background events, and the $K_L \to \pi^+\pi^-\pi^0$ background events are estimated to be 2.71, 0.14, and 0.87 events[1], respectively, after applying all the KOTO standard kinematic cuts in a 12-month data taking with the designed beam power of the J-PARC ($= 2 \times 10^{14}$ protons on target / 3.3 sec). The details of these backgrounds and the kinematic cuts in the KOTO experiment are described in Appendix A.2.1. In the following, I will study dependences of the numbers of such background events on the energy and position resolutions of the CsI calorimeter.

[1]These values are estimated by using the toy simulation by weighting the inefficiencies of the veto counters. More accurate estimation is found in [5].

Table 9.2: The number of background events after applying all the kinematic cuts, with different resolution parameters. The number of each decay mode were simulated by generating 10^8 K_Ls which decay to only that decay mode. The veto detectors were not considered.

	measured values	MC expectation	KOTO design
odd-pair $K_L \to \pi^0\pi^0$	$(936.0 \pm 3.1) \times 10^2$	$(935.3 \pm 3.1) \times 10^2$	$(937.6 \pm 3.1) \times 10^2$
$K_L \to \pi^+\pi^-\pi^0$	2474 ± 50	2462 ± 50	2537 ± 50

- The odd-pair $K_L \to \pi^0\pi^0$ background.

  The odd-pair $K_L \to \pi^0\pi^0$ background is suppressed by the $E-\theta$ cut and E ratio cut as shown in Fig. A.2 in Appendix A.2.1. I changed the parameters of the energy and position resolution functions around the measured values, as

$$a_E \text{ (or } b_E) = \sqrt{(a_E^{meas} \text{ (or } b_E^{meas}))^2 + \frac{i}{|i|}(i \times 1\%)^2} \quad (9.15)$$

$$a_X \text{ (or } b_X) = \sqrt{(a_X^{meas} \text{ (or } b_X^{meas}))^2 + \frac{i}{|i|}(i \times 1[\text{mm}])^2}, \quad (9.16)$$

  where $i = -4, -3, ..., 5$ as long as the value inside the square root > 0. The $a_{E(X)}^{meas}$ and $b_{E(X)}^{meas}$ represent the measured values shown in Table 9.1. When one of the parameters was changed, the i for the other parameters were set to 0. The energies and positions of photons were smeared based on those resolutions in the toy simulation. The changes in the estimated number of the background events was $< 0.5\%$, as shown in Fig. 9.12(a). The kinematic cuts for the $K_L \to \pi^0\pi^0$ background do not strongly depend on the resolutions of the CsI calorimeter.

  The number of the "odd-pair" $K_L \to \pi^0\pi^0$ background events after applying all the kinematic cuts were estimated with different resolution parameter sets: the measured parameters, the parameters expected from the Monte Carlo, and the parameters of the KOTO design value. The estimations are shown in Table 9.2. The differences between them are within 0.1%.

- The $K_L \to \pi^+\pi^-\pi^0$ background.

  The $K_L \to \pi^+\pi^-\pi^0$ background is largely suppressed by requiring π^0 Pt > 130 MeV/c as shown in Fig. A.3 in Appendix A.2.1. By changing the parameters of the resolution functions as described in Eq. (9.15), the estimated number of this background events changes at most 10% as shown in Fig. 9.12(b). The errors of the measured parameters described in Eq. (9.6) are also shown in Fig. 9.12(b) as horizontal bars. The number of the $K_L \to \pi^+\pi^-\pi^0$ background events fluctuated by less than 1% within the errors.

(a) The odd-pair $K_L \to \pi^0\pi^0$ event

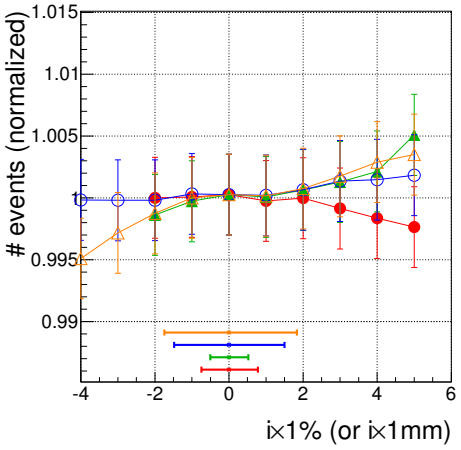

(b) The $K_L \to \pi^+\pi^-\pi^0$ event

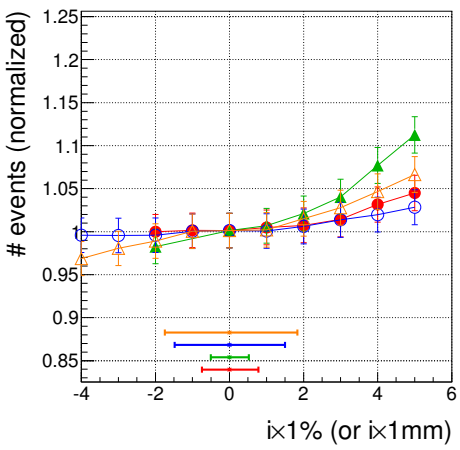

Figure 9.12: The number of the odd-pair $K_L \to \pi^0\pi^0$ background events (a) and the $K_L \to \pi^+\pi^-\pi^0$ background events estimated from the Monte Carlo simulation, by changing the parameters of the resolution functions. The x axis shows the "i" defined in Eq. (9.15). When one of the parameters was varied, the i for the other parameters were set to 0. The results with the varied a_E, b_E, a_X, and b_X are shown in red, green, blue, and orange points, respectively. The horizontal bars in the bottom of the plots represent the errors of the measured a_E, b_E, a_X, and b_X described in Eq. (9.6)

The number of the $K_L \to \pi^+\pi^-\pi^0$ background events after applying all the kinematic cuts were estimated with the measured parameter sets, the parameters expected from the Monte Carlo, and the KOTO design values. The result are shown in Table 9.2. The differences between them are within 3%.

As for the backgrounds from the beam neutrons, the resolution for the z position of the decay vertex influences the NCC-π^0 background estimation where the neutron interacts with the "NCC" detector located upstream of the decay region and produce a π^0, as described in Appendix A.2.2. Because we require the decay vertex to be 550 mm apart from the NCC downstream surface and the z resolution is much smaller, at most 100 mm as shown in Fig. 9.11, the influence of the CsI resolution on the NCC-π^0 background is estimated to be negligible.

In summary, the uncertainties of the energy and position resolutions measured in Chapter 7 are small enough that they do not change the background estimations. Even though the measured parameters have finite differences from those of the Monte Carlo expectation or the KOTO design values, the effect of such differences on the background estimations is negligible.

9.3 K_L Momentum Spectrum

The K_L momentum spectrum measured in Chapter 8 has almost the same shape with that obtained in the previous work, although there is a small difference of the shape in the momentum region > 4 GeV/c. (Hereafter these two spectrums are called "*new* spectrum" and "*previous* spectrum"). The uncertainty of the shape of the *new* spectrum is, however, much smaller than that of the *previous* spectrum, in particular in the high momentum region where the previous work had no sensitivity. To discuss the importance of this improvement of uncertainty, the number of the $K_L \to \pi^0\pi^0$ and the $K_L \to \pi^+\pi^-\pi^0$ background events were estimated with using the *new* and *previous* spectrums, and also using the spectrums modified by their 1σ deviations which are shown in dashed lines in Fig. 9.13. Each spectrum was normalized with its integral between 0 and 4 GeV/c. This integral range corresponds to the sensitive range of the K_L flux measurement conducted before.[2] In this estimation, I used the toy Monte Carlo simulation where any particle hitting any detector was stopped at its surface. The energies and hit positions of the photons hitting the CsI calorimeter were smeared with the energy resolution, σ_E, and position resolution, σ_X, which are approximated as

$$\sigma_E/E = 1\% \oplus \frac{2\%}{\sqrt{E[\mathrm{GeV}]}} \tag{9.17}$$

and

$$\sigma_X = \frac{5[\mathrm{mm}]}{\sqrt{E[\mathrm{GeV}]}}, \tag{9.18}$$

where E represents the photon energy. For each particle hitting the other detectors, the probability of not detecting the particle was calculated based on the KOTO veto inefficiency function [39], which depends on the momentum of the incident particle, detector type, and incident particle type. The event was weighted by the product of the veto inefficiencies of all particles.

9.3.1 The $K_L \to \pi^0\pi^0$ Background

Figure 9.14(a) shows the product of the decay probability, the geometrical acceptance, and the kinematic cut efficiency for the $K_L \to \pi^0\pi^0$ background events. Events with the K_L momentum > 3 GeV are suppressed with these effects. Such events are further suppressed by the veto detectors as shown in Fig. 9.14(b), although there remains some events with large veto inefficiencies in > 5 GeV region. In these events, extra photons tend to fly in the forward direction and hit the veto counter located on the beam axis which is called "Beam Hole Photon Veto (BHPV)". The inefficiency of

[2] This measurement was conducted simultaneously with the previous measurement for the K_L momentum spectrum.

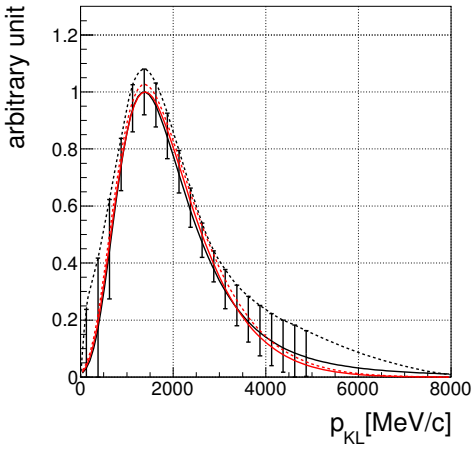

Figure 9.13: The K_L momentum spectrums used to study an influence of the spectrum shape on the background estimation. The black (red) solid line shows the *previous* (*new*) spectrum and the dashed line shows $+1\sigma$ deviation from it. For the momentum > 5 GeV/c, the *previous* spectrum does not have error data. I assumed the *previous* spectrum $+1\sigma$ deviation as the linear function in such region.

BHPV for photons are estimated as $\sim 10^{-3}$ which is relatively larger than those for other veto detectors (typically $10^{-5} \sim 10^{-6}$) because it is exposed to the beam core neutrons.

Table 9.3 summarizes the estimations of $K_L \to \pi^0\pi^0$ backgrounds by assuming the four spectrums: the *new* spectrum, the *previous* spectrum and the modified spectrums with their 1σ deviations. The estimated numbers between the *previous* spectrum and the "*previous* $+1\sigma$" spectrum, and between the *new* spectrum and the "*new* $+1\sigma$" spectrum, are consistent within their errors. The $K_L \to \pi^0\pi^0$ background events are not sensitive to the spectrum shape.

9.3.2 The $K_L \to \pi^+\pi^-\pi^0$ Background

For the $K_L \to \pi^+\pi^-\pi^0$ backgrounds, the probability to observe the high-momentum (> 4 GeV) K_L is larger than that for low-momentum (< 4 GeV) K_L before applying the kinematic cuts, as shown in Fig. 9.15. The high-momentum K_L events are, however, strongly suppressed with the Pt/Pz cut, which is the cut for the ratio of the transverse component to the z component of the reconstructed π^0 momentum. The details of this cut is described in Appendix A. The efficiency of the kinematic cuts is estimated as 0.51 by using the *previous* spectrum as shown in Table 9.3. If the "*previous* $+1\sigma$" spectrum is used, this value changes to 0.28. This 55% uncertainty for the cut efficiency arises from the uncertainty of the spectrum shape. The cut efficiencies estimated by using

(a) w/o Veto weight (b) w/ Veto weight

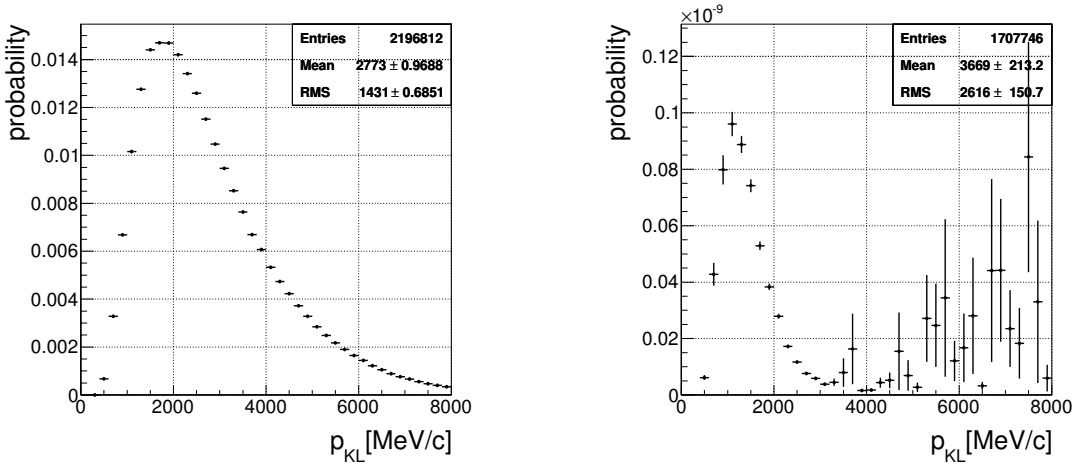

Figure 9.14: Product of the decay probability, the geometrical acceptance and the kinematic cut efficiency for the $K_L \to \pi^0\pi^0$ background events, without (a) and with (b) the weight of veto inefficiency.

Table 9.3: The number of the signal events, the $K_L \to \pi^0\pi^0$ background events, and the $K_L \to \pi^+\pi^-\pi^0$ background events estimated with different spectrum shapes by the toy Monte Carlo. The numbers in "loose kine. cuts" rows were estimated with applying the π^0 Pt cut and the Z-vertex cut, the E_γ cut and the calorimeter fiducial cut. The numbers in "all kine. cuts" rows were estimated with applying all the KOTO standard kinematic cuts.

		previous	previous $+1\sigma$	new	new $+1\sigma$
$K_L \to \pi^0\nu\bar{\nu}$	loose kine. cuts	4.93 ± 0.04	4.82 ± 0.04	4.88 ± 0.04	4.85 ± 0.04
$K_L \to \pi^0\nu\bar{\nu}$	all kine. cuts	2.75 ± 0.03	2.64 ± 0.03	2.73 ± 0.03	2.71 ± 0.03
$K_L \to \pi^0\pi^0$	loose kine. cuts	4.47 ± 0.23	4.41 ± 0.21	4.36 ± 0.22	4.30 ± 0.22
$K_L \to \pi^0\pi^0$	all kine. cuts	1.55 ± 0.03	1.53 ± 0.03	1.51 ± 0.02	1.49 ± 0.02
$K_L \to \pi^+\pi^-\pi^0$	loose kine. cuts	1.73 ± 0.52	2.93 ± 0.62	1.34 ± 0.50	1.39 ± 0.50
$K_L \to \pi^+\pi^-\pi^0$	all kine. cuts	0.89 ± 0.50	0.83 ± 0.46	0.88 ± 0.50	0.87 ± 0.49

the *new* spectrum and the "*new* $+1\sigma$" spectrum are 6.6 and 6.3, respectively. The difference is 4%; it is much smaller than that for the *previous* spectrum.

By the way, the Pt/Pz cut was originally designed for the KEK E391A experiment which was the pilot experiment of the KOTO, to reject the CV-η background. In this background, the beam neutrons interact with the charged veto counter named "CV", and produce η mesons. The details of the background is described in Appendix A.2.2. There is an opinion that this cut should be modified because the configuration of the CV is changed in the KOTO experiment from E391a experiment, but the cut is not optimized yet for KOTO. I suggest that we should be careful to the high-momentum $K_L \to \pi^+\pi^-\pi^0$ backgrounds when we modify this cut.

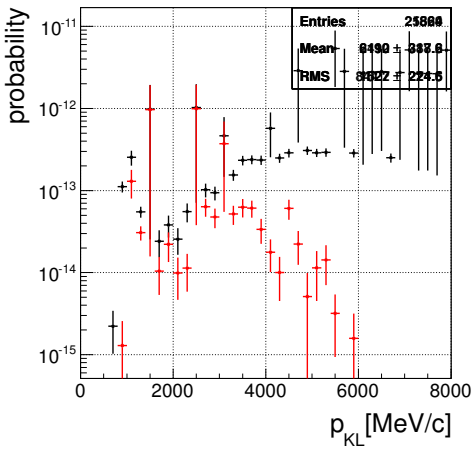

Figure 9.15: Product of the decay probability, the geometrical acceptance, and the kinematic cut efficiency for the $K_L \to \pi^+\pi^-\pi^0$ background events with the weight of veto inefficiency. For the black dots, only the E_γ cut, the calorimeter fiducial cut, the π^0 Pt cut and the Z-vertex cut are applied. All the kinematic cuts are applied for the red dots.

Chapter 10

Conclusion

The J-PARC KOTO experiment studies the $K_L \to \pi^0\nu\bar{\nu}$ decay, which is a sensitive probe for the direct CP violation in the Standard Model, and also a new physics beyond the Standard Model. Only two photons from the π^0 are observable in this decay mode. We observe them by using a CsI electromagnetic calorimeter.

The CsI calorimeter measures the energies and incident positions of the two photons. These are the sole kinematic information obtained in this experiment. The kinematic selection cuts based on these variables are important to distinguish the signal events from the background events. Because of the small crystal sizes, the shower shape information of the incident particles are also obtained with the calorimeter. Background events with abnormal cluster shapes are suppressed by using the shape information, in particular, the "fusion" $K_L \to \pi^0\pi^0$ background.

Before my studies described in this thesis, the energy and position resolutions of the calorimeter in the KOTO experimental condition had not been fully measured yet. As for the shower shape information, the study was developed based on the Monte Carlo simulation, but the consistency of the electromagnetic shower shape between the data and the Monte Carlo had not been checked yet.

I measured these values in the engineering runs conducted in February and June in 2012. I placed a spectrometer which consisted of a magnet and three drift chambers in upstream of the CsI calorimeter to measure the electrons from the $K_L \to \pi e\nu$ decays. By using the momentum-analyzed electrons as a reference, I measured the resolutions of the CsI calorimeter, and also studied the shower shapes. This is the first measurement of the CsI calorimeter performance with the actual CsI calorimeter, and also the first test using almost the same criteria with the physics run for the clustering, energy and position corrections in the CsI calorimeter.

The energy resolution was measured as $\sigma_E/E = (0.66\pm0.52)\%\oplus(1.81\pm0.04)\%/\sqrt{E[GeV]}$ for the small crystals, and $(1.71 \pm 0.17)\% \oplus (1.31 \pm 0.10)\%/\sqrt{E[GeV]}$ for the large

crystals of the calorimeter. The position resolution was measured as $\sigma_X = (1.99 \pm 0.23) \oplus (3.95 \pm 0.35)/\sqrt{E[GeV]}$ mm for small crystals, and $(6.17 \pm 0.18) \oplus (4.01 \pm 0.40)/\sqrt{E[GeV]}$ mm for the large crystals. These values were consistent with the Monte Carlo simulation within 1.5σ, except the energy resolution of the large crystals. The effect of the difference on the background estimation for the KOTO experiment was studied and estimated to be negligible. The uncertainties of the measurement are small enough that they do not change the background estimation.

There were inconsistencies between the data and the Monte Carlo in the distribution of the variables related to the shower shapes. Due to these inconsistencies, cut efficiencies for the shape χ^2, the number of crystals in the cluster, and the cluster RMS differ by at most 4 %, $10 \sim 15\%$, and $5 \sim 9\%$, respectively, between the data and the Monte Carlo. I modified the physics models used in the Monte Carlo simulation to improve the data – Monte Carlo consistency. The differences of the efficiencies became about a half with the modification.

I simultaneously measured the K_L momentum spectrum with the engineering run data. The spectrum was previously measured in 2010, but that measurement had large uncertainties and no sensitivity in the > 4 GeV/c range. I derived the spectrum by analyzing the $K_L \to \pi^+\pi^-$ decays and the $K_L \to \pi^+\pi^-\pi^0$ decays. The uncertainties of the spectrum shape around its peak became 1/2 of the previous measurement. The spectrum shape in the momentum region > 4 GeV/c was determined for the first time in KOTO.

These measurements reveals parameters of the KOTO experiment which are basic, but had not been fully understood before. The results described in this thesis will help to reduce several uncertainties of the KOTO physics run.

Appendix A

Cuts and Backgrounds of the KOTO Experiment

The kinematic cuts and the shower shape cuts prepared for the KOTO physics run are described in Section A.1. The types of backgrounds in the KOTO physics run are explained in Section A.2.

In this Appendix, I use a standard coordinate system in the KOTO experiment. The origin is placed at the upstream surface of the "Front Barrel" which is the most upstream veto counter in the KOTO detector. The z axis is parallel to the K_L beam axis. The y axis points vertically up, and the x axis points to the direction for the system to be right-handed. In this coordinate system, the upstream surface of the CsI calorimeter is located at $z = 6.148$ m.

A.1 Selection Cuts

The cut values described in this section are based on the Monte Carlo study, and are tentative. In the physics run, they will be fine-tuned with the data.

A.1.1 Kinematic Cuts

Cuts For π^0

As described in Section 1.3.2, the following two selection cuts are required to the reconstructed π^0 to identify the $K_L \to \pi^0\nu\bar{\nu}$ decay occurring inside the KOTO detector.

- Pt cut.

  The transverse momentum (Pt) of the π^0 should be greater than 130 MeV/c and less than 250 MeV/c. The requirement of lower limit ensures the existence of neutrino, and rejected backgrounds from the $K_L \to \pi^+\pi^-\pi^0$ decays and $K_L \to \gamma\gamma$ decays as described in the next section. The upper limit is determined from the $K_L \to \pi^0\nu\bar{\nu}$ kinematics whose the maximum Pt is 231 MeV/c.

- Z-vertex cut.

  The z position of the decay vertex of the π^0 should be located within 2-m decay volume between z=3 m and 5 m, which is illustrated in Fig. 1.6.

In addition, the following cut is required to suppress the background events.

- Pt/Pz cut.

  The ratio of the π^0 Pt to the z component of the π^0 momentum (Pt/Pz) should satisfy all the three conditions:

$$\begin{aligned} Pt/Pz &> 0.1 \\ Pt/Pz &> 0.05\,(z[\mathrm{m}] - 4) + 0.1 \\ Pt/Pz &< 0.07\,(z[\mathrm{m}] - 3) + 0.2, \end{aligned}$$

  where z represents the z position of the π^0 vertex. This cut are designed to suppress the CV-η background where the beam neutrons interact with the detector component and generate η mesons. The detail of the η background is described later in Section A.2.2. The cut values were optimized based on the study in the KEK E391a experiment and are not optimized for the KOTO experiment yet.

Cuts for 2 photons

The two photons measured with the CsI calorimeter are required to be satisfied conditions listed below.

- E_γ cut.

  Energies of both two photons should be greater than 100 MeV to reject hits due to electrical noises or accidental hits.

- Calorimeter fiducial cut.

  The measured incident position, X and Y, of both photons should satisfy

$$|X| > 150\mathrm{mm}, \quad |Y| > 150\mathrm{mm}, \quad \sqrt{X^2 + Y^2} < 850\mathrm{mm}. \tag{A.1}$$

  These requirements reduce the amount of energy leaking out of the calorimeter through its beam hole or the outer edge.

- Azimuthal angle cut.

  The difference of the azimuthal angles of the two photons should be less than 150 degrees. This requirement rejects photons from the $K_L \to \gamma\gamma$ decay where the difference of azimuthal angle is nearly 180 degrees.

- $E - \theta$ cut.

  The product of the energy and the incident angle of each photon should be less than 2.5 [GeV·degree]. This requirement suppresses a kind of the $K_L \to \pi^0\pi^0$ background where two photons from different π^0s hit the CsI calorimeter. This type of the $K_L \to \pi^0\pi^0$ background is called "odd-pair" background. The details of the background will be described in the next section.

- E ratio cut.

  The ratio of the smaller energy to the larger energy of the two photons should be greater than 0.2. This also suppresses the "odd-pair" $K_L \to \pi^0\pi^0$ background.

- E-total cut.

  The sum of energies of the two photons should be greater than 500 MeV. This requirement rejects π^0's produced downstream of the CsI calorimeter with photons traveling back upstream.

A.1.2 Shower Shape Cuts

Shape χ^2

In the signal events, a cluster should be made from a single electromagnetic shower. To evaluate a consistency of an observed cluster shape with an assumption of the single electromagnetic shower, we calculate a quantity called "shape χ^2" for each cluster in the calorimeter. The shape χ^2 is defined as

$$\chi^2 \equiv \frac{1}{N} \sum_{i}^{\text{in } 27\times 27 \text{ region}} \left(\frac{e_i/E_{inc} - \mu}{\sigma} \right)^2, \tag{A.2}$$

where e_i represents an energy deposit in the i-th crystal in the cluster, E_{inc} is the measured photon energy defined in Eq. (3.7), and N is the number of crystals used in the summation.[1] The range that the sum is calculated, μ and σ are explained below.

[1] The shape χ^2 was originally defined in my master thesis [40]. In that time, the summation range was 11×11 crystals.

1. The range of the summation

   To determine the range, we first calculate the total energy deposit in each row and each column of crystal arrays. The "center crystal" is then defined as the crystal at the intersection of the row and column with the maximum energy deposit. The summation is calculated for all the crystals which are included in the cluster and located in the 27×27 crystal array where the center crystal is located on the intersection of the 9-th row and the 9-th column of the array. A schematic view of the summation range is illustrated in Fig. A.1.

2. The μ and σ

   The μ and σ in Eq. (A.2) represent the mean and RMS of the e_i/E estimated with Geant4 simulation for photons. These are expressed as functions:

   $$\begin{aligned} \mu &= \mu(E_{inc}, \theta_{inc}, \phi_{inc}, q_{row}, q_{column}, x_i, y_i) \\ \sigma &= \sigma(E_{inc}, \theta_{inc}, \phi_{inc}, q_{row}, q_{column}, x_i, y_i), \end{aligned}$$

   where θ_{inc} and ϕ_{inc} are the polar angle and azimuthal angle of the incident photons which are calculated from the measured cluster position and the π^0 vertex position. The q_{row} is defined as

   $$q_{row} \equiv \frac{\max(E^+_{row}, E^-_{row})}{E^{ctr}_{row}}, \tag{A.3}$$

   where E^{ctr}_{row} is the total energy deposit in the row which includes the center crystal, and E^+_{row} and E^-_{row} represent those in the two neighboring rows. The operator "$\max(A, B)$" returns A if $A > B$, otherwise returns B. The q_{column} is the similar quantity to q_{row}, just replacing "row" to "column" in the above explanation. The x_i and y_i are the x and y positions of the i-th crystal.

   To save a computational resource, the μ and σ were prepared only for photons with $0° < \phi_{inc} < 45°$. The crystal positions were modified with y position inversion and rotation appropriately so that the azimuthal angle fitted in the ϕ_{inc} range.

The χ^2 is designed to be $\sim$1 if the incident particle is a photon. Otherwise it will have a larger value. By applying a cut on this value, we suppress backgrounds with an abnormal shower shape, the $K_L \to \pi^0\pi^0$ "fusion" background in particular. In that background, showers of two photons hitting the CsI calorimeter close to each other overlapped and look like one cluster. Such fused clusters tend to have the larger shape χ^2 values. The details of the fusion background will be described in the next section.

We require the shape χ^2 to be less than 2.5.

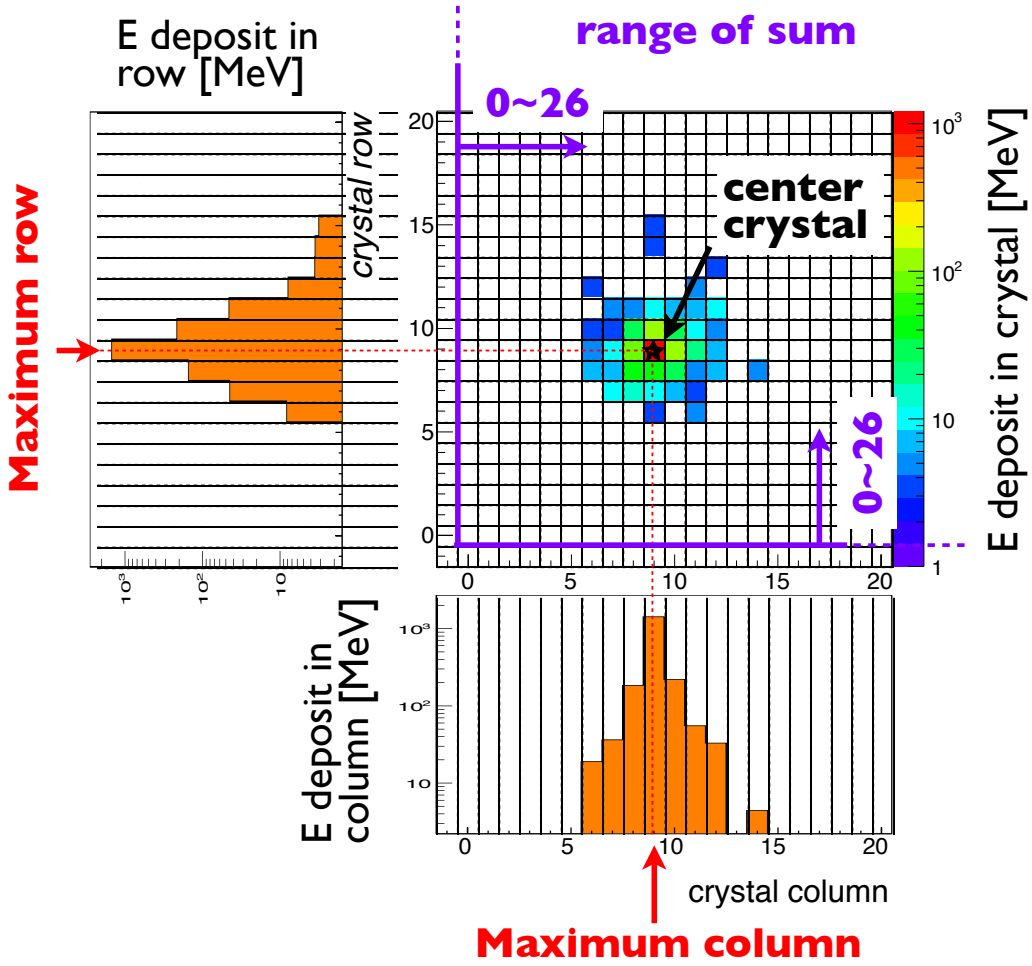

Figure A.1: Schematic view of the center crystal and the range of the summation used in the shape χ^2 calculation. A 2-dimensional histogram shows an example of energy deposits in the cluster. Each bin corresponds to a crystal. The 1-dimensional histograms on the left and bottom show the total energy deposit in each row and each column, respectively. The star mark represents the center crystal. The range of the summation corresponds to the square of 0∼26 columns × 0∼26 rows of the histogram. The purple lines show the edge of the range.

Table A.1: The numbers of signal and background events which are expected in 12-months of data taking with designed beam power. This estimation is quoted from [5].

	source	# expected
signal	$K_L \to \pi^0\nu\bar{\nu}$	2.39 ± 0.03
K-decay backgrounds	$K_L \to \pi^0\pi^0$	1.32 ± 0.04
	$K_L \to \pi^+\pi^-\pi^0$	0.11 ± 0.01
	$K_L \to \pi e\nu$	0.07 ± 0.04
neutron backgrounds	NCC-π^0	0.05 ± 0.02
	CV-π^0	0.04 ± 0.04
	CV-η	0.01 ± 0.01

Other shape variables

The number of crystals in the cluster is a convenient quantity to check the size of the shower. A cluster RMS is defined as

$$RMS_{clus} \equiv \sqrt{\frac{1}{E_{clus}} \sum_i \left\{ e_i \times \left((x_i - X_{clus})^2 + (y_i - Y_{clus})^2 \right) \right\}}, \tag{A.4}$$

where E_{clus}, X_{clus}, and Y_{clus} are an energy, x position, and y position of the cluster defined in Eq. (3.4), and x_i and y_i are the x and y position of the i-th crystal in the cluster. This quantity represents the width of the shower.

Definite cut values are not set for these values, but these are useful to qualify the cluster shape as an electromagnetic shower. For example, I use the number of the crystals to distinguish the electron clusters from the clusters made by MIPs in Chapter 5.

A.2 Backgrounds

Two background sources are considered. One is other K_L decay modes, another is halo neutrons in the beam. The number of signal events and background events in a 12-month data taking with the design beam power (2×10^{14} protons on target per 3.3 seconds) are estimated as shown in Table A.1. The estimation is based on the Monte Carlo study assuming that all the veto detector fully functions as their designs. Each background in the table is explained in the following.

A.2.1 K_L Decay

In all the K_L decays except the $K_L \to \pi^0\nu\bar{\nu}$ and the $K_L \to \gamma\gamma$ decays, there are at least two charged particles or at least two extra photons. Because the KOTO veto system detects those particles with a high efficiency, only the decays with relatively large branching ratio (BR) are possible to be background sources. The $K_L \to \pi^0\pi^0$ decay, $K_L \to \pi^+\pi^-\pi^0$ decay, and $K_L \to \pi e\nu$ decays are considered to be the main background sources. The contribution from the $K_L \to 3\pi^0$ decay is estimated to be negligible. Although the branching ratio is relatively large ($BR = 19.52\%$), the decay accompanies 4 extra photons in its final state and is vetoed easily. The contribution from the $K_L \to \gamma\gamma$ decay is also expected to be negligible, because there is no missing transverse momentum in the event and the Pt cut effectively distinguishes this decay from the $K_L \to \pi^0\nu\bar{\nu}$ decay.

1. The $K_L \to \pi^0\pi^0$ decay.

   The $K_L \to \pi^0\pi^0$ decay ($BR = 8.64 \times 10^{-4}$) is expected to be the largest background source of the KOTO experiment. There are three mechanisms that this decay becomes the background.

   The first one is that the two photons from the same π^0 hit the CsI calorimeter and the other two photons escape detection. This is called "even-pair" background. In this case, the undetected two photons carried the missing transverse momentum as if the neutrinos in the $K_L \to \pi^0\nu\bar{\nu}$ decay. The vertex of the π^0 or the directions of the detected photons are correctly reconstructed. As a result, neither the kinematic cuts nor the shower shape cuts are effective for the even background.

   The second one is that the two photons from the *different* π^0s hit the CsI calorimeter and the other two photons escape. This is called "odd-pair" background. The kinematic cuts are effective for this background because the π^0 should not be reconstructed correctly. The $E - \theta$ cut and the E ratio cut are effective in particular, as shown in Fig. A.2.

   The third type is called "fusion" background where the three of four photons hit the CsI calorimeter, and two of them are so close to each other that their electromagnetic showers overlap and mimic one shower. In this case, the veto efficiency should be lower than other two types because there is only one extra photon. The fused cluster, however, tends to have a different shower shape from that of a normal electromagnetic shower. The cuts on shower shape strongly suppress this background.

   Table A.2 shows a Monte Carlo estimation of the numbers of the three backgrounds in a 12-month data taking with the designed beam power. The odd-pair background is suppressed by a factor 23 by the kinematic cuts for the two

Table A.2: The expected numbers of the $K_L \to \pi^0\pi^0$ background events in 12-month data taking with the design beam power (2×10^{14} protons on target per 3.3 seconds). The acceptance loss due to accidental activities is not included. The estimation for the signal event is also shown.

type	π^0 kine. cuts. & veto	# w/ 2γ kine. cuts	# w/ shape cuts
even-pair	1.99 ± 0.09	1.23 ± 0.07	1.12 ± 0.07
odd-pair	4.35 ± 0.72	0.21 ± 0.13	0.20 ± 0.13
fusion	9.56 ± 0.34	6.75 ± 0.28	0.82 ± 0.10
$K_L \to \pi^0\pi^0$ total	15.92 ± 0.79	8.19 ± 0.31	2.16 ± 0.17
$K_L \to \pi^0\nu\bar{\nu}$	8.07 ± 0.02	4.91 ± 0.01	4.54 ± 0.01

photons and the fusion background is suppressed by a factor 8 by the shower shape cuts. The contribution of the even-pair background becomes largest after applying all the cuts.

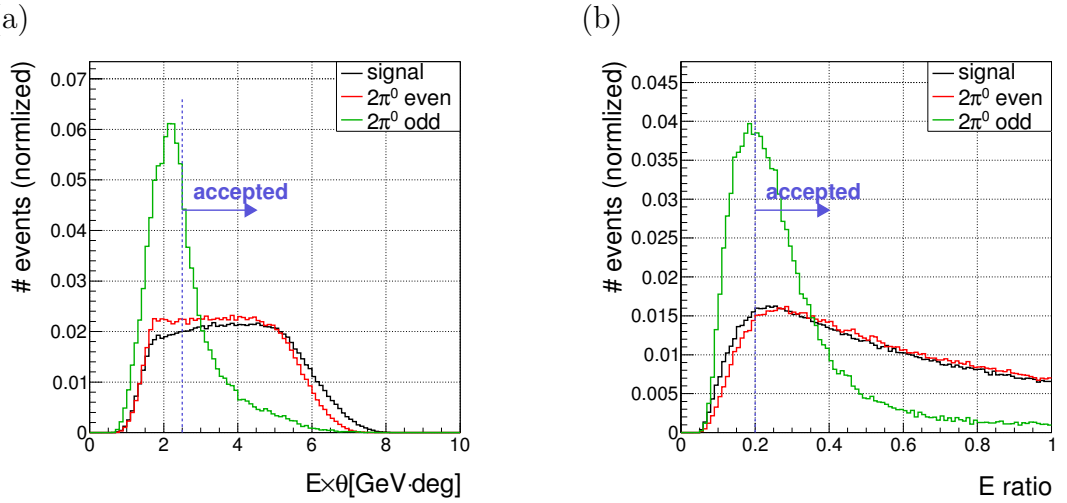

Figure A.2: Kinematics of photons in the signal events (black), the even-pair (red), and the odd-pair $K_L \to \pi^0\pi^0$ backgrounds (green). An energy multiplied by an incident angle of each photon shown in (a). An energy ratio of the two photons shown in (b). A vertical dashed line in each plot represents the cut value. All the kinematic cuts except cuts for quantities drawn here are applied, and neither the veto nor the shower shape cuts are required.

2. The $K_L \to \pi^+\pi^-\pi^0$ decay.

   The $K_L \to \pi^+\pi^-\pi^0$ decay becomes a background source if the two charged pions escape detection. Contributions of the events where one of the two pions escapes through the beam hole is especially dominant, because a detection efficeincy of a charged veto counter in the beam ("BHCV" in Fig. 1.6), is lower than the

other veto counters due to the high flux of beam particles. The Pt of the π^0 is, however, kinematically limited to be less than 133 MeV/c, as shown in Fig. A.3. The Pt cut effectively suppress this background.

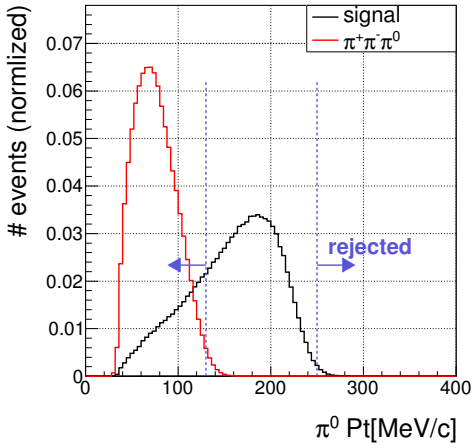

Figure A.3: Transverse momentum of the reconstructed π^0 of the signal events (black) and the $K_L \to \pi^+\pi^-\pi^0$ events (red). Vertical dashed lines show the cut values. All the kinematic cuts except the π^0 Pt cut are applied. Neither the veto nor the shower shape cuts are applied.

3. The $K_L \to \pi e \nu$ decay.

The $K_L \to \pi e \nu$ decay does not accompany a π^0 or two photons. The positron from this decay, however, often annihilates with electrons in the charged veto counter located upstream of the CsI calorimeter ("CV" in Fig. 1.6), and converts to two photons. The π^- is also possible to convert to two photons via the charge exchange interaction with a proton in the CV, that is, $\pi^- + p \to \pi^0(\to 2\gamma) + n$. If both of these interactions occur at the surface of the CV before depositing sufficient energies, the charged particles are not detected in our veto system. If two of the four photons are missed, this decay event becomes a background. Dominant contributions come from the events as follows [41]. The two photons from the π^+ hit the CsI calorimeter and the low energy photon from the e^+ escapes the detection. If the other photon from the e^+ hits close to one of the two photons from the π^+, then their showers overlap and seems as one photon. A schematic view of the event is shown in Fig. A.4. Because there is a fused shower, these events are suppressed with the shower shape cuts by a factor 10.

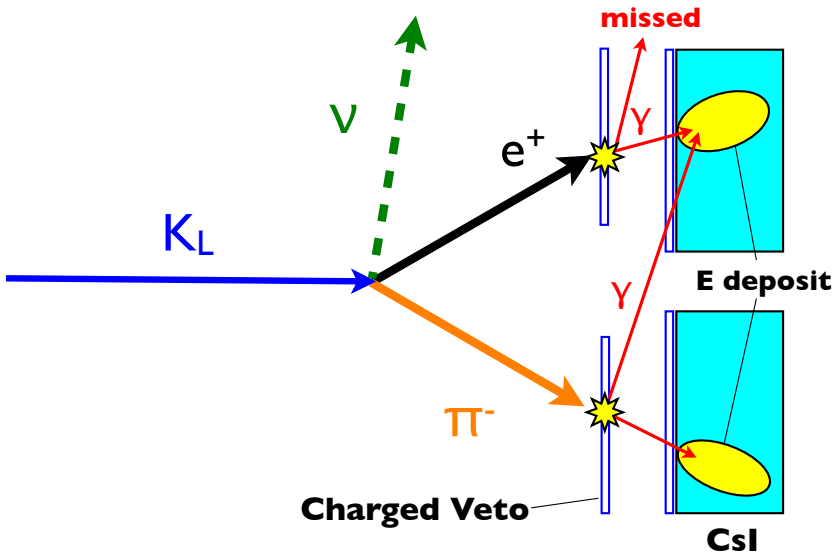

Figure A.4: Schematic view of the $K_L \to \pi e \nu$ background.

A.2.2 Beam Halo Neutron

The beam halo neutrons are possible to be a background source if they interact with a detector component near the beam axis and produce a particle decaying to two photons.

NCC-π^0 background

The largest contribution of the halo neutron backgrounds comes from the π^0 production at "NCC", which is a photon veto counter located upstream of the decay volume as illustrated in Fig. 1.6. If the two photons from π^0 were not detected in the NCC, and hit the CsI calorimeter, this event becomes a background. This is called NCC-π^0 background. We can strongly reject this background by the Z-vertex cut because the π^0 decay vertex is correctly reconstructed at the NCC position if the energies of two photons from the π^0 are correctly measured. Only if the energy of either of the photons is mis-measured lower than the actual energy due to energy leakage or photonuclear interaction, the reconstructed vertex shifts downstream and is possible to be inside the decay volume.

CV-π^0 background

The π^0 produced at the CV is also possible to be a background. This is called CV-π^0 background. Because the decay vertex is reconstructed at the CV position, this

background is also suppressed by the Z-vertex cut. In contrast to the NCC-π^0 background, the reconstructed vertex is possible to be inside the decay volume if the energy of either photon from the π^0 is mis-measured *larger* than the actual energy. This mis-measurement occurs when the energies of extra secondary particles, which are simultaneously produced with the π^0, are added to one of the photon cluster. In that case, the shape of the cluster is different from a normal photon cluster and the shower shape cut is therefore effective to reject this background. The contribution of this background becomes comparable or smaller than the NCC-π^0 background after applying the kinematic cuts and the shower shape cuts.

CV-η background

The η produced at the CV is also possible to be a background if it decays to 2 photons ($BR(\eta \rightarrow 2\gamma) = 39.3\%$). This is called CV-$\eta$ background. The decay vertex is reconstructed more upstream than the actual vertex, because we assumed that the invariant mass of the two photons is equal to the π^0 mass in the vertex reconstruction as described in Section 1.3, but the assumption is wrong in this case. The Z-vertex cut is therefore not effective to this background unlike the NCC-π^0 or the CV-π^0 background. Instead, the shower shape cuts are effective to this background because the incident angles of the photons are reconstructed much smaller than the actual angles, and consequently the observed shower shapes are different from the shapes expected from those incident angles.

Appendix B

Monte Carlo

I used a Monte Carlo simulation based on Geant4 to reproduce the data. The result of the simulation was used in Section 4.3 to derive the momentum resolution and the position resolution of the spectrometer, in Chapter 7 to estimate the energy and position fluctuation of electrons due to the materials in the experimental area, and in Chapter 8 to evaluate the acceptance of the $K_L \to \pi^+\pi^-$ and $K_L \to \pi^+\pi^-\pi^0$ decays. In addition, the Monte Carlo expectations were shown in several plots to check the consistency with the measured result.

In the simulation, primary particles, K_Ls and neutrons which are described in Section B.1, were generated from Z=-1m. The interactions of the primary particle and its daughter particles with the materials except for the CsI calorimeter were simulated based on FTF_BIC package in Geant4. Hits on the drift chambers and hits on the trigger scintillators were reproduced with a criteria described in Section B.2. As for the CsI calorimeter, the electromagnetic or hadronic showers in it took long CPU time to simulate. To save the time, the interactions in the calorimeter were simulated only for the events where there were at least two hits on the trigger scintillators, and at least one hit in every wire plane of the drift chambers. The interactions in the CsI calorimeter were simulated based on Geant4 QGSP_BERT package . The reproduction of the response of the CsI calorimeter is described in Section B.2. The same analysis criteria was then applied to the simulation data as the measured data.

B.1 Primary Particle Generation

B.1.1 K_L

Initial position and direction

The initial position and direction of the primary K_L was determined with the following steps, based on the geometry of the production target and the beam-line collimators which were described in Section 2.1. First we decided a x and y point on the target, X_{tgt} and Y_{tgt}. The X_{tgt} and Y_{tgt} virtually corresponded to the interaction point of the proton from the accelerator, and randomly distributed in $-9.1 \sim 9.1$ mm for X_{tgt} and in $-1 \sim 1$ mm for Y_{tgt} according to the target geometry. The K_L was assumed to be produced from that point, and its flight direction was decided at isotropically random. We then required the K_L flight trajectory to pass through the entrance of the collimator which is located 7 m downstream of the target. The size was $-7.6 \sim 7.6$ mm in x and $-12.5 \sim 12.5$ mm in y. The X_{tgt}, Y_{tgt}, and K_L flight direction were chosen repeatedly until this requirement was satisfied, and was adopted as the initial direction of the primary K_L. The K_L trajectory was then extrapolated to 20 m downstream of the target which corresponded to z=-1m. The position of the trajectory there was adopted as the initial position of the primary K_L.

Momentum spectrum

To calculate the acceptance of the $K_L \to \pi^+\pi^-$ decays and $K_L \to \pi^+\pi^-\pi^0$ decays in Chapter 8, the momentum of the primary K_L distributed uniformly between 0 and 10 GeV/c . Otherwise the momentum spectrum measured in Chapter 8 was used.

Decays

The standard K_L in Geant4 has only 4 main decay modes: $K_L \to \pi e \nu$, $K_L \to \pi \mu \nu$, $K_L \to 3\pi^0$, and $K_L \to \pi^+\pi^-\pi^0$. It does not have the $K_L \to \pi^+\pi^-$ decay channel which was used to measure the K_L momentum spectrum in Chapter 8. Furthermore, a flat phase space is assumed for the $K_L \to 3\pi^0$ decay and the $K_L \to \pi^+\pi^-\pi^0$ decay in Geant4. We therefore designed and used custom K_L decay routines.

The decay matrices, M, for the $K_L \to 3\pi^0$ decay and the $K_L \to \pi^+\pi^-\pi^0$ decay were replaced as [26]

$$|M|^2 \propto 1 + g\frac{s_3 - s_0}{m^2_{\pi^+}} + h\left(\frac{s_3 - s_0}{m^2_{\pi^+}}\right)^2 + k\left(\frac{s_2 - s_1}{m^2_{\pi^+}}\right)^2, \tag{B.1}$$

where $s_i (i = 0 \sim 3)$ were defined as

$$s_i \equiv (p_K - p_i)^2 \text{, for } i = 1, 2, 3, \tag{B.2}$$

$$s_0 \equiv \frac{1}{3}\left(m_K^2 + m_1^2 + m_2^2 + m_3^2\right). \tag{B.3}$$

Here p_K and p_i are the four-vectors of the K_L and the i-th pion, respectively. Similarly m_K and m_i are their masses. The index 3 is allocated for a π^0, and the indexes 1 and 2 are allocated for the other two pions. The g, h and k in Eq. (B.1) were [26]

$$g = 0 \tag{B.4}$$

$$h = -0.005 \tag{B.5}$$

$$k = 0 \tag{B.6}$$

for the $K_L \to 3\pi^0$ decay and

$$g = 0.678 \tag{B.7}$$

$$h = 0.076 \tag{B.8}$$

$$k = 0.0099 \tag{B.9}$$

for the $K_L \to \pi^+\pi^-\pi^0$ decay. The directions and energies of the three pions were determined according to this $|M|^2$.

We separately prepared the K_L decaying to only $\pi^+\pi^-$ channel, because this decay mode has a relatively small branching ratio, $BR(K_L \to \pi^+\pi^-) \sim (1.97 \pm 0.01) \times 10^{-3}$, and it is not efficient to simulate this decay mode simultaneously with the main decay modes. The two daughter pions with the same energies were produced isotropically in the K_L rest frame, by using G4PhaseSpaceDecayChannel class prepared in Geant4.

B.1.2 Neutron

The initial positions, directions and the energies of the primary neutrons were obtained by an independent Monte Carlo simulation with Geant3 [24]. In the simulation, the neutrons produced in the target were propagated to the exit of the collimator. The simulation included interactions with the materials in the beam line such as the collimator or the gamma absorber. The position, direction, and energy of each neutron at the exit of the collimator were stored, and used for the primary neutrons in our simulation.

B.2 Detector Response

B.2.1 Trigger Scintillators

Energy deposits in trigger scintillator modules were summed. The sum of deposits greater than 1.5 MeV was treated as a hit. The timing information was not stored because the drift length in the drift chambers were reproduced without using it, as described next.

B.2.2 Drift Cambers

Neither the production nor the drift of ionization electrons in the chamber gas were simulated. Instead, I stored the passage point of charged particles at each wire plane. The nearest wire to the passage point was assumed to have a hit, and the drift length d was calculated as

$$d = |X_{path} - X_{wire}| \cos\theta_X \tag{B.10}$$

for x-wire planes, where X_{path} and X_{wire} represent the x position of the passage point and the hit-wire position, respectively. The θ_X denotes the incident angle projected in x-z plane. A schematic view of drift length reproduction is shown in Fig. B.1. For y-wire planes, replace x in this explanation with y.

In addition, the drift lengths were fluctuated as

$$d \to d' = d + \mathrm{rand}(f_{com}) + \mathrm{rand}(f_{int}), \tag{B.11}$$

where f_{com} and f_{int} were the probability distributions of fluctuations measured in Section 4.3.1. The "rand(f)" means a random value based on a given distribution f. The rand(f_{com}) was common to all the drift lengths in that event, while the rand(f_{int}) differed for each hit.

B.2.3 CsI Calorimeter

In Geant4 simulation, a particle in a material moves step by step, and an interaction between a particle and a material is simulated for each step. The step length is determined according to the cross-sections of interactions implemented in the simulation. The energy deposit on the material is calculated by each step. We stored the energy deposit, timing, and position of every step in the CsI calorimeter. An energy deposit in a CsI crystal, E, was then calculated as

$$E = \sum_{i}^{\text{in the CsI}} e_i \tag{B.12}$$

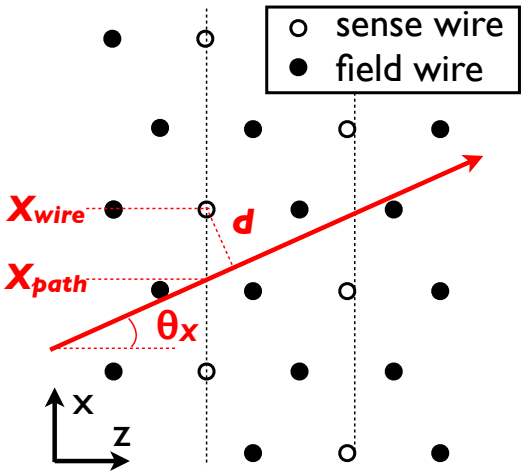

Figure B.1: Schematic view of the drift length reproduction in the simulation.

where e_i represents an energy deposit of the i-th step in the crystal, and the sum is calculated for all the steps in the crystal. The index i is assigned in the order of time. The timing of the crystal, T, was defined as

$$T = t_j, \tag{B.13}$$

where t_j represents a timing of the j-th step in the crystal, where the index j satisfies

$$\sum_{i=0}^{j-1} e_i < \frac{E}{2} < \sum_{i=0}^{j} e_i. \tag{B.14}$$

The *real* CsI crystals, however, have several sources of the fluctuations in both energy and timing which were not included in the simulation. To reproduce the response of the CsI calorimeter as realistically as possible, the energy in Eq. (B.12) and timing in Eq. (B.13) were modified to include such effects. The sources of fluctuations and the modifications for them are explained below.

1. Light yield dispersion

   The scintillation light yield was different among the CsI crystals. In addition, the light yield was not uniform along z direction. The relative light yield and the "nonuniformity" along the z direction of each crystal was measured before the crystals were installed, by using a ^{137}Cs radioactive source. The PMT output for 667 keV gamma-rays from ^{137}Cs was measured for every 2.5-cm step along the z direction. We defined the relative light yield as

$$LY_{rel}(z, ID_{CsI}) = \frac{LY_{^{137}Cs}(z, ID_{CsI})}{\langle \langle LY_{^{137}Cs}(z, ID_{CsI}) \rangle_z \rangle_{CsI}} \tag{B.15}$$

where $LY_{^{137}Cs}(z, ID_{CsI})$ represents the output of the crystal with a crystal ID=ID_{CsI} due to ^{137}Cs placed at z. The $\langle X \rangle_z$ means the average of X for all the 2.5-cm steps along the z direction, while the $\langle X \rangle_{CsI}$ means the average for all the crystals. Figure B.2 shows the distribution of the relative light yield averaged along the z direction, or $\langle LY_{rel}(z, ID_{CsI}) \rangle_z$. The light yield differed by ∼20% among the crystals. We also found that the light yield differed along the z direction, as shown in Fig. B.3. The difference fell within ±10% for most of crystals.

To reproduce this effect in the simulation, Eq. (B.12) was modified as

$$E = \sum_{i}^{\text{in the CsI}} e_i \times LY_{rel}(z_i) \tag{B.16}$$

where z_i represent the z position of the i-th interaction, and $LY_{rel}(z)$ is the relative light yield of the crystal at z.

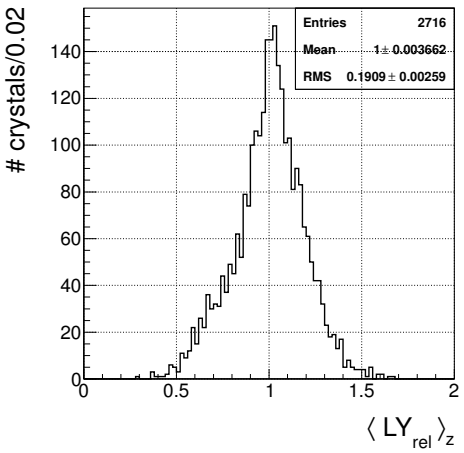

Figure B.2: The $\langle LY_{rel} \rangle_z$: a relative light yield of each crystal averaged along the z direction.

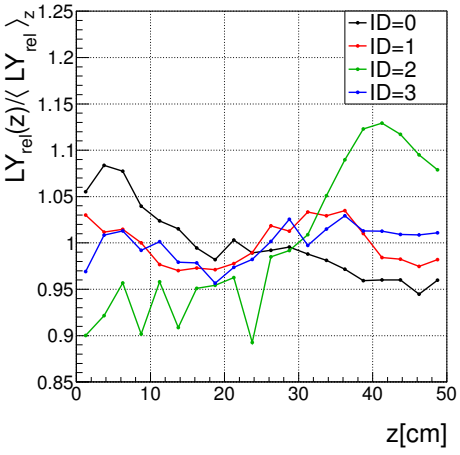

Figure B.3: Position dependence of light yield of each crystal. The relative light yields of four crystals (ID=0∼4) are shown as a function of the z position in the crystal (the PMT surface coressponds to z=0).

2. A photoelectron fluctuation.

The number of photoelectrons at the PMT should fluctuate according to Poisson distribution. The typical number of the photoelectrons per MeV, $n_{p.e.}$, was measured using cosmic-rays [4], as $n_{p.e.} = 12.7$ [photoelectrons/MeV]. To reproduce this fluctuation in the simulation, the energy of each crystal, E in Eq. (B.16), was modified as

$$E \to \frac{\text{Poisson}(E \times n_{p.e.})}{n_{p.e.}}, \tag{B.17}$$

where Poisson(x) means a random value according to the Poisson distribution whose mean value is x.

3. The accuracy of the energy calibration.

   In the data, the energy in each crystal was calculated from the waveform integral of the crystal by multiplying the calibration factor. The accuracy of the calibration factor was measured as $0.669 \pm 0.016\%$ in Section 5.4. The energy of each crystal, E, in the simulation was fluctuated according to the normal distribution whose width was equal to this accuracy.

4. The timing resolution of each crystal.

   The timing resolution of a crystal was measured in the past beam test [4], as already shown in Eq. (3.5). The timing of each crystal, T in Eq. (B.13), in the simulation was fluctuated according to the normal distribution whose σ was equal to this resolution.

Appendix C

Chamber Alignment

The drift chambers were placed so that their wire planes were perpendicular to the z-axis. Their positions were measured with a LASER marking instrument and a stainless steel ruler. The accuracy of the measurement was estimated as 0.5 mm for x and y directions from the width of the LASER maker. The accuracies in the z direction were estimated as 0.5 mm for the 1st chamber, and 2 mm for the 2nd and 3rd chambers.

A displacement of the measured positions of the drift chambers from the real positions were estimated by using charged tracks in the data. In this Appendix, I will describe how the displacements were determined.

C.1 Displacement of Drift Chambers

The center positions of the three drift chambers are denoted as

$$\vec{r}_i^{ctr} \equiv (x_i^{ctr}, y_i^{ctr}, z_i) \quad (i = 1, 2, 3), \tag{C.1}$$

where $i = 1, 2$, and 3 indicates the 1st, 2nd, and 3rd chamber, respectively. The hit position on the chamber relative to its center is described as

$$\vec{r}_i^{wire} \equiv (x_i^{wire}, y_i^{wire}, 0) \quad (i = 1, 2, 3). \tag{C.2}$$

If there is no displacement, the hit position on the i-th chamber, $\vec{r}_i$, is then represented as

$$\vec{r}_i \equiv \vec{r}_i^{wire} + \vec{r}_i^{ctr} \tag{C.3}$$

$$\equiv (x_i, y_i, z_i) \quad (i = 1, 2, 3). \tag{C.4}$$

The displacement of the chambers are expressed with the rotations around their centers and the parallel translations . I defined the translation vectors and the rotation matrix of i-th chamber as

$$\vec{\delta_i} \equiv (\delta_{ix}, \delta_{iy}, \delta_{iz}) \,, \tag{C.5}$$

and

$$\hat{\theta}_i \equiv \begin{pmatrix} 0 & -\theta_{iz} & \theta_{iy} \\ \theta_{iz} & 0 & -\theta_{ix} \\ -\theta_{iy} & \theta_{ix} & 0 \end{pmatrix}, \tag{C.6}$$

where I assumed $\theta_{ix(yz)} \ll 1$ and ignored $\mathrm{O}(\theta^2)$ terms. A variable with "hat", like $\hat{A}$, means a matrix.

Considering the displacement, Eq. (C.3) is modified as

$$\vec{r_i} \to \vec{r'}_i \equiv \left(1 + \hat{\theta}_i\right) \vec{r}_i^{wire} + \vec{r}_i^{ctr} + \vec{\delta_i} \tag{C.7}$$

$$\equiv (x'_i, y'_i, z'_i) \quad (i = 1, 2, 3). \tag{C.8}$$

Hereafter, I use the prime mark ($'$) for quantities which take the displacement into account.

Our task is to derive the $\vec{\delta_i}$ and $\hat{\theta}_i$ from the data. These displacement were determined with reference to the 1st chamber, that is, I assumed the $\vec{\delta_1} = \vec{0}$ and $\hat{\theta}_1 = \hat{1}$. The $\vec{\delta_2}$, $\hat{\theta}_2$ and $\hat{\theta}_3$ were derived by using data with straight tracks. The δ_{3x} and δ_{3y} were determined by using the $K_L \to \pi^+\pi^-$ events. The δ_{3z} cannot be derived from the data and I assumed $\delta_{3z} = 0$. In the rest of this section, I will explain the details of the derivation of the $\vec{\delta}$s and $\hat{\theta}$s.

C.1.1 Translation and Rotation of the 2nd Chamber

The $\vec{\delta_2}$ and $\hat{\theta}_2$ were determined by using a special run data where the spectrometer magnet was turned off. In the data, charged tracks should be straight, and the hit position recorded in the 2nd chamber should lie on the straight line which joined the hit positions on the 1st and 3rd chambers. Assuming that the 1st and 3rd chamber have no displacement, the straight track can be reconstructed as

$$\vec{X}(z) = \vec{s}(z - z_1) + \vec{r}_1, \tag{C.9}$$

where $\vec{s}$ represents the slope of the track:

$$\vec{s} \equiv (\vec{r}_3 - \vec{r}_1)/(z_3 - z_1) \tag{C.10}$$

$$\equiv (s_x, s_y, 1) \,. \tag{C.11}$$

The hit position on the 2nd chamber, $\vec{r'}_2$, should be on this track, *i.e.*:

$$\vec{r'}_2 - \vec{X}(z'_2) = \vec{0}. \tag{C.12}$$

We do not know yet the displacement of the 2nd chamber and the $\vec{r'}_2$ is not observable but $\vec{r}_2$ is. Replacing $\vec{r'}_2$ in Eq. (C.12) with $\vec{r}_2$, I defined the observable quantity $\vec{\Delta}_2$ as

$$\begin{aligned} \vec{\Delta}_2 &\equiv \vec{r}_2 - \vec{X}(z_2) \\ &= (\Delta_{2x}, \Delta_{2y}, 0)\,. \end{aligned} \tag{C.13}$$

Rewriting Eq. (C.12) to make the $\vec{\Delta}_2$ visible,

$$\begin{aligned} \vec{r'}_2 - \vec{X}(z'_2) &= 0 \\ &= \left(1+\hat{\theta}_2\right)\vec{r}_2^{wire} + \vec{r}_2^{ctr} + \vec{\delta}_2 - \left(\vec{X}(z_2) - \vec{s}(z_2 - z'_2)\right) \\ &= \vec{r}_2 - \vec{X}(z_2) + \hat{\theta}_2\vec{r}_2^{wire} + \vec{\delta}_2 - \vec{s}\left(-x_2^{wire}\theta_{2y} + y_2^{wire}\theta_{2x} + \delta_{2z}\right) \\ &= \vec{\Delta}_2 + \hat{\theta}_2\vec{r}_2^{wire} + \vec{\delta}_2 - \vec{s}\left(-x_2^{wire}\theta_{2y} + y_2^{wire}\theta_{2x} + \delta_{2z}\right) \\ \therefore \begin{pmatrix} \Delta_{2x} \\ \Delta_{2y} \end{pmatrix} &= -\begin{pmatrix} \delta_{2x} \\ \delta_{2y} \end{pmatrix} + \begin{pmatrix} s_x \\ s_y \end{pmatrix}\delta_{2z} \\ &\quad + \begin{pmatrix} y_2^{wire}s_x \\ y_2^{wire}s_y \end{pmatrix}\theta_{2x} - \begin{pmatrix} x_2^{wire}s_x \\ x_2^{wire}s_y \end{pmatrix}\theta_{2y} + \begin{pmatrix} y_2^{wire} \\ -x_2^{wire} \end{pmatrix}\theta_{2z}. \end{aligned} \tag{C.14}$$

Each component of the $\vec{\delta}_2$ and $\hat{\theta}_2$ were observed as the correlation between its coefficient vector in this equation and the $\vec{\Delta}_2$. For example, the θ_{2x} was observed as the slope of a plot of $\Delta_{2x(y)}$ vs $y_2^{wire}s_{x(y)}$. Because the coefficient vectors were not independent each other, I adopted the iteration process to determine the $\vec{\delta}_2$ and $\hat{\theta}_2$. First, the δ_{2x} and δ_{2y} were determined as the peak position of the Δ_{2x} and Δ_{2y} shown in Fig. C.1(a), respectively. The θ_{2z} was also derived as the slope of $\Delta_{2x}(\Delta_{2y})$ vs $y_2^{wire}(-x_2^{wire})$ plot which is shown in Fig. C.1(b). By taking the derived δ_{2x}, δ_{2y}, and θ_{2z} into consideration, the $\vec{\Delta}_2$ was calculated again, and then the remaining components were determined. The δ_{2z} was derived as the slope of the Δ_{2x} (Δ_{2y}) vs s_x (s_y) plot which is shown in Fig. C.1(c). The θ_{2x} was derived from the slopes of the plots of Δ_{2x} (Δ_{2y}) vs $-y_2 s_x$ ($-y_2 s_y$) which is shown in Fig. C.1(d). Similarly θ_{2y} was derived from the Δ_{2x} (Δ_{2y}) vs $-x_2 s_x$ ($-x_2 s_y$) plot. Furthermore, the $\vec{\Delta}_2$ was iteratively calculated 4 more times, and the $\vec{\delta}_2$ and $\hat{\theta}_2$ were updated in each iteration.

C.1.2 Rotation of the 3rd Chamber

The rotation of the 3rd chamber, $\hat{\theta}_3$, was derived by also using the straight-track data. Events with two tracks were used, which originated dominantly in K_L decays. Each of the two tracks could be expressed with hit positions on the 1st and 3rd chamber,

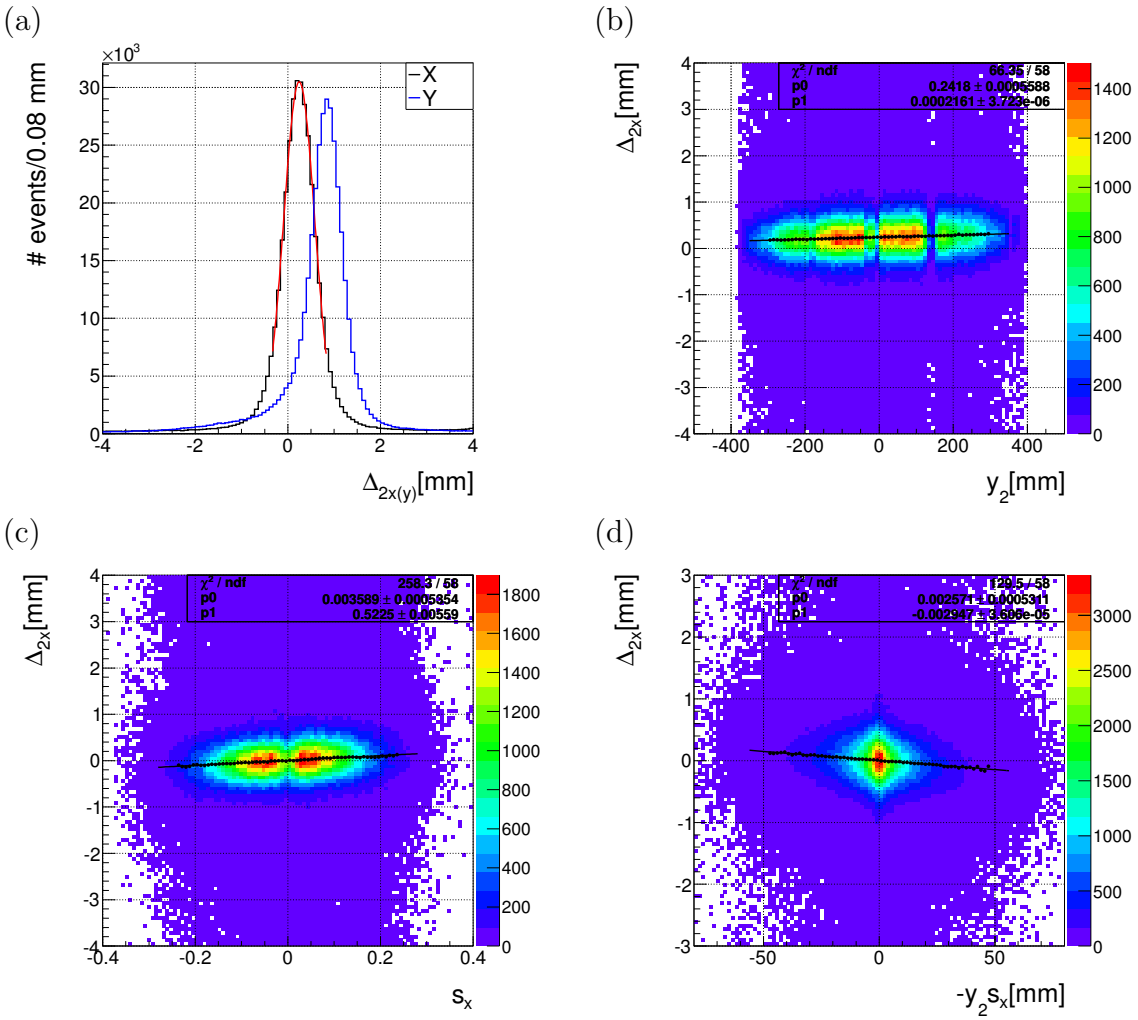

Figure C.1: Plots to derive the displacement of the 2nd chamber, $\vec{\delta}_2$ and $\hat{\theta}_2$. (a) The Δ_{2x} (black) and Δ_{2y} (blue) measured in the data. The peak positions were determined by fitting Gaussian which is shown in a red line. (b) Dependence of the Δ_{2x} on the y_2^{wire}. (c) Dependence of the Δ_{2x} on the s_x. (d) Dependence of the Δ_{2x} on the $-y_2^{wire}s_x$. The θ_{2z}, δ_{2z}, and θ_{2x} were determined from the slopes of (b),(c), and (d), respectively.

$\vec{r}_1$ and $\vec{r'}_3$, as

$$\vec{X'}_T(z) = \vec{s'}_T(z - z_1) + \vec{r}_{1T} \quad (T = A \text{ or } B), \tag{C.15}$$

where $T = A$ or B represents a tag of track. The s_T represents the slope of the track and is defined as

$$\begin{aligned} \vec{s'}_T &\equiv \left(\vec{r'}_{3T} - \vec{r}_{1T}\right)/(z'_{3T} - z_1) && \text{(C.16)} \\ &= \left(s'_{xT}, s'_{yT}, 1\right). && \text{(C.17)} \end{aligned}$$

The position difference between the two tracks at a given z is

$$\begin{aligned} \vec{X'}_A(z) - \vec{X'}_B(z) &= \left(\vec{s'}_A - \vec{s'}_B\right)(z - z_1) + (\vec{r}_{1A} - \vec{r}_{1B}) \\ \left(\Delta_{AB}\vec{X'}(z)\right) &= \left(\Delta_{AB}\vec{s'}\right)(z - z_1) + \left(\Delta_{AB}\vec{r}_1\right), \end{aligned} \tag{C.18}$$

where the notation $\Delta_{AB}Q$ means $Q_A - Q_B$ for a given quantity Q. The $|\left(\Delta_{AB}\vec{X'}(z)\right)|$ becomes minimum at

$$z'_{min} = z_1 - \frac{\left(\Delta_{AB}\vec{s'}\right)\cdot\left(\Delta_{AB}\vec{r}_1\right)}{\left(\Delta_{AB}\vec{s'}\right)^2}. \tag{C.19}$$

Because the two tracks comes from the same vertex, the minimum value should be zero, *i.e.*:

$$\begin{aligned} \left(\Delta_{AB}\vec{X'}(z'_{min})\right) &= -\left(\Delta_{AB}\vec{s'}\right)\frac{\left(\Delta_{AB}\vec{s'}\right)\cdot\left(\Delta_{AB}\vec{r}_1\right)}{\left(\Delta_{AB}\vec{s'}\right)^2} + \left(\Delta_{AB}\vec{r}_1\right) && \text{(C.20)} \\ &= \vec{0}. && \text{(C.21)} \end{aligned}$$

Because we do not know the displacement of the 3rd chamber yet, the $\vec{r'}_{3T}$ is not an observable but $\vec{r}_{3T}$ is. Consequently, the $\vec{s'}_T$, z'_{min} and $\left(\Delta_{AB}\vec{X'}(z'_{min})\right)$ are not observables. The observable quantities are

$$\vec{s}_T \equiv \left(\vec{r}_{3T} - \vec{r}_{1T}\right)/(z_{3T} - z_1), \tag{C.22}$$

$$z_{min} \equiv z_1 - \frac{\left(\Delta_{AB}\vec{s}\right)\cdot\left(\Delta_{AB}\vec{r}_1\right)}{\left(\Delta_{AB}\vec{s}\right)^2}, \tag{C.23}$$

and

$$\left(\Delta_{AB}\vec{X}(z_{min})\right) = -\left(\Delta_{AB}\vec{s}\right)\frac{\left(\Delta_{AB}\vec{s}\right)\cdot\left(\Delta_{AB}\vec{r}_1\right)}{\left(\Delta_{AB}\vec{s}\right)^2} + \left(\Delta_{AB}\vec{r}_1\right). \tag{C.24}$$

I define $\vec{\epsilon}$ as the difference of the $\vec{s'}$ and the $\vec{s}$, *i.e.*:

$$\vec{\epsilon}_T \equiv \vec{s'}_T - \vec{s}_T. \tag{C.25}$$

The difference of $\vec{\epsilon}$'s of two tracks can be written as

$$\begin{aligned}(\Delta_{AB}\vec{\epsilon}) &= \vec{\epsilon}_A - \vec{\epsilon}_B \\ &= \frac{1}{z_3 - z_1}\left\{(\Delta_{AB}\vec{c}_x)\,\theta_{3x} + (\Delta_{AB}\vec{c}_y)\,\theta_{3y} + (\Delta_{AB}\vec{c}_z)\,\theta_{3z} + (\Delta_{AB}\vec{s})\,\delta_{3z}\right\},\end{aligned} \tag{C.26}$$

where

$$\vec{c}_x = \begin{pmatrix} -y^{wire}_{3T} s_{Tx} \\ -y^{wire}_{3T} s_{Ty} \\ 0 \end{pmatrix}, \quad \vec{c}_y = \begin{pmatrix} x^{wire}_{3T} s_{Tx} \\ x^{wire}_{3T} s_{Ty} \\ 0 \end{pmatrix}, \quad \vec{c}_z = \begin{pmatrix} y^{wire}_{3T} \\ x^{wire}_{3T} \\ 0 \end{pmatrix}. \tag{C.27}$$

The computation process to derive Eq. (C.26) is described in Appendix D.4.1: "Verbose Calculation".

Substituting Eq. (C.23), Eq. (C.24) and Eq. (C.25) into Eq. (C.20),

$$\begin{aligned}\left(\Delta_{AB}\vec{X}'(z'_{min})\right) \sim\ & \left(\Delta_{AB}\vec{X}(z_{min})\right) + (z_{min} - z_1)\,(\Delta_{AB}\vec{\epsilon}) \\ & -\frac{(\Delta_{AB}\vec{s})}{(\Delta_{AB}\vec{s})^2}\left\{\left(2\left(\Delta_{AB}\vec{X}(z_{min})\right) - (\Delta_{AB}\vec{r}_1)\right)\cdot(\Delta_{AB}\vec{\epsilon})\right\}\end{aligned} \tag{C.28}$$

The computation process to derive Eq. (C.28) is also described in Appendix D.4.2. Note that the left-hand side, $\left(\Delta_{AB}\vec{X}'(z'_{min})\right)$, is 0. Substituting Eq. (C.26),

$$\left(\Delta_{AB}\vec{X}(z_{min})\right) = \vec{d}_x\theta_{3x} + \vec{d}_y\theta_{3y} + \vec{d}_z\theta_{3z}, \tag{C.29}$$

where

$$\begin{aligned}\vec{d}_r &= \frac{1}{z_3 - z_1} \times \\ &\left\{\frac{(\Delta_{AB}\vec{s})}{(\Delta_{AB}\vec{s})^2}\left(2\left(\Delta_{AB}\vec{X}(z_{min})\right) - (\Delta_{AB}\vec{r}_1)\right)\cdot(\Delta_{AB}\vec{c}_r) - (z_{min} - z_1)\,(\Delta_{AB}\vec{c}_r)\right\},\end{aligned} \tag{C.30}$$

where $r = x, y$ and z. The θ_{3x}, θ_{3y}, and θ_{3z} were thus related to the $\Delta_{AB}\vec{X}(z_{min})$. I calculated the inner product of $\Delta_{AB}\vec{X}(z_{min})$ and each coefficient vector, $\vec{d}_x, \vec{d}_y$, and $\vec{d}_z$. The $\theta_{3x(y,z)}$ was derived as a slope of a 2-dimensional plot of the inner product versus $|\vec{d}_{x(y,z)}|$, as shown in Fig. C.2. Because the $\vec{d}_x, \vec{d}_y$, and $\vec{d}_z$ had correlations between each other, I determined them with an iterative process. Once estimating the θs, I made the 2-dimensional plots again with taking the estimated θs into account, and the θs were updated from the plots. This process was iterated 4 times.

(a) (b)

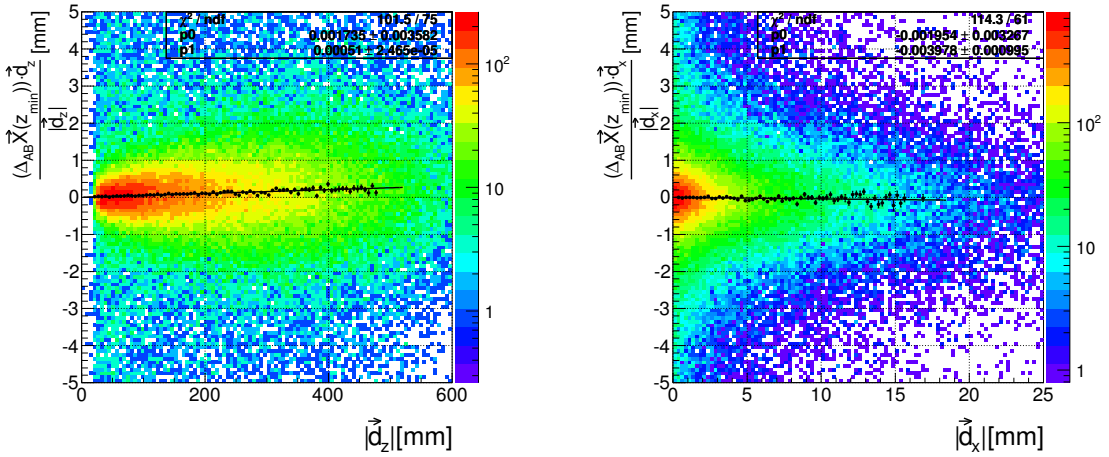

Figure C.2: Plots to derive the rotation of the 3rd chamber, $\hat{\theta}_3$. (a)$\left(\Delta_{AB}\vec{X}(z_{min})\right)\cdot\vec{d}_z/|\vec{d}_z^2|$. (b)$\left(\Delta_{AB}\vec{X}(z_{min})\right)\cdot\vec{d}_x/|\vec{d}_x^2|$.

C.1.3 Translation of the 3rd Chamber

The K_L beam direction was measured with a beam profile monitor [42] before the runs started. The direction of the K_L beam was also reconstructed with the spectrometer by using the $K_L \to \pi^+\pi^-$ decays, although that direction depends on the translation of the 3rd chamber $\vec{\delta}_3$. I determined the x and y translation of the 3rd chamber δ_{3x} and δ_{3y} so that the K_L direction reconstructed with the spectrometer became consistent with the direction measured with the monitor.

After the $\vec{\delta}_2$, $\hat{\theta}_2$, and $\hat{\theta}_3$ were determined, I did the tracking process described in Section 4.1 and reconstructed the two charged particle events. I described the total momentum of the two charged particles as $\vec{p}$, and the vector from the production target to the vertex of the two tracks as $\vec{V}$. If $\vec{\delta}_3 = \vec{0}$, and the events came from the $K_L \to \pi^+\pi^-$ decay, the $\vec{p}$ should be equal to the K_L momentum, and be parallel to the $\vec{V}$, *i.e:*

$$\frac{\vec{p}}{p_z} - \frac{\vec{V}}{V_z} = \vec{0}, \tag{C.31}$$

where p_z and V_z are the z-components of $\vec{p}$ and $\vec{V}$. If $\vec{\delta}_3 \neq \vec{0}$, the momentum direction of K_L was observed to be different from the real direction. As a result, Eq. (C.31) was modified to be

$$\frac{\vec{p}}{p_z} - \frac{\vec{V}}{V_z} \sim \frac{\vec{\delta}_3}{z_3 - z_1}. \tag{C.32}$$

Figure C.3(a) and (b) show the measured $p_x/p_z - V_x/V_z$ and $p_y/p_z - V_y/V_z$. A sharp peak was considered to come from the $K_L \to \pi^+\pi^-$ decays. The peak position was

Table C.1: Estimation of the chamber displacement.

(translation)

chamber	δ_x[mm]	δ_y[mm]	δ_z[mm]
1st	0 ± 0.5	0 ± 0.5	0 ± 0.5
2nd	0.1956 ± 0.0009	-1.2398 ± 0.0006	0.522 ± 0.011
3rd	0.558 ± 0.047	-0.526 ± 0.086	0 ± 2

(rotation)

chamber	θ_x[mrad]	θ_y[mrad]	θ_z[mrad]
1st	0 ± 1	0 ± 0.7	0 ± 0.7
2nd	1.349 ± 0.075	1.031 ± 0.033	0.670 ± 0.004
3rd	-4.67 ± 0.82	0.78 ± 0.63	0.513 ± 0.010

determined by fitting a double-Gaussian as also shown in the figures. Consequently, δ_{3x} and δ_{3y} were determined from Eq. (C.32).

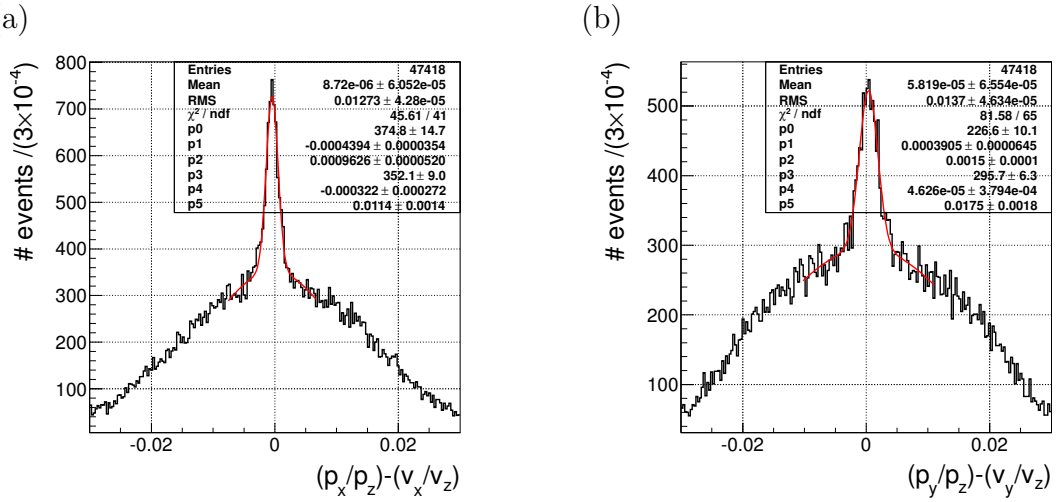

Figure C.3: Components of the left-hand side of Eq. (C.32) observed in the data. The x and y component is shown in (a) and (b), respectively. The peaks in the plots were considered to originate from the $K_L \to \pi^+\pi^-$ decays, and their position were determined by fitting double-Gaussians shown in red lines.

C.1.4 Accuracy

The estimated values of the $\vec{\delta}$s and $\hat{\theta}$s are shown in Table C.1. The $\vec{\delta}_1$, $\hat{\theta}_1$, and δ_{3z} were assumed to be 0, and their errors are the uncertainties of the measurement with the ruler and the LASER marking instrument. The errors of δ_{3x} and δ_{3y} are the errors of fitting which were described in Section C.1.3 and are shown in Fig. C.3. To estimate

errors of the $\vec{\delta}_2$, $\hat{\theta}_2$, and $\hat{\theta}_3$, I divided the data into 6 subsets. The derivation of those values were executed for each subset, and the RMS of the 6 results was adopted as the error of the value.

Appendix D

Verbose Calculation

D.1 Calculation in Chapter4

D.1.1 Double Integral in Eq. (4.6)

As described in Section 4.1.3, I used the tracking method based on [31, 32]. In this method, the track path was represented by the function in Eq. (4.6) as,

$$\begin{aligned} x_{\rm path}(z) &= x_{\rm path}(0) + x'_{\rm path}(0)z + \frac{1}{p}\int_0^z dz \int_0^{z'} dz\ p x''_{\rm path}(z) \\ y_{\rm path}(z) &= y_{\rm path}(0) + y'_{\rm path}(0)z + \frac{1}{p}\int_0^z dz \int_0^{z'} dz\ p y''_{\rm path}(z). \end{aligned} \tag{D.1}$$

In this section, I will describe how we can estimate the double integrals in the equations, without knowing the exact form of $x_{\rm path}(z)$ and $y_{\rm path}(z)$.

From the equation of motion of a charged particle with a mass m in magnetic field $\vec{B} \equiv (B_x, B_y, B_z)$,

$$\frac{d^2 x_{path}}{dt^2} = \left(\frac{dy_{path}}{dt}B_z - \frac{dz}{dt}B_y\right) \times \frac{1}{m} \tag{D.2}$$

$$\frac{d^2 y_{path}}{dt^2} = \left(\frac{dz}{dt}B_x - \frac{dx_{path}}{dt}B_z\right) \times \frac{1}{m} \tag{D.3}$$

$$\frac{d^2 z}{dt^2} = \left(\frac{dx_{path}}{dt}B_y - \frac{dy_{path}}{dt}B_x\right) \times \frac{1}{m}. \tag{D.4}$$

The x'_{path} can be rewritten using time derivatives as

$$\begin{aligned} x'_{path} &\equiv \frac{dx_{path}}{dz} \\ &= \frac{dx_{path}}{dt}\frac{dt}{dz} \\ &= \frac{dx_{path}}{dt}\Big/\frac{dz}{dt}. \end{aligned} \tag{D.5}$$

Similarly,

$$y'_{path} = \frac{dy_{path}}{dt}\Big/\frac{dz}{dt}. \tag{D.6}$$

The x''_{path} can be rewritten as

$$\begin{aligned} x''_{path} &\equiv \frac{d^2x_{path}}{dz^2} \\ &= \frac{d}{dz}\frac{dx_{path}}{dz} \\ &= \frac{d}{dz}\frac{dx_{path}}{dt}\Big/\frac{dz}{d_t} \\ &= \left(\frac{dz}{dt}\right)^{-3}\left(\frac{dz}{dt}\frac{d^2x_{path}}{dt^2} - \frac{dx_{path}}{dt}\frac{d^2z}{dt^2}\right). \end{aligned} \tag{D.7}$$

By inserting Eqs. (D.2), (D.4), and (D.6) into Eq. (D.7),

$$x''_{path} = m^{-1}\left(\frac{dz}{dt}\right)^{-1}\left(y'_{path}B_z - \left(1 + x'_{path}\right)B_y + x'_{path}y'_{path}B_x\right). \tag{D.8}$$

The momentum p can be expressed as

$$\begin{aligned} p &\equiv m\left(\left(\frac{dx_{path}}{dt}\right)^2 + \left(\frac{dy_{path}}{dt}\right)^2 + \left(\frac{dz}{dt}\right)^2\right) \\ &= m\frac{dz}{dt}\left(\left(x'_{path}\right)^2 + \left(y'_{path}\right)^2 + 1\right). \end{aligned} \tag{D.9}$$

With Eq. (D.8) and Eq. (D.9), the px''_{path}, which is the function to be integrated in Eq. (D.1), can be written as

$$px''_{path} = \left(\left(x'_{path}\right)^2 + \left(y'_{path}\right)^2 + 1\right)\left(y'_{path}B_z - \left(1 + x'_{path}\right)B_y + x'_{path}y'_{path}B_x\right). \tag{D.10}$$

The slopes, x'_{path} and y'_{path}, in the right-hand side of this equation are unknown, but we can roughly estimate them by interpolating the hit positions on the three chambers

with a cubic-spline curve. I evaluated the slopes and the magnetic field on every 20-mm intervals on the spline curve, and calculated the px''_{path} on each interval. An interpolation with a cubic-spline curve was then taken for the px''_{path} values. Reminding a cubic-spline curve is just a set of N polynomial functions of the third order where N is the number of intervals, we can calculate its double integral analytically without any numerical calculation. We thus can estimate the double integral in Eq. (4.6). This estimation was a rough approximation. After once executing the fitting as described in Section 4.1.3, however, we can calculate the px''_{path} on each interval more precisely with using the fitted track path. Iterating the fitting 6 times, the estimation of the double integral was well converged.

D.1.2 Minimization of χ^2 Defined in Eq. (4.7)

We do not need any numerical calculation to minimize the χ^2 defined in Eq. (4.7). This saves a computing time for tracking, which is an advantage of this tracking method.

Substituting Eq. (4.6), Eq. (4.7) is rewritten as

$$\begin{aligned}\chi^2 &= \sum_{i}^{\text{x wire plane}} \frac{\left(X_i - x_{\text{path}}(0) - x'_{\text{path}}(0)Z_i - p^{-1}D_x(Z_i)\right)^2}{\sigma_{di}^2} \\ &+ \sum_{i}^{\text{y wire plane}} \frac{\left(Y_i - y_{\text{path}}(0) - y'_{\text{path}}(0)Z_i - p^{-1}D_y(Z_i)\right)^2}{\sigma_{di}^2},\end{aligned} \tag{D.11}$$

where $D_x(z)$ and $D_y(z)$ represent the double integrals appeared in Eq. (4.6). The free parameters are $x_{\text{path}}(0)$, $x'_{\text{path}}(0)$, $y_{\text{path}}(0)$, $y'_{\text{path}}(0)$, and p^{-1}. Partial differentials of

the χ^2 by those parameters are

$$\begin{aligned}
\frac{\partial\chi^2}{\partial x_{\rm path}(0)} &= \sum_i^{\text{x wire plane}} \frac{-1\times 2}{\sigma_{di}^2}\left(X_i - x_{\rm path}(0) - x'_{\rm path}(0)Z_i - p^{-1}D_x(Z_i)\right)\\
\frac{\partial\chi^2}{\partial x'_{\rm path}(0)} &= \sum_i^{\text{x wire plane}} \frac{-Z_i\times 2}{\sigma_{di}^2}\left(X_i - x_{\rm path}(0) - x'_{\rm path}(0)Z_i - p^{-1}D_x(Z_i)\right)\\
\frac{\partial\chi^2}{\partial y_{\rm path}(0)} &= \sum_i^{\text{y wire plane}} \frac{-1\times 2}{\sigma_{di}^2}\left(Y_i - y_{\rm path}(0) - y'_{\rm path}(0)Z_i - p^{-1}D_y(Z_i)\right)\\
\frac{\partial\chi^2}{\partial y'_{\rm path}(0)} &= \sum_i^{\text{y wire plane}} \frac{-Z_i\times 2}{\sigma_{di}^2}\left(Y_i - y_{\rm path}(0) - y'_{\rm path}(0)Z_i - p^{-1}D_y(Z_i)\right)\\
\frac{\partial\chi^2}{\partial p^{-1}} &= \sum_i^{\text{x wire plane}} \frac{-D_x\times 2}{\sigma_{di}^2}\left(X_i - x_{\rm path}(0) - x'_{\rm path}(0)Z_i - p^{-1}D_x(Z_i)\right)\\
&+ \sum_i^{\text{y wire plane}} \frac{-D_y\times 2}{\sigma_{di}^2}\left(Y_i - y_{\rm path}(0) - y'_{\rm path}(0)Z_i - p^{-1}D_y(Z_i)\right)
\end{aligned} \tag{D.12}$$

It should be noted that the right-hand sides of all of these equations are the linear combination of the parameters. When the χ^2 becomes minimum, all the partial differentials should be zero. The parameter set which minimizes the χ^2 are then determined as the solution of these 5 simultaneous equations. Because all of them are linear equations, we can solve them by using Gaussian elimination. Thus the χ^2 is minimized without any numerical calculation.

D.2 Calculation in Chapter 7

D.2.1 Error of the E Resolution of the Calorimeter

The energy resolution and position resolution of the CsI calorimeter derived in Chapter 7 were expressed with the same functional form, as

$$f(E) = p_1 \oplus \frac{p_2}{\sqrt{E[GeV]}} \oplus \frac{p_3}{E[GeV]}, \tag{D.13}$$

except that the p_3 is fixed to zero for the position resolution. The parameters were determined by fitting this equation to the data. The error of f can be written with covariance matrix elements, cov_{ij}, which were calculated in the fitting process, and

partial derivatives $\partial f/\partial p_i$ as

$$\sigma_f(E) = \sqrt{\sum_i \sum_j \frac{\partial f}{\partial p_i}\frac{\partial f}{\partial p_j}\mathrm{cov}_{ij}} \tag{D.14}$$

where, i, j = 1,2,3. The diagonal elements of the covariance matrix, cov_{ii}, are defined as square of errors of parameters. Each partial derivatives are analytically calculated as

$$\frac{\partial f}{\partial p_1} = \frac{p_1}{f} \tag{D.15}$$

$$\frac{\partial f}{\partial p_2} = \frac{p_2}{fE[GeV]} \tag{D.16}$$

$$\frac{\partial f}{\partial p_3} = \frac{p_3}{fE^2[GeV^2]}. \tag{D.17}$$

D.3 Calculation in Chapter 8

D.3.1 Error of the Function of Momentum Spectrum

The momentum spectrum $f(p_{K_L})$ was represented with the function in Eq. (8.7), as

$$f(p_{K_L}) = A \cdot \exp\left(-\frac{(p_{K_L}[\mathrm{GeV}] - \mu)^2}{2\left(\sigma(p_{K_L})\right)^2}\right), \tag{D.18}$$

where σ is a function of p_{K_L}, defined as

$$\sigma(p_{K_L}) = a\left(1 - (b + cp_{K_L}[\mathrm{GeV}]) \cdot (p_{K_L}[\mathrm{GeV}] - \mu)\right). \tag{D.19}$$

The error of the function was calculated as

$$\sigma_f = \sqrt{\sum_i^5 \sum_j^5 \frac{\partial f}{\partial p_i}\frac{\partial f}{\partial p_j}\mathrm{cov}_{ij}}, \tag{D.20}$$

where p_is ($i = 1 \sim 5$) correspond to 5 parameters of $f(p_{K_L})$, that is, A, μ, a, b, and c, respectively. The cov_{ij} is a covariance matrix which was derived in the fitting process, and its diagonal elements, cov_{ii}, is the square of the fitting error of the i-th parameter.

The partial derivatives are calculated as

$$\begin{aligned}
\frac{\partial f}{\partial A} &= \frac{f}{A} \\
\frac{\partial f}{\partial \mu} &= f\left\{\frac{p_{K_L}[\mathrm{GeV}]-\mu}{\sigma^2}+\frac{\left(p_{K_L}[\mathrm{GeV}]-\mu\right)^2}{\sigma^2}\frac{b+cp_{K_L}[\mathrm{GeV}]}{1-\left(b+cp_{K_L}[\mathrm{GeV}]\right)\left(p_{K_L}[\mathrm{GeV}]-\mu\right)}\right\} \\
\frac{\partial f}{\partial a} &= f\frac{\left(p_{K_L}[\mathrm{GeV}]-\mu\right)^2}{a\sigma^2} \\
\frac{\partial f}{\partial b} &= f\left(\frac{\left(p_{K_L}[\mathrm{GeV}]-\mu\right)^2}{\sigma^2}\frac{\mu-p_{K_L}[\mathrm{GeV}]}{1-\left(b+cp_{K_L}[\mathrm{GeV}]\right)\left(p_{K_L}[\mathrm{GeV}]-\mu\right)}\right) \\
\frac{\partial f}{\partial c} &= f\left(\frac{\left(p_{K_L}[\mathrm{GeV}]-\mu\right)^2}{\sigma^2}\frac{p_{K_L}[\mathrm{GeV}]\left(\mu-p_{K_L}[\mathrm{GeV}]\right)}{1-\left(b+cp_{K_L}[\mathrm{GeV}]\right)\left(p_{K_L}[\mathrm{GeV}]-\mu\right)}\right)
\end{aligned} \tag{D.21}$$

D.4 Calculation in Appedix C

D.4.1 Derivation of Eq. (C.26)

Substituting Eq. (C.7) into Eq. (C.16), the $\vec{s'}_T$ is written as

$$\begin{aligned}
\vec{s'}_T &= \frac{\vec{r'}_{3T}-\vec{r}_{1T}}{z'_{3T}-z_1} \\
&= \frac{\hat{\theta}_3\vec{r}^{wire}_{3T}+\vec{\delta}_3+\vec{r}_{3T}-\vec{r}_{1T}}{\left(\hat{\theta}_3\vec{r}^{wire}_{3T}+\vec{\delta}_3\right)_z+z_3-z_1} \\
&= \left(\vec{s}_T+\frac{\hat{\theta}_3\vec{r}^{wire}_{3T}+\vec{\delta}_3}{z_3-z_1}\right)\left(1+\frac{\left(\hat{\theta}_3\vec{r}^{wire}_{3T}+\vec{\delta}_3\right)_z}{z_3-z_1}\right)^{-1},
\end{aligned} \tag{D.22}$$

where the notation $(\vec{Q})_z$ means a z component of a given vector $\vec{Q}$. Because $\left(\hat{\theta}_3\vec{r}^{wire}_{3T}+\vec{\delta}_3\right)_z \ll z_3-z_1$, the $\vec{s'}_T$ can be approximated as

$$\begin{aligned}
\vec{s'}_T &\sim \left(\vec{s}_T+\frac{\hat{\theta}_3\vec{r}^{wire}_{3T}+\vec{\delta}_3}{z_3-z_1}\right)\left(1-\frac{\left(\hat{\theta}_3\vec{r}^{wire}_{3T}+\vec{\delta}_3\right)_z}{z_3-z_1}\right) \\
&\sim \vec{s}_T+\frac{\hat{\theta}_3\vec{r}^{wire}_{3T}+\vec{\delta}_3}{z_3-z_1}-\vec{s}_T\frac{\left(\hat{\theta}_3\vec{r}^{wire}_{3T}+\vec{\delta}_3\right)_z}{z_3-z_1}.
\end{aligned} \tag{D.23}$$

where I ignored $O((\delta/(z_3 - z_1))^2)$ term. Substituting Eq. (D.23) into the definition of $\vec{\epsilon}$ in Eq. (C.25),

$$\begin{aligned} \vec{\epsilon}_T &= \frac{1}{z_3 - z_1}\left\{\hat{\theta}_3 \vec{r}_{3T}^{wire} + \vec{\delta}_3 - \vec{s}_T\left(\hat{\theta}_3 \vec{r}_{3T}^{wire} + \vec{\delta}_3\right)_z\right\} \\ \therefore (\Delta_{AB}\vec{\epsilon}) &= \frac{1}{z_3 - z_1}\left\{\hat{\theta}_3\left(\Delta_{AB}\vec{r}_3^{wire}\right) - (\Delta_{AB}\vec{s})\,\delta_{3z} - \theta_{3x}\left(\Delta_{AB}\vec{s}y_3^{wire}\right) + \theta_{3y}\left(\Delta_{AB}\vec{s}x_3^{wire}\right)\right\}. \end{aligned} \tag{D.24}$$

I defined $\vec{c}_x, \vec{c}_y$ and $\vec{c}_z$ as Eq. (D.4.1), *i.e.*:

$$\vec{c}_{Tx} = \begin{pmatrix} -y_{3T}^{wire} s_{Tx} \\ -y_{3T}^{wire} s_{Ty} \\ 0 \end{pmatrix}, \quad \vec{c}_{Ty} = \begin{pmatrix} x_{3T}^{wire} s_{Tx} \\ x_{3T}^{wire} s_{Ty} \\ 0 \end{pmatrix}, \quad \vec{c}_{Tz} = \begin{pmatrix} y_{3T}^{wire} \\ x_{3T}^{wire} \\ 0 \end{pmatrix}.$$

Then,

$$\left(\Delta_{AB}\vec{s}y_3^{wire}\right) = (\Delta_{AB}\vec{c}_x), \quad \left(\Delta_{AB}\vec{s}x_3^{wire}\right) = (\Delta_{AB}\vec{c}_y), \quad \hat{\theta}_3\left(\Delta_{AB}\vec{r}_3^{wire}\right) = (\Delta_{AB}\vec{c}_z)\,\theta_{3z}. \tag{D.25}$$

Substituting Eq. (D.25) into Eq. (D.24), we obtained Eq. (C.26), *i.e.*:

$$(\Delta_{AB}\vec{\epsilon}) = \frac{1}{z_3 - z_1}\left\{(\Delta_{AB}\vec{c}_x)\,\theta_{3x} + (\Delta_{AB}\vec{c}_y)\,\theta_{3y} + (\Delta_{AB}\vec{c}_z)\,\theta_{3z} + (\Delta_{AB}\vec{s})\,\delta_{3z}\right\}.$$

D.4.2 Derivation of Eq. (C.28)

Substituting Eq. (C.25) into Eq. (C.20),

$$\begin{aligned} \left(\Delta_{AB}\vec{X}'(z'_{min})\right) &= -(\Delta_{AB}\vec{s} + \Delta_{AB}\vec{\epsilon})\,\frac{(\Delta_{AB}\vec{s} + \Delta_{AB}\vec{\epsilon})\cdot(\Delta_{AB}\vec{r}_1)}{(\Delta_{AB}\vec{s} + \Delta_{AB}\vec{\epsilon})^2} + (\Delta_{AB}\vec{r}_1) \\ &\sim -(\Delta_{AB}\vec{s} + \Delta_{AB}\vec{\epsilon})\,\frac{(\Delta_{AB}\vec{s} + \Delta_{AB}\vec{\epsilon})\cdot(\Delta_{AB}\vec{r}_1)}{(\Delta_{AB}\vec{s})^2\left(1 + 2\frac{(\Delta_{AB}\vec{s})\cdot(\Delta_{AB}\vec{\epsilon})}{(\Delta_{AB}\vec{s})^2}\right)} + (\Delta_{AB}\vec{r}_1), \end{aligned} \tag{D.26}$$

where a value with ϵ^2 is ignored. Because the $\vec{\epsilon}$ is minute, the denominator in this equation can be approximated as

$$\left(1 + 2\frac{(\Delta_{AB}\vec{s})\cdot(\Delta_{AB}\vec{\epsilon})}{(\Delta_{AB}\vec{s})^2}\right)^{-1} \sim 1 - 2\frac{(\Delta_{AB}\vec{s})\cdot(\Delta_{AB}\vec{\epsilon})}{(\Delta_{AB}\vec{s})^2}. \tag{D.27}$$

Using this approximation and ignoring the term with ϵ^2, Eq. (D.26) becomes

$$\begin{aligned}\left(\Delta_{AB}\vec{X}'(z'_{min})\right) &\sim -\left(\Delta_{AB}\vec{s}+\Delta_{AB}\vec{\epsilon}\right)\frac{\left(\Delta_{AB}\vec{s}+\Delta_{AB}\vec{\epsilon}\right)\cdot\left(\Delta_{AB}\vec{r}_1\right)}{\left(\Delta_{AB}\vec{s}\right)^2}\left(1-2\frac{\left(\Delta_{AB}\vec{s}\right)\cdot\left(\Delta_{AB}\vec{\epsilon}\right)}{\left(\Delta_{AB}\vec{s}\right)^2}\right)\\ &\quad +\left(\Delta_{AB}\vec{r}_1\right)\\ &\sim -\left(\Delta_{AB}\vec{s}\right)\frac{\left(\Delta_{AB}\vec{s}\right)\cdot\left(\Delta_{AB}\vec{r}_1\right)}{\left(\Delta_{AB}\vec{s}\right)^2}+\left(\Delta_{AB}\vec{r}_1\right)\\ &\quad -\left(\Delta_{AB}\vec{\epsilon}\right)\frac{\left(\Delta_{AB}\vec{s}\right)\cdot\left(\Delta_{AB}\vec{r}_1\right)}{\left(\Delta_{AB}\vec{s}\right)^2}-\left(\Delta_{AB}\vec{s}\right)\frac{\left(\Delta_{AB}\vec{\epsilon}\right)\cdot\left(\Delta_{AB}\vec{r}_1\right)}{\left(\Delta_{AB}\vec{s}\right)^2}\\ &\quad +2\left(\Delta_{AB}\vec{s}\right)\frac{\left(\Delta_{AB}\vec{s}\right)\cdot\left(\Delta_{AB}\vec{r}_1\right)}{\left(\Delta_{AB}\vec{s}\right)^2}\frac{\left(\Delta_{AB}\vec{\epsilon}\right)\cdot\left(\Delta_{AB}\vec{s}\right)}{\left(\Delta_{AB}\vec{s}\right)^2}. \qquad \text{(D.28)}\end{aligned}$$

Substituting Eq. (C.23) and Eq. (C.24), we obtained Eq. (C.28), *i.e.*:

$$\begin{aligned}\left(\Delta_{AB}\vec{X}'(z'_{min})\right) &= \left(\Delta_{AB}\vec{X}\left(z_{min}\right)\right)+\left(\Delta_{AB}\vec{\epsilon}\right)\left(z_{min}-z_1\right)\\ &\quad -\frac{\left(\Delta_{AB}\vec{s}\right)}{\left(\Delta_{AB}\vec{s}\right)^2}\left\{\left(2\left(\Delta_{AB}\vec{X}\left(z_{min}\right)\right)-\left(\Delta_{AB}\vec{r}_1\right)\right)\cdot\left(\Delta_{AB}\vec{\epsilon}\right)\right\}.\end{aligned}$$

Bibliography

[1] D. M. Straub, in *Proceedings of the 6th International Workshop on the CKM Unitarity Triangle, UK, 2010*, edited by Tim Gershon, eConf C100906, (2010), arXiv:1012.3893 [hep-ph].

[2] S. Nagamiya, Progress of Theoretical and Experimental Physics **2012** (2012).

[3] J-PARC web cite : http://j-parc.jp/.

[4] E. Iwai, *CsI calorimeter for the J-PARC KOTO experiment*, PhD thesis, Osaka University, 2012.

[5] K. Shiomi, *Measurement of KL flux at the J-PARC neutral-kaon beam line for the KL->pi0 nu nubar*, PhD thesis, Kyoto University, 2012.

[6] J. H. Christenson, J. W. Cronin, V. L. Fitch, and R. Turlay, Phys. Rev. Lett. **13**, 138 (1964).

[7] (KTeV Collaboration), A. Alavi-Harati *et al.*, Phys. Rev. Lett. **83**, 22 (1999).

[8] (NA48 Collaboration), V. Fanti *et al.*, Phys. Lett. **B465**, 335 (1999).

[9] (Belle Collaboration), K. Abe *et al.*, Phys. Rev. Lett. **87**, 091802 (2001).

[10] (BABAR Collaboration), B. Aubert *et al.*, Phys. Rev. Lett. **87**, 091801 (2001).

[11] M. Kobayashi and T. Maskawa, Prog. Theor. Phys. **49**, 652 (1973).

[12] A. J. Buras, M. E. Lautenbacher, and G. Ostermaier, Phys. Rev. D **50**, 3433 (1994).

[13] L. Wolfenstein, Phys. Rev. Lett. **51**, 1945 (1983).

[14] A. Buras, arXiv:hep-ph/9806471 (1998).

[15] T. Inami and C. S. Lim, Prog. Theor. Phys. **65**, 297 (1981).

[16] G. Buchalla, A. J. Buras, and M. K. Harlander, Nucl. Phys. B **349**, 1 (1991).

[17] W. J. Marciano and Z. Parsa, Phys. Rev. D **53**, R1 (1996).

[18] F. Mescia and C. Smith, Phys. Rev. D **76**, 034017 (2007).

[19] J. Brod, M. Gorbahn, and E. Stamou, Phys. Rev. D **83**, 034030 (2011).

[20] A. J. Buras, T. Ewerth, S. Jager, and J. Rosiek, Nucl. Phys. B **714**, 103 (2005).

[21] (E949 Collaboration), A. V. Artamonov *et al.*, Phys. Rev. D **79**, 092004 (2009).

[22] (E391a Collaboration), J. K. Ahn *et al.*, Phys. Rev. D **81**, 072004 (2010).

[23] (KOTO Collaboration), K. Shiomi *et al.*, Nucl. Inst. Meth. A **664**, 264 (2012).

[24] (KOTO Collaboration), T. Shimogawa, Nucl. Inst. Meth. A **623**, 585 (2010), 1st International Conference on Technology and Instrumentation in Particle Physics.

[25] ANSYS web cite : http://www.ansys.com/.

[26] (Particle Data Group), J. Beringer *et al.*, Phys. Rev. D **86**, 010001 (2012).

[27] M. Itaya *et al.*, Nucl. Inst. Meth. A **522**, 477 (2004).

[28] T. Masuda *et al.*, Nuclear Instruments and Methods in Physics Research Section A: Accelerators, Spectrometers, Detectors and Associated Equipment **746**, 11 (2014).

[29] T. Ohska *et al.*, Nuclear Science, IEEE Transactions on **33**, 98 (1986).

[30] T. Masuda, *Development and Experimental Study of the KOTO Detector System using Three KL Neutral Decay Modes*, PhD thesis, Kyoto University, 2014.

[31] H. Wind, Nucl. Inst. Meth. **115**, 431 (1974).

[32] H. Wind, Nucl. Inst. Meth. **153**, 195 (1978).

[33] R. Brun and F. Rademakers, Nucl. Inst. Meth. A **389**, 81 (1997), See also http://root.cern.ch/.

[34] S. Schmitt, arXiv:1205.6201 [physics.data-an] (2012).

[35] (KTeV Collaboration), T. Alexopoulos *et al.*, Phys. Rev. D **70**, 092006 (2004).

[36] J. Allison *et al.*, IEEE Trans. Nucl. Sci. **53**, 270 (2006).

[37] N.Gagunashvili, arXiv:physics/0605123 [physics.data-an] (2006).

[38] see Geant4 9.5 Release Note, http://geant4.cern.ch/.

[39] J. Confort *et al.*, (2006), "Proposal for $K_L \to \pi^0\nu\bar{\nu}$ Experiment at J-Parc", http://j-parc.jp/researcher/Hadron/en/pac 0606/pdf/p14-Yamanaka.pdf.

[40] K. Sato, Discrimination of background events by shower shape on csi calorimeter, Master's thesis, Osaka University, 2008, (written in Japanese).

[41] K. Shiomi, Studies on background events in j-parc e14 experiment, Master's thesis, Kyoto University, 2008, (written in Japanese).

[42] (KOTO Collaboration), G. Takahashi *et al.*, Jpn. J. Appl. Phys **50**, 036701 (2011).